Experimental and computational studies of hydroxyl radical kinetics at very low temperatures.

Robin Joseph Shannon

Submitted in accordance with the requirements for the degree of Doctor of Philosophy

The University of Leeds
School of Chemistry

July, 2012

The candidate confirms that the work submitted is his own, except where work which has formed part of jointly-authored publications has been included. The contribution of the candidate and the other authors to this work has been explicitly indicated below. The candidate confirms that appropriate credit has been given within the thesis where reference has been made to the work of others.

The chapter within this thesis which has been based upon work from a jointly authored publication is Chapter 4. Information regarding the jointly authored publication is as follows:

Observation of a large negative temperature dependence for rate coefficients of reactions of OH with oxygenated volatile organic compounds studied at 86 – 112 K. Robin J. Shannon, Sally Taylor, Andrew Goddard, Mark A. Blitz, Dwayne Heard, *Phys. Chem. Chem. Phys.* **2010**, *12,* 13511-13514.

The work contained within this publication which is directly attributable to the candidate are the measurements of rate coefficients for the OH + acetone and OH + DME reactions apart from at 86 K for acetone.

The work contained within this publication which is directly attributable to Sally Taylor are measurements of the OH + MEK rate coefficients and the 86 K OH + acetone rate coefficient.

The work contained within this publication which is directly attributable to Andrew Goddard is the design of the apparatus and technical support.

Mark A. Blitz was a senior researcher in the lab who helped in a supportive role.

Dwayne E. Heard was the supervisor for the work that was carried out in this publication

Acknowledgements

First of all I would like to thank my supervisor Dwayne Heard for his persistent enthusiasm, encouragement and advice throughout the course of my PhD. Both Mark Blitz and Andrew Goddard have also been a constant source of advice and the help of all three has been greatly appreciated. My thanks also go to Mike Pilling for nudging me in the direction of MESMER and to Paul Seakins, Struan Robertson and the MESMER authors also for tips and advice with regards to kinetics both from the experimental and theoretical perspective.

There are a number of fellow students who have made life extremely enjoyable in Leeds and many thanks go to my long suffering comrades and drinking partners both old (Rob, Lottes, Katie) and new (Rebecca, James, Fred, Luke, Alan) and many others. Finally on a personal note I especially wish to thank Claire, and my parents Liz and Mike for both putting up with me whilst writing this thesis, and offering constant support along the way.

Abstract

In this thesis low temperature rate coefficients have been measured for a number of reactions involving the OH radical using a pulsed Laval nozzle apparatus. All these reactions exhibit an energy barrier between reactants and products and in each case this barrier is preceded by either a hydrogen bonded complex (OH + acetone, OH + DME, OH + methanol) or a weaker Van der Walls complex (OH + acetylene, OH + ammonia). The rate coefficients for these reactions are observed to increase by up to three orders of magnitude between 200 K and 63 K and complimentary Master equation calculations are able to reproduce the complicated temperature dependences that these rate coefficients exhibit. From these master equation calculations, the negative temperature dependencies of the measured rate coefficients are attributed to a mechanism involving the pre-reaction complex, in most cases including a contribution from quantum mechanical tunnelling. This tunnelling contribution is most especially important in the case of OH + methanol and in this case, hydrogen abstraction products through a 15 kJ mol^{-1} barrier are observed directly at 79 K on the same timescale as OH loss.

The association between an OH radical and its co-reagent to form a weakly bound adduct, is further explored through performing the first proxy method experiments below 200 K. The proxy method is designed to give the high pressure limiting rate coefficient for two associating reactants A and B through measuring the rate coefficients for the A($v=i$) + B reaction. The reactions listed above are revisited and OH vibrational levels up to v = 3 are probed. From these measurements, lower limits for the high pressure limiting rate coefficients of these reactions are obtained at 80 K and the validity of the proxy method is explored in each case.

Table of Contents

List of Tables

List of Figures

List of commonly used abbreviations

CASSCF - Complete active space self-consistent field calculation

CCSD(T) – Coupled cluster theory including single and double excitations and perturbative treatment of triple excitations

CRESU - Cinétique de Réaction en Ecoulement Supersonique Uniform (continuous Laval nozzle apparatus in Bordeaux)

DFT – Density functional theory

ILT – Inverse Laplace transform

IRC – Intrinsic reaction coordinate

ISM – Interstellar Medium

LIF – Laser induced fluorescence

MEP – Minimum energy pathway

MP2 – Moller Plesset perturbation theory second order

PES - Potential energy surface

RRKM – Rice Ramspberger Kassel and Markus theory for calculating microcanonical rate coefficients

SSH - Schwartz and Slawsky and Herzfeld theory of energy transfer

VOC – Volatile organic compound

WKB – Wentzel Kramers and Brillouin semiclassical approximation

Chapter 1. Introduction to low temperature environments and kinetics

The quantitative assessment of the speed or rate of a particular process is of significant importance in everyday life. In the subject of chemistry we are often interested in the rate at which particular chemical reaction will occur and the field of chemical kinetics aims to give quantitative answers to such questions. This thesis will focus upon the rates of gas phase reactions at temperatures below 125 K, and by way of introduction, this chapter aims to put the specific field of low temperature kinetics into a wider context by describing some scientifically relevant systems which exhibit these low temperatures. Subsequently there will be a summary of the methods available for studying low temperature kinetics and the previous work that has been performed.

1.1. Low Temperature Environments

In many fields of science, from biology to combustion studies, scientists are presented with highly complicated chemical systems. It is the role of many researchers to unravel and understand such systems with the ultimate goal of modelling the way in which the systems evolve with time. Such modelling is by no means a trivial task and the understanding of these systems depends not only upon identifying the important chemical species present, but also upon knowledge of the way in which the identified chemical species interact. In order to model how the species concentrations evolve over time it is important then to know both the rates at which these reactions are occurring, and the products that are formed and the purpose of chemical kinetics is to answer these questions.

1.1.1. Earth's atmosphere

The first system that will be examined more closely in this section is the Earth's atmosphere. Given the far reaching implications of issues such as

global warming and deteriorating air quality, a considerable amount of scientific effort is being applied to modelling the complicated physical and chemical processes occurring. The chemistry of the Earth's atmosphere is largely comprised of gas phase chemistry and in parts of the atmosphere, temperatures regularly reach below 200 K (1) which is often the lowest temperature obtainable in a conventional kinetics experiment.

The Earth's atmosphere consists of four distinct regions, the troposphere, the stratosphere, the mesosphere and the thermosphere. Although our atmosphere exhibits temperature changes with longitude, latitude, and season, the temperature variation with altitude is by far the most significant, and average temperature profiles of the form of Figure 1.1 can be drawn. It can be seen in temperature profiles like this, that the temperature goes through two minima, the tropopause with average temperatures of 220 K and the mesopause with average temperatures of 170 K (1) although temperatures as low as 100 K have been observed in the mesosphere. (2)

In the lower atmosphere in particular the chemistry mainly consists of neutral -radical reactions with daytime tropospheric oxidation chemistry being dominated by the hydroxyl radical (OH). Anthropogenic and biogenic emissions from a large number of sources including fossil fuel burning and agriculture lead to relatively large abundances of pollutants in the troposphere and when understanding issues such as air quality and global warming, the chemistry of the troposphere is very important.

As has been said, much of the daytime chemistry in the troposphere is dominated by the OH radical and this radical has an important oxidising effect in the atmosphere. The OH radical is formed predominantly through reaction of water vapour with $O(^1D)$ atoms which are formed in turn through photolysis of ozone (O_3). Many of the trace constituents or pollutants in the Earth's atmosphere fall in the category of volatile organic compounds, or VOC's. Many of these VOC's contribute to global warming and or issues of air quality such as smog formation, and reaction with OH is often the dominant removal process for such species. As such, the atmospheric lifetime of these VOC's is very sensitive to both the rate of their reaction with OH and the local concentration of OH in that part of the atmosphere.

Consequently a large amount of research effort is directed to measuring both the concentration of OH in the atmosphere and the rate of reaction between OH and various atmospheric pollutants.

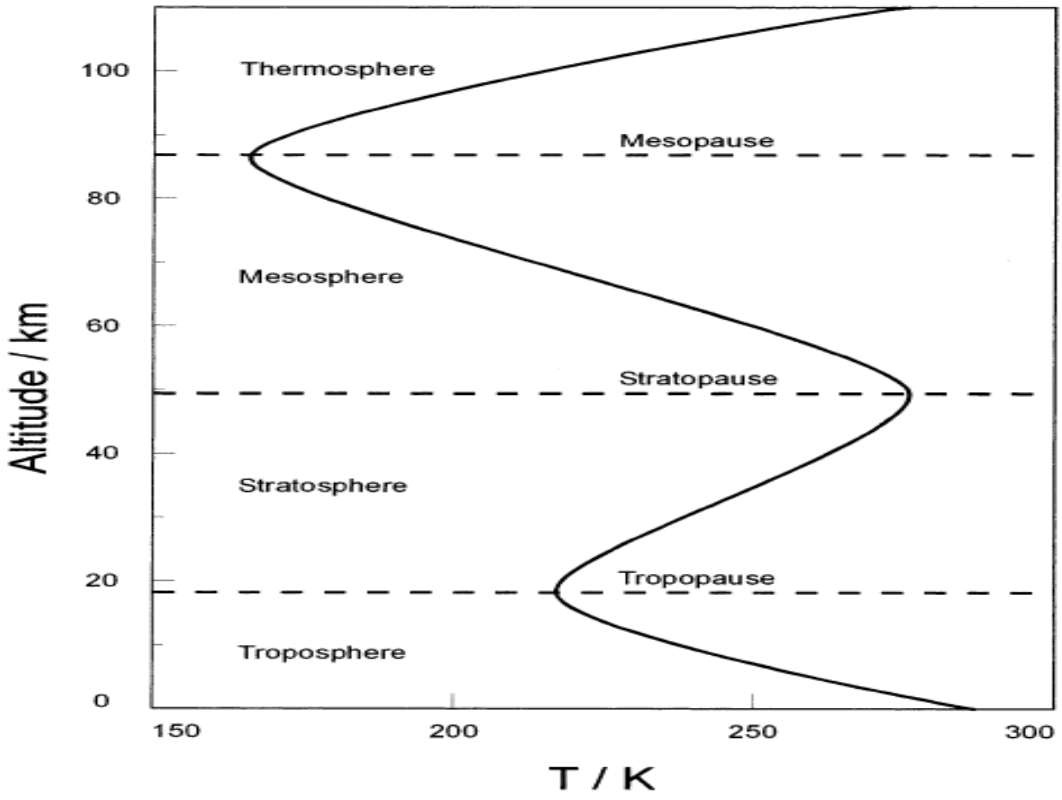

Figure 1.1: Average temperatures within the Earth's atmosphere as a function of altitude. Taken from Wayne. (1)

1.1.2. The atmosphere of Titan.

Whilst unsurprisingly the Earth's atmosphere receives a large amount of attention from scientific community, it is not the only planet in our solar system that has aroused scientists interest. A number of planets in our solar system exhibit substantial atmospheres and the constituents of these atmospheres vary significantly. (1)

An extra-terrestrial atmosphere that has received significant attention in recent years is that of Saturn's moon Titan. Unlike many satellites in the solar system, pictures from the Voyager and the Cassini Huygens mission show the surface of Titan to be obscured by a dense gaseous atmosphere (3) and interestingly this atmosphere is the only one in the solar system apart from Earth's to be comprised predominantly of nitrogen. (4, 5) It has

been revealed that like Earth's, the atmosphere of Titan has a relatively large abundance of VOC's and photochemical formation of hazes is common. (6, 7) Some atmospheric constituents and their mixing ratios in Titans atmosphere are given in Table 1.1.

Species	Mixing ratio
N_2	0.9-0.99
Ar	<0.006
CH_4	0.017-0.045
H_2	0.0006-0.0014
C_2H_6	$1.\times10^{-5}$
C_2H_2	3×10^{-6}
C_3H_8	5×10^{-7}
C_3H_4	5×10^{-9}
CO_2	1×10^{-8}
CO	5×10^{-5}

Table 1.1: Mixing ratios of some of the more abundant constituents of Titan's atmosphere. This table is a reduced version of the table presented by Gautier (10).

In the context of low temperature environments, the atmosphere of Titan exhibits conditions well below those accessible by conventional kinetics measurements with average temperatures of 95 K at the surface and 70 K at the tropopause. (1) In addition to being cold, the atmosphere of Titan is also dense with a surface pressure of 1.5 atm, (1) facilitating a large number of molecular collisions. Since the conditions in Titan's atmosphere are difficult to obtain in a kinetics experiment, models of the chemistry occurring have often resorted to extrapolating high temperature rate coefficients to lower temperatures when experimental data is unavailable. (8) A recent modelling study highlighted the errors introduced through such extrapolations and by extension the importance of collecting experimental measurements of reaction rates at low temperatures. (9)

1.1.2. The interstellar medium

The interstellar medium (ISM) is an umbrella term for the matter which makes up the space between star systems, and this term comprises many different environments with large variations in temperature and gas density. (11) From a chemistry point of view, molecules tend to exist in the cooler regions of space in either diffuse or dense clouds. (12)

As the density of these clouds increases, the temperature is decreased, with the majority of the molecular species found in regions of the highest density. These “dense” molecular clouds typically form cold cores with average temperatures of 10K and gas densities of 10^4 molecule cm^{-3}. These cold cores are then surrounded by more diffuse matter in which temperatures can rise to ~25 K. (11)

In this thesis, when the ISM is mentioned, it is the conditions within these

Species	Abundance relative to H_2
CO	8×10^{-5}
OH	2×10^{-7}
CCCH	9×10^{-8}
HCN	2×10^{-8}
NH_3	2×10^{-8}
HCCCN	2×10^{-8}
Cyclic C_3H_2	1×10^{-8}
CH_3OH	3×10^{-9}
CH_3COCH_3	1×10^{-9}

Table 1.2: Abundances relative to H_2 for a number of species in the dense cloud TMC-1. This table has been adapted from Herbst ,(12) and the CH_3OH abundance is taken from Smith and co-workers (13) whilst the abundance of CH_3COCH_3 is taken from Herbst and Dishoeck. (17)

cold cores that is generally referred to. Given the extremely low temperatures, a surprising number of molecular neutral species have been

observed in the ISM, typically using spectroscopic methods, such as vibrational or rotational absorption spectroscopy. (11) A table of some of these species, including their relative abundances compared to hydrogen, is given below. These abundances are for the particularly well studied cloud TMC-1. (13-16)

While ion-molecule chemistry dominates under ISM conditions, an increasing body of literature has shown that neutral-neutral reactions can also play an important role at such low temperatures . However, databases of reactions important in the ISM such as the UMIST and KIDA databases (18,19) still contain relatively few neutral – neutral reactions, and many uncertainties remain with regard to modelling the chemistry occurring in the ISM. (20)

1.2. Experimental Techniques available for low temperature kinetics measurements.

Before taking a more rigorous stance with regards to chemical kinetics, the second part of this introduction will endeavour to give a broad overview to the body of previous experimental work in the field of low temperature kinetics, focussing on the experimental techniques available. Whilst chapter 2 will aim to explicitly define the nomenclature of chemical kinetics, it is worthwhile at this point to make a few broad statements about the rate of chemical reactions.

In the previous section there were numerous occasions where the rate of a reaction was referred to and specifically there has been mention of measuring the rates of reactions. Rather than measuring rates it is more correct to say that rate coefficients for a particular reaction are measured. The rate coefficient (*k)* for a particular reaction is a coefficient of proportionality which determines the rate at which the concentration of one species in the reaction changes with time and these rate coefficients typically vary with temperature and sometimes pressure. This rate coefficient is mathematically defined by the following relationship:

$$\frac{d[\mathrm{A}]}{dt} = -k[\mathrm{A}]^a[\mathrm{B}]^b \qquad \text{(Eq. 1)}$$

where species A and B are the reactants involved in the reaction and *a* and *b* are the orders with respect to each reactant. The order of a reaction is related to the number of molecules involved in the slowest, or rate determining, reaction step and the overall reaction order is the sum of the individual orders with respect to each reactant. It is these rate coefficients that are used to model complex chemical environments, and if for a given reaction both the rate coefficient and concentrations of the species involved are known then the rate at which the reactants are used up can be determined.

This thesis will primarily concern bimolecular reactions, that is reactions where the slowest step involves two reactants colliding together, and for now it is simply necessary to know that in order to measure a bimolecular rate coefficient it is necessary to measure how the concentration of one species evolves over the course of the reaction and to accurately know the concentration of the species it is reacting with. Practically, instead of directly monitoring the species concentration, a typical kinetics experiment will measure some property of the system that is proportional to the species concentration such as fluorescence intensity or pH. Then by initiating the reaction at a defined time, the relative growth or decay of a particular species concentration can be obtained through monitoring this property at a number to different time intervals after the start of the reaction.

At temperatures above 200 K, kinetics experiments have been routinely performed and there is a large body of data detailing the rate coefficients of many different gas phase reactions. As a reflection of this huge amount of kinetic data there are numerous databases detailing the rate coefficients for important reactions in different environments such as the Earth's atmosphere or the interstellar medium. (21, 22) When modelling such environments it is this large body of experimental data which is utilised, however below 200 K, experimental data are scarce and when rate coefficients at low temperatures are required, it often necessary to either extrapolate the higher temperature rate coefficients, or to use theoretical rather than experimental data.

While it is clear that more kinetics experiments are needed at low temperatures, such experiments are challenging. There are two common problems associated with measuring rate coefficients at low temperatures. The first of these problems arises due to the presence of cold walls or surfaces within the reaction chamber which the gas phase reactants have a tendency to condense onto. This then introduces difficulties in accurately measuring the gas phase concentrations of reactants in the reaction chamber. The second problem occurs in obtaining a thermally averaged energy distribution in the cooled gas. This is often a problem in expansion techniques as described in more detail below and if there are insufficient collisions within the cold jet, then the temperature of the expansion is ill defined. These issues will be discussed in more detail with reference to particular experimental methods that have been used to create low temperature environments suitable for measuring kinetics.

1.2.1. Cryogenic Cooling

One of the simplest of these methods is that of cryogenic cooling. This method involves surrounding the walls of the reaction cell with refrigerant such as liquid nitrogen or helium and then introducing a buffer gas which is cooled through contact with the walls. Gaseous reagents can then be added and cooled through the removal of thermal energy via collisions with the buffer gas. Given sufficient time, thermal equilibrium is then reached, though care must be taken that secondary reactions do not occur. This technique has been used to achieve temperatures down to 18 K using He (23, 24) as a refrigerant but this type of cooling has only really been practical at temperatures above ~ 80 K using liquid N_2.(25, 26) The main drawback of this experiment is due to the tendency of the reactants to condense at the cooled walls of the cell. This can be overcome by ensuring that the partial pressures for each constituent gas are kept below the equilibrium vapour pressure for that gas at the temperature of the cell walls, but it is also important that concentrations of gases within the cell are large enough that kinetic measurement are still viable. This problem becomes significant at

temperatures below 200 K and increases with lower temperatures, making this a challenging method for low temperature kinetics experiments.

1.2.2. Free Jet Expansions

Another technique that has been used for low temperature kinetics is that of free jet expansions. (27, 28) Here the cooling effect is produced by an isoentropic expansion of gas through a nozzle or pinhole to produce a cold jet. Using this method temperatures below 1 K (27) can be produced, but there are limitations to its use for measuring reaction kinetics. The main problem is that the flow is not thermally equilibrated and hence there exist significant temperature and pressure gradients that are prohibitive to the measurement of any reaction rates. The flow gradually becomes more uniform, but by the time this point is reached the collision frequency is too low for any equilibrium to be established. This has meant that free jet expansions are very limited in their effectiveness in measuring rate constants for neutral-neutral reactions. However, this method has had some success in measuring the rate constants of ion-molecule reactions since the stronger attractive electrostatic forces between reagents help maintain a sufficient amount of collisions. (29) It should be noted that while jet expansions are limited in their kinetic use, they have been used to good effect in many spectroscopic studies (30) and in particular, the study of unstable complexes that can exist for extended periods in the cold environment of the beam.

1.2.3. Continuous Systems (CRESU)

In the past 20 years there has also been extensive use of Laval nozzles in order to provide low temperature environments suitable for measuring rate constants. Laval nozzles were initially developed by Gustaf de Laval and have been used extensively in studies of aerodynamics. However since the construction of the Cinétique de Réaction en Ecoulement Supersonique Uniform (CRESU) apparatus in 1984 (31) they have been increasingly used for chemical applications. A Laval nozzle is a convergent-divergent shaped

nozzle designed to accelerate gas flow through it, in order to provide a stable supersonic flow of gas.(32) Again the cooling occurs by isoentropic expansion but in the CRESU system, some of the disadvantages of free jet expansion techniques have been overcome.

The shape of the Laval nozzle leads to a flow that is uniform in pressure and temperature for a sufficient distance to allow kinetic measurements and the density in the flow and hence the number of collisions is large enough to produce a Boltzmann distribution. Also in a Laval nozzle system, the constituent reagents are carried within the flow so the reactions can be considered as occurring without walls (33) thus overcoming the problem of reagent condensation.

The CRESU technique uses a continuous flow of gas that is expanded through one of a range of specifically designed nozzles in order to provide a stable flow of gas that has been cooled by isotropic and adiabatic expansion in order to reach temperatures below 10 K. The initial results for this technique were obtained for ion-molecule reactions but with more and more neutral-neutral reactions being discovered to exhibit unusual temperature dependences, cooling via a Laval nozzle expansion has proved to be the only reliable method for measuring the low temperature kinetics of these reactions. (26, 34-36)

Though this type of apparatus has had its successes, there are drawbacks to this technique as well. A major problem is due to the large quantity of gas (~50 slm) required in order to maintain the continuous flow and also subsequently the large pumping capacities (~30,000 m^3 hr^{-1} at 0.1 mbar (32)) that are needed in order to remove this gas. This leads to the technique being highly expensive and many reactions, involving species that are expensive or have to be synthesised, are uneconomical to run. (33) Another drawback is that rate coefficients below ~10^{-12} cm^3 $molecule^{-1}$ s^{-1} cannot be measured. This limitation is due to two factors, the relatively small reagent concentrations (2% of the total flow) that can be used in Laval nozzle experiments before the resulting gas flow becomes unstable, and the velocity at which the gas flows through the system, as this provides only a very short window in which kinetic measurements can be made. In general

however, this problem is of relatively little significance since any reaction that has a negligible rate at low temperatures is unlikely to exhibit the non-Arrhenius behaviour that is of interest in these low temperature kinetic experiments.

1.2.4. Pulsed Laval Nozzle Systems

The final experimental method that this thesis will look at is that of Pulsed Laval Nozzle Systems.(37) These are based upon the continuous CRESU systems mentioned earlier but rather than have a continuous flow of gas this method uses two valves in order to release pulses of gas. Due to pulsed operation, the temperature profiles of the resulting supersonic flow tend to be slightly less stable than in the continuous systems and the resulting stable flows also tend to be shorter in length, but this method has its advantages as well.

First, the gas flow and pumping requirements are smaller (2-3slm) so it becomes possible to study experiments using gases that would be prohibitively expensive using a continuous system. Secondly, using a pulsed system it is possible to monitor the products of the reaction rather than just the reagents using a time of flight mass spectrometry technique. (38) In a continuous system, this is not possible and this can provide useful information about branching ratios.

A number of pulsed systems have been designed and used. The first pulsed Laval nozzle apparatus was created by Atkinson and Smith in Arizona (37) followed by groups in Colarado (38) (now Berkeley California), Gottingen(39) and Leeds. (40) There is also a smaller version of the CRESU apparatus in Bordeaux (41) which operates with reduced gas flows. It is this pulsed Laval nozzle method which has been used throughout this thesis and Table 1.3 shows the neutral reactions which have been measured using these different apparatus giving an overview of the breadth of the reactions which have been studied.

1.3. Overview of the rest of this thesis.

This thesis will describe the study of a number of similar reaction using both Laval nozzle experiments and theoretical calculations. A detailed overview of the theoretical techniques used will be given in chapter 2 and in chapter 3 the experimental details and common procedures used, will be described. Chapters 4 to 7 then comprise the experimental results for individual systems.

The experimental chapters 4, 5 and 6 present rate coefficients measured for reactions between the OH radical and various species. In chapter 4 the reactions between the OH radical and two oxygentated organic species, acetone and dimethyl ether, are presented. Both these reactions have many similarities, involving the formation of hydrogen bonded complexes over the course of the reaction. In Chapter 5 the reaction of OH with methanol reaction is considered. This reaction has many similarities with the two reactions considered in Chapter 4, however it is considered sperately due the particularly interesting nature of the reaction mechanism at low temperatures. In Chapter 6, two further OH reactions will be considered, namely those with acetylene and ammonia. In many ways these systems are analogous to the three systems studied in chapters 4 and 5, however rather than forming hydrogen bonded complexes, these reactions involve weaker van der Waals complexes, and the effect of this at low temperatures is investigated.

In Chapter 7, the first study of the proxy method at low temperatures is presented. This method is a way of approximating the way in which a reaction will behave in the limit of high pressure and such experiments are performed by introducing an amount of vibrational energy to the OH reactant used in this study. In this chapter vibrationally excited OH molecules are studied in the presence of acetone, dimethyl ether, methanol and acetylene, and these measurements help to complete the work presented in chapters 4, 5 and 6.Finally Chapter 8 gives a brief conclusion to the thesis and discuss future work using the Leeds pulsed Laval nozzle apparatus.

Radical	Neutral Species	Temperature / K	Reference
OH	NO	90 - 220	Atkinson and Smith (1994) (27)
	HBr	76 - 242	Atkinson *et al.*. (1997) (42)
		53 - 135	Mullen and Smith (2005) (43)
	CH_2=$CHCH_3$ (propene)	103	Vakhtin *et al.*. (2001) (44)
		96 - 296	Vakhtin *et al.*. (2003) (45)
		58 - 293	Spangenburg *et al.*. (2004) (39)
	CH_2=$CHCH_2CH_3$ (1-butene)	103	Vakhtin *et al.*. (2001) (44)
		96 - 296	Vakhtin *et al.*. (2003) (45)
	C_2H_4 (ethene)	96 - 296	Vakhtin *et al.*. (2003) (45)
	CH_2=$C(CH_3)C$=CH_2 (isoprene)	58 - 293	Spangenburg *et al.*. (2004) (39)
	H_2O_2 (hydrogen peroxide)	96 - 296	Vakhtin *et al.*. (2003) (45)
	CH_3CHO (acetaldehyde)	60 – 300	Vohringer-Martinez (2007) (46)
	C_2H_4	69-86	Taylor *et al.* (2008)(40)
	C_2H_2		
	C_3H_4		
	Benzene		
	Toluene		
	Propene	50-220K	Daranlot *et al.* (2010) (47)
	1-butene		
	allene		
C_2	acetylene	77-296	Daugey *et al.*. (2008) (41)
	methylacetylene		
	allene		
	propene		
CH	CH_4	77 – 170	Daugey *et al.*. (2005) (48)

	CH_2=C=CH_2 (allene)		
	$CH_3C{\equiv}CH$ (propyne)		
	CH_2=$CHCH_3$ (propene)		
C_2H	C_2H_2 (acetylene)	90 - 120	Lee *et al.*. (2000) (38)
		103	Vakhtin *et al.*. (2001) (44)
	O_2	90 - 120	Lee *et al.*. (2000) (38)
		103	Vakhtin *et al.*. (2001) (44)
	$CH_3C{\equiv}CH$ (propyne)	103	Vakhtin *et al.*. (2001) (44)
	CH_2=C=CH_2 (allene)		
	C_2H_6 (ethane)	96 - 296	Murphy *et al.*. (2003) (45)
	C_3H_8 (propane)		
	C_4H_{10} (n-butane)		
	C_2H_4 (ethene)	103 - 296	Vakhtin *et al.*. (2001) (44)
	CH_2=$CHCH_3$ (propene)		
	CH_2=$CHCH_2CH_3$ (1-butene)	103 - 296	Vakhtin *et al.*. (2001) (44)
		104 - 296	Nizamov and Leone (2004) (49)
	C_4H_{10} (isobutane)	104 – 296	Nizamov and Leone (2004) (49)
	CH_2=$C(CH_3)CH_3$ (isobutene)		
	(CH_2=CHCH=CH_2 (1,3-butadiene)		
	CH_3CN (methyl cyanide)		
	CH_3CH_2CN (ethyl cyanide)		
	$CH_3CH_2CH_2CN$ (propyl cyanide)		
	NH_3	104 – 296	Nizamov and Leone (2004) (49)
	ND_3		

	C_6H_6 (benzene)	105 - 298	Goulay *et al.*. (2006) (50)
NO	CH_4	53	Mullen *et al.*. (2005) (43)
	C_2H_6 (propane)		
	NO	53 – 188 K	
	C_2H_2 (acetylene)		
	C_2H_4 (ethene)		
	C_3H_6 (propene)		
	C_4H_2 (diacetylene)		
Cl	Ethane	50 - 220 K	Hickson *et al.* (2010) (51)
	Propane		
N	OH	50 – 220 K	Daranlot *et al.* (2011) (52)

Table 1.3: Neutral-neutral reactions studied using pulsed Laval nozzle systems and the small continuous apparatus in Bordeaux. (41) Adapted from S E Taylor (33) and extended.

1.4. References

1. R. P. WAYNE. *Chemistry of Atmospheres.* Third Edition ed. Oxford, U.K.: Oxford University Press, 2002.
2. NORDBERG, W., L. KATCHEN, J. THEON and W.S. SMITH. Rocket Observations of Structure of Mesosphere. *Journal of the Atmospheric Sciences*, 1965, **22**(6), pp.611-&.
3. LINDAL, G.F., G.E. WOOD, H.B. HOTZ, D.N. SWEETNAM, V.R. ESHLEMAN and G.L. TYLER. The Atmosphere of Titan - an Analysis of the Voyager-1 Radio Occultation Measurements. *Icarus*, 1983, **53**(2), pp.348-363.
4. D. W. CLARKE and J. P. FERRIS. Chemical evolution of Titan: Comparisons to the prebiotic Earth. *Oragins Life Evol. Biosphere*, 1997, **27**, pp.225 - 248.
5. F. RAULIN, P. COLL, N. SMITH, Y. BENILAN, P. BRUSTON and M. C. GAZEAU. New insights into Titan's organic chemistry in the gas and aerosool phases. *Adv. Space Res.*, 1999, **24**(4), pp.453 - 460.
6. FERRIS, J., B. TRAN, J. JOSEPH, V. VUITTON, R. BRIGGS and M. FORCE. The role of photochemistry in Titan's atmospheric chemistry. *Space Life Sciences: Astrobiology: Steps toward Origin of Life and Titan before Cassini*, 2005, **36**(2), pp.251-257.
7. STROBEL, D.F. Photochemistry in Titan's atmosphere. *Proceedings of the International Conference Titan: From Discovery to Encounter*, 2004, pp.365-368.

8. SMITH, G.P. and D. NASH. Local sensitivity analysis for observed hydrocarbons in a Jupiter photochemistry model. *Icarus*, 2006, **182**(1), pp.181-201.
9. HEBRARD, E., M. DOBRIJEVIC, P. PERNOT, N. CARRASCO, A. BERGEAT, K.M. HICKSON, A. CANOSA, S.D. LE PICARD and I.R. SIMS. How Measurements of Rate Coefficients at Low Temperature Increase the Predictivity of Photochemical Models of Titan's Atmosphere. *Journal of Physical Chemistry A*, 2009, **113**(42), pp.11227-11237.
10. GAUTIER, D. and F. RAULIN. Chemical Composition of Titan's Atmosphere. *Huygens: Science, Payload and Mission, Proceedings of an ESA conference. Edited by A. Wilson*, 1997.
11. SMITH, I.W.M. *Low temperatures and cold molecules.* London: Imperial College Press, 2008.
12. HERBST, E. Chemistry of star-forming regions. *Journal of Physical Chemistry A*, 2005, **109**(18), pp.4017-4029.
13. SMITH, I.W.M., E. HERBST and Q. CHANG. Rapid neutral-neutral reactions at low temperatures: a new network and first results for TMC-1. *Monthly Notices of the Royal Astronomical Society*, 2004, **350**(1), pp.323-330.
14. OHISHI, M. and N. KAIFU. Chemical and physical evolution of dark clouds - Molecular spectral line survey toward TMC-1. *Faraday Discussions*, 1998, **109**, pp.205-216.
15. FREEMAN, A. and T.J. MILLAR. Formation of Complex-Molecules in Tmc-1. *Nature*, 1983, **301**(5899), pp.402-404.
16. SCHLOERB, F.P., R.L. SNELL and J.S. YOUNG. Structure of Dense Molecular Gas in Tmc-1 from Observations of 3 Transitions of Hc3n. *Astrophysical Journal*, 1983, **267**(1), pp.163-173.
17. HERBST, E. and E.F. VAN DISHOECK. Complex Organic Interstellar Molecules. *Annual Review of Astronomy and Astrophysics, Vol 47*, 2009, **47**, pp.427-480.
18. WOODALL, J., M. AGUNDEZ, A.J. MARKWICK-KEMPER and T.J. MILLAR. The UMIST database for astrochemistry 2006. *Astronomy & Astrophysics*, 2007, **466**(3), pp.1197-U203.
19. WAKELAM, V., E. HERBST, J.C. LOISON, I.W.M. SMITH, V. CHANDRASEKARAN, B. PAVONE, N.G. ADAMS, M.C. BACCHUS-MONTABONEL, A. BERGEAT, K. BEROFF, V.M. BIERBAUM, M. CHABOT, A. DALGARNO, E.F. VAN DISHOECK, A. FAURE, W.D. GEPPERT, D. GERLICH, D. GALLI, E. HEBRARD, F. HERSANT, K.M. HICKSON, P. HONVAULT, S.J. KLIPPENSTEIN, S. LE PICARD, G. NYMAN, P. PERNOT, S. SCHLEMMER, F. SELSIS, I.R. SIMS, D. TALBI, J. TENNYSON, J. TROE, R. WESTER and L. WIESENFELD. A Kinetic Database for Astrochemistry (Kida). *Astrophysical Journal Supplement Series*, 2012, **199**(1).
20. GARROD, R., I.H. PARK, P. CASELLI and E. HERBST. Are gas-phase models of interstellar chemistry tenable? The case of methanol. *Faraday Discussions*, 2006, **133**, pp.51-62.
21. ATKINSON, R., D.L. BAULCH, R.A. COX, J.N. CROWLEY, R.F. HAMPSON, R.G. HYNES, M.E. JENKIN, M.J. ROSSI and J. TROE. Evaluated kinetic and photochemical data for atmospheric chemistry:

Volume I - gas phase reactions of O(x), HO(x), NO(x) and SO(x) species. *Atmospheric Chemistry and Physics*, 2004, **4**, pp.1461-1738.

22. MILLAR, T.J., P.R.A. FARQUHAR and K. WILLACY. The UMIST database for astrochemistry 1995. *Astronomy & Astrophysics Supplement Series*, 1997, **121**(1), pp.139-185.
23. H. BOHRINGER and F. ARNOLD. Studies of ion/molecule reactions, ion mobilities and their temperature dependence to very low temperatures using a liquid helium cooled ion drift tube. *Int. J. Mass Spectrom. Ion Processes*, 1983, **49**(11), pp.61 - 83.
24. Temperature and pressure dependence of the reaction of He^+ ions with H_2. *J. Chem. Phys.*, 1986, **84**(3), pp.1459 - 1462.
25. F. GOULAY, C. REBRION-ROWE, J. L. LE GARREC, S. D. LE PICARD, A. CANOSA and B.R. ROWE. The reaction of anthracene with OH radicals: An experimental study of the kinetics between 58 and 470 K. *J. Chem. Phys.*, 2005, **122**(30), p.104308.
26. I. R. SIMS, J. -L. QUEFFELEC, A. DEFRANCE, C. REBRION-ROWE, D. TRAVERS, P. BOCHEREL and I. W. M. SMITH. Ultra-low temperature kinetics of neutral-neutral reactions. The technique and results for reactions CN + O_2 down to 13 K and CN + NH_3 down to 25 K. *J. Chem. Phys.*, 1994, **100**(6), pp.4229 - 4241.
27. D. B. ATKINSON and M. A. SMITH. Radical-molecule kinetics in pulsed uniform supersonic flows: Termolecular association of OH + NO between 90 and 220 K. *J. Phys. Chem.*, 1994, **98**(23), pp.5797 - 5800.
28. R. M. HAWLEY and M. A. SMITH. The gas phase reaction of $C_2H_2^+$ with H_2 below 3 K: The reopening of the bimolecular $C_2H_3^+$ channel at low energy. *J. Chem. Phys.*, 1992, **96**(2), pp.1121 - 1127.
29. SMITH, M.A. and M. HAWLEY. Ion/Molecule Reaction-Rate Coefficients at Translational Temperatures Below 5 K - Selected Bimolecular Reactions of C2h2+ and Nh4+. *International Journal of Mass Spectrometry and Ion Processes*, 1995, **149**, pp.199-206.
30. E. N. SHARP, M. A. ROBERTS and D.J. NESBITT. Rotationally resolved infrared spectroscopy of a jet-cooled phenyl radical in the gas phase. *Physical Chemistry Chemical Physics*, 2008, **10**(44), pp.6581-6728
31. SMITH, I.W.M. and B.R. ROWE. Reaction kinetics at very low temperatures: Laboratory studies and interstellar chemistry. *Accounts of Chemical Research*, 2000, **33**(5), pp.261-268.
32. JAMES, P.L., I.R. SIMS, I.W.M. SMITH, M.H. ALEXANDER and M.B. YANG. A combined experimental and theoretical study of rotational energy transfer in collisions between NO(X (2)Pi(1/2), v=3,J) and He, Ar and N-2 at temperatures down to 7 K. *Journal of Chemical Physics*, 1998, **109**(10), pp.3882-3897.
33. S. E. TAYLOR. *Reaction Kinetics at Very Low Temperatures Measured Using a Pulsed Laval Nozzle Apperatus.* thesis, University of Leeds, 2007.
34. A. PARAMO, A. CANOSA, S. D. LE PICARD and I. R. SIMS. An experimental study of the intersystem crossing and reactions of $C_2(X^1\Sigma_g^+)$ and $C_2(a^3\Pi_u)$ with O_2 and NO at very low temperature (24 - 300 K). *J. Phys. Chem. A*, 2006, **110**(9), pp.3121 - 3127.

35. A. CANOSA, I. R. SIMS, D. TRAVERS, I. W. M. SMITH and B. R. ROWE. Reactions of the methylidine radical with CH4, C2H2, C2H4, C2H6 and but-1-ene studied between 23 and 295 K with a CRESU apparatus. *Astron. Astrophys.*, 1997, **323**(2), pp.644 - 651.
36. P. SHARKEY, I. R. SIMS and I. W. M. SMITH. Pressure and temperature dependence of the rate constants for the association reaction of OH radicals with NO between 301 and 23 K. *J. Chem. Soc. Faraday Trans.*, 1994, **90**(24), pp.3609 - 3616.
37. D. B. ATKINSON and M. A. SMITH. Design and characterisation of pulsed uniform supersonic expansions for chemical applications. *Rev. Sci. Instrum.*, 1995, **66**(9), pp.4434 - 4446.
38. S. LEE, R. J. HOOBLER and S. R. LEONE. A pulsed Laval nozzle apparatus with laser ionization mass spectroscopy for direct measurements of rate coefficients at low temperatures with condensable gases. *Rev. Sci. Instrum.*, 2000, **71**(4), pp.1816 - 1823.
39. T. SPANGENBURG, S. KÖHLER, B. HANSMANN, U. WACHSMUTH, B. ABEL and M. A. SMITH. Low-temperature reactions of OH radicals with propene and isoprene in pulsed Laval nozzle expansions. *J. Phys. Chem. A*, 2004, **108**(37), pp.7527 - 7534.
40. TAYLOR, S.E., A. GODDARD, M.A. BLITZ, P.A. CLEARY and D.E. HEARD. Pulsed Laval nozzle study of the kinetics of OH with unsaturated hydrocarbons at very low temperatures. *Physical Chemistry Chemical Physics*, 2008, **10**(3), pp.422-437.
41. DAUGEY, N., P. CAUBET, A. BERGEAT, M. COSTES and K.M. HICKSON. Reaction kinetics to low temperatures. Dicarbon plus acetylene, methylacetylene, allene and propene from 77 <= T <= 296 K. *Physical Chemistry Chemical Physics*, 2008, **10**(5), pp.729-737.
42. D. B. ATKINSON, V. I. JARAMILLO and M. A. SMITH. Low temperature kinetic behaviour of the bimolecular reaction OH + HBr (76 - 242 K). *J. Phys. Chem. A*, 1997, **101**(18), pp.3356 - 3359.
43. C. MULLEN and M. A. SMITH. Temperature dependence and kinetic isotope effects for the OH + HBr reaction and H/D isotopic variants at low temperatures (53 - 135 K) measured using a pulsed supersonic Laval nozzle flow reactor. *J. Phys. Chem. A*, 2005, **109**(17), pp.3893 - 3905.
44. A. B. VAKHTIN, S. LEE, D. E. HEARD, I. W. M. SMITH and S. R. LEONE. Low-temperature kinetics of reactions of the OH radical with propene and 1-butene studied by a pulsed Laval nozzle apparatus combined with Laser-Induced Fluorescence. *J. Phys. Chem. A.*, 2001, **105**(33), pp.7889 - 7895.
45. J. E. MURPHY, A. B. VAKHTIN and S. R. LEONE. Laboratory kinetics of C_2H radical reactions with ethane, propane, and *n*-butane at T = 96 - 296 K: implications for Titan. *Icarus*, 2003, **163**, pp.175 - 181.
46. E. VOHRINGER-MARTINEZ, B. HANSMANN, H. HERNANDEZ, J. S. FRANCISCO, J. TROE and B. ABEL. Water catalysis of a radical-molecule gas-phase reaction. *Science*, 2007, **315**, pp.497 - 501.
47. DARANLOT, J., A. BERGEAT, F. CARALP, P. CAUBET, M. COSTES, W. FORST, J.C. LOISON and K.M. HICKSON. Gas-Phase Kinetics of Hydroxyl Radical Reactions with Alkenes: Experiment and Theory. *Chemphyschem*, 2010, **11**(18), pp.4002-4010.

48. N. DAUGEY, P. CAUBET, B. RETAIL, M. COSTES, A. BERGEAT and G. DORTHE. Kinetic measurements on methylidyne radical reactions with several hydrocarbons at low temperatures. *Phys. Chem. Chem. Phys.*, 2005, **7**(15), pp.2921 - 2927.
49. B. NIZAMOV and S. R. LEONE. Rate coefficients and kinetic isotope effect for the C_2H reactions with NH_3 and ND_3 in the 104 - 294 K temperature range. *J. Phys. Chem. A*, 2004, **108**(17).
50. F. GOULAY and S. R. LEONE. Low-temperature rate coefficients for the reaction of ethynyl radical (C_2H) with benzene. *J. Phys. Chem. A*, 2006, **110**(5), p.1875.
51. HICKSON, K.M., A. BERGEAT and M. COSTES. A Low Temperature Study of the Reactions of Atomic Chlorine with Simple Alkanes. *Journal of Physical Chemistry A*, 2010, **114**(9), pp.3038-3044.
52. DARANLOT, J., M. JORFI, C.J. XIE, A. BERGEAT, M. COSTES, P. CAUBET, D.Q. XIE, H. GUO, P. HONVAULT and K.M. HICKSON. Revealing Atom-Radical Reactivity at Low Temperature Through the N plus OH Reaction. *Science*, 2011, **334**(6062), pp.1538-1541.

Chapter 2.Theoretical methods in chemical kinetics.

Many of the experimental results in this thesis will be complemented by theoretical calculations. This chapter will aim to give a broad overview of the various theoretical methods which have been applied to calculate low temperature rate coefficients with extra emphasis applied to the theoretical tools used in this work.

2.1. Basic chemical kinetics

2.1.1. The rate equation

The concept of a rate coefficient for a reaction has been introduced briefly in the previous chapter but here some of the terms used in this thesis are defined more precisely and give a brief introduction to the field of chemical kinetics is given.

For simplicity the discussion in this section shall be confined to unimolecular (first order) reactions and bimolecular (second order) reactions and two simple examples of such reactions are shown below respectively.

$$A \rightarrow B \qquad \text{(R1)}$$

$$A + B \rightarrow C + D \qquad \text{(R2)}$$

The rate of change in the concentration of species A is then proportional to the product of the concentrations of the reactants and the following rate equations for the unimolecular and bimolecular cases are obtained: (1)

$$\frac{\mathrm{d}[\mathrm{A}]}{\mathrm{d}t} = -k_{uni}[\mathrm{A}] \qquad \text{(Eq. 1)}$$

$$\frac{\mathrm{d[A]}}{\mathrm{d}t} = -k_{\mathrm{bi}}[\mathrm{A}][\mathrm{B}] \qquad \text{(Eq. 2)}$$

It should be noted here that the rate equation for a reaction can be expressed with respect to the change in concentration of any species involved in the reaction and it will take on slightly different form in each case. In order to resolve any ambiguity, when the rate coefficient for reaction between A and B is referred to in this thesis it is assumed the rate equation is assumed to be of the form given in Eq. 2 where the rate coefficient is the bimolecular rate coefficient for the loss of species A in the presence of species B, irrespective of the products formed.

Taking the unimolecular case, the rate equation can be integrated to yield equation :

$$[\mathrm{A}] = [\mathrm{A}]_0 e^{-kt} \qquad \text{(Eq. 3)}$$

where $[A]_0$ in molecule cm^{-3} is the initial concentration of species A, *t* is the time after the start of the reaction in seconds and *k* is the rate coefficient in s^{-1}. If [A], or in practical terms some property proportional to [*A*] is measured at different times *t*, then by fitting the resulting experimental trace with an exponential decay, the rate coefficient *k* can be determined.

Except in the particular case where species A and B are the same it is not possible to integrate the bimolecular rate coefficient in the same way since [B] is also a function of *t* and as such, it is desirable to reduce the second order problem to a pseudo-first order one. (2) In order to carry out pseudo first order experiments, the concentration of one reactant is held in excess over the other ([B] > [A]) such that [B] can be considered constant over the course of the reaction. An order of magnitude difference in the concentrations is generally sufficient. The rate equation can then be rewritten as follows:

$$\frac{\mathrm{d}[\mathrm{A}]}{\mathrm{d}t} = -k'[\mathrm{A}] \qquad \text{(Eq. 4)}$$

where

$$k' = k_{\mathrm{bi}}[\mathrm{B}] \qquad \text{(Eq. 5)}$$

Again by experimentally observing how some property proportional to [A] changes at different times *t* after the start of the reaction, the pseudo first order rate coefficient *k*' for the reaction is obtained. Then by measuring *k*' at different [B] the linear relationship in Eq. 5 can be exploited in order to extract k_{bi}.

2.1.2. The temperature dependence of reaction rate coefficients

Often the rate coefficient for a reaction will be described as a rate constant however, the rate coefficient for a reaction is actually a function of temperature (*k* (T)) and the way in which it changes with temperature depends upon a property of the reaction known as the potential energy surface. (2) When two molecules interact there are various attractive and repulsive forces that arise due to the various interactions between the electrons and the protons in the system. As the configuration of the various atoms in the system changes, this potential energy interaction will also change and the way in which the energy of the system changes as the atoms move defines the potential energy surface (PES) for the reaction. (3) This potential energy surface is analogous to the landscape which the constituent atoms of the system have to traverse and the steepness of the energy contours will influence the way in which the atoms move.

Of course when considering polyatomic systems only two co-ordinates out of the many (3N-6) possible coordinates can be visualised in any one PES diagram. In a large system, considering only two co-ordinates at a time is uninformative and it is common instead to consider the change in potential

energy along single co-ordinate named the reaction co-ordinate. This reaction co-ordinate is also commonly referred to as the minimum energy path (MEP) and this corresponds to the sequence of atomic co-ordinate changes that leads to most favourable, or lowest energy, path from reactants to products.

It is the shape of the PES that determines the rate at which a reaction will proceed. Typically, intuition would suggest that as the temperature gets lower, reaction rate coefficients will get smaller. This is certainly true for many chemical reactions and this type of temperature is described by the famous Arrhenius equation:

$$k(T) = A \exp\left(\frac{-E_a}{RT}\right) \qquad \text{(Eq. 6)}$$

where in this equation $k(T)$ is the rate coefficient for the reaction as a function of temperature, A is the pre-exponential factor, E_a is the activation energy, R is the gas constant and T is the temperature. Assuming a positive value for E_a, this Arrhenius equation predicts that the natural logarithm of the rate coefficient should decrease linearly with $1 / T$ and therefore that the rate coefficient will increase as the temperature is raised. If one plots $\ln(k(T))$ versus $1 / T$ then from the gradient of such a graph it is possible to obtain the quantity E_a the activation energy and the physical interpretation of this activation energy is key to understanding the positive temperature dependence of a rate coefficient.

Over the course of a reaction it will often be necessary to break and remake one or more chemical bonds and in order break a chemical bond, energy is required. Put in other terms, pulling two atoms apart is an energetically unfavourable process and such a process manifests itself as a barrier on the PES for that reaction. The activation energy in the Arrhenius equation is then often related to the difference in energy between the top of the barrier and the reactants. A schematic of this type of PES along the reaction co-ordinate is shown in Figure 2.1. Depending upon the height of the energy barrier, only a fraction of collisions between molecules A and B, will have sufficient

energy to react. As the temperature is increased the average collision energy will be larger and therefore the fraction of successful collisions will increase and the rate coefficient will display an Arrhenius temperature dependence.

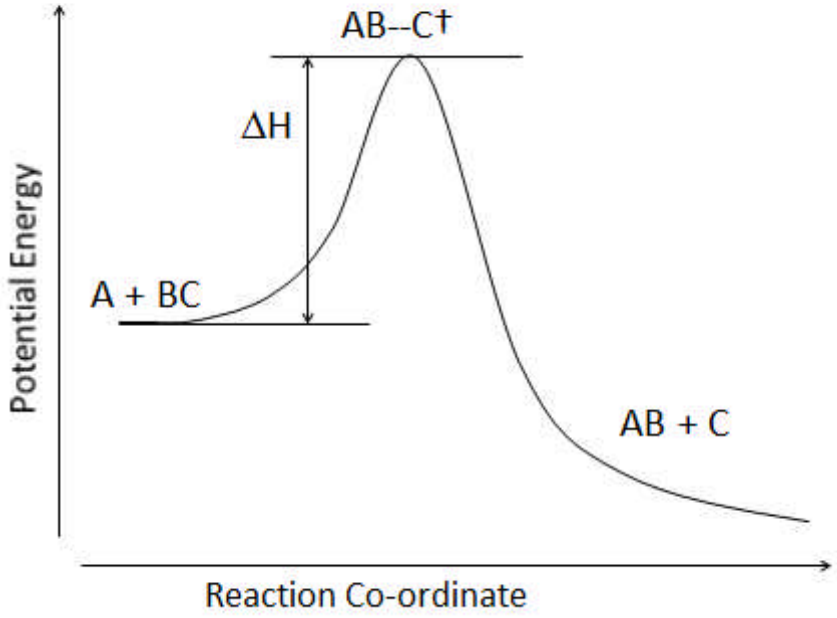

Figure 2.1: Potential energy surface diagram for an example reaction in which an energy barrier separates reactants and products. Here ΔH is the difference in enthalpy between the reactants and the top of the barrier, and the empirical activation energy, is often closely related to this quantity. The species AB--C† at the top of the barrier is a transient species known as a transition state.

If the Arrhenius equation is extended to low temperatures with any significant activation energy, the rate coefficient becomes vanishingly small. This is understandable since at very low temperatures only a tiny fraction of the molecules involved in collisions will ever have enough energy to cross the barrier. If then all reactions occurred over the type of PES shown in Figure 2.1, it would be expected that the kinetics of environments such as the interstellar medium (ISM) would be relatively uninteresting. However it has long been known that low temperature environments often display a rich variety of reactions with surprisingly large rate coefficients. (4-6)

The first reactions shown to exhibit these large low temperature rate coefficients were those involving ionic species reacting with molecules. (7) In such cases the reaction is dominated by the long range attractive forces between the two reacting partners and rather than exhibiting a barrier, the PES will instead have a potential well. This type of PES is shown in Figure 2.2. In this type of surface the two colliding partners simply stick together to form some association adduct and since there is no barrier to overcome the rate coefficients for such reactions tend to be temperature independent or exhibit a negative temperature dependence.

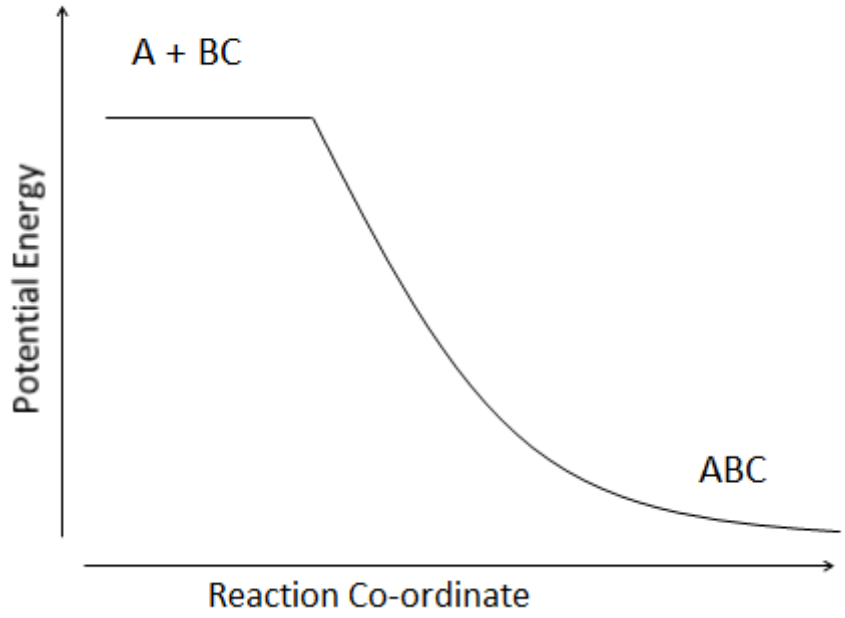

Figure 2.2: Example potential energy surface showing a barrierless association reaction.

The two schematic potential energy surfaces shown above represent the limiting cases of a reaction with and without a barrier but in reality, reactive PES's are far more complicated. While the reactions discussed thus far have been presented as occurring in a single step, they will instead involve a number of elementary reactions. If for example we again consider the fictitious reaction between molecules A and BC then a possible reaction could be written as a single step as follows.

$$A + BC \rightarrow CA + B$$

However if the reaction is looked in more detail, it can be seen to comprise a number of elementary steps;

$$A + BC \rightarrow ABC \quad \text{(R3)}$$

$$ABC \rightarrow CAB \quad \text{(R4)}$$

$$CAB \rightarrow CA + B \quad \text{(R5)}$$

where in this example the reactants first form the adduct or complex ABC which then rearranges or isomerises to form CAB before forming products CA + B. When a reactive system is studied experimentally it will generally consist of a number elementary steps and the measured rate coefficient will be a combination of the rate coefficients for these elementary reactions. This complexity is then reflected in the PES's for real systems.

As the potential energy surfaces become more complex, they are typically simplified and rather than explicitly showing the change in energy along the minimum energy path (MEP), only the energies of the barriers and wells are evaluated and these are simply connected by straight lines. An example of this type of potential energy surface which is encountered in this thesis is shown below in Figure 2.3. This type of PES will be encountered throughout this thesis since computations describing the shape of the MEP are non trivial and there are generally insufficient data available to accurately plot the change in potential energy as function of the reaction co-ordinate. However, where such data are available, the shape of the MEP will be shown.

When considering reactions of importance at low temperatures, with very few exceptions, the reactions previously shown to be fast below 200 K have been barrierless reactions. Here barrierless means that there are no energy thresholds on the reactive PES above the entrance energy of the reactants. However, the PES can still exhibit submerged energy barriers. These can be illustrated by considering part of the potential energy surfaces for $O(^3P)$

reactions with various alkenes. The MEP's are shown for both the $O(^3P)$ + ethene and $O(^3P)$ + trans-butene reactions in Figure 2.4. Here it can be seen that both reactions proceed by first forming a weakly bound species (van der Waals complex) before encountering a barrier to further products. However it can be seen that not only does the depth of the pre-reaction well increase with the size of the alkene, but also with the heavier alkanes the difference in energy between the reactants and the top of the barrier (ΔH) becomes negative and can be described as being submerged.

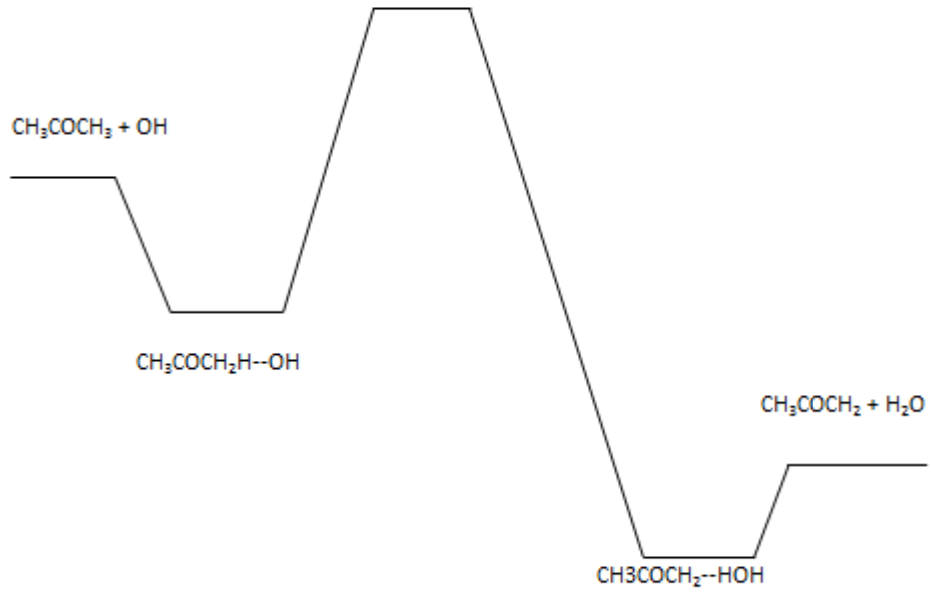

Figure 2.3 Schematic potential energy surface for the reaction between OH and acetone, showing the important stationary points. This shows only one of the possible reaction pathways which have been calculated by various groups. (8-10)Here a -- symbol indicates a hydrogen bond interaction. The top of the barrier is another type of stationary point known as a transition state but these will be described in greater detail presently.

The low temperature kinetic behaviour of these reactions has been extensively studied in a paper by Sabbah and co-workers (11). The rate coefficients from this study are shown in Figure 2.5. The smallest rate coefficients are those from the $O(^3P)$ reaction with ethene, consistent with

the presence of a barrier on its potential energy surface. As the size of the alkene increases and the barriers become submerged, it can be seen that the rate coefficients become larger and a negative temperature dependence to the rate coefficients is observed.

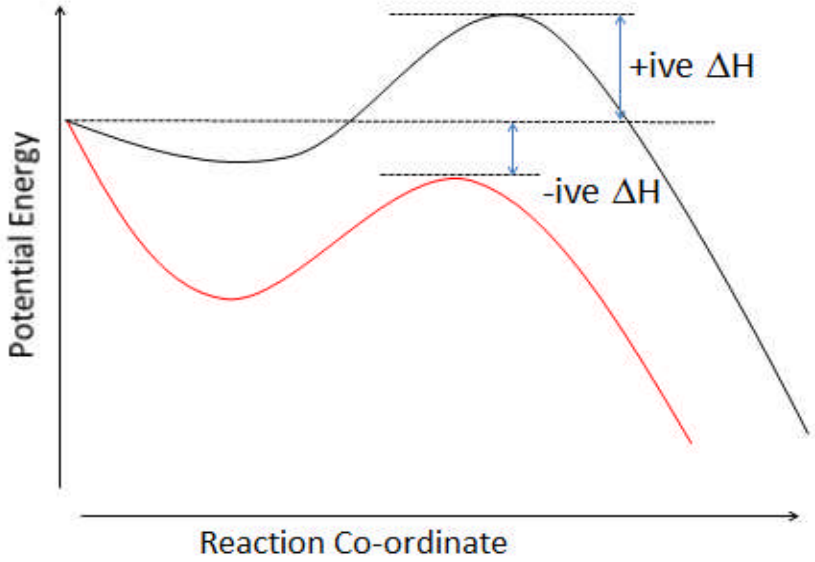

Figure 2.4: Qualitative representation of the minimum energy paths for the O(^{3}P)+ethene (black) and O(^{3}P)+trans-butene reactions (red). These potentials are adapted from the calculations of Sabbah *et al.* (11)

There are many reactions between neutral species for which the PES's display no barriers above the energy of the reactants. The rate coefficients for such reactions vary from being relatively independent of temperature, to exhibiting a marked increase as the temperature is lowered and as illustrated above, the extent of this negative temperature dependence will often be influenced by the heights of any submerged barrier on the PES. These barrierless reactions generally have rate coefficients which are greater than 10^{-11} molecule^{-1} cm^3 s^{-1} (11) at room temperature and it has been proposed that the room temperature rate coefficient is a good diagnostic for assessing the importance of a reaction at low temperature. Another diagnostic which has been used to predict whether a reaction may be competitive at low temperature is based upon ionisation energies and electron affinities. This diagnostic was first proposed by Smith *et al.*. (2006) (12) and if the ionisation enthalpy (I.E)- the electron affinity (E.A) < 9, then this is often a good indication that the rate coefficients for a reaction may exhibit a negative temperature dependence.

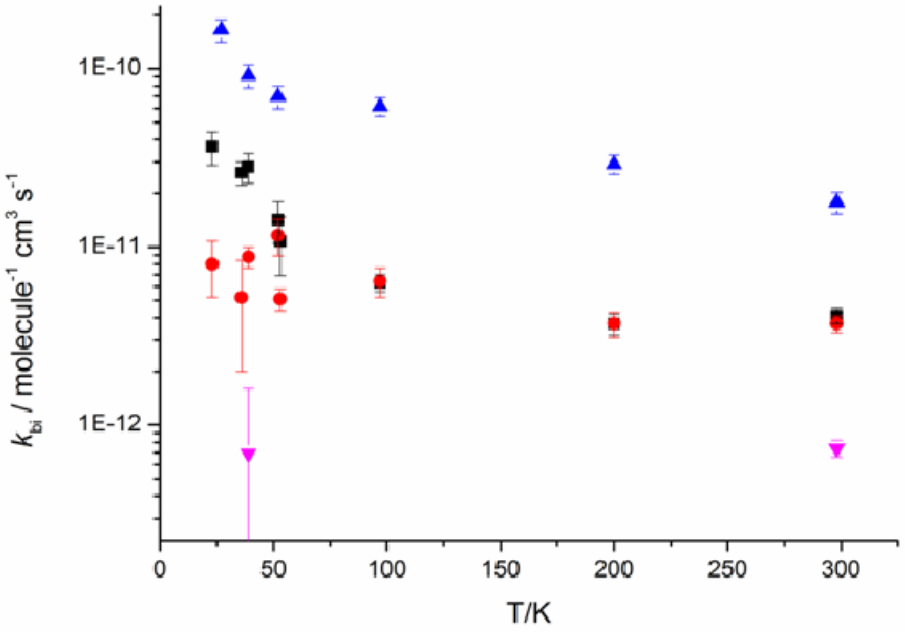

Figure 2.5: Rate coefficients for O(^{3}P) reacting with various alkenes measured by Sabbah *et al.* (11) Here the pink triangle are rate coefficients for O(^{3}P) + ethene, the red circles are rate coefficients are for O(^{3}P) + propene, the back squares are rate coefficients for O(^{3}P) + 1-butene and the blue triangles are rate coefficients for O(^{3}P) + iso-butene. Error bars are taken at the 2σ level.

2.1.3. The pressure dependence of rate coefficients.

While rate coefficients often exhibit temperature dependence, the rate coefficients for an association reaction will also display an overall dependence upon total gas density or pressure. In order to understand how this occurs an alternative description of the rate coefficient is required. In the Arrhenius equation the rate coefficient $k(T)$ was defined as a function of temperature, and such rate coefficients are known as canonical or macroscopic. Another way of defining the rate coefficient is as a function of energy to give microscopic or microcanonical $k(E)$'s and the advantage of such a formalism is that rate coefficients for a non-Boltzmann distribution of energies are then defined.

In order to explore the pressure dependence of an association reaction the simple reaction;

$$A + B \rightarrow AB \qquad \text{(R7)}$$

is considered. The key observation, made simultaneously by Lindemann and Christiansen (13) is that upon association the AB adduct will be formed with a large degree of internal excitation (AB*) which must be removed in order to prevent the adduct dissociating back to A and B. More correctly the derivations of Lindemann concerned unimolecular dissociation reactions but the analysis can be readily adapted to deal with association reactions according to the following kinetic scheme.

$$A + B \rightarrow AB^* \qquad k_a \qquad \text{(R8)}$$

$$AB^* \rightarrow A + B \qquad k_{-a} \qquad \text{(R9)}$$

$$AB^* + M \rightarrow AB + M \qquad k_M \qquad \text{(R10)}$$

Here M is some inert bath gas in the reaction system and the *k*'s are the microscopic rate coefficients for each elementary process. It is through collision with this bath gas M that excess energy within AB* is removed in order to form a stabilised adduct. Under this scheme the rate equation for the loss of the A can be expressed as follows:

$$\frac{\mathrm{d}[\mathrm{A}]}{\mathrm{d}t} = -k_a[\mathrm{A}][\mathrm{B}] + k_{-a}[\mathrm{AB}]^* \qquad \text{(Eq. 7)}$$

Since [AB]* is a short lived species the steady state hypothesis (d[AB]*/dt = 0) can be invoked to give

$$\frac{\mathrm{d}[\mathrm{AB}^*]}{\mathrm{d}t} = -k_{-a}[\mathrm{AB}^*] - k_m[\mathrm{M}][\mathrm{AB}^*] + k_a[\mathrm{A}][\mathrm{B}] = 0 \qquad \text{(Eq. 8)}$$

$$[\mathrm{AB}^*] = \frac{k_a[\mathrm{A}][\mathrm{B}]}{k_m[\mathrm{M}] + k_{-a}} \qquad \text{(Eq. 9)}$$

Whereupon Eq . 7 can be rewritten to give:

$$\frac{\mathrm{d[A]}}{\mathrm{d}t} = -k_{obs}[\mathrm{A}][\mathrm{B}] \qquad \text{(Eq. 10)}$$

$$k_{obs} = \frac{k_m[\mathrm{M}]k_a}{k_m[\mathrm{M}] + k_{-a}} \qquad \text{(Eq. 11)}$$

In the limit of high pressure k_m[M] >> k_{-a} and the observed rate coefficient for the loss of A (k_{obs}) reduces to:

$$k_{obs} = k_a \qquad \text{(Eq. 12)}$$

giving a pressure independent rate coefficient limited only by the rate at which the excited complex is formed. However in the limit of low pressure k_m[M] << k_{-a} and k_{obs} instead reduces to:

$$k_{obs} = \frac{k_m k_a[\mathrm{M}]}{k_{-a}} \qquad \text{(Eq. 13)}$$

predicting that the observed rate coefficient varies linearly with the total pressure or gas density.

2.2. Electronic structure theory calculations

In order to complement experimental measurements or to help extend measured rate coefficients to experimentally unobtainable conditions, theoretical methods are widely employed in order to calculate rate coefficients for different reactions. Before any calculations can be performed, the PES for the chosen reaction needs to be known. Discussion in the previous section showed how from a rough idea of the shape of the PES, qualitative predictions on the temperature dependence for the rate coefficients of the reaction can be made. However, in order to perform rate theory calculations, the energies and vibrational properties of the species corresponding to the wells and the barriers of the system, must be known. (14)

The way in which potential data are obtained for a particular system is through electronic structure theory calculations. Specifically this involves

solving the Schrödinger equation for a given configuration of the atoms of the system in order to obtain the total energy: (15)

$$H\Psi = E\Psi \qquad \text{(Eq. 14)}$$

where H is the Hamiltonian operator for the system, Ψ is the total wavefunction for the system and E is the total energy. The Hamiltonian for a system of nuclei and electrons is then given by the following equation:

$$H = -\sum_k \frac{\hbar^2}{2M_k}\Delta_k - \sum_i \frac{\hbar^2}{2m_e}\Delta_i + \sum_{k>l} \frac{Z_k Z_l e^2}{r_{kl}} + \sum_{i<j} \frac{e^2}{r_{ij}} - \sum_i \sum_k \frac{Z_k e^2}{r_{ik}} \qquad \text{(Eq. 15)}$$

where indices *i* and *j* run over the electrons whilst indices *k* and *l* run over the nuclei, M_k is the mass of nucleus *k*, m_e is the mass of an electron, Z_k is the charge of atom *k*, *e* is the elementary charge and r_{ij} is the distance between particles *i* and *j*. The first two terms in this Hamiltonian represent the kinetic energy of the nuclei and the electrons respectively whilst the final three terms represent the potential energy due to nucleus-nucleus, electron-electron and nucleus-electron interactions.

An electron has approximately 1/1804 the mass of a proton and consequently moves significantly faster. To a first approximation we can then assume that the electrons will instantaneously react to any change in nuclear coordinates to the extent that the two motions can be considered separable. This is known as the Born Oppenheimer approximation and through the use of this approximation, the nuclear and electronic motions can be decoupled and Eq. 14 can be rewritten as:

$$(H_{el} + V_N)\,\psi_{el} = E_{el}\psi_{el} \qquad \text{(Eq. 16)}$$

where

$$H_{el} = -\sum_i \frac{\hbar^2}{2m_e}\Delta_i + \sum_{i<j} \frac{e^2}{r_{ij}} - \sum_i \sum_k \frac{Z_k e^2}{r_{ik}} \qquad \text{(Eq. 17)}$$

and V_n is the nuclear –nuclear repulsion energy which is evaluated as a constant for a given geometry. In the Born Oppenheimer approximation, since the nuclei are considered stationary on the timescale of the movement of the electrons, the term corresponding to kinetic energy of the nuclei can be removed.

The removal of the nuclear–nuclear kinetic energy term, simplifies the Schrödinger equation for a molecular system, however the inter-electron potential energy term still prevents an analytical solution of the Schrodinger equation for all but the simplest of cases. The exact solution to the Schrödinger equation can be approximated by performing extremely detailed calculations, however the more detailed the calculation, the more computer resources are required and as such a compromise has to be reached between accuracy and efficiency. Electronic structure theory calculations are characterised by the level of theory used and the basis set used and over the next few sections, these concepts will be explained.

2.2.1. Basis sets

The Schrödinger equation (Eq. 14) for a molecular system, cannot be solved exactly and so it is necessary to guess the initial form of the wavefunction, Φ before performing any electronic structure theory calculations . Having chosen a functional form for Φ, it is necessary to refine the guess wavefunction and this is achieved through the use of the variational principle. (14) The variational principle is expressed mathematically as follows:

$$\int \varphi H \varphi \, dr \geq E_o \qquad \text{(Eq. 18)}$$

Where H is the Hamiltonian operator from Eq . 15 and E_o is the lowest eigenvalue, which in this case is the energy of the ground electronic state of the molecule on which the calculations are being performed. From this relationship it can be seen that the energy calculated using a trial

wavefunction, ψ, will always be greater than or equal to, the true ground state energy, and by altering ψ so as to minimise the total energy, the optimum wavefunction can be found.

This then raises the question as to what form ψ should take. In principle any functional form could be used, though an obvious choice is to form the trial wavefunction ϕ as a linear combination of atomic wavefunctions (orbitals) centred upon the nuclei of the system: (14)

$$\phi = \sum_{i=1}^{N} a_i \varphi_i \qquad \text{(Eq. 19)}$$

where φ_i are functions chosen to represent atomic orbitals, and the a_i are coefficients which can be varied according to the variational principle. The larger the number of atomic orbitals *N*, the closer ϕ comes to spanning the entire co-ordinate space and as such the closer the variational energy E will be to the true ground state energy E_0. The aim of basis set design is to choose a functional form for the trial wavefunction that accurately describes the chemically important regions of co-ordinate space, with the minimum number of basis functions *N* and there are various basis set methodologies which have been developed.

Whilst using atomic orbitals as basis functions is attractive from a chemistry standpoint, computationally such functions need to be integrated numerically which is computationally intensive. Because of this, in modern basis sets the atomic orbitals are commonly approximated by a linear combination of Gaussian functions which can be integrated analytically. (15) A typical Gaussian function is represented as:

$$g = \frac{2\alpha}{\pi}^{3/4} \left[\frac{(8\alpha)^{i+j+k} i!\, j!\, k!}{(2i)!(2j)!(2k)!} \right] x^i y^j z^k e^{-\alpha(x^2+y^2+z^2)} \qquad \text{(Eq. 20)}$$

where α determines the width of the Gaussian function and *i*, *j*, and *k* determine the angular momentum of the orbital that the gaussian function approximates. The atomic orbitals are represent by a linear combination of these Gaussian functions:

$$\varphi = \sum_{a=1}^{M} c_a g(\alpha_a) \qquad \text{(Eq. 21)}$$

where the coefficients *c*, are chosen to optimise the shape of the resulting atomic orbital, and *M* is the total number of Gaussian functions or primitives.

Different basis sets methodologies have developed separate sets of *c* and α which have been optimised for most atoms of the Periodic Table. The two families of basis set used in this thesis are the Pople basis sets, (16) and the correlation consistent basis sets of Dunning and co workers (17) and these will be described briefly.

An example of a Pople basis is 6-31+G** and this nomenclature can be translated in the following manner. The initial 6 indicates that 6 Gaussian functions or primitives, make up the linear combination for the core electrons and the following 3 and 1 indicate the number or primitives used for valence electrons. The fact there are two numbers and the hyphen indicates that the basis set is decontracted, meaning that the valence electron orbitals are formed from two separate linear combinations, one with 3 primitives and one with 1 primitive. Next there is a + which indicates that diffuse functions have been included. These are functions which are specially designed to treat long range interactions, which may be poorly described by normal atomic orbitals. Finally, the two * indicate that additional polarisation functions have been included, i.e, p orbitals on hydrogen's and d and f orbitals on heavier elements.

Another common type of basis set is the correlation constant family developed by Dunning and co-workers . These basis sets are denoted cc-pVDZ, cc-pVTZ ... etc, and the D(double) and T(triple) refer to whether the valence orbitals are decontracted into 2 or 3 ... etc atomic orbitals. These basis sets are particularly well suited for use in extrapolation schemes which aim to approximate the infinite basis set limit and the number of polarisation functions is increased systematically according to the amount of decontraction. Diffuse functions within these basis sets are denoted by the prefix aug.

2.2.2. Hartree Fock theory

Theories which attempt to solve the Schrödinger equation (Eq. 14) without the inclusion of any empirical parameters, are known as *ab initio,* or wavefunction, methods and Hartree Fock theory (18) is the simplest of these. In Hartree Fock theory, the many electron wavefunction for the system is expressed in terms of one electron orbitals, otherwise known as molecular orbitals (MO's) which are eigenfunctions of the Fock operator defined as:

$$f_i = -\frac{1}{2}\nabla_i^2 - \sum_k^{nuclei} \frac{Z_k}{r_{ik}} + V_i^{HF}[j] \qquad \text{(Eq. 22)}$$

where the first two terms are the kinetic energy of the electron and the potential attraction between the electron and the nuclei expressed in the same manner as in the total electronic Hamiltonian for the system H_{elec}. However whilst H_{elec} includes a third term describing the potential repulsion between electron *i* and all other electrons in the system, *j*, in the Fock operator this is dealt with in an average way via the Hartree Fock potential $V^{HF}[j]$. This Fock operator, approximates the one electron Hamiltonian for the system and by replacing H in the Schrödinger equation with f_i, one obtains the molecular orbital wavefunctions, Φ_{MO} and energies of the system, which can then be combined to give the many electron wavefunction Ψ.

In order to do this it is necessary to solve the secular equation:

$$\begin{vmatrix} F_{11} - ES_{11} & \cdots & F_{1N} - ES_{1N} \\ \vdots & \vdots & \vdots \\ F_{N1} - ES_{N1} & \cdots & F_{NN} - ES_{NN} \end{vmatrix} = 0 \qquad \text{(Eq. 23)}$$

where

$$F_{ij} = \int \varphi_i f \varphi_j \qquad \text{(Eq. 24)}$$

$$S_{ij} = \int \varphi_i \varphi_j \qquad \text{(Eq. 25)}$$

and *N* is the number of basis functions. Unfortunately, although it is necessary to solve this equation in order to determine the different $\Phi_{MO,}$ the

matrix elements $F_{ij,}$ already depend upon these molecular obitals via the $V^{HF}[j]$ term in f_i. This can be understood since in order to determine the average potential interaction between electron *i* and all other electrons *j*, it is necessary to define the average positions of the j electrons, by a quantitiy known as the density matrix ***P***, which is in turn defined by the different Φ_{MO}. This problem is solved by performing what is known as a self-consistent field procedure (SCF) (19) and in this procedure the elements of the density matrix are initially guessed and then new Φ_{MO} are obtained from solution of Eq. 23. These new Φ_{MO} can then be used to create a new density matrix and this procedure is repeated until the difference between the Φ_{MO} determined from Eq. 23 and the Φ_{MO} used to create the density matrix meets some convergence criteria.

For a closed shell system, the Hartree-Fock procedure above is relatively straightforward, however open shelled molecules introduce complications to the above process. In order to understand this it is necessary to look at the way in which the molecular orbitals are combined in order to form the many electron wavefunction Ψ.

All electrons have a spin quantum number which can take values of ±1/2 and to account for this the spatial molecular orbitals, Φ_{MO} have associated spin orbitals α and β, representing each of the two possible spin quantum numbers. Following Hund's rules, each spatial molecular orbital may then be occupied by two electrons each with different spin orbit quantum numbers. However it is also necessary to satisfy Pauli's exclusion principle which states that any wavefunction should be anti-symmetric with respect to the exchange of an electron and this principle has ultimately led to the representation of many electron wavefunctions as Slater determinants: (20)

$$\Psi_{HF} = \frac{1}{\sqrt{N!}} \begin{vmatrix} \chi_1(1) & \cdots & \chi_N(1) \\ \vdots & \vdots & \vdots \\ \chi_1(N) & \cdots & \chi_N(N) \end{vmatrix} \qquad \text{(Eq. 26)}$$

where *N* is the number of electrons, the χ_i are the different spin orbitals (products of spin and spatial orbital), and the numbers in brackets identify which electron occupies each spin orbital.

Now for a closed shell system with *N* electrons, there will be *N*/2 spatial orbitals Φ_{MO} and the *N* spin orbitals can be grouped into two sets, one with α spin and one with β spin, where it is assumed that the spatial parts of these α and β , are identical. However, for an open shell system, the situation is not as simple.

One approach is carry out the open shell Hartree Fock procedure in an analogous manner to the closed shell scenario. This is referred to as restricted open shell Hartree Fock theory (ROHF) (14) and in this method, the spatial parts of the α spin and β spin orbitals remain identical and the unpaired electron(s) are simply placed in a new spin orbital with a different spatial component. In a real molecule, however, if for example the odd electron in the open shell system is placed in an α spin orbital this unpaired electron will interact repulsively with all the other α orbitals, perturbing the spatial components of the α spin orbitals relative to the spatial components of the β orbitals and ROHF theory cannot account for this interaction.

Alternatively, the spatial parts of the α spin and β spin orbital's can be optimised independently using unrestricted Hartree Fock (UHF) theory. This incorporates the way in which the lone electron perturbs the two different sets of spin orbitals differently and can to some extent treat some non-dynamical electron correlation or multireference behaviour which will be described in due course. The drawback to these unrestricted calculations is that the wavefunction is no longer strictly an eigenfunction of the spin operator S and consequently such wavefunctions can be contaminated by electronic states of higher spin. Depending upon the extent of this spin contamination, the energies from UHF theory can be unreliable although techniques do exist to correct the wavefunction for spin contamination .

2.2.3. Dynamical electron correlation

Solving the Hartree Fock equations is relatively efficient in terms of computational resources, however the wavefunctions Ψ_{HF} obtained from such calculations are not eigenfunctions of the true electronic Hamiltonian for the system, but are instead eigenfunctions of the closely related Fock operators, f_i. Although these Fock operators capture much of the chemical

nature of a molecular system, they are limited by the very approximate way in which they treat inter-electron repulsion. The $V^{HF}[j]$ term does account for this repulsion in an average manner, but it cannot account for instantaneous movement of electrons which is known as electron correlation. Thus while Hartree Fock theory is useful for giving qualitative predictions, quantitative calculations require the use of more advanced methods or levels of theory.

First of all dynamical electron correlation will be considered and subsequently there will be a brief discussion on levels of theory which account for non-dynamical electron correlation, otherwise known as multirefence methods. From a dynamical correlation perspective, there are three methods or levels of theory which are commonly used to treat electron correlation. These are configuration interaction, perturbation theory, (21) and coupled cluster theory, (22) and some of these will be encountered in this thesis. Rather than describe these methods in too much detail, a brief overview will be given.

Although Hartree Fock theory is unable to account for electron correlation, the Hartree Fock wavefunctions, it still describes much of the character of a molecular system and the general philosophy used in treating electron correlation is to use the Hartree Fock, determinant wavefunction, Ψ_{HF} as a first approximation towards a more accurate wavefunction. This more accurate wavefunction can be written as a linear combination:

$$\Psi_{elec} = a_0\Psi_{HF} + a_1\Psi_1 + \ldots \qquad \text{(Eq. 27)}$$

where the leading term in the linear combination is the Hartree Fock wavefunction weighted by some coefficient a_1 and in cases where only dynamical correlation is important $a_1 >> a_2 + a_3 + \ldots$ and the Hartree Fock wavefuntion is the dominant term in the linear combination. The idea is then that using the variational principle the above linear combination can be minimised in order to more accurately approximate the true many electron wavefunction for the system.

Of the three levels of theory described above, configuration interaction is the easiest to understand, conceptually. In this case the higher wavefunctions in the linear combination are created by exciting electrons from the occupied

Hartree Fock orbitals into the virtual Hartree Fock orbitals (those eigenfunctions in Eq. 23 which lead to higher energies and are thus unoccupied by electrons and do not appear in the Slater determinant) . A full CI calculation would consider every possible excitation, but such calculations are rarely practical computationally. Instead it is common to restrict the number of excited configurations to those differing from the Hartree Fock configuration by 1, 2,3 ... excitations. For example CISD is translated as configuration interaction with single and double excitations and the wavefunction for this level of theory would be described as:

$$\Psi = a_o \Psi_{HF} + \sum_{i}^{occ} \sum_{r}^{vir} a_i^r \Psi_i^r + \sum_{i<j}^{occ} \sum_{r<s}^{vir} a_{ij}^{rs} \Psi_{ij}^{rs} \qquad \text{(Eq. 28)}$$

where *i* and *j* refer to occupied Φ_{MO} whilst *r* and *s* refer to vitual $\Phi_{M.}$ The second term on the right hand side is a sum of wavefunction formed by a single electron excitation, i.e moving an electron from orbital *i* to orbital *r* and the third term on the left is a sum of all wavefunctions formed by the excitation of 2 electrons, i.e electrons move from occupied orbital *i* and *j* to virtual orbitals *r* and *s*. The coefficients a can then be determined variationally by solving the secular equation:

$$\begin{vmatrix} H_{11} - E & \dots & F_{1N} - E \\ \vdots & \vdots & \vdots \\ F_{N1} - E & \dots & F_{NN} - E \end{vmatrix} = 0 \qquad \text{(Eq. 29)}$$

where

$$\mathrm{H}_{nm} = \int \Psi_m \mathrm{H}_{ele} \Psi_n \qquad \text{(Eq. 30)}$$

It should be noted that modern applications of configuration interaction utilise an improvement known as quadratically convergent configuration interaction theory (QCI) (23) but a detailed discussion of the difference between the two will be omitted.

The other levels of theory mentioned, perturbation theory and coupled cluster theory, follow a similar methodology to the configuration interaction

theory but differ in their implementation. Perturbation theory is applicable to many fields and problems and it was adapted for use in electronic structure theory calculations by Moller and Plesset. (21) In this method, the Hartree Fock wavefunction is again used as a first order approximation and then the true wavefunction for the system is approximated by acting upon this Hartree Fock wavefunction using a perturbing operator. The details of perturbation theory will not be presented, but the nomenclature of Moller Plesset perturbation theory is MPn where n refers to order of terms at which the perturbation expansion is terminated. By increasing n the perturbed wavefunction get closer and closer to the true wavefunction but at increased computational expense. The most commonly used example of perturbation theory is MP2. This level of theory is generally less accurate than QCISD or CCSD (coupled cluster singles and doubles) calculations, but is often used as a relatively computationally efficient method for optimising the geometries of molecular species. By increasing n, the perturbation theory wavefunction approaches the true many electron wavefunction for the system, but above values of n = 4, coupled cluster and configuration interaction methods represent a more computationally efficient way of achieve the same level of accuracy in the calculation.

The final level of theory to be considered is coupled cluster theory which gives results very similar to quadratically convergent interaction theory. In coupled cluster theory the many electron wavefunction is expressed as follows:

$$\Psi = e^{T}\Psi_{HF} \qquad \text{(Eq. 31)}$$

where

$$T = T_1 + T_2 + \cdots + T_n \qquad \text{(Eq. 32)}$$

n is the number of electrons an T_i is an operator which generates wavefunctions with I electron excitations. In this way it can be seen that coupled cluster theory follows the same methodology as configuration interaction theory, but with a different mathematical implementation. Like configuration interaction theory, the *T* operator can be truncated at a certain degree of electron excitation and the QCISD(T) and CCSD(T) levels of

theory, in which triple electron excitations are treated perturbatively have emerged as the “gold standard” of electronic structure theory. Of course it is possible to increase the accuracy of the calculation by including further excitations, but this is computationally impractical for all but the smallest of systems and the two levels of theory given above are of sufficient accuracy for most systems. In order to give some idea of the typical errors associated with *ab initio* levels of theory in Table 2.1, taken from Cramer (15) shows the average errors in the electronic energies, calculated by different levels of theory, compared to full CI calculations, for three species HB, H_2O and HF.

Level of theory	Average error in energies / kcal mol^{-1}
MP2	17.4
CCSD	4.5
QCISD	4.0
MP4	3.7
CCSD(T)	0.5
QCISD(T)	0.5
CCSDT(Q)	0.02

Table 2.1: Average errors in calculated electronic energies compared to full CI calculations for different levels of theory. These calculations were performed for HB, H_2O and HF and the results are taken from Cramer (15). These results correspond to elongated geometries rather than the equilibrium geometries of the species, and at these geometries the errors in the energies are larger.

2.2.4. Non-dynamical electron correlation

While levels of theory such as CCSD(T) usually give the most accurate results which are computationally feasible, there are cases of CCSD(T) calculations which are well outside average errors given in Table 2.1. In these cases another type of electron correlation, non-dynamical, is important.

To understand this type of electron correlation, it is necessary to refer to Eq. 27. As stated in the previous section, in most cases the Hartree Fock wavefunction determinant will dominate the linear combination. However there are cases where this is not the case, and two or more wavefunctions, will have similar coefficients a_i. This occurs when the molecule in question has a small energy separation between the different frontier molecular orbitals and the lowest of the virtual molecular orbitals and is common in systems with degenerate pi states and molecules with different resonance structures.

In dynamical electron correlation, different electronic configurations are considered, but the virtual molecular orbitals which are used are those obtained as eigenfunctions during the Hartree Fock process. Unfortunately, the quality of the molecular orbitals obtained in such a process, depends upon whether these orbitals are occupied or unoccupied in the Slater determinant and unoccupied orbitals tend to be less well defined. Cases such as those listed above, are then poorly described by a single determinant wavefunction, and the orbital shapes, instead need to be optimised, considering all chemically relevant configurations of electrons. This is done using a multi-determinant variant of Hatree Fock theory known as multi-configurational self-consistent field theory (MCSCF) . (24)

In order to perform MCSCF calculations, an active space (m,n) must be defined where m is number of Hartree Fock MO's (both occupied and unoccupied) which may be occupied in one or more of the important electronic configurations of the molecule, and n is the number of electrons which may appear in different orbitals in the different electronic configurations. Having defined the active space, different electronic configurations are formed, consisting of all the ways in which the n electrons may be distributed among the m orbitals and an SCF procedure is carried out, from which new MO's and energies are obtained. Such a calculation is referred to as a complete active space calculation (CASSCF) however there is a variant in which only selected electronic configurations are considered know as a restricted active space calculation (RASSCF).

The easiest way to think of the MCSCF method is as an analogue of the Hartree Fock procedure for cases where the ground state wavefunction cannot be described by a single Slater determinant. Although some of the dynamical election correlation in the system can be accounted for by the different electronic configurations considered, MCSCF is still very much a first order approximation, and multireference variants of perturbation theory

(25) and configuration interaction theory (26) exist in which the MCSCF wavefunction is used as the leading term in an expansion rather than the Hartree Fock wavefunction.

In open shelled systems multireference calculations are the proper way to overcome the limitations of the unrestricted and restricted open shell formulations of Hartree Fock theory. Using unrestricted calculations does to some extent account for the multireference character of these systems and for most of the species in this thesis, single reference calculations have been used. However, diagnostics have been developed to indicate whether single reference coupled cluster calculations can accurately reproduce the energy of the system in question and these diagnostics have been utilised in chapter 5 of this thesis.

One such diagnostic is the T1 diagnostic developed by Lee. (27) This diagnostic works by examining the amplitudes of the T1 coupled cluster operator and if the T1 value is greater than 0.02 then this suggests that multireference effects could be important. A related diagnostic (D1) has been developed for open shell systems. The values for this diagnostic are strongly influenced by the T1 value, but it has been proposed that a ratio T1/D1 < $1/\sqrt{2}$ is another indicator of multireference behaviour . (28)

2.2.5. Density Functional theory

A final short section here will deal with electronic structure theory calculations using Density Functional theory (DFT) methods. Discussion of these methods is beyond the scope of this thesis and many good review articles exist, (29, 30) however, since a small number of density functional calculations have been performed in this thesis a brief discussion will be given here.

Whereas the levels of theory described so far are based upon determining the many electron wavefunction, density functional calculations follow a different methodology where the electronic energy is determined instead from the electron probability distribution. Modern density functional calculations follow the SCF procedure formulated by Kohn and Sham but the mathematical details will be omitted here. The important point is that through the use of different functionals, density functional calculations account to some extent for electron correlation, but with a computational cost comparable to that for Hartree Fock calculations. The disadvantage of DFT calculations is that there is no systematic way of improving the

accuracy of the calculation since the different functionals are essentially semi-empirical and while a particular functional may perform well for a particularly type of system, that is no guarantee that it will also give accurate results for an unrelated system.

In the current work, the MPW1K DFT method has been used on numerous occasions. This functional was created by Truhlar and co-workers (31) and has been shown to reproduce transition state geometries and barrier heights well . (32) Since this method has been extensively benchmarked against systems similar to those studied in this thesis a certain degree of confidence can be given to this method. (33, 34) However, although these calculations are computationally efficient, they are unlikely to be quite as accurate as full CCSD(T) calculations, and in this thesis MPW1K calculations have only been used in cases where many *ab initio* energies are required, such as in calculating minimum energy paths (IRC calculations) or in calculating potentials for rotation about a particular bond.

2.3. Calculating rate coefficients

There are many theories for calculating rate coefficients theoretically and these can be loosely grouped under statistical theories, classical trajectory methods and quantum scattering calculations. In the current thesis only statistical calculations have been used and such calculations can be performed relatively routinely, and can yield excellent agreement between theory and experiment. (35) Statistical calculations are the type of calculation which has been used in the thesis and therefore only these will be discussed here.

This section will discuss theories for calculating elementary rate coefficients for reactions proceeding both over a barrier and over a well. As well as distinguishing between reactions with a barrier and barrierless reactions, this section also deals with both macroscopic and microscopic theories. Experimentally the rate coefficient for a reaction is typically measured as a function of temperature to give the macroscopic rate coefficient k(T) but a more fundamental quantity is the microcanonical rate coefficient k(E). By calculating the rate coefficient as a function of energy, non Boltzmann energies distributions can then be considered, which are essential for the proper treatment of any short lived intermediates in a reaction. Through calculating micro-canonical rate coefficients, it is then possible to examine the complex interplay between reactive process and energy transfer, and potential energy surfaces consisting of an arbitrary number of reaction

intermediates can then be examined using the chemical master equation techniques described in Section 2.4.

2.3.1. Reactions over a barrier

2.3.1.1. Macroscopic theories

Two common theories of chemical reactivity are that of simple collision theory and transition state theory. Both of these theories retain the exponential term from the Arrhenius equation but then evaluate the pre-exponential factor *A*, to expressions involving known physical constants and molecular parameters. The exponential part of these theories can be understood by thinking of a chemical reaction over a potential energy surface as translational motion over a barrier, the height of which is related to E_{act}. The term in the denominator represents the average internal energy of a molecule at a given temperature and as the activation energy increases, relative to the average internal energy, then the number of reactive collisions and hence the rate coefficient, decays exponentially.

The earliest method for calculating rate coefficients is that of collision theory. Collision theory calculations are now largely obsolete and rarely yield qualitative, let along quantitative agreement with experiments. It is however worth considering this method before moving on to more sophisticated methods in order to get a feel for the way in which the different theories have evolved. In collision theory, the reacting atoms are modelled as impenetrable spheres and the expression for the rate coefficients consists of two parts, the number of collisions between molecules and the chance that a particular collision will be reactive. The second of these parts corresponds to the exponential factor in the Arrhenius equation, so this leaves the *A* factor which is equated with the average number of collisions between reacting molecules. In order to obtain an expression for the average number of collisions, the collision cross section for the reaction needs to be known.

$$\sigma = \pi b_{\max}^2 \qquad \text{(Eq. 32)}$$

In this expression b_{max} is the maximum impact parameter, i.e, the maximum separation between the centres of the two reacting molecules at which a collision can be said to occur. For a reaction between two molecules A and B with radii r_A and r_B then $b_{max} = r_A + r_B$. Once the collision cross section is known, then the average speed of the molecules is also required in order to determine the collision frequency and this can be determined from the Maxwell-Boltzmann distribution of kinetic energies:

$$< v_r >= \left(\frac{8k_B T}{\pi \mu} \right)^{\frac{1}{2}} \qquad \text{(Eq. 33)}$$

where k_B is the Boltzmann constant, T is the temperature, and μ is the reduced mass of the colliding species.

The collision frequency will depend also upon the number of molecules, N_A and N_B but these cancel out in the full derivation leaving the following expression for the rate coefficient *k(T)* :

$$k(T) = \left(\frac{8k_B T}{\pi \mu} \right)^{\frac{1}{2}} \sigma e^{\frac{-E_a}{k_B T}} \qquad \text{(Eq. 34)}$$

where *Ea* is the activation energy for the reaction.

The simple collision theory model is limited in its accuracy. Results from this equation can often be used to get qualitative results over a limited temperature range but actual rate coefficients are rarely predicted with any accuracy. (3) This is largely due to the initial assumption that the reacting molecules are hard spheres which does not take into account any chemical interactions between the respective molecules.

A more detailed approach to calculating rate constants is provided by transition state theory. This theory rests on the assumption that as a reaction progresses from reactants to products, a transient transition state is

formed between the two colliding bodies. The kinetic scheme for this is shown below:

$$A + B \rightarrow AB^{\dagger} \quad (k_1) \qquad \text{(R11)}$$

$$AB^{\dagger} \rightarrow A + B \quad (k_{-1}) \qquad \text{(R12)}$$

$$AB^{\dagger} \rightarrow C + D \quad (k_2) \qquad \text{(R13)}$$

where this scheme refers to the fictitious reaction in which reactants A and B form products C and D. Here $AB^{\dagger}$ is a transient reaction intermediate, known as a transition state.

A steady state hypothesis on the reaction scheme can then be used in order to express the formation of products in terms of the equilibrium constant $K^{\neq}$ where $K^{\neq} = k_1 / k_{-1}$ and using statistical mechanics this equilibrium constant can be expressed in terms of the molecular partition functions of both the reagents and the transition state.

$$\frac{d[products]}{dt} = k_2 \frac{k_1}{k_{-1}}[A][B] = k_2 K^{\neq}[A][B]$$

(Eq. 35)

$$k_2 K^{\neq} = k^{\neq} = k_2 \frac{Q_{AB^{\neq}}}{Q_A Q_B} \exp\left(\frac{-\Delta E_0^{\neq}}{k_B T}\right) \qquad \text{(Eq. 36)}$$

where Q_{AB}, Q_A and Q_B are the molecular partition functions for the transitions state and reagent molecules respectively.

When the two reagents form the transition state, one of the 3N-6 vibrational frequencies in the new species is imaginary and this frequency corresponds to translation over the top of the potential energy barrier. This vibration can be separated from the molecular partition function for the transition state and then evaluated as follows.

$$Q_{vib} = \lim_{\nu^{\neq} \to 0} \frac{1}{1 - e^{-h\nu^{\neq}/k_B T}} \approx \frac{k_B T}{h\nu^{\neq}} \qquad \text{(Eq. 37)}$$

where $\nu^{\neq}$ is the imaginary vibrational frequency and *h* is Plancks constant.

Finally the unimolecular decomposition rate coefficient k_2 can be equated with the imaginary vibrational frequency giving the final result:

$$k(T) = \frac{k_B T}{h} \frac{Q^{\neq}}{Q_A Q_B} \exp\left(\frac{-\Delta E_0^{\neq}}{k_B T}\right) \qquad \text{(Eq. 38)}$$

2.3.1.2. Microscopic theories

After a series of modifications to the Lindemann mechanism, the Rice Ramsperger Kassel Marcus (RRKM) (36) theory of unimolecular reactions was developed. The mechanism involved in this theory is a Lindemann mechanism for a unimolecular dissociation with the inclusion of a transition state as shown below.

$$A + M \rightarrow A^*(E^* \rightarrow E^* + \delta E) \quad (\delta k_1) \qquad \text{(R14)}$$

$$A^*(E^* \rightarrow E^* + \delta E) + M \rightarrow A \quad (k_2) \qquad \text{(R15)}$$

$$A^*(E^* \rightarrow E^* + \delta E) \rightarrow A^{\dagger} \quad (k_a) \qquad \text{(R16)}$$

$$A^{\dagger} \rightarrow \text{Products} \quad (k^{\dagger}) \qquad \text{(R17)}$$

This theory includes the explicit consideration of molecular internal energy in and the mechanism has been further extended to include both the energised molecule A^* and a transition state A^+, prior to the formation of products. RRKM theory requires the evaluation of two equilibrium constants, the ratio of rate coefficients $\delta k_1 / k_R$ which is equal to the equilibrium constant for the

formation of A^* and the equilibrium constant for the formation of A† and a quantum-statistical mechanical treatment is employed in order to do this. In this treatment the equilibrium expressions are calculated as a ratio of molecular partition functions giving the flowing equations:

$$\frac{\delta k_1(E^* \rightarrow E^* + \delta E^*)}{k_2} = \frac{\rho(E^*)\exp(-E^*/kT)}{Q_2}\delta E^* \qquad \text{(Eq. 39)}$$

$$\left([A^+]/[A^*]\right)_{eqm} = \Sigma g_i / \Sigma g_i^* = \rho(E^+)/\rho(E^*) \qquad \text{(Eq.40)}$$

where $\rho(E^*)$ and $\rho(E^+)$ are the densities of states for the exited molecule and the energised molecule respectively, Q_2 is the molecular partition function for molecule A and k is the Boltzmann constant.

In order to evaluate $k_a(E)$, a transition state theory approach is used where, invoking a steady state treatment of [A] we obtain:

$$k_a(E^*) = \sum_{E_{vr}^+}^{E^+} \frac{1}{2} k^+(x) \left(\frac{[A^+_{(E_{vr}^+, x)}]}{[A^*_{(E^*)}]} \right)_{eqm} \qquad \text{(Eq. 41)}$$

where x is the translational energy in the reaction coordinate and E_{vr} is the vibrational and rotational energy contribution to the transition state as opposed to the translational energy contribution.

The equilibrium expression has already been evaluated so an expression is required for $k^+(x)$. This is achieved by modelling the decomposition of the transition state as translation of a particle in a box giving.

$$k^+(x) = (2x/\mu)^{1/2}/\delta \qquad \text{(Eq. 42)}$$

where μ is the reduced mass of the atoms involved in the reaction co-ordinate, and δ is the width.

Finally after some manipulation the RRKM expression is obtained:

$$k_a(E^*) = \frac{W(E^+_{vr})}{hp(E^*)} \qquad \text{(Eq. 43)}$$

where

$$W(E^+_{vr}) = \sum_{E^+_{vr}}^{E^+} P(E^+_{vr}) \qquad \text{(Eq. 44)}$$

and *P(* E^+_{vr} *)* is the number of vibrational–rotational states with a total energy of exactly E^+_{vr} .

2.3.2. Barrierless reactions.

In the case of barrierless reactions the calculation of either *k*(T) or *k*(E) is significantly more complicated. Since RRKM and transition state theory do not allow for trajectories that re-cross from the product side of the barrier to the reactants, the calculated rate coefficients can be thought of as upper bounds to the true values and transition state is chosen such that the calculated rate coefficient are minimised. (37) In this sense, the transition state may be considered a bottleneck to the reaction and formally this transition state will be located as a maximum in the Gibbs energy (38) of the molecule defined as:

$$G = H - TS \qquad \text{(Eq. 45)}$$

where *G* is the Gibbs energy, *H* is the enthalpy and *S* is the entropy.

Potential energy surfaces, such as those discussed so far consider only the change in enthalpy. When there is a barrier upon the potential surface, the enthalpy term will dominate and the maximum in the Gibbs energy can be equated with the maximum in the enthalpy. However, when there is no enthalpic barrier upon the potential energy surface, the entropic term

becomes significant, the location of the transition state is less apparent from the PES. In the barrierless case, the position of the transition state is also a function of temperature, or energy and detailed variational calculations are required.

Variational (39) or flexible (40, 41) transition state theory approaches, are available in both macroscopic or microscopic forms but the implementation of these methods is significantly more complicated than in the simple RRKM/ TST approaches discussed above. The main difficulty in performing such calculations is due to the amount of information about the potential energy surface for the reaction that is required. Specifically, *ab initio* energies are needed along the whole minimum energy path describing the barrierless process, and at each of these points, vibrational frequencies are required in order to map the change in entropy. Creating such a potential is computationally demanding and as such the reaction path potential is typically fit to relatively low level *ab initio* calculations. The accuracy of these variational transition state theory calculations, is then limited by the quality and amount of *ab intio* data describing the potential.

In the context of very low temperature kinetics, reactions of interest will naturally involve barrierless processes. Variational calculations are reliable given a sufficiently accurate potential but there is a significant computational bottleneck associated with obtaining such information. As such, a number of methods involving simplified potentials have been used extensively in calculating rate coefficients at low temperature, such as the statistical adiabatic channel mode (SACM). (42-44)

Both variational calculations and the simplified approaches mentioned above have been used on many occasions, (6) and the details of these methods will be omitted in this thesis. Instead this section will focus upon the simplest of theories for calculating rate coefficients at low temperatures, capture theory, followed by the pragmatic inverse Laplace transform approach used extensively in this thesis. Finally the conceptual rather than mathematical details of a method known as the two transition state model will be described. (45)

2.3.2.1. Capture theory (macroscopic)

One class of kinetic theory that has met with some success is that of capture theory. For reactions with a purely attractive potential from reactants to products it is often long range attractive forces that dominate and we can model the potential energy surface in terms of an interaction potential (V) depending upon the intermolecular forces present and the internuclear separation.

$$V(R) = -\frac{C_n}{R^n} \qquad \text{(Eq. 46)}$$

In this equation C_n is a coefficient depending on the properties of the species involved and n describes the type of chemical interactions present.
Although the reactions we are describing take place on PES's with no barrier to reaction, they still can exhibit small maxima due to a centrifugal barrier.
(3) In terms of reaction dynamics between two particles there are two types of energy that need to be considered. When considering the reaction between two species, the radial motion will have a large effect in determining the energy and frequency of collisions between particles. However, the angular motion is also an important factor in determining reaction dynamics. This angular component to the potential energy can be described mathematically as $V = L^2/2\mu r^2$ where L is the orbital angular momentum of the particle, μ is the collisional reduced mass and R is the separation of the centres of mass of the two particles. Since

$$L = \mu v b \qquad \text{(Eq. 47)}$$

and

$$\mathrm{E} = \frac{\mu v^2}{2} \qquad \text{(Eq. 48)}$$

where b is the impact parameter for the reaction and v is the relative velocity of the collision partners, we can obtain the following expression for the angular or centrifugal motion.

$$V = \frac{\mathrm{E}b^2}{\mathrm{R}^2} \qquad \text{(Eq. 49)}$$

With both the interaction potential and the centrifugal term, an effective potential can then be described:

$$V_{eff}(R) = \frac{\mathrm{E}b^2}{\mathrm{R}^2} - \frac{C_n}{\mathrm{R}^n} \qquad \text{(Eq. 50)}$$

From this equation it can be seen that while the interaction potential is attractive, the centrifugal term is repulsive and, being proportional to R^2, also relatively long range. The combination of the two terms leads to a small barrier in the potential energy termed the centrifugal barrier and the height of this barrier increases with an increase in firstly the impact parameter and then consequently also with an increase in the orbital angular momentum. The separation at which the maximum (R_{max}) in the potential occurs can be evaluated through differentiation of V_{eff} with respect to R.

$$R_{\max} = \left(\frac{nC_n}{2b^2\mathrm{E}} \right)^{1/(n-2)} \qquad \text{(Eq. 51)}$$

In classical capture theory, the assumption is made that if the maximum in the potential is lower than the collision energy then the reaction will always occur and if the converse is true the reaction will never occur. This means that the maximum value of the impact parameter at which reaction can occur (b_{max}) can be determined by solving the equality $V_{eff}(R_{max}) = E$ to obtain:

$$b_{\max}^2 = \left(\frac{C_n}{2\mathrm{E}} \right)^{2/n} \frac{n}{(n-2)^{(n-2)/n}} \qquad \text{(Eq. 52)}$$

Finally having obtained a maximum value for the impact parameter an expression for the reaction cross section is determined

$$\sigma_R = \int_0^{\infty} 2\pi b P(b) db = \pi b_{\max}^2 \qquad \text{(Eq. 53)}$$

and integration of this cross section over a Boltzmann distribution of velocities yields a value for the rate constant for the reaction.

Such capture theory calculations are limited in their accuracy. For ion molecule reactions, the long range potential dominates and capture theory predictions can often be seen to yield good agreement with experiment. However for neutral-neutral reactions, the attractive dipole or dispersion interactions are typically shorter range and the potential is thus complicated by other interactions between the associating species. For the neutral-neutral case the simplified potentials used in capture theory calculations are generally insufficient to provide quantitative agreement between experiment and theory . (46)

2.3.2.3. The inverse Laplace transform method (microscopic)

The inverse Laplace transform method described here is actually a method for converting macroscopic rate coefficients, to microscopic rate coefficients rather than calculating barrierless rate coefficients *a priori*. However this method is included here as it has been used extensively throughout this thesis to treat barrierless reaction steps. This method is commonly used in master equation simulations, and works by taking experimental or theoretical *k*(T)'s and converting these into *k*(E's).

More specifically it is the high pressure limiting *k*(T)'s which are required. In many cases such data can be determined or estimated from the available experimental data and when using the ILT method in conjunction with a master equation analysis, the parameters determining the high pressure limiting *k*(T)'s may be fit to the existing experimental measurements. In the current thesis, all the reactions studied involve the association of the reacting moieties to form a weakly bound complex or adduct. These are all

barrierless reactions and it has been assumed in this thesis that the formation of these complexes is limited almost entirely by the rate at which the reacting partners collide (capture limited). As such a high pressure limiting rate coefficient of 3×10^{-10} molecule^{-1} cm^3 s^{-1}has been used. (47) It is also assumed that the high pressure limiting rate coefficients for these species are independent with temperature. It is possible that the *k*(T)'s may exhibit a very slight negative temperature dependence, as predicted by capture theory, but unfortunately, no experiments have been performed for these species which explore this.

It is appreciated that these capture theory association rate coefficients may have significant errors associated with them but the high pressure limiting rate coefficients estimated in chapter 7 show that these capture theory rate coefficients are certainly accurate to within a factor of two.

The Inverse Laplace transform method was first proposed by Slater (48) but was formulated for use in Master equation calculations by Robertson and co-workers. (49) A master equation simulation deals with unimolecular reactions and while an association reaction (A+B→AB) is a bimolecular process, the reverse dissociation process (AB→A+B) is unimolecular and the rate coefficients for the two processes are related by detailed balance:

$$k^{\infty}a(T) = k^{\infty}d(T)K_{eq} \qquad \text{(Eq. 54)}$$

where k^{∞}a(T) and k^{∞}d(T) are the high pressure limiting rate coefficients for the association and dissociation respectively and K_{eq} is the equilibrium constant for the reaction.

Following the derivation of Robertson *et al.* (49) macroscopic rate coefficient k^{∞}d(T) can be written in terms its associated microscopic rate coefficients as follows:

$$k^{\infty}d(T) = \frac{1}{Q(T)}\int \rho(E)k_d(E)\exp(\frac{E}{k_BT})\,dE \qquad \text{(Eq. 55)}$$

where Q(T) is the molecular partition function for the molecule AB, ρ(E) corresponds to the density of states of AB at energy E and k_d(E) are the microcanonical rate coefficients for the dissociation process. The right hand side of equation Eq. 55 can be expressed as a Laplace transform but before

utilising this, it was recognised that while k^{∞}d(T) often depends strongly upon temperature, the barrierless process k^{∞}a(T) generally has a weak temperature dependence and experimentally it is these k^{∞}a(T) which more readily obtainable. As such Eq. 56 was rewritten in terms of k^{∞}a(T) and rearranged to give:

$$k_d(E) = \ell^{-1}[Q(T)K_{eq}k^{\infty}a]/\rho(E) \qquad \text{(Eq. 56)}$$

where ℓ^{-1} denotes an inverse Laplace transform.

Finally assuming k^{∞}a(T) can be written in the form:

$$k^{\infty}a(T) = A^{\infty}(\frac{1}{k_B T})^{n\infty}\exp(\frac{-E\infty}{k_B T}) \qquad \text{(Eq. 57)}$$

then Eq. 57 can be solved to give:

$$k_d(E) = \frac{CA^{\infty}}{\rho(E)\Gamma(n^{\infty}+1.5)}\int_0^{E^*}\rho(x)[(E)-x]^{n\infty+0.5}dx \qquad \text{(Eq. 58)}$$

where

$$C = \left[\frac{2\pi M_a M_b}{h^2(M_a+M_b)}\right] \qquad \text{(Eq. 59)}$$

$$E^* = E - E^{\infty} - \Delta H \qquad \text{(Eq. 60)}$$

Γ is the gamma function, $\rho(x)$ is the convolved density of states in the bimolecular species (A and B), M_a is the mass of molecule a and ΔH is the change in enthalpy during the reaction.

2.3.2.2. The two transition state model.

Two transition state theory calculations of Greenwald and co-workers (45) have been used successfully to calculate rate coefficients for a number of barrierless reactions between neutral species. (11, 50, 51) Given a generic potential energy surface of the type in Figure 2.6 with a weak well followed by a submerged barrier, the two transition state model assigns an outer transition state corresponding to the barrierless association and an inner transition state corresponding to the submerged barrier.

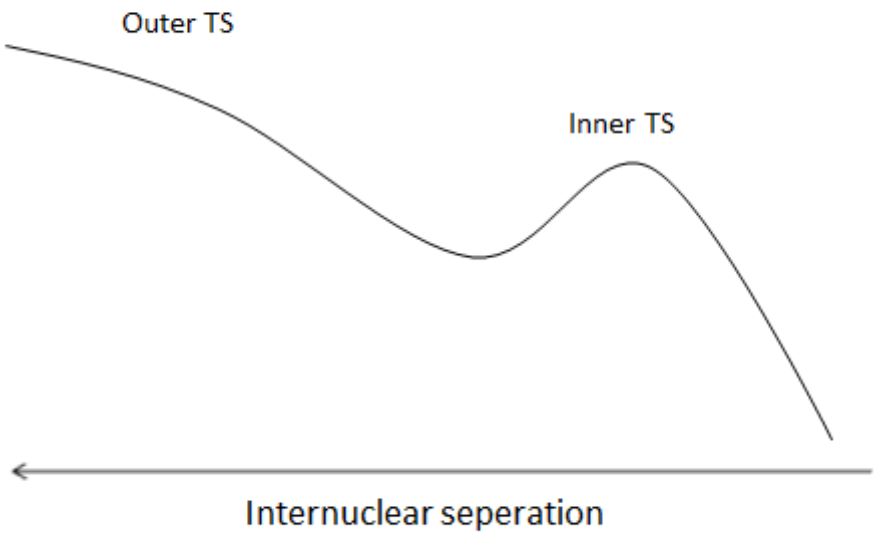

Figure 2.6: Schematic diagram showing the inner and outer transition states. At large separations the reaction is controlled by the barrierless, outer transition state, and as the molecules approach each other, the submerged barrier provides a second, inner transition state.

In the theory of Greenwald *et al. (45)* the outer transition state is treated using a variational method known as long range transition state theory (52) which calculates an accurate rate coefficient resolved not only with respect to energy, but also with respect to rotational energy level *J*. However, although such accurate calculations have not been performed here, the two transition state model can be used to qualitatively explain the temperature dependencies of the rate coefficients for real systems with complicated PES's involving a submerged barrier.

The key to the two transition state model is the observation that the dominant transition state will change at different temperatures. At low temperatures and therefore energies, the sum of states of the outer transition state will generally be largest but at high temperatures and energies the sum of states of the inner transition state will overtake those of the outer transition state. Referring to the RRKM rate coefficients in Eq. 43 the reactive flux is determined by the sum of states and therefore the dominant reaction bottleneck will vary from the outer transition state to the inner transition state as the temperature is reduced. At some intermediate

temperature both transition states will contribute appreciably to the overall rate coefficient and the effective sum of states will comprise will be effected by both transition states.

To date the two transition state model has only been used for cases where the inner transition state is submerged, but the same arguments apply to the case where the inner transition state is above the energy of the reactants. In this case, at high temperatures, the rate coefficients will follow an Arrhenius temperature dependence and the temperature dependence may become increasingly non-Arrhenius as the barrierless transition state begins to dominate at low temperature. This model will be used to explain some of the experimental results obtained in the current thesis and more detail will be given in these specific cases.

2.4. Master equation methods

2.4.1. Basic methodology

The preceding section which summarised some of the theories of reaction kinetics, was necessary in order to introduce the concept of any energy grained master equation (EGME) a model which will be used throughout this thesis to calculate kinetic data. (36) This approach can be used to treat coupled isomerisation and dissociation reactions over any number of interconnected wells and transition states and association reactions can be treated as bimolecular source terms. The master equation approach can then treat complex potentials as shown in Figure 2.7 and calculate the time evolution of the different species as a function of both temperature and pressure.

In this approach all maxima and minima (wells and transition states) involved in the reaction need to be defined and energy levels for all these are partitioned into energy grains of a set energy width. The time evolution of the grain populations are then calculated individually in order to obtain the time evolution for the concentration of each species. The smaller the size of the grains the more closely this method approximates the true system and below a certain grain size the results become convergent.

When considering the time evolution of the grain populations both reactive loss and gain and collisional energy transfer are calculated. Reactive loss and gain from an energy grain in one species to the same energy grain in another is modelled using unimolecular *k(E)'s* calculated from RRKM theory whilst collisional energy transfer between different grains of the same species is modelled using an exponential down model. (53) These processes are shown in schematic form in Figure 2.7.

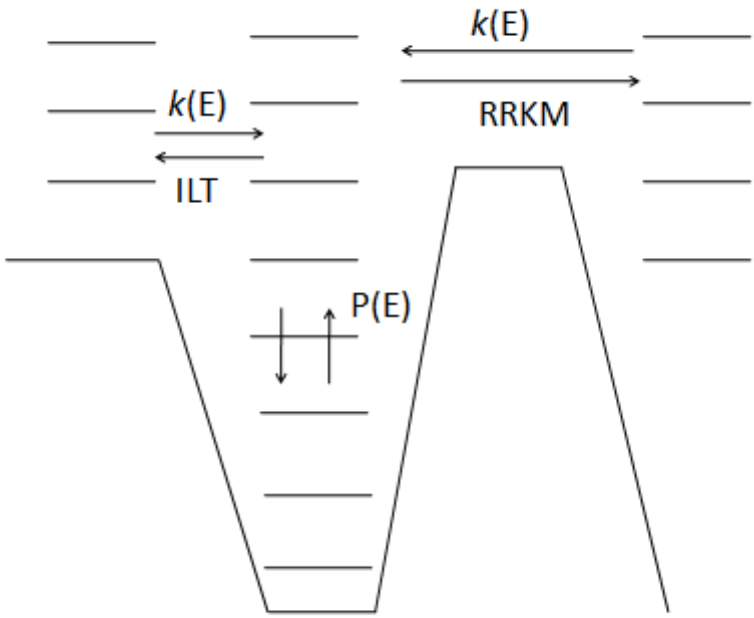

Figure 2.7: Schematic showing the formulation of an energy grained master equation calculation. Here the energies of each stable species are bundled into grains. Between grains of the same energy and different species, reactive rate coefficients are calculated using an ILT method for a barrierless process and using RRKM for a process with a barrier. Between grains of different energies in the same species the collisional transfer probability, P(E), is calculated using an exponential down model.

All these processes are then formulated mathematically:

$$\frac{dn_i(E)}{dt} = \omega \int_{E_{0i}}^{\infty} P(E \leftarrow E')n_i(E')dE' \; - \; \omega n_i(E)$$
$$- \sum_{j \neq i}^{M} k_{ji}(E)n_i(E) \; + \sum_{j \neq i}^{M} k_{ij}(E)n_j(E)$$
$$- \; k_{Pi}(E)n_i(E) \; + \; K_{Ri}^{eq} k_{Ri}(E) \frac{\rho_i(E)e^{-\beta E}}{Q_i(T)} n_R n_m \qquad \text{(Eq. 61)}$$
$$- \; k_{Ri}(E)n_i(E)$$

where $n_i(E)$ is the population of the grain with energy E in species *i,* ω is the Leonard-Jones collision frequency $P(E)$ is the probability of energy transfer from grain *E'* to grain *E* on collision represented by an exponential down model. The first two terms in the equation represent the collision population of grain *E* and the collisional loss grain *E.* The third and fourth terms represent population loss or gain from isomerisation reactions between two wells on the potential surface with k_{ij} being the RRKM rate coefficients for the reaction from species *i* to *j* and the fifth term represents an infinite loss through dissociation where k_{pi} is the unimolecular rate coefficient for the dissociation of species *i*.

The final two terms represent a bimolecular source term. Master equation methods are designed to model unimolecular processes namely isomerisation reactions between an arbitrary number of wells and dissociation reactions. As mentioned in section 2.3.2.2 bimolecular association reactions are the reverse of a unimolecular dissociation and the forward and reverse rate coefficients are related by detailed balance. As such a bimolecular association can be modelled by Master equation methods using a bimolecular source term. In the bimolecular source terms k_{Ri} is the reverse, dissociation rate coefficient of a bimolecular association, K_{Ri}^{eq} is the equilibrium constant between isomer *i* and the reactants. Rate coefficients for the association reactions are typically expressed using an ILT method .

Returning to the mathematical formulation of the master equation, Eq 61 can be written in matrix notation:

$$\frac{dn}{dt} = [\omega(P - I) - k]n = Mn \qquad \text{(Eq. 62)}$$

where *P* is a matrix made of up of transition probabilities, *I* is the identity matrix, *k* is a diagonal matrix consisting of microcanonical rate coefficients and n is the population vector.

This then yields the solution,

$$n(t) = \sum_i u_i c_i \exp(\lambda_1 t) \qquad \text{(Eq. 63)}$$

where the u_i are eigenvectors with corresponding eigenvalues λ_l and the c_i are a formed from a product of the inverse of the eigenvalue matrix and the initial population vector.

Finally, in order to obtain experimentally observed or phenomenological rate coefficients from the master equation calculations there are two commonly used methods. (54, 55) In this thesis the master equation analysis utilises the Bartis Widom method of eigenvalue analysis. The solution to the master equation yields a number of eigenvalues and the Bartis Widom method relies on the fact that that in general a system of *m* wells will have *m-1* eigenvalues that are significantly less negative than the others. These are referred to as the chemically significant eigenvalues, (CSE's) whilst the remaining eigenvalues describe short timescale relaxation and are referred to as the internal relaxation eigenvalues (IRE's). These CSE's are then used to obtain the rate coefficients

2.4.2. Technical points relating to the implementation of the master equation.

2.4.2.1. Ro-vibrational densities of states.

When calculating rate coefficients, the molecular density of states is a quantity that appears repeatedly in the RRKM and ILT expressions for determing rate coefficients. This is determined by the rotational and vibrational energy levels of the species involved in the reaction and there

are various algorithms which determine the number of energy levels as a function of internal energy. Typically when determining the density of states, it is assumed the molecule does not change its structure as it rotates, (rigid rotor approximation) and that the molecular vibrations can be described using harmonic potentials (harmonic oscillator approximation). Neither of these assumptions are correct, but it is the harmonic oscillator approximation (36) which introduces the largest error into calculations and this will be discussed here.

Real vibrational energies are described by the following infinite series:

$$E_v = (v + \frac{1}{2})\nu_e + (v + \frac{1}{2})^2 x_e \nu_e + ... \qquad \text{(Eq. 64)}$$

The dominant term is the first order term and under the harmonic approximation the energies are truncated at this term. However more accurate energies are given by including higher order terms which describe anharmonicity though as the order increase, the terms become vanishingly small. No molecular vibration is described completely by the harmonic oscillator approximation, however certain types of vibration are particularly poorly described by a harmonic potential, especially the vibrations with the lowest energies or frequencies. (36) In particular, some vibrational normal modes actually correspond to an internal rotation about one of the molecular bonds defined by some hindrance potential.

Example potential energy functions are shown for the harmonic case, the anharmonic case and the hindered rotor case in Figure 2.8. Comparing first the harmonic and anharmonic functions it can be seen that whilst the harmonic energy levels are equally spaced, in the true anharmonic potential, the energy levels gradually get closer in energy until they converge at some threshold energy D_0 above which the vibrating bond dissociates. If the anharmonic coefficients are known, the density of states for a molecule can be readily altered to account for this anharmonicity, however, there is a significant computational bottleneck associated with the *ab initio* calculation of the higher order coefficients in Eq. 64 and such calculations are rarely performed for all but the smallest molecules. (56)

In the case of the hindered rotor potential, at low energies this mode will act as an anharmonic oscillator. As the energy increases, the energy levels will become closer together until they eventually converge at the top of the barrier V_0 However rather than dissociate at this point, this torsion described by this potential will begin to rotate freely, and the energy levels at high energies, will instead be described by those for a rotation. In the case of a threefold potential like the one shown in Figure 2.8 this mode will, at low energies, act like three degenerate anharmonic oscillators (one for each well) and this degeneracy is then lifted at energies above the rotational barrier.

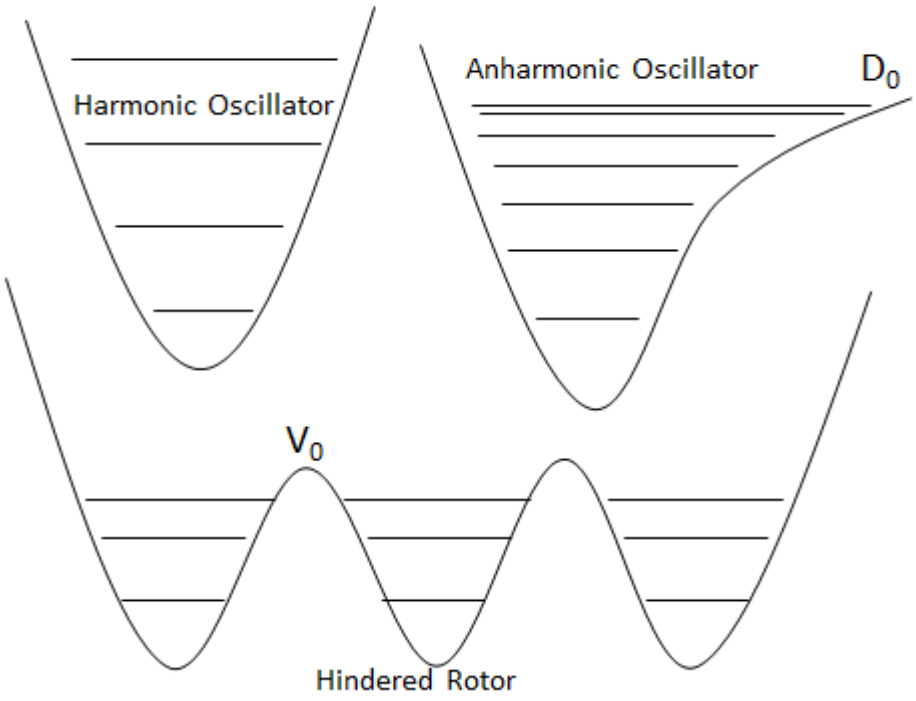

Figure 2.8: Example potentials showing the harmonic oscillator, anharmonic oscillator and hindered rotor cases. Here D_0 is the threshold energy for dissociation and V_0 is the barrier to free rotation.

There are various methods which have been used to calculate partition functions or energy levels for a hindered rotor . (57, 58) In the current thesis these energy levels are calculated as follows. First of all the Hamiltonian for a rotating molecule subject to some hindrance potential is given by:

$$\frac{-\hbar}{I}\frac{d^2\psi}{dx^2} + V(x)\psi = E\psi \qquad \text{(Eq. 65)}$$

where *I* is the moment of inertia for the rotating body and *V*(*x*) is some function describing the change in potential energy with rotational co-ordinate *x*.In order to obtain the energy levels it is then necessary to solve this Schrodinger equation.

In the current work, the wavefunctions are described by a basis of free rotor wavefunctions:

$$\psi_{FR} = 2\pi^{1/2} e^{imx} \qquad \text{(Eq. 66)}$$

Then the potential energy function is fit to a trigonometric series and the Schrodinger equation may be solved to yield the different energy levels *E*. In order to obtain the potential energy functions for these hindered rotations electronic structure theory calculations must be carried out. These potentials can be obtained using two methods. Rigid potentials for the molecule are obtained by simply rotating the bond describing the rotation, through 360 degrees, calculating the *ab initio* energies in the process in order to describe the change in potential energy as a function of the dihedral angle describing the rotation. Alternatively relaxed potentials can be obtained in which as a particular bond is rotated, the other atoms in the molecule may rearrange themselves so as to minimise the total energy. These relaxed scans, account in an average way for the fact that all the vibrational normal modes for a molecule will couple together and as such produce lower barriers to rotation, and in the current thesis, relaxed potentials have been used.

Often the harmonic oscillator approximation, is seen to be sufficient for the calculating of rate coefficient. Since RRKM and ILT rate coefficients depend upon the relative density of states between two species, provided the neighbouring species have similar hindered rotor and anharmonic modes, there is often a fortuitous cancellation of error. However for the systems in the current work, the association of two molecules to form a weak complex leads to a number of low frequency vibrations and hindered rotations, which have no direct analogous vibration in the separated reactants. In this thesis it is found that treating hindered rotors due to the orbiting motion of one reactant fragment about the other, has large consequences with regards to

the calculated rate of stabilisation at low temperatures. For these systems, it is likely that treatment of non-hindered rotor, anharmonicity, and the couplings between hindered rotor modes and anharmonic modes will have a similarly large effect though these have not been performed at present. Despite this, it is found in this work that any inadequacies in the treatment of anharmonicity may be compensated for by artificially increasing the depth of the potential well.

2.4.2.2. Tunneling transmission coefficients

Classically, for a reaction proceeding over a potential energy barrier, at energies below the top of this barrier, the reaction probability will be zero. However quantum mechanically, this is not the case and there is a finite probability that a molecule will “tunnel” through the barrier, when it has insufficient energy to get over it. (59)

The rate theories presented so far do not account for the phenomena, but tunnelling can be accounted for as a transmission coefficient $\kappa(E)$ which describes the tunnelling probability. This tunnelling probability then exponentially decays with the energy below the barrier according to a quantity known as the barrier penetration integral $\theta(E)$. Qualitatively this penetration integral decreases with the height of the potential energy barrier and the width of the potential energy barrier and increases with the effective mass. However, it depends linearly upon the width of a barrier but upon the square root of the barrier height, so barrier width often is the dominant factor over barrier height. (60)

There are various methods which have been developed for calculating these transmission coefficients and then can be split into two categories, single dimensional methods, and multidimensional methods. Single dimensional methods only consider tunnelling along one co-ordinate, the reaction co-ordinate and these methods require the change in potential energy along this co-ordinate only, in order to calculate rate coefficients. Typically, the majority of tunnelling will occur along the narrowest path through the barrier, and this will be represented by the reaction co-ordinate, but a significant amount of tunnelling may occur through orthogonal co-ordinates and more

sophisticated, multidimensional tunnelling methods are necessary to correctly account for this. (61-63)

The main bottleneck for performing more advanced tunnelling calculations involves the amount of potential data used to describe the shape of the barrier. The simplest of methods requires only the imaginary vibrational frequency of the transition state though which tunnelling occurs and the energy of this transition state relative to the neighbouring stable species. More sophisticated single dimensional methods require a number of *ab initio* points along the minimum energy path to be evaluated in order to represent the true shape of the potential barrier. Finally multidimensional methods require *ab inito* energies along not only the reaction co-ordinate but also the other 3N-7 co-ordinates in the vicinity of the transition state.

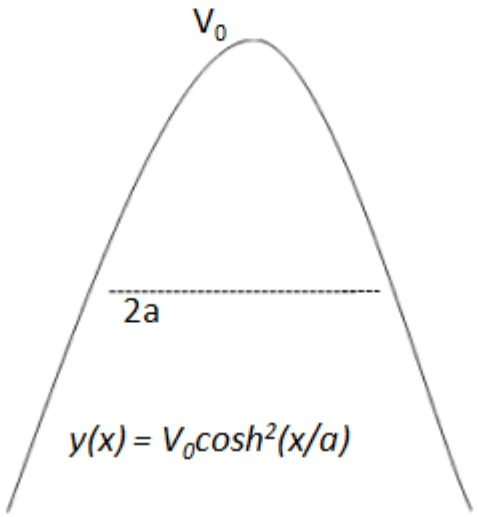

Figure 2.9: Schematic of an Eckart potential illustrating barrier height V_0 and the width at half height height, 2a.

There are two tunnelling methods used in this thesis, the Eckhart method proposed by Miller (64), and the semiclassical method of Truhlar and Garret. (65) The method of Miller utilises the fact that for a potential described by an Eckhart function, the tunnelling problem can be solved analytically. The barrier for the reaction is then approximated as an Eckhart potential using

the imaginary frequency of the transition state as shown in Figure 2.9. Transmission coefficients using this method are then given by the following formula:

$$\kappa(E\ ) = \frac{\sinh(a)\sinh(b)}{\sinh^2(\frac{a+b}{2}) + \cosh^2(c)} \qquad \text{(Eq. 67)}$$

where

$$a = \frac{4\pi}{\hbar\omega_b}\sqrt{E_1 + V_0}(V_0^{-1/2} + V_1^{-1/2})^{-1} \qquad \text{(Eq. 68)}$$

$$b = \frac{4\pi}{\hbar\omega_b}\sqrt{E_1 + V_1}(V_0^{-1/2} + V_1^{-1/2})^{-1} \qquad \text{(Eq. 69)}$$

$$c = 2\pi\sqrt{\frac{V_0 V_1}{(\hbar\omega_b)^2} + \frac{1}{16}} \qquad \text{(Eq. 70)}$$

where E_1 is the energy of the grain, V_0 is the barrier height relative to reactants, V_1 is the barrier height relative to products and ω_b is the imaginary frequency.

In the semiclassical method of Truhlar and Garret (65) rather than approximating the barrier potential using some functional form, the exact *ab initio* barrier is used as defined by electronic structure theory calculations, and a numerical intergration is performed. This method is not exact in the way the Eckhart method is, but given a potential barrier, the semiclassical approximations used in this method agree to within 5 % (65) of exact calculations. Using this method the transmission coefficients are expressed as follows.:

$$\kappa(E) = \frac{1}{1 + \exp(2\theta(E)} \qquad \text{(Eq. 71)}$$

where

$$\theta(E) = \frac{2\pi}{h}\int_{s1}^{s2}\sqrt{\mu(E - V)}ds \qquad \text{(Eq. 72)}$$

μ is the effect reduced mass, s1 and s2 are the classical turning points along the reaction coordinate s and V is the barrier height.

When perfoming these calculations, one of the biggest uncertainties is in the *ab initio* imaginary frequencies obtained. Imaginary frequencies can vary significantly with the level of theory used to calculate them and in particular they tend to scale to the barrier height predicted at a particular level of theory. Unfortunately vibrational frequency calculations are typically performed using levels of theory which are insufficiently accurate for calculating relative energies, and in this thesis, it is found that MP2 and DFT imaginary frequencies are typically overestimates. However when high level imaginary frequencies have been obtained in this thesis, they typically yield good agreement between experiment and theory without any adjustment required.

The semiclassical (65) method has two advantages over the Eckart method. First of all it does not fit the barrier to an Eckhart function, and second of all, the shape of the potential along the minimum energy path appears, from the results in this thesis, to be less sensitive to the level of theory used. However significant computational effort can be required to obtain the potential data, and the necessary intrinsic reaction co-ordinate calculations required to obtain this data have not always been successful in this thesis.

In this thesis, the semiclassical method has been seen to slightly underestimate the experimental data. Using the Eckart method does not seem to have the same problem, however this is largely due to the fact that the imaginary frequencies have often been varied in order to fit the experimental data. The fact that the semiclassical method can be seen to underpredict the experiments could be indicative of the need for considering tunnelling along additional co-ordinates using a multidimensional method and studies have shown that single dimensional methods can substantially underpredict (63, 66) the amount of tunnelling observed. Unfortunately, to the authors knowledge no study has yet coupled a multidimensional tunnelling method to a master equation, and no such calculations have been performed here.

2.4.2.3. Lennard jones parameters and ΔE_{down}.

One of the largest sources of uncertainty in a Master equation calculation, involves the treatment of collisional energy transfer for which it is necessary to know both the rate at which two molecules collide and the amount of energy transferred upon each collision.

Considering the collision rate first, the master equation calculations performed in the current thesis assume that the interaction between the two species can be assumed to follow a Lennard-Jones potential shown in Figure 2.10. Assuming such a potential, the collision rate Z_{AB} between two molecules A and B can be calculated from the following expression:

$$Z_{AB} = \varepsilon_{AB}\pi\sigma_{AB}\sqrt{\frac{8k_BT}{\pi\mu_{AB}}}[M] \qquad \text{(Eq. 73)}$$

where μ_{AB} is the reduced mass of A and B, ε_{AB} and σ_{AB} are the Lennard Jones parameters for A and B and [M] is the concentration of bath gas.

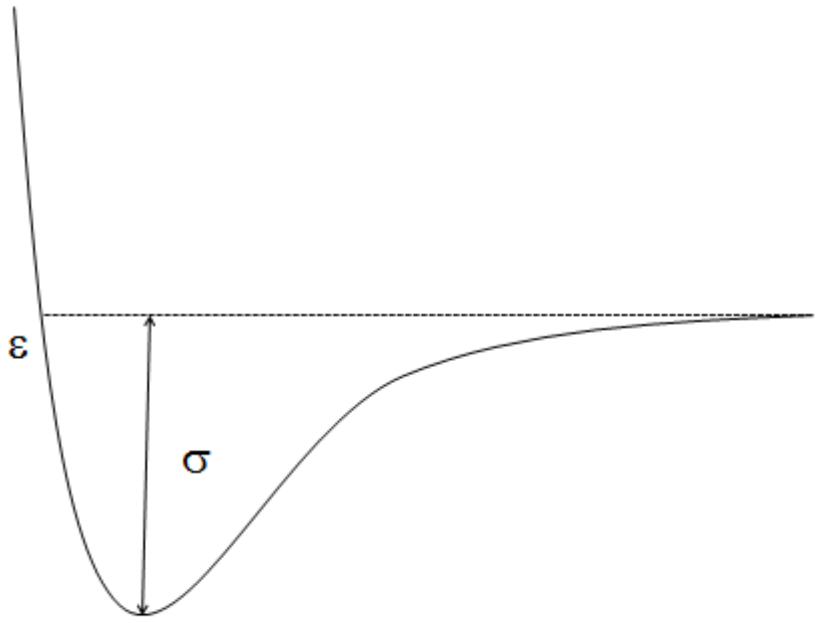

Figure 2.10 Lennard Jones potential showing the physical meanings of the σ and ε parameters.

The approach above implies that the Lennard Jones parameter for every collision between two molecules A and B would need to be known, and in

general this is not the case. However, the Lennard Jones parameters for the molecule AB collision can be described in terms of the parameters for the AA and BB collisions as follows:

$$\sigma_{AB} = \frac{1}{2}(\sigma_{AA} + \sigma_{BB}) \qquad \text{(Eq. 73)}$$

$$\varepsilon_{AB} = (\varepsilon_{AA}\varepsilon_{BB})^{\frac{1}{2}} \qquad \text{(Eq. 74)}$$

Once the collision rates have been calculated, it is necessary to calculate the amount of energy transferred in each collision using some mathematical model. A number of different models have been proposed, but one which has been used widely, and is utilised in the current work, is the exponential down model. In this model every stable intermediate is assigned a parameter ΔE_{down} which corresponds to the average energy transferred upon collision with a bath gas molecule, (N_2 in the current work). Once these parameters are defined the amount of energy transferred in each collision can be calculated as follows:

$$P(E/E') = A(E)\exp(-\frac{(E-E')}{\Delta E_{down}}) \qquad \text{(Eq. 75)}$$

where *P*(*E/E'*) is the probability of a deactivating collision, causing a reduction in energy from E to E' and *A*(*E*) is a normalisations constant.

There have been a number of experiments and trajectory calculations which have studied ΔE_{down} , (67-70) however, the database of known values is still relatively small and the temperature dependence of ΔE_{down} in particular is poorly understood. As such ΔE_{down} is typically varied in order to fit any available experimental data though as a rule inert collides typical exhibit values of 100 cm^{-1} while strong colliders can have value of over 1000cm^{-1}. (71) In the current work N_2 is used as the bath gas and typically values of between 200 cm^{-1} and 400 cm^{-1} are used. (71)

2.5. References

1. MOORE, J.W., R.G. PEARSON and A.A. FROST. *Kinetics and mechanism.* 3rd ed. New York ; Chichester: Wiley, 1981.

2. PILLING, M.J. and P.W. SEAKINS. *Reaction kinetics.* Oxford: Oxford University Press, 1995.
3. BROUARD, M. *Reaction dynamics.* Oxford chemistry primers. Oxford New York: Oxford University Press, 1998.
4. HERBST, E. Chemistry in the Interstellar-Medium. *Annual Review of Physical Chemistry*, 1995, **46**, pp.27-53.
5. SMITH, I.W.M. Reactions at very low temperatures: Gas kinetics at a new frontier. *Angewandte Chemie-International Edition*, 2006, **45**(18), pp.2842-2861.
6. SMITH, I.W.M. and B.R. ROWE. Reaction kinetics at very low temperatures: Laboratory studies and interstellar chemistry. *Accounts of Chemical Research*, 2000, **33**(5), pp.261-268.
7. HERBST, E. and KLEMPERE.W. Formation and Depletion of Molecules in Dense Interstellar Clouds. *Astrophysical Journal*, 1973, **185**(2), pp.505-533.
8. HENON, E., S. CANNEAUX, F. BOHR and S. DOBE. Features of the potential energy surface for the reaction of OH radical with acetone. *Physical Chemistry Chemical Physics*, 2003, **5**(2), pp.333-341.
9. T. YAMADA, P. H. TAYLOR, A. GOUMRI and P. MARSHALL. The reaction of OH with acetone and acetone-d_6 from 298 to 832 K: Rate coefficients and mechanism. *J. Chem. Phys.*, 2003, **119**(20), pp.10600 - 10606.
10. VANDENBERK, S., L. VEREECKEN and J. PEETERS. The acetic acid forming channel in the acetone plus OH reaction: A combined experimental and theoretical investigation. *Physical Chemistry Chemical Physics*, 2002, **4**(3), pp.461-466.
11. SABBAH, H., L. BIENNIER, I.R. SIMS, Y. GEORGIEVSKII, S.J. KLIPPENSTEIN and I.W.M. SMITH. Understanding reactivity at very low temperatures: The reactions of oxygen atoms with alkenes. *Science*, 2007, **317**(5834), pp.102-105.
12. SMITH, I.W.M., A.M. SAGE, N.M. DONAHUE, E. HERBST and D. QUAN. The temperature-dependence of rapid low temperature reactions: experiment, understanding and prediction. *Faraday Discussions*, 2006, **133**, pp.137-156.
13. HOLBROOK, K.A., M.J. PILLING, S.H. ROBERTSON and P.J. ROBINSON. *Unimolecular reactions.* 2nd ed. Chichester ; New York: Wiley, 1996.
14. JENSEN, F. *Introduction to computational chemistry.* Chichester ; New York: Wiley, 1999.
15. CRAMER, J., CHRISTOPHER. *Essentials of computational chemistry: Theories and models.* Chichester ; New York: Wiley, 2002.
16. HEHRE, W.J., R.F. STEWART and J.A. POPLE. Self-Consistent Molecular-Orbital Methods .I. Use of Gaussian Expansions of Slater-Type Atomic Orbitals. *Journal of Chemical Physics*, 1969, **51**(6), pp.2657-&.
17. WOON, D.E. and T.H. DUNNING. Gaussian-Basis Sets for Use in Correlated Molecular Calculations .5. Core-Valence Basis-Sets for Boron through Neon. *Journal of Chemical Physics*, 1995, **103**(11), pp.4572-4585.

18. HARTREE, D.R. The wave mechanics of an atom with a non-Coulomb central field Part I theory and methods. *Proceedings of the Cambridge Philosophical Society*, 1928, **24**, pp.89-110.
19. ROOTHAAN, C.C.J. New Developments in Molecular Orbital Theory. *Reviews of Modern Physics*, 1951, **23**(2), pp.69-89.
20. SLATER, J.C. Note on Hartree's method. *Physical Review*, 1930, **35**(2), pp.0210-0211.
21. MOLLER, C. and M.S. PLESSET. Note on an approximation treatment for many-electron systems. *Physical Review*, 1934, **46**(7), pp.0618-0622.
22. CIZEK, J. On Correlation Problem in Atomic and Molecular Systems . Calculation of Wavefunction Components in Ursell-Type Expansion Using Quantum-Field Theoretical Methods. *Journal of Chemical Physics*, 1966, **45**(11), pp.4256-&.
23. POPLE, J.A., M. HEADGORDON and K. RAGHAVACHARI. Quadratic Configuration-Interaction - a General Technique for Determining Electron Correlation Energies. *Journal of Chemical Physics*, 1987, **87**(10), pp.5968-5975.
24. WERNER, H.J. and P.J. KNOWLES. A 2nd Order Multiconfiguration Scf Procedure with Optimum Convergence. *Journal of Chemical Physics*, 1985, **82**(11), pp.5053-5063.
25. ROOS, B.O. and K. ANDERSSON. Multiconfigurational Perturbation-Theory with Level Shift - the Cr-2 Potential Revisited. *Chemical Physics Letters*, 1995, **245**(2-3), pp.215-223.
26. WERNER, H.J. and P.J. KNOWLES. An Efficient Internally Contracted Multiconfiguration Reference Configuration-Interaction Method. *Journal of Chemical Physics*, 1988, **89**(9), pp.5803-5814.
27. LEE, T.J. and P.R. TAYLOR. A Diagnostic for Determining the Quality of Single-Reference Electron Correlation Methods. *International Journal of Quantum Chemistry*, 1989, pp.199-207.
28. LEE, T.J. Comparison of the T-1 and D-1 diagnostics for electronic structure theory: a new definition for the open-shell D-1 diagnostic. *Chemical Physics Letters*, 2003, **372**(3-4), pp.362-367.
29. KOHN, W., A.D. BECKE and R.G. PARR. Density functional theory of electronic structure. *Journal of Physical Chemistry*, 1996, **100**(31), pp.12974-12980.
30. PARR, R.G. Density Functional Theory. *Annual Review of Physical Chemistry*, 1983, **34**, pp.631-656.
31. LYNCH, B.J., P.L. FAST, M. HARRIS and D.G. TRUHLAR. Adiabatic connection for kinetics. *Journal of Physical Chemistry A*, 2000, **104**(21), pp.4811-4815.
32. HEMELSOET, K., D. LESTHAEGHE, V. VAN SPEYBROECK and M. WAROQUIER. Bifunctional acid-base catalyzed reactions in zeolites from the HSAB viewpoint. *Chemical Physics Letters*, 2006, **419**(1-3), pp.10-15.
33. ZHAO, Y., N. GONZALEZ-GARCIA and D.G. TRUHLAR. Benchmark database of barrier heights for heavy atom transfer, nucleophilic substitution, association, and unimolecular reactions and its use to test theoretical methods (vol 109A, pg 2015, 2005). *Journal of Physical Chemistry A*, 2006, **110**(14), pp.4942-4942.

34. ZHAO, Y., J.Z. PU, B.J. LYNCH and D.G. TRUHLAR. Tests of second-generation and third-generation density functionals for thermochemical kinetics. *Physical Chemistry Chemical Physics*, 2004, **6**(4), pp.673-676.
35. FERNANDEZ-RAMOS, A., J.A. MILLER, S.J. KLIPPENSTEIN and D.G. TRUHLAR. Modeling the kinetics of bimolecular reactions. *Chemical Reviews*, 2006, **106**(11), pp.4518-4584.
36. ROBINSON, P.J. and K.A. HOLBROOK. *Unimolecular reactions.* London ; New York: Wiley-Interscience, 1972.
37. BAER, T. and W.L. HASE. *Unimolecular reaction dynamics : theory and experiments.* The international series of monographs on chemistry. New York: Oxford University Press, 1996.
38. ATKINS, P.W. and J. DE PAULA. *Atkins' Physical chemistry.* 9th ed. Oxford: Oxford University Press, 2010.
39. TRUHLAR, D.G. and B.C. GARRETT. Variational Transition-State Theory. *Accounts of Chemical Research*, 1980, **13**(12), pp.440-448.
40. ROBERTSON, S.H., A.F. WAGNER and D.M. WARDLAW. Canonical flexible transition-state theory for generalized reaction paths. *Faraday Discussions*, 1995, **102**, pp.65-83.
41. ROBERTSON, S.H., D.M. WARDLAW and A.F. WAGNER. Flexible transition state theory for a variable reaction coordinate: Derivation of canonical and microcanonical forms with angular momentum conservation. *Journal of Chemical Physics*, 2002, **117**(2), pp.593-605.
42. TROE, J. Simplified Statistical Adiabatic Channel Model for Unimolecular Bond Fission Reactions. *Abstracts of Papers of the American Chemical Society*, 1980, **180**(Aug), pp.257-PHYS.
43. Statistical Adiabatic Channel Model of Ion Neutral Dipole Capture Rate Constants. *Chemical Physics Letters*, 1985, **122**(5), pp.425-430.
44. Statistical adiabatic channel model for ion-molecule capture processes .2. Analytical treatment of ion-dipole capture. *Journal of Chemical Physics*, 1996, **105**(15), pp.6249-6262.
45. GREENWALD, E.E., S.W. NORTH, Y. GEORGIEVSKII and S.J. KLIPPENSTEIN. A two transition state model for radical-molecule reactions: A case study of the addition of OH to C_2H_4. *Journal of Physical Chemistry A*, 2005, **109**(27), pp.6031-6044.
46. SMITH, I.W.M. *Low temperatures and cold molecules.* London: Imperial College Press, 2008.
47. HERBST, E. Tunneling in the C_2H-H_2 Reaction at Low-Temperature. *Chemical Physics Letters*, 1994, **222**(3), pp.297-301.
48. SLATER, N.B. New Formulation of Gaseous Unimolecular Dissociation Rates. *Journal of Chemical Physics*, 1956, **24**(6), pp.1256-1257.
49. ROBERTSON, S.H., M.J. PILLING, D.L. BAULCH and N.J.B. GREEN. Fitting of Pressure-Dependent Kinetic Rate Data by Master Equation Inverse Laplace Transform Analysis. *Journal of Physical Chemistry*, 1995, **99**(36), pp.13452-13460.
50. GREENWALD, E.E., S.W. NORTH, Y. GEORGIEVSKII and S.J. KLIPPENSTEIN. A two transition state model for radical-molecule reactions: Applications to isomeric branching in the OH-Isoprene reaction. *Journal of Physical Chemistry A*, 2007, **111**(25), pp.5582-5592.

51. KLIPPENSTEIN, S.J., Y. GEORGIEVSKII, H. SABBAH, L. BIENNIER, I.R. SIMS and I.W.M. SMITH. COMP 217-Two transition state model for radical-molecule reactions. *Abstracts of Papers of the American Chemical Society*, 2008, **235**.
52. GEORGIEVSKII, Y. and S.J. KLIPPENSTEIN. Long-range transition state theory. *Journal of Chemical Physics*, 2005, **122**(19).
53. BAER, T. and W.L. HASE. *Unimolecular reaction dynamics: theory and experiments.* New York: Oxford University Press, 1996.
54. BARTIS, J.T. and B. WIDOM. Stochastic-Models of Interconversion of 3 or More Chemical Species. *Journal of Chemical Physics*, 1974, **60**(9), pp.3474-3482.
55. KLIPPENSTEIN, S.J. and J.A. MILLER. From the time-dependent, multiple-well master equation to phenomenological rate coefficients. *Journal of Physical Chemistry A*, 2002, **106**(40), pp.9267-9277.
56. NGUYEN, T.L. and J.R. BARKER. Sums and Densities of Fully Coupled Anharmonic Vibrational States: A Comparison of Three Practical Methods. *Journal of Physical Chemistry A*, 2010, **114**(10), pp.3718-3730.
57. BARKER, J.R. and C.N. SHOVLIN. An approximation for hindered rotor state energies. *Chemical Physics Letters*, 2004, **383**(1-2), pp.203-207.
58. PFAENDTNER, J., X. YU and L.J. BROADBELT. The 1-D hindered rotor approximation. *Theoretical Chemistry Accounts*, 2007, **118**(5-6), pp.881-898.
59. BELL, R.P. *The tunnel effect in chemistry.* London: Chapman and Hall, 1980.
60. SCHREINER, P.R., H.P. REISENAUER, D. LEY, D. GERBIG, C.H. WU and W.D. ALLEN. Methylhydroxycarbene: Tunneling Control of a Chemical Reaction. *Science*, 2011, **332**(6035), pp.1300-1303.
61. LIU, Y.P., D.H. LU, A. GONZALEZLAFONT, D.G. TRUHLAR and B.C. GARRETT. Direct Dynamics Calculation of the Kinetic Isotope Effect for an Organic Hydrogen-Transfer Reaction, Including Corner-Cutting Tunneling in 21 Dimensions. *Journal of the American Chemical Society*, 1993, **115**(17), pp.7806-7817.
62. ALBU, T.V., B.J. LYNCH, D.G. TRUHLAR, A.C. GOREN, D.A. HROVAT, W.T. BORDEN and R.A. MOSS. Dynamics of 1,2-hydrogen migration in carbenes and ring expansion in cyclopropylcarbenes. *Journal of Physical Chemistry A*, 2002, **106**(21), pp.5323-5338.
63. PU, J.Z. and D.G. TRUHLAR. Validation of variational transition state theory with multidimensional tunneling contributions against accurate quantum mechanical dynamics for H+CH4 -> H-2+CH3 in an extended temperature interval. *Journal of Chemical Physics*, 2002, **117**(4), pp.1479-1481.
64. MILLER, W.H. Tunneling Corrections to Unimolecular Rate Constants, with Application to Formaldehyde. *Journal of the American Chemical Society*, 1979, **101**(23), pp.6810-6814.
65. GARRETT, B.C. and D.G. TRUHLAR. Semi-Classical Tunneling Calculations. *Journal of Physical Chemistry*, 1979, **83**(22), pp.2921-2926.

66. CORCHADO, J.C., J. ESPINOSAGARCIA, W.P. HU, I. ROSSI and D.G. TRUHLAR. Dual-Level Reaction-Path Dynamics (the ///-Approach to Vtst with Semiclassical Tunneling) - Application to $Oh+NH_3$-]H_2O+NH_2. *Journal of Physical Chemistry*, 1995, **99**(2), pp.687-694.
67. BARKER, J.R., M. ROSSI and G.P. SMITH. Energy-Transfer Dynamics of Azulene (S0) Excited to High Vibrational Energies. *Abstracts of Papers of the American Chemical Society*, 1981, **182**(Aug), pp.199-PHYS.
68. BARKER, J.R., M.J. ROSSI and J.R. PLADZIEWICZ. Level-to-Level Vibrational-Energy Transfer Studies - Energy-Dependence and Observation of Product Species for Azulene(S0,Evib)+CO_2. *Chemical Physics Letters*, 1982, **90**(2), pp.99-104.
69. BARKER, J.R., L.M. YODER and K.D. KING. Vibrational energy transfer modeling of nonequilibrium polyatomic reaction systems. *Journal of Physical Chemistry A*, 2001, **105**(5), pp.796-809.
70. TROE, J. Collisional Energy-Transfer in Thermal Unimolecular Reactions. *Berichte Der Bunsen-Gesellschaft-Physical Chemistry Chemical Physics*, 1973, **77**(9), pp.665-674.
71. PILLING, M.J. and S.H. ROBERTSON. Master equation models for chemical reactions of importance in combustion. *Annual Review of Physical Chemistry*, 2003, **54**, pp.245-275.

Chapter 3. Experimental

There are a number of Laval nozzle apparatus around the world, both of the continuous (1, 2) and the pulsed variety. (3-5) The Leeds (6) pulsed Laval nozzle is based upon the pulsed Laval nozzle apparatus in Berkeley (4) and in the first part of this chapter the experimental set up will be described. Since the experimental technique described in this thesis relies upon the use of a Laval nozzle, the second section of this chapter will focus upon the Laval nozzles themselves and upon both their fluid dynamics and construction. Finally an outline of the commonly used experimental and master equation methods will be given.

3.1.The Leeds Pulsed Laval Nozzle Apparatus

3.1.1. The reaction chamber and pumping system

The main chamber of the Leeds apparatus consists of a 774 mm length stainless steel cylinder with access provided by two 240 mm diameter stainless steel flanges (Leybold DN ISO-K250) at either end of the chamber and a further six 160 mm diameter flanges (Leybold DN ISO-K160) situated along the chamber. The six smaller flanges mounted on the cylindrical body of the chamber serve two main functions. At one end of the cylinder there are two flanges (flanges 1 and 2 in Figure 3.1) situated opposite each other on the sides of the chamber and these provide electrical feeds governing the pulsed valves and pressure measurements within the chamber. The other four 160 mm flanges are located at the other end of the chamber and are situated at right angles to each other. These four flanges govern the laser processes and include Brewster angled windows for laser access and mountings for internal optics. Brewster angled windows are also mounted on the two 240 mm flanges defining a centre axis along the chamber to which the internal parts of the chamber are aligned. Finally there is a 40 mm diameter flange (Leybold KF40) located next to flange 4 (see Figure 3.1) which is used for further electrical feeds.

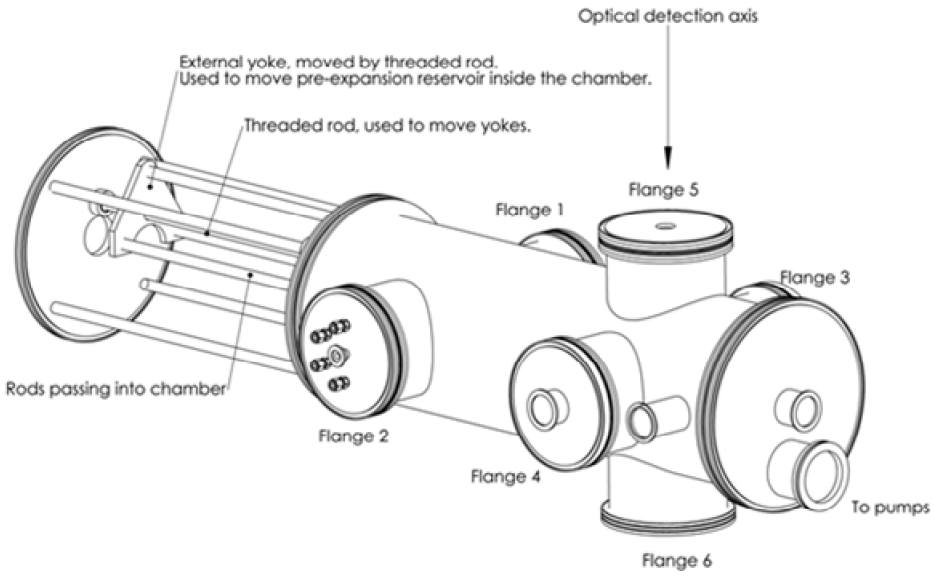

Figure 3.1: The main Laval nozzle chamber showing the positions of the access flanges (7) drawn by A Goddard.

The pumping system consists of a Leybold D65B rotary pump and a Leybold RUVAC 251 roots pump, which are connected to the chamber through a 240 mm diameter flange (see above) using a 63 mm diameter stainless steel line. These pumps allow a pumping capacity of ~ 210 $m^3 h^{-1}$ and can maintain a vacuum of 10^{-5} mbar when there is no gas flow into the chamber. In order to accurately adjust the chamber pressure a gate valve (Leybold DN63150-F H adapted by Leeds mechanical workshops) has been fitted to the pumping line allowing the pressure to be controlled to ±0.1 Torr precision. When necessary an additional rotary pump (Edwards 210 ED660) and roots blower (Edwards EH250) may be set up in parallel in order to maintain sufficiently low chamber pressure for the lowest temperature nozzle to operate.

3.1.2. Gas Manifold and Reservoir

All gases required for a particular experiment are introduced to the chamber from a separate gas manifold via a ballast tank and a pre-expansion reservoir. Flow rates are controlled through four mass flow controllers (MKS Instruments Mass-Flo® Controller) which are calibrated frequently using Drycal® DC-Lite DCL-M and DCL-L flow meters. Each of the four mass flow controllers (MFC's) is of a different size and these are used to flow different components of the total gas flow. Following the MFC's there is a two meter, ¼ inch external diameter stainless steel tube that connects the gas manifold to a 2 litre stainless steel ballast tank. The ballast tank is necessary in order to provide a stable backing pressure for two pulsed solenoid valves (Parker series 9, normally closed, 24V DC, stainless steel body, 0.116 inch orifice) situated within the main chamber and a Baratron® pressure transducer (MKS, 0-5000 Torr, model number 722A53TCB2FC) is used to measure the ballast pressure. Following the ballast tank, the gas enters the inside of the chamber through Flange 2 (Figure 3.1) using 30 cm stainless steel ¼ inch external diameter tubing. From the internal side of Flange 2, the stainless steel tubing is replaced by Teflon tubing to connect the flow of gas to aforementioned solenoid valves. It is these pulsed valves that differentiate between pulsed and continuous Laval nozzle expansions and a delay generator (Berkeley Nucleonics Corporation (BNC) box, pulse/delay generator, model 555), and home built control box, control the repetition rate and width of the gas pulses.

The two pulsed valves are situated either side of a 1 cm^3 pre-expansion reservoir onto which the Laval nozzle is attached. Inside this reservoir there is a piezo-resistive pressure transducer (Omega, PX170 DE28 Inch H_2O), with one end connected to a separate vacuum line as a reference, allowing measurement of the gas pressure build up in the reservoir prior to expansion through the nozzle.

When the Laval nozzles are characterised (described in detail later), the conditions within the flow are probed at a fixed position in space. Therefore in order to characterise the conditions along the length of the Laval expansion, the reservoir and nozzle need to be moveable. Attached to one of the 250 mm flanges there is a yoke mounted on three rods and through

this runs a threaded rod which is connected to the reservoir through a second yoke. A stepper motor (McLennan) with a homemade driver is then used to turn the threaded rod, providing 25 cm of movement in the position of the reservoir to ±1 mm accuracy.

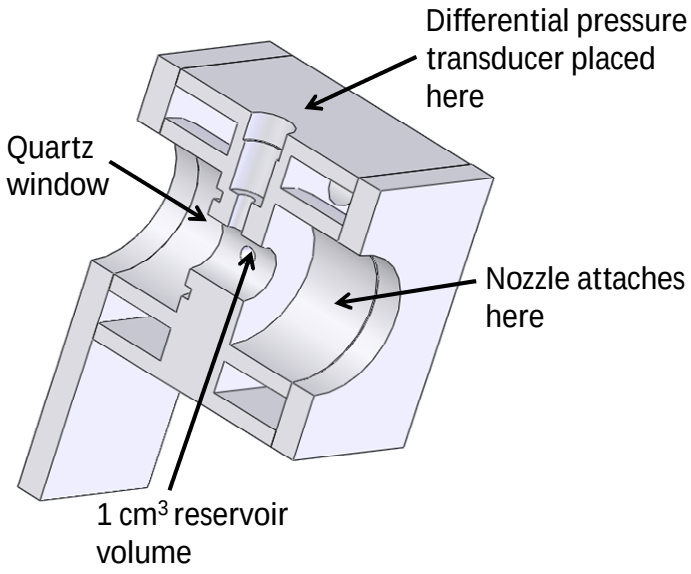

Figure 3.2: Cross-section of the pre-expansion reservoir prior to expansion through the Laval nozzle. Modified from Solidworks™ drawing by A Goddard.

3.1.3. Fluorescence Collection and Optics

In order to probe the relative reagent concentration during the kinetics experiments an optical method, laser induced fluorescence spectroscopy, is used. In the centre of the four-way cross formed by 160 mm flanges 3-6 (Figure 3.1) there are two rails passing vertically down the chamber from flange 5 to flange 6. Upon these rails are fixed two 50 mm diameter plano-convex quartz lenses (Cystran) of 100 mm focal length and a 40 mm diameter plano-concave back reflector (Cystran) of 40 mm focal length, the positions of which are shown in Figure 3.3.

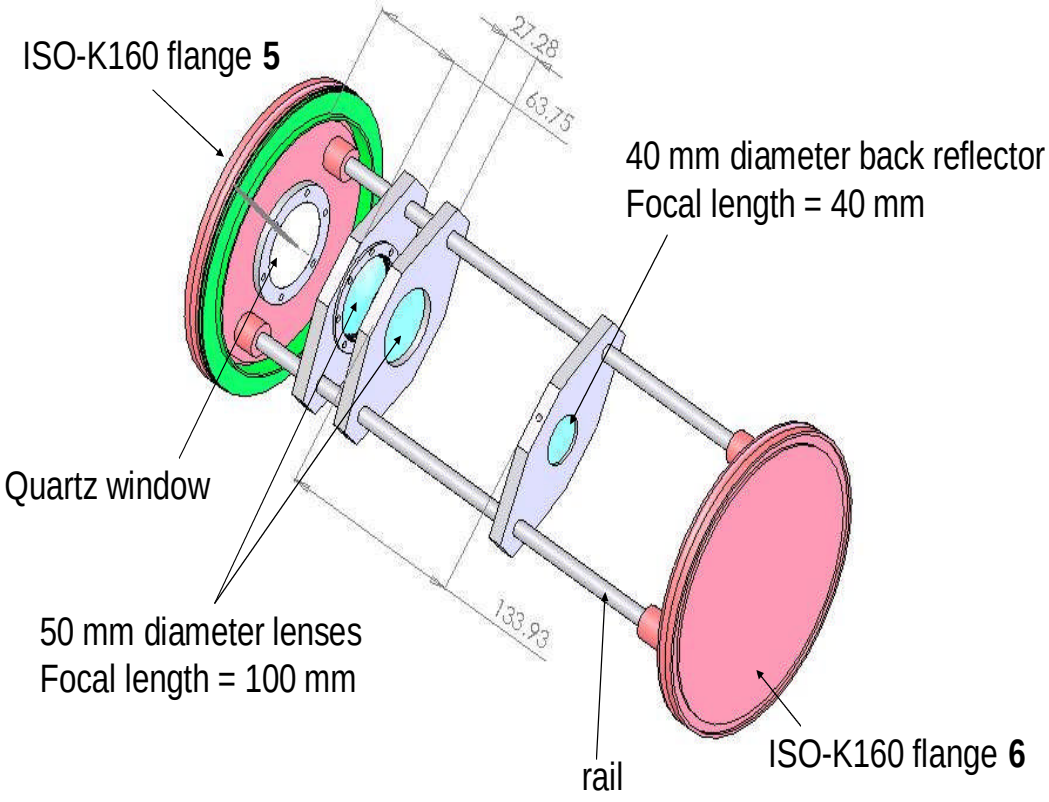

Figure 3.3: The positions of the fluorescence detection optics within the Laval nozzle chamber (7) drawn by A Goddard

The lasers are aligned so that fluorescence can be collected between these lenses and the back reflector. The two 50 mm lenses focus the fluorescence produced onto a photomultiplier tube (PMT) situated on top of flange 5, while the 40 mm mirror is positioned in order to reflect any fluorescence in the opposite direction to the PMT. In order for the fluorescence to reach the PMT, there is a 3 mm thick quartz window (Cystran) placed within flange 5 and in addition, a suitable interference filter is fitted in between the window and the PMT to remove unwanted wavelengths.

3.1.4. Laser Systems

Like a large number of kinetics experiments, those described in this thesis make substantial use of laser (light amplification by stimulated emission) radiation in order to both initiate and monitor the reactions occurring within the Laval nozzle expansion medium. Two key concepts relating to laser action are that of stimulated emission and population inversion.

If we consider an atomic or molecular system with two non-degenerate energy levels, then species in the higher energy excited state may undergo a radiative transition to the ground state, emitting a photon in the process. This process is known as spontaneous emission and in this process, photons will be emitted in a random direction. However if a photon, with an energy equal to the energy difference between the two levels, interacts with the system then the probability of radiative transfer from the excited to ground state is enhanced and the photon will be emitted in the same direction as the photon that caused the interaction. This process is known as stimulated emission and is shown schematically in Figure 3.4. Referring to this figure when a single photon interacts with the system two photons, the initial photon and one produced from radiative transfer, are emitted and through many applications of this amplification process an intense, directed beam of light is produced.

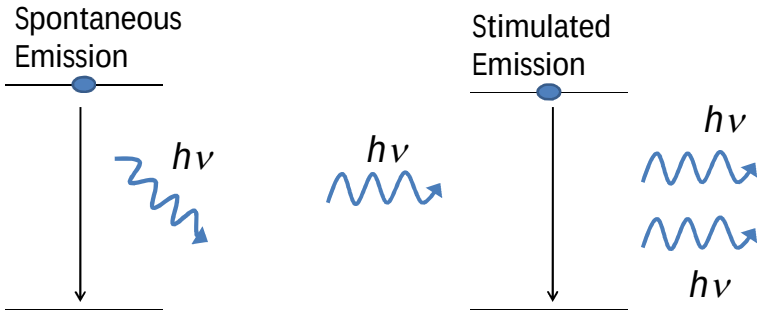

Figure 3.4: Schematic showing the difference between spontaneous and stimulated emission of a photon.

In all the reactions studied in this thesis the OH radical is one of the reagents and since this is not a stable molecule it must be created *in situ.* In order to do this laser radiation at 248 nm is used in order to photolyse a suitable OH precursor. This radiation is provided by an exciplex laser (Lambda Physik LPX 200). In an exciplex laser the lasing substance (active medium) is an electronically excited diatomic complex (8) in this case formed between Krypton and Flourine. This complex, like all others used in exciplex laser systems, exhibits the unusual property that whilst the electronically excited

state is has a minimum in its potential energy surface, the ground state is dissociative since there is no potential minimum in order to support a stable complex. These excited KrF complexes are initially formed using an electronic discharge and since only the excited state is stable, a population inversion is maintained throughout. In the case of KrF, the emission wavelength is 248 nm and in the current experiments typical laser pulse energies of 100-200 mJ were observed.

Once the OH radical has been produced, a second laser system is used to monitor the relative OH population. This laser system is used to induce fluorescence in the OH molecule and in order to do this the laser wavelength must be resonant with a ro-vibrational transition with the OH molecule. A Nd:YAG laser (Spectron Laser Systems SL803) pumping a separate dye laser (Sirah Gmbh-Cobra Stretch) is used to achieve this. In a Nd:YAG laser the active medium is neodymium ions in a yttrium aluminium garnet crystal lattice. This Nd:YAG crystal is pumped using a flash lamp and fundamental laser emission occurs at 1064 nm. In the current experiments, the second harmonic (532 nm) is produced using a built in frequency doubling crystal. This 532 nm light is then used to pump a dye laser system. In a dye laser the active medium is some organic dye solution, and these dyes have a continuum of energy levels to which radiative transitions can occur. This means that over a particular range of energies, any desired emission wavelength may be selected using an optical grating. The 532 nm radiation from the Nd:YAG exhibits a typical pulse energy of 10 mJ whilst the wavelength selected emission from the dye laser had typical pulse energies of 1 mJ.

3.2. The Laval Nozzle

3.2.1. Introduction

The convergent – divergent (de) Laval nozzle was invented by Gustaf de Laval in 1888. It was designed such that upon expansion, the gas flow exhibits maximal conversion into directed kinetic energy and such nozzles have been used extensively in both rocket engines and steam turbines. It was not until 1984, (2) that a Laval nozzle expansion was used as a reaction

medium for low temperature kinetics, and since then the use of a Laval nozzle expansion has become the standard method of measuring rate coefficient of gas phase reactions at low temperatures.

A key parameter when considering gas flow through a nozzle is the Mach number *M* of the expansion:

$$M = \frac{v}{a} \qquad \text{(Eq. 1)}$$

$$a = \sqrt{\frac{\gamma\ RT}{M}} \qquad \text{(Eq. 2)}$$

where *v* is the velocity of gas, a is the local speed of sound, γ is the ratio of heat capacities (C_p/C_v), *R* is the gas constant in J mol^{-1} K^{-1} and *T* is the temperature in K. When the gas is accelerated to *M* > 1 then the flow is said to become supersonic and the supersonic expansion of gas through a nozzle, whether it be a free jet expansion or a Laval expansion, is an adiabatic process *i.e* the energy of the system is constant. The cooling effect upon expansion can then be understood in terms of the conservation of energy. As the gas is accelerated to higher Mach numbers the net velocity and kinetic energy of the gas flow is increased and in order to conserve energy, the internal energy of the constituent gas molecules must be reduced. Then despite an increase in the overall kinetic energy of the gas flow, the inter particle kinetic energy is decreased upon supersonic expansion leading to a reduction in the temperature of the gas molecules. This mechanism can be understood mathematically from the following relationship: (9)

$$C_p T + \frac{v^2}{2} = C_p T_0 \qquad \text{(Eq. 3)}$$

where T_0 and *T* are the temperatures of the gas flow pre and post expansion and *v* is the velocity of the gas.

The problem with a free jet expansion is that thermodynamic equilibrium is not maintained throughout the expansion. Individual molecules within the jet may exhibit rotational temperatures down to 1K, (10) but the small number of

collisions post expansion means that the thermodynamic quantities of the jet are poorly defined and large temperature and pressure gradients exist. Conversely expansion through a Laval nozzle is an isentropic process and thus equilibrium is maintained at all points within the expansion.

The convergent divergent shape of a Laval nozzle is shown is Figure 3.5 and the cross sectional area of the nozzle and the flow velocity are related by the following:

$$\frac{\mathrm{d}A}{A} = \frac{\mathrm{d}v}{v}(M^2 - 1) \qquad \text{(Eq. 4)}$$

where *A* is the cross-sectional area of the nozzle. In the convergent region $\frac{dA}{A}$<0 and the gas is accelerated from a stagnation Mach number of 0 is the pre expansion reservoir, to a Mach number of 1 at the throat. The divergent region then accelerates supersonic flow since $\frac{dA}{A}$>0 and M >1 to produce a uniform jet of gas that is stable for 10-20 cm or longer.

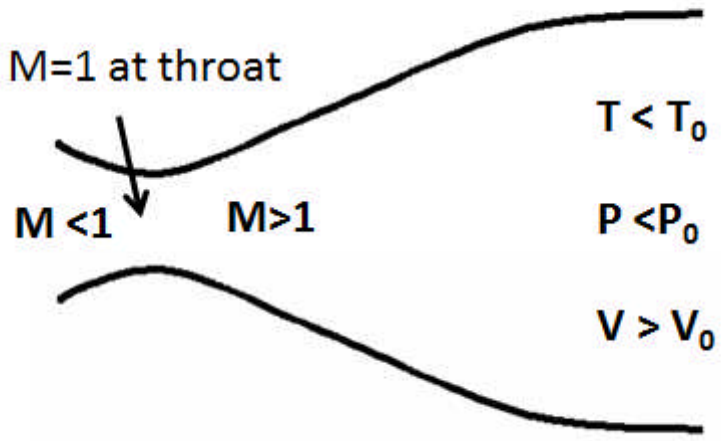

Figure 3.5: Schematic showing change in Mach number with different sections of the Laval and the relationships between the flow conditions and those prior to expansion

3.2.2. Laval nozzle design

A given Laval nozzle will generally produce a stable supersonic expansion at a given Mach number and this Mach number will determine the temperature, pressure and density of the flow from the relationships:

$$\frac{T_0}{T} = 1 + \frac{\gamma - 1}{2} M^2 \qquad \text{(Eq. 4)}$$

$$\frac{p_0}{p} = \left(\frac{T_0}{T} \right)^{\gamma/(\gamma-1)} \qquad \text{(Eq. 5)}$$

$$\frac{\rho_0}{\rho} = \left(\frac{T_0}{T} \right)^{1/(\gamma-1)} \qquad \text{(Eq. 6)}$$

where T_0 , p_0 and ρ_0 are the reservoir values of temperature, pressure and density respectively. This means that there is a lack of tuneability with regards to flow conditions arising from expansion through a particular nozzle and generally a different nozzle must be designed for each set of conditions. In order to design the nozzles used within the Leeds apparatus, a computer code developed by Atkinson *et al.* (3) was used.

When designing a nozzle there are three sections that need to be considered, the convergent section of the nozzle, the divergent section and a boundary layer. The need for a boundary layer arises due to the fact that the nozzle wall introduces viscosity and heat transfer effects which complicate the problem at hand and the boundary layer itself is defined as the region of flow where wall effects are considered important. The boundary layer surrounds the isentropic core of the divergent section and the width of the boundary layer is equal to the displacement thickness δ^* defined as the distance from the wall at which viscosity and heat transfer effects are no longer considered.

The first section to consider is the convergent part of the nozzle. In order to achieve a stable supersonic expansion upon leaving the nozzle, it is necessary for the flow to reach a Mach number of 1 at the throat of the nozzle but in practice the convergent section is not as important as the divergent section of the nozzle. For the nozzles designed in the current work the contour of the convergent part of the nozzle was expressed by Eq. 7:

$$y = \sqrt{x + 0.2} \qquad \text{(Eq. 7)}$$

Where *x* is the displacement from the throat of the nozzle along the nozzle axis, and y is the perpendicular distance from the nozzle axis. This function was used to form a ¼ of a circle and the radius of 0.2 cm was determined by the physical dimensions of the nozzle mount. This choice of function may seem arbitrary, but it has been noted in the literature that the precise functional form of this convergent part has little effect on the nozzle performance. (3)

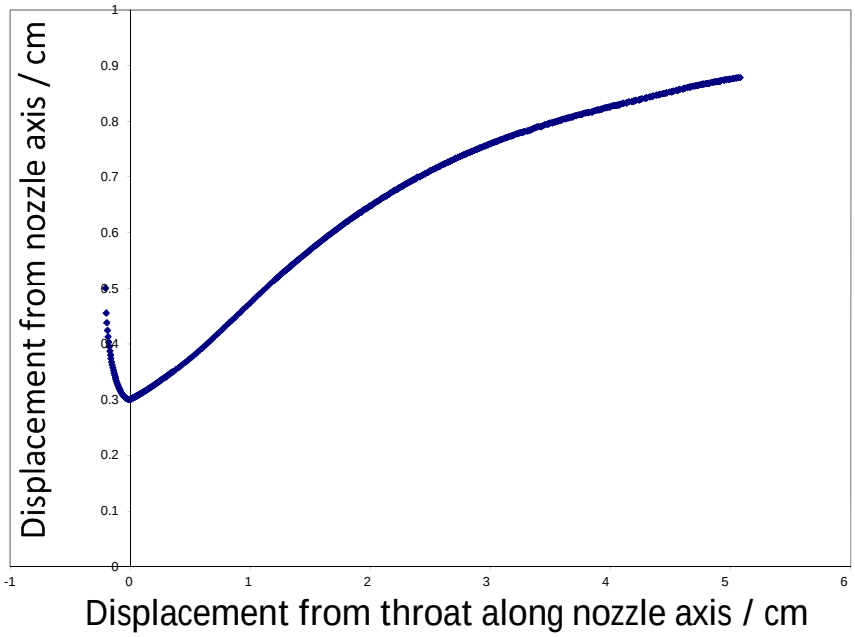

Figure 3.6: Calculated nozzle contour for the T81Pvar nozzle. The convergent part is define using Eq. 7 and the divergent part is determined from the code developed by Atkinson. (3)

The first part of the nozzle contour to be calculated by the program of Atkinson et al. (3) is the isentropic core in the divergent region. In order to do this it is assumed that the nozzle can be split into three distinct sections as shown in Figure 3.7. In the first of these, region 1, the flow undergoes rapid acceleration in order to reach approximately half the terminal Mach number by the time it reaches the line BC. Region 2 is referred to as the source flow region and here is assumed that the flow streamlines are straight lines originating from source point O. Finally in the third region the effects of the rapid expansion in region 1 are removed and the flow is accelerated to its terminal Mach number.

The existence of these three distinct regions of the isentropic core is assumed in the Moger and Ramsay (11) method of calculating wall contours. This method utilises the mathematical technique of characteristics. Characteristic curves are curves in the parameter space of a given problem along which the partial differential equations (PDE's) of the system can be described as ordinary differential equations (ODE's) and in the Laval nozzle, these characteristics can physically be thought of as describing the way in which a change in the wall contour of the nozzle propagates into the flow (3). Referring to region 2 in Figure 3.7 the assumption of source flow means that the Mach number at any point in the source flow region is pre-determined before the nozzle contour is calculated. Characteristics can then be extrapolated from this region towards the walls in order calculate the contours of the isentropic core. The wall contour in region 3 is then designed such that once a characteristic meets it, the characteristic is reflected parallel to the nozzle axis in order to produce the desired, collimated, expansion upon leaving the nozzle.

Once the isentropic core has been calculated the boundary layer for the nozzle must be determined. To do this it is necessary to determine the size of the displacement thickness along the flow axis and to add this to the contour for the isentropic core. The method used for this boundary layer calculation is that of Cohen and Reshotko (3) though the details of these calculations are beyond the scope of this thesis.

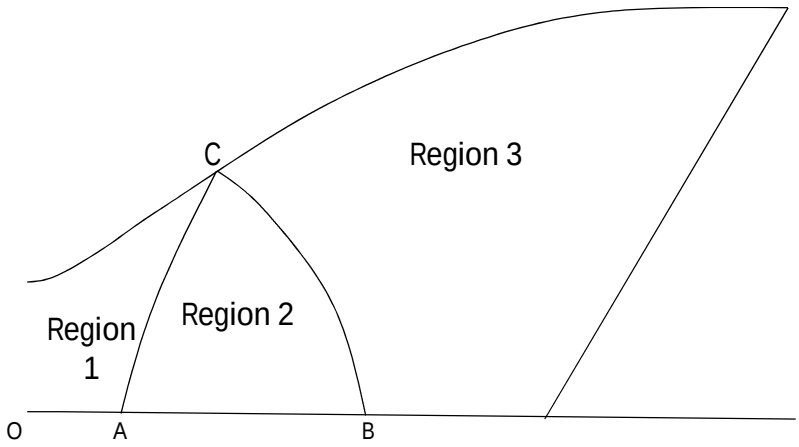

Figure 3.7: The three flow regions as defined in the isentropic core calculations of Moger and Ramsay. (11)

.

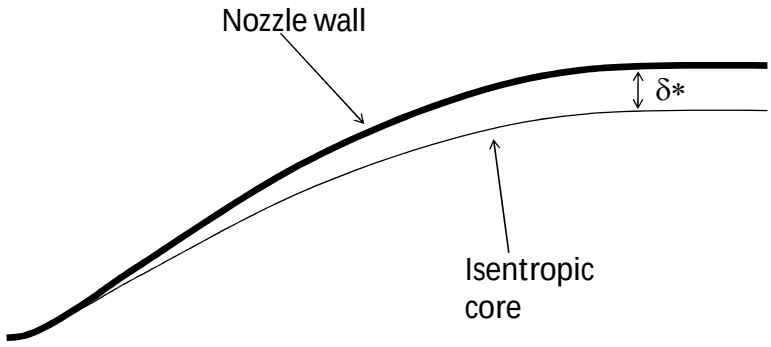

Figure 3.8: The addition of a boundary layer into the nozzle design through applying a displacement thickness to the isentropic core.

When using the nozzle design program a number of parameters must be defined by the user before the isentropic core is calculated. To begin with the terminal Mach number and the Mach number at the end of region 1 must be specified. Then the next parameter required is the angle of the wall at point C (Figure 3.8) with respect to the nozzle axis. This point is an inflection point between the positive curvature of wall required for rapid acceleration of

the flow in region 1 and the negative curvature of the wall in region 3 required for flow shaping. Finally the ratio of heat capacities, γ, for the carrier gas and the desired throat diameter of the nozzle must also be defined. These parameters define the size of the three regions shown in Figure 3.8 and a net of characteristic curves can then be calculated in order to define the isentropic core contours.

For this part of the calculation both the angle at C and the Mach number at the end of region 1 were found to be particularly sensitive parameters. If these parameters were poorly defined it was found that the computer program either failed to calculate the characteristic net or the program produced an unphysical contour for the isentropic core. The larger the angle at point C, the more rapidly the flow will attain its terminal Mach. This produces a shorter Laval nozzle which is desirable as this will limit the extent to which the boundary layer has grown by the nozzle exit. However if this angle is too large the flow will be unable to follow the wall contours and this means that the computer program fails to calculate a sufficient number of characteristics to define the contour. As recommended (3) it has been found that the angle needs to be <15° in order to produce a well formed nozzle. The Mach number of the flow at the end of region 1 determines how early or late the source flow region occurs after the nozzle throat and for the nozzles designed in the current work it was found that a value of between 1.1 and 1.3 gave the best results.

The boundary layer calculation requires a number of other parameters as input including the pre-expansion temperature, the stagnation temperature at the wall and the desired flow density. Ideally the boundary layer should be as small as possible and it was found that the size of the boundary layer was very sensitive to the desired flow density, and to the contour of the isentropic core itself.

3.2.3. Nozzles designed in the current work

A number of nozzles have already been designed for use with the Leeds apparatus (12) and the conditions resulting from expansion through some of these nozzles will be discussed in the next section. In addition to the existing

nozzles, a further two have been designed. These two nozzles were designed to give a temperature of 90K. One of the existing nozzles also produces a supersonic expansion with this temperature and two new nozzles were designed to produce gas expansions of higher total densities (1×10^{17} and 5×10^{17} molecule cm^{-3}) compared to the density of 5×10^{16} molecule cm^{-3} for the existing nozzle.

Higher density flows are desirable for two reasons. One reason, is that in order to maintain flow conditions, the concentration of reagent used in a Laval nozzle apparatus must usually be restricted to <1- 2% of the total gas concentration such that the ratio of heat capacities of the total gas flow, γ, is approximately equal to the γ of the bath gas. With a total higher gas density it is then possible to admit a larger concentration of reagent into the gas flow, whilst remaining below the 2% limit and this means that larger pseudo first order rate coefficients can be obtained (k'=[excess reagent] k_{bi}) which in turn means that reactions with small bimolecular rate coefficients can be measured.

The other advantage of higher densities is that if a number of flows can be achieved that exhibit the same temperature but different densities, the pressure dependence of a reaction may be explored. Many of the reactions studied in this thesis involve the formation of a weakly bound association complex. The dependence of the rate coefficient for an association reaction upon total gas density or pressure was explained in Chapter 2 and by measuring low temperature rate coefficients at different densities, the possibility of stabilising into a weak adduct can be explored.

The Nozzle design program (3) outputs the contour for the divergent part of each nozzle as a series of discrete points. A generic convergent region was then added and the entire nozzle contour was then achieved via a spline fit to these discrete data points. Using this wall contour a 3D picture of each nozzle was created in Solidworks™ and the nozzles were manufactured in aluminium by the mechanical engineering workshops at the University of Leeds.

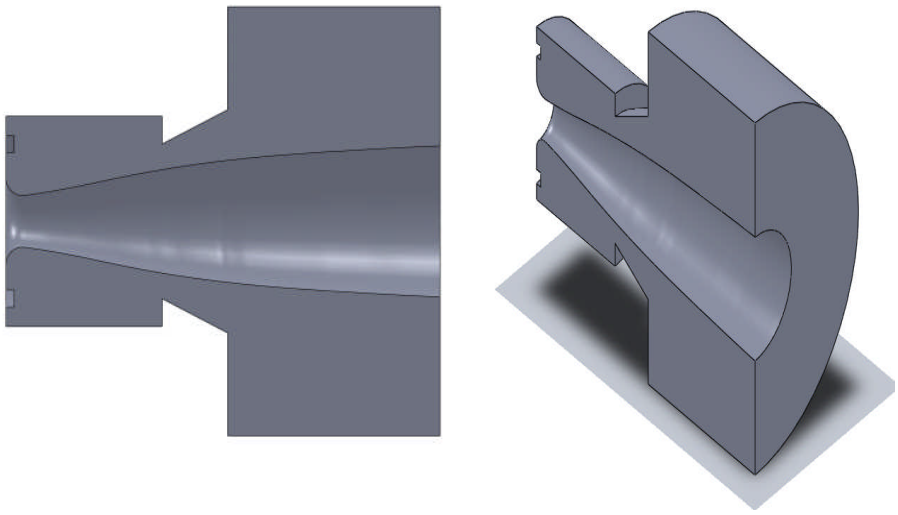

Figure 3.9: Cross-section of the T81Pvar nozzle designed using Solidworks™

3.2.4. Nozzle Characterisations

The techniques used to characterise the flow conditions of the various nozzles will be described in the next section so for now only the results will be discussed. In Table 3.1 the nozzles used in the current work are listed along with their flow conditions and the experimental conditions required for stable flow.

It was found that for a given total flow and backing pressure, there was a small window of chamber pressures ~0.1 Torr over which the most stable conditions could be observed. Here stability is defined in terms of the Mach number deviation along the length of the flow as a percentage of the average flow Mach number. In a free jet expansion optimum flow conditions are found when the chamber pressure is at its lowest. However in a Laval expansion, it is necessary to maintain a background pressure in order to counter any perpendicular expansion in the flow (3) and this constraint means that there is an optimum chamber pressure for each nozzle. Generally it has been found in the Leeds apparatus that nozzle expansions show two extremes of behaviour at high and low chamber pressures. When the chamber pressure is too high for a particular nozzle, it is found that the conditions of the expansion show little variation for a short period (1-5 cm) before the flow rapidly breaks down. Conversely when the chamber pressure

is too low, the nozzle expansion is stable for a much longer distance but along the length of the flow there are large oscillations (>10%) in conditions.

Nozzle	Chamber pressure / Torr	Ballast pressure / Torr	Length of stable flow /cm	T_{flow} / K	ρ / molecule cm^{-3}
T110P9E16	0.9	650	12	110±8	$(9.1\pm1.4)\times10^{16}$
T93P6E16	0.8	1060	20	93±4	$(6.3\pm0.5)\times10^{16}$
T63P3E16	0.4	540	25	63±2	$(3.4\pm0.3)\times10^{16}$
T81Pvar	0.6	600	13	80±4	$(4.6\pm0.4)\times10^{16}$
	0.9	860	15	83±3	$(6.1\pm0.4)\times10^{16}$
	1.1	1150	16	83±3	$(8.9\pm0.9)\times10^{16}$
	1.6	1380	15	81±4	$(1.3\pm0.2)\times10^{17}$
	2.0	2260	14	79±3	$(1.7\pm0.2)\times10^{17}$

Table 3.1: Flow conditions for the nozzles used in the current work. The numbers in the naming conventions correspond to the nozzle' temperature and pressure respectively apart from for the the T81Pvar nozzle where "var" denotes that the nozzle operates at a number of different pressures. Errors is this table are taken at the 1σ level.

The extremes of nozzle behaviour are shown in Figure 3.10. The optimum flow conditions shown in this plot represent a compromise between stability (minimum deviation in temperature and pressure) and the length of flow. At the point of flow breakdown, the Mach number can be seen to steadily rise producing a lower temperature in the expansion. However although this apparent rise in the Mach number is indicative of flow breakdown, once a flow is no longer supersonic, the isentropic flow equations (Eq. 4-6) are no longer valid and the rise in Mach number does not necessarily mean that the velocity of the gas is increasing or that the temperature is decreasing.

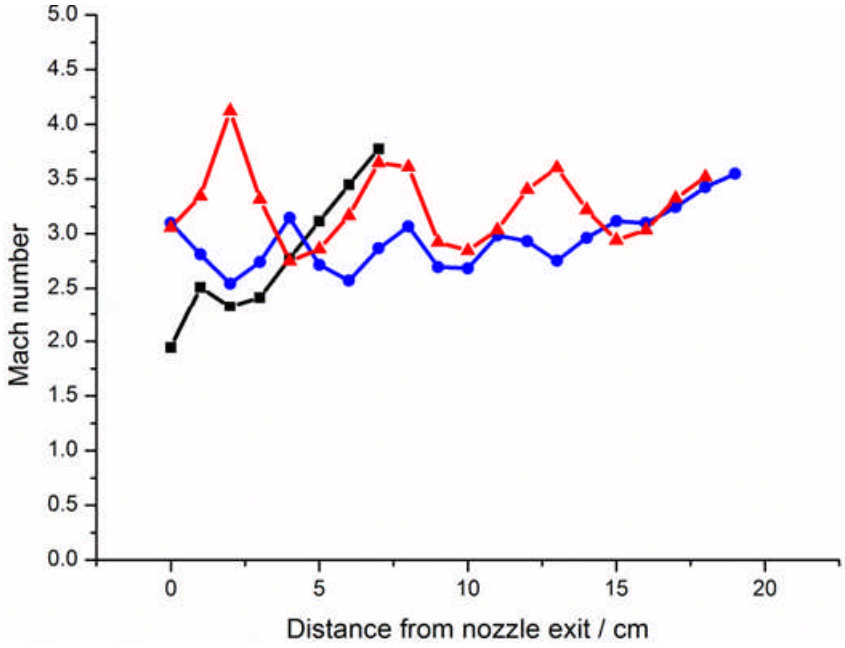

Figure 3.10: Impact pressure measurement when the chamber pressure is too low (red) optimum (blue) and too high (black) for the T81Pvar Nozzle.

Typically a nozzle is designed to give one particular flow density, however when considering the T81Pvar, nozzle designed for the current experiments it is found that one nozzle can be used to obtain a number of total gas densities within the Laval expansion. It should be noted that similar behaviour was found in the other nozzle designed for use in the current work however the expansion conditions from this nozzle were found to be very similar to the conditions from the T81Pvar nozzle and hence only this nozzle was used for experiments. Using this T81Pvar nozzle it was found that flow densities between 4.6×10^{16} and 1.7×10^{17} molecule cm^{-3} could be achieved through varying the total flow rate of the gas mixture. The temperatures of these different density expansions agreed within error and this nozzle could then be used to explore pressure dependent kinetics at 81K. The impact pressure measurements for this nozzle at three different total densities are shown in Figure 3.11.

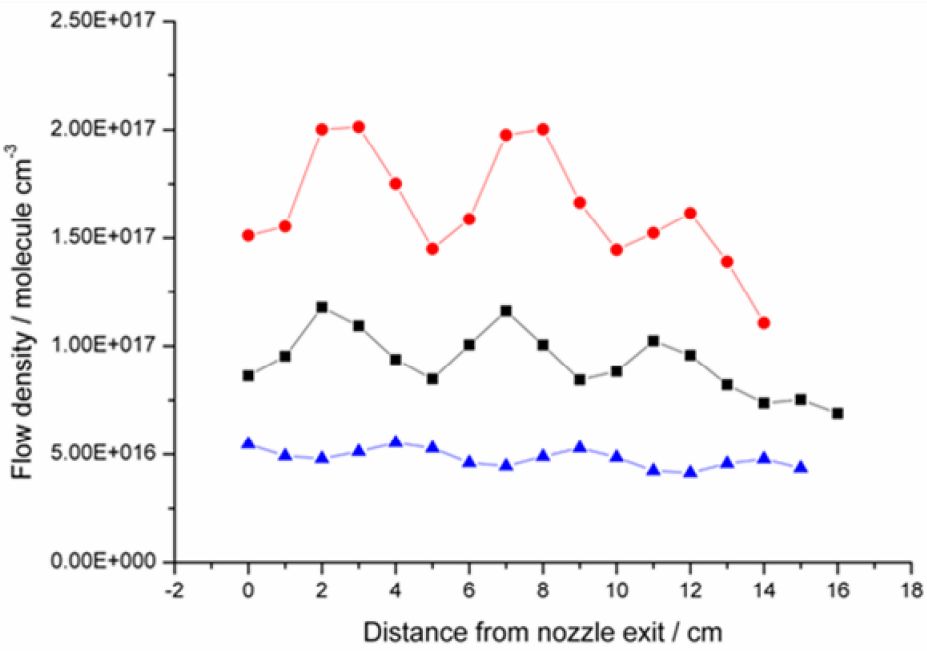

Figure 3.11: Impact pressure measurements for the T81Pvar Nozzle with backing pressures of 860 Torr (blue) 1150 Torr (black) and 2260 Torr (red) giving average flow densities of 6.1 ×10^{16} molecule cm^{-3}, 8.9 ×10^{16} molecule cm^{-3} and 1.7×10^{17} molecule cm^{-3} respectively. The average temperatures of these flows are 83K, 83K, and 79K for the blue, black and red plots respectively

3.3. Techniques and software used for experiments and theory.

3.3.1. Flow characterisation (impact pressure measurements)

It is not possible to take direct temperature readings with a conventional thermocouple without disturbing the flow, so indirect methods have been developed in order fully characterise flow conditions. The method of characterisation that is used predominantly in the Leeds apparatus is that of impact pressure measurements.

The flow through a Laval nozzle is considered one dimensional and this means that the flow conditions of pressure, temperature and density can all be derived from the values of these properties prior to expansion using only the Mach number of the flow. The Mach number for the flow depends on the ratio between the impact pressure and the stagnation pressure in the pre-expansion reservoir according to the Rayleigh formula:

$$\frac{p_i}{p_0} = \left[\frac{(\gamma+1)M^2}{(\gamma-1)M^2+2}\right]^{\gamma/(\gamma-1)} \left(\frac{\gamma+1}{2\gamma M^2-\gamma+1}\right)^{1/(\gamma-1)} \quad \text{(Eq. 8)}$$

where; p_i is the impact pressure, p_0 is the stagnation (reservoir) pressure, γ is the ratio of heat capacities (C_p/C_v) for the carrier gas (e.g. He = $^5/_3$ and N_2 = $^7/_5$) and M is the Mach number for the nozzle.

In addition to the pressure transducer located in the reservoir mentioned earlier (Figure 3.2), there is a second differential pressure transducer (PX170-14DV DE 7 Inch H_2O), aligned along the axis of flow on a pitot tube (designed to measure flow velocities whilst causing the minimum amount of perturbation to a supersonic gas flow), and one side of each of these transducers is connected to a separate vacuum line (<10^{-5} mbar) which provides an effective zero reference pressure. The reference sides of each transducer are connected to the external vacuum using Teflon pipe which is admitted to the chamber via flanges 2 and 4. This allows measurement of the pressure within the flow termed the impact pressure. The Rayleigh formula can then be solved for the Mach number but since Eq. 8 cannot be solved analytically, the Mach number must be calculated via an iterative process.

Once the Mach number for the flow has been obtained, values for the pressure density and temperature can be obtained from the stagnation values from equations Eq. 4-6 given in section 3.2.2.

Before impact pressure measurements can be performed, it is necessary to calibrate the voltage output of the pressure transducers against pressure. The transducers themselves are powered by two 9V batteries and their output is viewed using an oscilloscope (LeCroy Waverunner LT 264, 500 MHz, 8 bit vertical resolution) via two homemade low pass filters. In order to accurately measure the pressure difference experienced by the pressure transducers, a 10 Torr capacitance manometer (Leybold Ceravac CTR 90 0 – 10 Torr) is placed on the vacuum line attached to the reference side of each transducer. A second manometer (Leybold Ceravac CTR 90 0 – 1000

Torr) records the pressure in the Laval nozzle chamber. The Laval nozzle chamber is then evacuated, and the chamber pressure is controlled via opening or closing a release valve. A homemade LabVIEW™ program then records the mean output voltage measured on the oscilloscope for each tranducer and the corresponding pressure taken from the difference between the two manometer readings. When performing these calibrations, data were collected at 10 Hz and the output voltages integrated over 5 ms. Typically each set of datapoints was averaged 50 times using the labview code and from the resulting data output a calibration graph of voltage versus pressure could be obtained for each transducer.

Using the gradient from each calibration graph the impact pressure measurements could be performed. The chamber was once again evacuated and both manometers were used to measure the pressure within the chamber. Nitrogen was flowed into the pre expansion reservoir and the pulsed valves were triggered at 5 Hz and held open for 12 ms each. The resulting chamber pressure could be controlled using the gate valve on the pumping line. Again the voltage output from the two pressure transducers was visualised using an oscilloscope and the mean voltage was recorded over a 2 ms window coinciding with the point in each gas pulse at which the laser would fire in a typical kinetics experiment. This oscilloscope setup is shown in Figure 3.12.

In order to map the flow conditions resulting from nozzle expansion as a function of the distance into the flow, the pulsed Laval nozzle and reservoir are mounted onto a threaded yoke. As described earlier, the distance between the pitot pressure transducer and the nozzle exit can then be varied using a stepper motor (McLennan).

The impact pressure measurements are performed using a homemade LabVIEW™ virtual instrument (VI). This program controls the stepper motor position, and then records the output voltage from each pressure transducer using the oscilloscope. These readings are then typically averaged 50 times at each stepper motor position. In order to get accurate pressure measurements from each pressure transducer the data is collected from the oscilloscope at 10 Hz in order to give both online (during a gas pulse) and

offline (in between gas pulses) readings with respect to the gas pulses. The offline reading is then subtracted from the online and the calibration factor for each pressure transducer is used to convert the voltage into pressure (mbar). At each stepper motor position, the pressure readings from each transducer are used to solve Eq. 8 in order to obtain the Mach number and hence the temperature, pressure and density at that point within the flow.

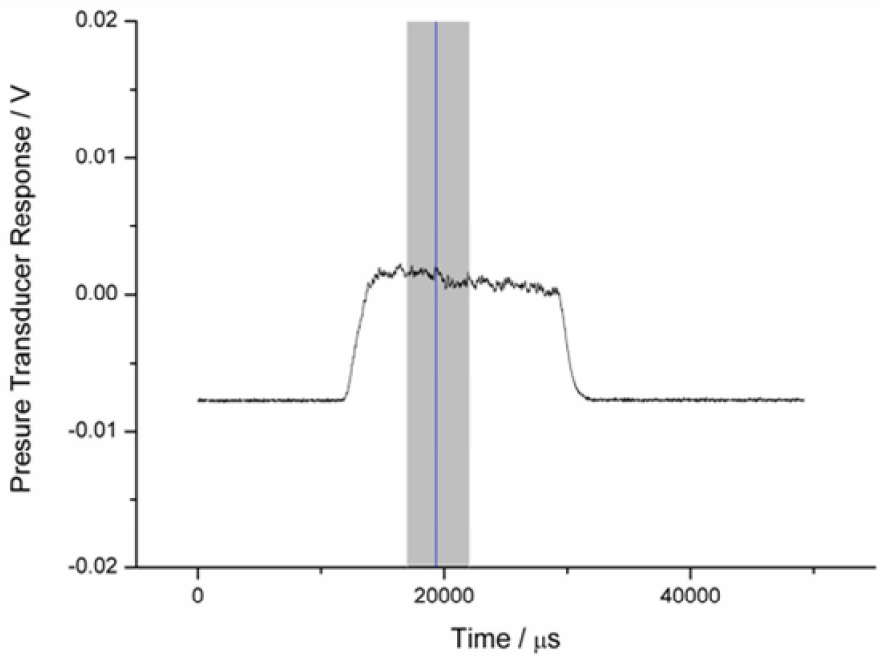

Figure 3.12: Oscilloscope readings in a typical impact pressure experiment. The black line is the impact pressure pulse recorded for the pitot pressure transducer (along the flow axis), the blue line shows the point in the gas pulse at which the lasers would fire and the shaded area is the area over which the transducer signal is typically averaged.

3.3.2. Flow characterisation (OH spectroscopy)

An alternative method of determining the flow temperature in a Laval nozzle expansion is that of rotationally resolved fluorescence excitation spectroscopy. This is a more time consuming method of characterising the temperature than the method of impact pressure measurements but this method offers a valuable check to confirm that the impact pressure measurements are correct.

Fluorescence excitation spectroscopy works in the following manner. When light of the correct wavelength is absorbed by a molecule in its ground electronic state, then the energy of this photon of light may be used to excite the molecule into an excited electronic state, by promoting one electron into an unoccupied molecular orbital. The excess energy of the excited state may then be remove in one of two ways, either energy can be transferred to another molecule during a collision (non-radiative energy transfer) or the energy can be emitted in the form of light radiation (radiative energy transfer). Assuming the electronic transition is allowed, this radiative energy transfer is termed fluorescence and the energy or wavelength of the emitted photon will be equal to the energy or wavelength gap between the exited and ground states.

In reality, since the separation between electronic energy levels is larger than that between vibrational and rotational energy levels, there will usually be a concomitant change in both vibrational and rotational energy. Therefore for two electronic energy levels there may be many transitions between the varying rotational levels of the upper and lower states. The intensity of the fluorescence resulting from each transition will be proportional to the population in the lower electronic and rotational level and this population will in turn depend upon the Boltzmann distribution. Since the Boltzmann distribution depends upon temperature, the relative fluorescence intensity resulting from different rotationally resolved transitions can be used as an accurate thermometer. This can be seen by comparing the excitation spectrum for the OH radical at 300K and 80K shown in Figure 3.13.

In the current work the fluorescence excitation spectrum of the OH radical is used in order to determine the temperature. In this case OH radicals in the ground electronic state ($X^2\Pi_i$) with vibrational energy v=0, are excited to the second electronically excited state ($A^2\Sigma^+$) and vibrational level v=1. Within this $A^2\Sigma^+$-$X^2\Pi_{3/2}$ (1,0) vibronic (vibrational and electronic) band there is rotational structure and the $Q_1(1.5)$ transition of this band may be excited by laser radiation at 282 nm.

.

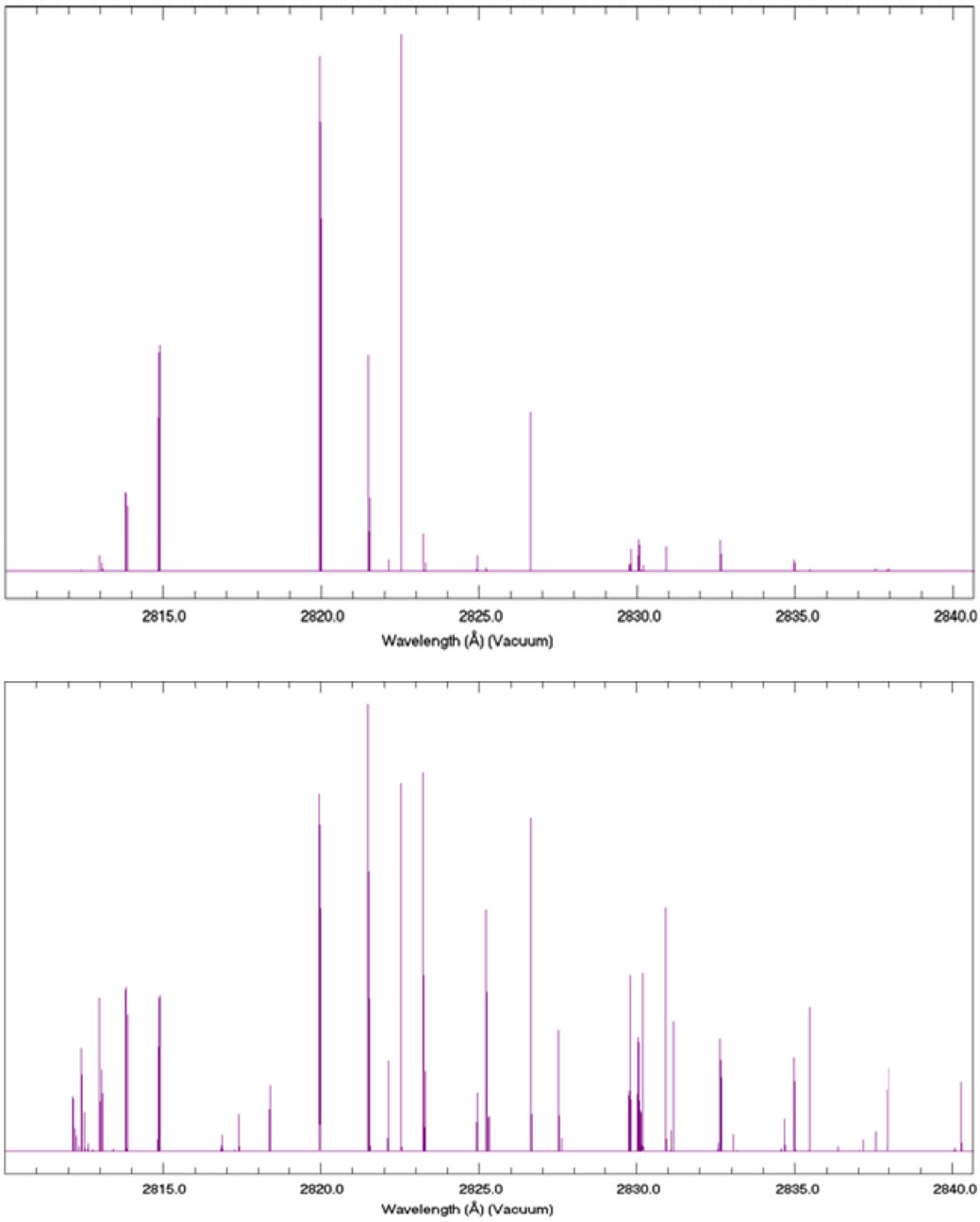

Figure 3.13: Simulated OH spectra showing the $A^2\Sigma^+$-$X^2\Pi_i$ (1,0) vibronic band at 300 K and 80 K (bottom) plotted using the LIFEBASE software.

Fluorescence may occur in one of two ways, either the fluorescence occurs directly from the rotational levels within the $A^2\Sigma^+$ state with v=1, or the vibrational energy in the electronically excited $A^2\Sigma^+$ state can be removed via collision and fluorescence can occur from the v=0 level of the $A^2\Sigma^+$ state. The second of these is known as off resonance fluorescence since the

fluorescence occurs at higher wavelengths than the initial excitation wavelength from the laser. It is this off resonance fluorescence scheme that is used in the current work, and this has the advantage that light from the excitation or probe laser can be removed using a suitable filter whilst still allowing all the fluorescence from the v=0 level to be collected. This OH fluorescence scheme is shown in Figure 3.14.

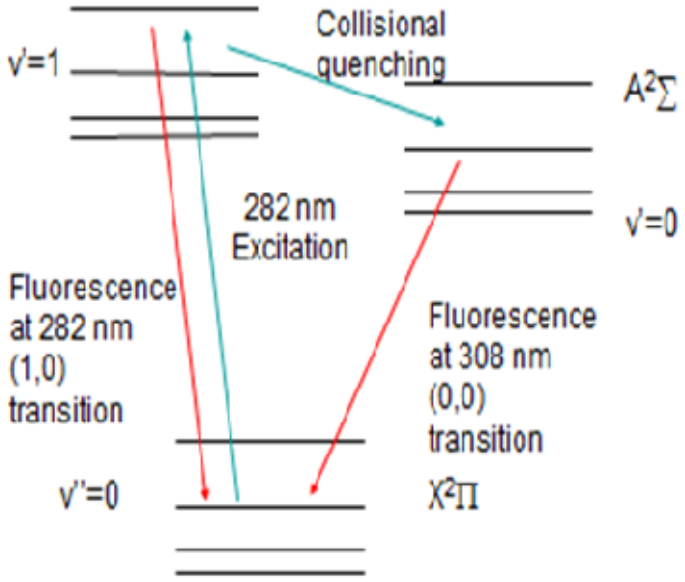

Figure 3.14: Schematic representation of resonance and off-resonance fluorescence in the OH radical. 282 nm and 308 nm refer to the Q1(1.5) transition in each band.

Given an experimental spectrum, there are two methods that may be used to determine the temperature at which the spectrum was recorded. The first of these methods is to perform a least squares fitting procedure between an experimental spectrum and simulated spectra at different temperatures in order to determine the temperature at which the simulated spectrum gives the best fit to the experimental one. An alternative method, which has been used in this work, is to undertake Boltzmann analysis of the experimental spectrum.

To begin with, this method requires an experimental spectrum consisting of a number of lines from the same rotational branch or progression. For this work the R1 branch of rotational transitions was used. The signal from each peak is then taken by either calculating the area underneath the peak or the height of the peak and can be given by the formula:

$$S_{J''} = CB_{J''}\phi_{J''}g_{J''}\exp(-E_{J''}/k_BT) \qquad \text{(Eq. 9)}$$

where $S_{J''}$ is the laser induced fluorescence (LIF) signal, $B_{J''}$ is the Einstein B coefficient for absorption, $\phi_{J''}$ is the fluorescence quantum yield and C is a constant.

From this we then obtain the equation

$$\ln\left(\frac{S_{J''}}{B_{J''}g_{J''}}\right) = D - \frac{E_{J''}}{k_BT} \qquad \text{(Eq. 10)}$$

where D is a constant and a plot of $\ln\left(\frac{S_{J''}}{B_{J''}g_{J''}}\right)$ versus $E_{J''}$ can be used to obtain the temperature.

In order to obtain an experimental spectrum, a suitable precursor must be added to the reaction chamber in order to produce OH radicals upon photolysis with laser radiation from the exciplex (Lambda Physik LPX 200) laser. The most common precursor used in this thesis is tertiary butyl hydroperoxide (Sigma Aldrich, 70% aqueous solution) which produces OH radicals according to the following simple scheme.

$$t\text{-BuOOH} + h\nu(248\text{nm}) \rightarrow \text{OH} + \text{other products} \qquad \text{(R1)}$$

Having chosen a precursor the OH laser excitation spectrum could be recorded as follows. First the reaction chamber was evacuated and the pulsed valves were operated at 5 Hz. Next the gas mixture for the experiments was admitted to the chamber via an external 2L ballast reservoir to ensure thorough mixing. This gas mixture consisted of two separate gas flows. The bulk of this gas mixture consisted of nitrogen bath gas though a 20 slm flow controller (MKS). In addition there was a second flow of nitrogen attached to a bubbler containing tert-BuOOH. This was passed through a 0.5 slm flow controller and the flows were adjusted such that the tert-BuOOH made up ~0.5% of the total gas flow. The gate valve and total gas flow were then adjusted such to give the optimum chamber

pressure and ballast pressure for the nozzle in use as determined from performing impact pressure measurements.

OH radicals were produced within the Laval expansion using the exciplex laser at 248nm at pulse energies of between 100 and 200 mJ. At some later time the OH molecules were probed at right angles using laser radiation from the Nd:YAG (Spectron Laser Systems SL803) pumped dye laser (Spectron Laser Systems SL803) which was then frequency doubled using a BBO crystal. The doubled laser frequency was varied between 281.1 nm and 281.4 nm to obtain a typical spectrum and the probe power was typically 1 mJ pulse^{-1}. The timings of both the lasers and the pulsed valves were controlled using a delay generator (Berkley Nucleonics Corporation 555) and all were fired at 5 Hz. The delay time between the excimer laser and the probe should be long enough to ensure that the OH molecules are rotationally relaxed but short enough such that the fluorescence signal is not too diminished by first order loss processes and a typical delay of 20 μs was used.

The photolysis and probe lasers were aligned such that the 25 mm^2 overlap region between the two was in the centre of the optical collection area described in section 3.1.3 and these optics were used to focus light onto a PMT (Thorn EMI 9813QB photocathode voltage -2.1 kV). As the probe laser left the reaction chamber a photodiode was also used in order to monitor the relative laser power. The output from both the PMT and photodiode were visualised on an oscilloscope.

When making temperature measurements using LIF in the current work, there were two issues which required particular attention, rotational level dependent quenching, and line saturation. With regards to the quenching issue it was important to collect the fluorescence with a prompt gate (fluorescence at early times only was recorded) to ensure that quenching at long times did not systematically alter the heights of some lines relative to others. Line saturation can also cause systematic error, and as such it was necessary to ensure that the laser power was sufficiently low, that all the lines in the excitation spectrum were still linearly dependent upon the rotational level population. When recording the OH laser fluorescence and

the probe laser power , the area of the signals from the PMT and the photodiode was generally integrated over 5 ns and the probe laser power was typically 1mJ pulse^{-1}. The laser probe laser power was varied between 0.5 mJ pulse^{-1} and 1.5 mJ pulse^{-1} and the integration window varied between 2 ns and 10 ns. The resulting spectra were observed to be independent of either laser power or integration window width suggesting that neither line saturation or rotational level dependent quenching were a problem in these experiments.

The experimental spectra were recorded using a homemade LabVIEW^{TM} program which could be used to vary the laser wavelength between two specified values at a given increment. For each point both the areas of both the PMT and photodiode channels within the 5 ns integration window were recorded and each point could be averaged a number of times, specified by the user. This program could be used to scan over a number of different wavelength ranges, in order to resolve specific lines.

Using the fluorescence signal and probe power output from this program the individual spectra could be analysed. Firstly the fluorescence signal at each point was divided by the photodiode signal in order to normalise the fluorescence signal with respect to laser power. Having done this the normalised signal was corrected to give a zero baseline. A corrected experimental spectrum showing the R1(1.5) – R1(5.5) Progression in the OH A-X transition is shown below.

Using this corrected spectrum the area of each peak was integrated using the graphical software origin, and then these peak areas were used in conjunction with equations Eq. 9 and Eq. 10 to give a Boltzmann plot as shown below. All constants used in these equations were taken from LIFBASE (13).

By recording spectra at different nozzle positions relative to the optical collection setup, the temperature could be probed at different points within the flow. Figure 3.17 shows temperatures measured using the Boltzmann plot method at different points within the flow through the T93P6E16 nozzle. These temperatures are compared with the impact pressure measurements and very good agreement (average temperature agree to within 2%) is

observed, giving confidence that the impact pressure experiments offer a reliable temperature measurement within the Leeds apperatus.

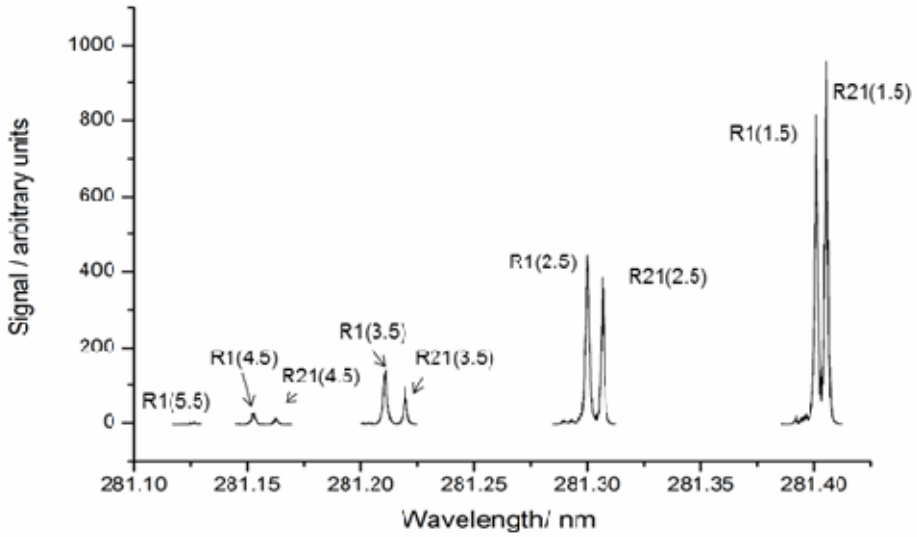

Figure 3.15: Fluorescence excitation spectrum showing the R21 and R1 rotational branches of the $A^2\Sigma^+$- $X^2\Pi_{3/2}$ (1,0) band for the OH radical. The OH radicals were created within a stable supersonic expansion from the T93P6E16 nozzle via pulsed laser photolysis of tertiary butyl hydrogen peroxide. The delay time between pump and probe laser was set to 20 μs. The probe laser power was 1 mJ $pulse^{-1}$ and the resulting fluorescence was integrated over 5 ns.

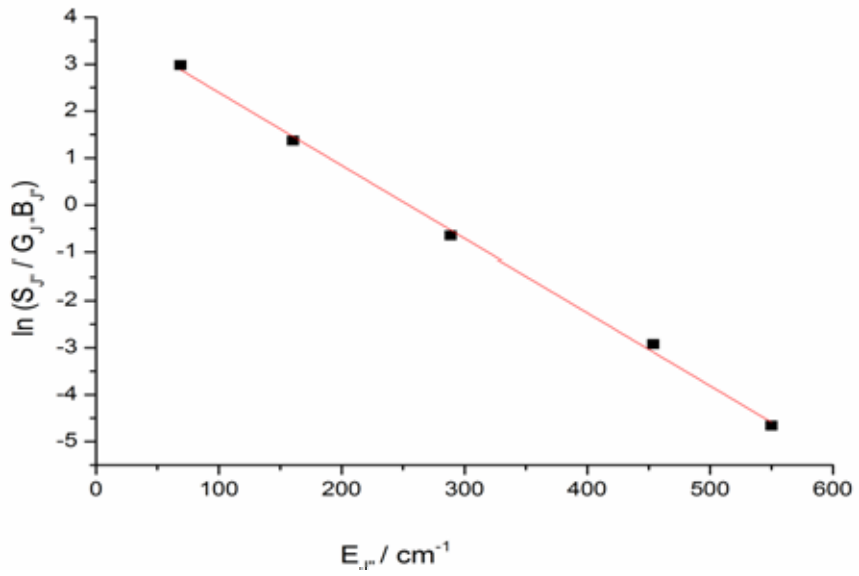

Figure 3.16: Boltzmann plot for the R1 branch of the $A^2\Sigma^+$- $X^2\Pi_{3/2}$ (1,0) band for the OH radical. The LIF signal heights were taken within the supersonic flow from the T93P6E16 nozzle at a distance between nozzle exit and optical collection region of 5 cm. This plot gives a temperature of 94±7 K.

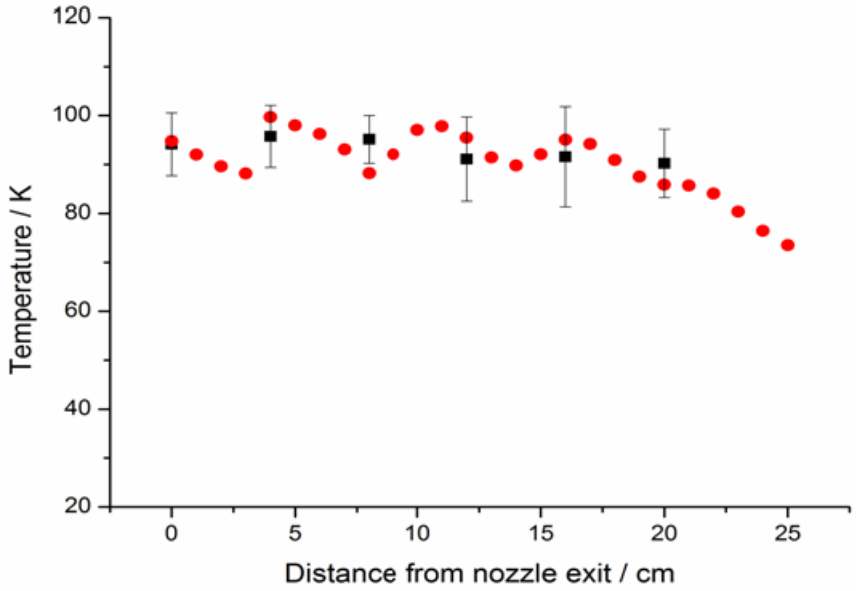

Figure 3.17: Comparison of temperature profiles for the T93P6E16 nozzle obtained using both the impact pressure method and the LIF method. The impact pressure measurements yield an average temperature of 93±4 K along the length of the flow whilst the LIF measurements give an average temperature of 95±2 K. From the impact measurements the average gas density within this flow is $(6.3\pm0.5)\times10^{16}$.

3.3.2. Pulsed laser photolysis – laser induced fluorescence (PLP-LIF) technique for kinetic studies of radical reactions.

Once a nozzle has been characterised, the standard experiments performed with the Laval nozzle apparatus involve the collection of kinetic data from which bimolecular rate coefficients can be extracted. As has been mentioned in chapter 2, in order to experimentally measure the rate coefficient for a reaction it is necessary to measure some property of one of the reagent molecules that is proportional to its concentration and these measurements must be resolved in time. In this case LIF spectroscopy is used. Assuming that there is no saturation of the probed transition then the fluorescence intensity will be proportional to the concentration of the fluorescing species and if the change in fluorescence with respect to time is monitored, then a kinetic trace can be obtained.

All the bimolecular kinetics experiments are performed under pseudo first order conditions and it is the deficient species, generally the OH radical, which is probed. As described in the context of OH spectroscopic characterisations, the deficient reagent radicals are produced along the length of the Laval nozzle expansion using pulsed laser photolysis (PLP) of a suitable precursor. The YAG pumped dye laser system is then used to probe their concentration. The wavelength of this dye laser is then tuned to be in resonance with a rotational transition within the species being monitored. In the case of the OH radical the dye laser is tuned to the Q1(1.5) rotational transition in the (1,0) vibrational band of the A-X transition. This transition occurs at 281.9 nm and laser light of wavelength 563.8 nm is frequency doubled using a BBO (β-BaB_2O_4) doubling crystal to give the 281.9 nm required.

In order to perform these experiments the reaction chamber is evacuated and a suitable reaction mixture of gases is admitted to the pre-expansion reservoir. This reaction mixture typically consists of nitrogen bath gas, a flow containing the excess reagent and a flow containing the photolytic precursor for the radical being studied. Species with a low vapour pressure such as

tert–BuOOH are admitted to the chamber via flowing a small amount of nitrogen through a bubbler containing the desired compound.

As described in the context of the LIF temperature measurements, the OH fluorescence is focussed onto a PMT and subsequently digitised using an oscilloscope. In the case of collecting kinetic data the area of the fluorescence signal upon the oscilloscope was typically taken over 8 μs. Typically an interference filter (Barr Associates Inc., 50 mm diameter, λ_{centre} = 308.5 nm, FWHM = 5 nm, in the case of OH) was placed between the optics and the PMT in order prevent scattered light from the probe laser reaching the PMT.

In all kinetics experiments the pulsed valves and both lasers were fired at 5 Hz. The length of the gas pulses, total gas flow and the position of the gate valve to the pumps, were then altered in order to give the optimum flow condition for the nozzle being used. The distance between the Laval nozzle and the fluorescence collection region was held at the length of the stable flow for the given nozzle and this defined the maximum time period over which the kinetics could be studied which was between 200 and 300 μs for the current selection of nozzles.

Once the apparatus was set up, the temporal evolution of the fluorescence signal and hence the deficient species concentration could be studied by varying the time delay between the photolysis and probe lasers. All timings were controlled using the delay generator and a homemade LabVIEW™ program was used to interface with both the delay generator and the oscilloscope in order to collect a kinetic trace.

Zero time for a kinetic trace was defined as the time at which the photolysis and probe lasers overlapped. The LabVIEW™ program was then used to incrementally increase the time delay between photolysis and subsequent probing up to a user specified maximum time delay. At each increment the delays of the pulsed values and the probe laser are increased by a small time amount Δt relative to the photolysis laser and the PMT and photodiode areas on the oscilloscope are recorded. A user specified number of scans were then taken and averaged and the resulting data was output in ASCII format.

In a similar manner to the experimental OH spectra, the kinetic data obtained from the this program was normalised with respect probe power on a shot-to-shot basis and a baseline correction was added before the trace was analysed. A kinetic trace can take the form of either a growth or a decay depending upon whether reactant or product molecules are being probed respectively. In the majority of the work in the thesis the kinetic data will take the form of a decay and the general method of analysing such data will briefly be described here.

A standard kinetic decay under pseudo first order conditions (see section 2.1.1) follows a single exponential decay according to the following equation:

$$[\mathrm{A}] = [\mathrm{A}]_0 \exp(-k' t) \qquad \text{(Eq. 11)}$$

$$k_{bi} = k'[\mathrm{B}] \qquad \text{(Eq. 12)}$$

where [A] is the concentration of the species being probed, $[A]_0$ is the concentration of A at time t=0, *k'* is the pseudo first order rate coefficient for the reaction being studied [B] is the concentration of the co-reagent which is held in excess over A and k_{bi} is the bimolecular rate coefficient for the reaction between A and B. By fitting Eq. 11 to the experimental data, *k*' can be obtained and if a number of kinetics experiments are performed at different excess reagent concentrations then a plot of *k*' versus [B] can be used to obtain the bimolecular rate coefficient from the gradient of a linear fit to the data as described by Eq. 12. Many of the bimolecular plots in this thesis exhibit significant intercepts when [B] is zero and these can be attributed to radical loss via either diffusion or reaction with the precursor.

3.3.4. MESMER(Master Equation Solver for Multi-Energy Well Reactions)(14)

In addition to measuring experimental rate constants, master equation analyses have been carried out using the MESMER (14) code. MESMER (14) is an open source C++ code designed to formulate and solve an energy

grained master equation for a reactive system for which the potential energy surface is known.

As described in section 2.4, in an energy grained master equation such as MESMER, the internal, ro-vibrational energy states of all species are partitioned into energy grains of a set size which is defined by the user. The program then calculates the change in population of each grain of species *n*, $\frac{\mathrm{d}n_i(E)}{\mathrm{d}t}$, taking into account reactive loss and gain using an Rice, Ramsperger, Kassel and Marcus (RRKM) calculation for grain to grain *k(E)'s* between species, and collisional energy transfer in an upwards and downwards direction using an exponential down model. In addition to the basic RRKM formalism, a tunnelling correction can be included in the RRKM *k(E)'*s using either the Eckart method of Miller (15), or the semi-classical method of Garret and Truhlar (16).

MESMER can deal with unimolecular isomerisation reactions over an arbitrary number of wells and barriers. A bimolecular source term can be included prior to any isomerisation processes through convoluting the densities of states of the two reacting partners. If this bimolecular source term has a well defined transition state, RRKM theory is used to calculate rate coefficients. Alternatively if the reaction is barrierless of the transition state parameters are unknown, an inverse Laplace transform (ILT) method can be used to obtain rate microcanonical rate coefficients for the association step. The ILT method can also be used to include dissociation reactions to bimolecular products.

As input, MESMER requires all vibrational and rotational frequencies of all species on the potential energy surface that are not infinite sinks (products of an irreversible reaction) in order to calculate densities of states and therefore RRKM *k*(E)'s. These densities of states are normally calculated using a rigid rotor harmonic oscillator approximation, however some vibrational modes are more correctly described as the internal rotation of one molecular fragment with respect to the rest of the molecule. In such cases the energy levels of this mode can be calculated using the theoretical techniques described in section 2.4.2.1.

The reactive potential energy surface for a MESMER calculation is determined using the electronic plus zero point vibrational energies of each stationary point , well or barrier, involved in the reaction and these energies are generally taken from electronic structure theory calculations. The reactions that connect each stationary point are then defined by the user. A MESMER input file may be displayed in the internet browser Firefox in order to graphically represent the potential energy surface over which the reaction occurs as shown in Figure 3.18. Finally for each minimum on the potential surface Lennard Jones parameters are required to define the collision frequency and a value ΔE_{down} must be given in order calculate the rate of collisional energy transfer in the given molecule.

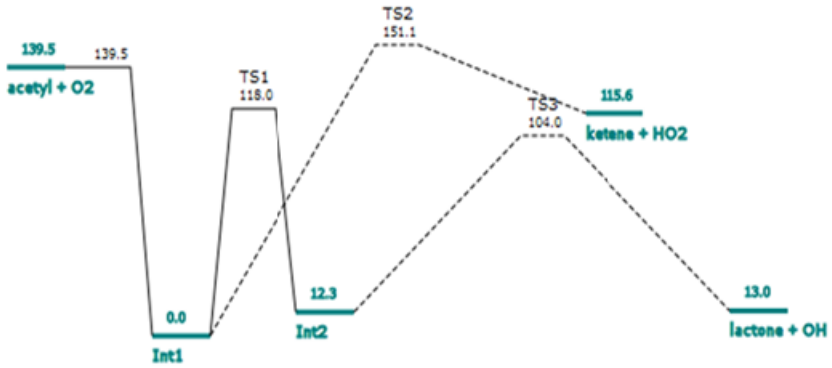

Figure 3.18: Part of a MESMER input file for the acetyl + O2 reaction viewed in Firefox in order to display the potential energy surface

One facility of the MESMER code which is used extensively in this thesis is that of data fitting. *Ab initio* calculations of molecular energies have significant errors associated with them and even relatively high levels of theory can exhibit errors of ±1 kcal mol^{-1} (17) (as shown in section 2.2.3) to the relative energies of species involved in a calculation. In addition, there are a number of parameters such as ΔE_{down} and the ILT parameters which are often not known *a priori*. In MESMER, parameters such as these may be adjusted in order to fit experimental data using a Levenberg Marquardt algorithm. The goodness of fit parameter used in these calculations is χ^2 which is defined as:

$$\chi^2 = \sum \frac{(k_{obs} - k_{calc})^2}{\sigma k_{obs}{}^2} \qquad \text{(Eq. 11)}$$

where k_{obs} are experimental rate coefficients, k_{calc} are the corresponding calculated rate coefficients and σk_{obs} is the experimental error. A number of parameters may then be varied over a specified range in order to minimise χ^2.

It should be noted that at no point in this thesis is it suggested that Master equations calculations offer a predictive theory for calculating rate coefficient without the need for experiments. However master equation calculations are a valuable tool when used in conjunction with experimental results. Their value is twofold. First, master equation calculations offer a reliable way of extrapolating existing experimental rate coefficients to experimentally inaccessibly pressure and temperature conditions. A second important function of master equation calculations and one that is used extensively in this work, is to probe mechanistic details of a reaction in order to elucidate which reaction pathways are operating in order to give the observed experimental rate coefficient.

3.3. References

1. DAUGEY, N., P. CAUBET, B. RETAIL, M. COSTES, A. BERGEAT and G. DORTHE. Kinetic measurements on methylidyne radical reactions with several hydrocarbons at low temperatures. *Physical Chemistry Chemical Physics*, 2005, **7**(15), pp.2921-2927.
2. ROWE, B.R., G. DUPEYRAT, J.B. MARQUETTE and P. GAUCHEREL. Study of the Reactions $N_2^+ + 2N_2 \rightarrow N_4^+ + N_2$ and $O_2^+ + 2O_2 \rightarrow O_4^+ + O_2$ from 20 to 160 K by the Cresu Technique. *Journal of Chemical Physics*, 1984, **80**(10), pp.4915-4921.
3. ATKINSON, D.B. and M.A. SMITH. Design and Characterization of Pulsed Uniform Supersonic Expansions for Chemical Applications. *Review of Scientific Instruments*, 1995, **66**(9), pp.4434-4446.
4. LEE, S., R.J. HOOBLER and S.R. LEONE. A pulsed Laval nozzle apparatus with laser ionization mass spectroscopy for direct measurements of rate coefficients at low temperatures with condensable gases. *Review of Scientific Instruments*, 2000, **71**(4), pp.1816-1823.

5. SPANGENBERG, T., S. KOHLER, B. HANSMANN, U. WACHSMUTH, B. ABEL and M.A. SMITH. Low-temperature reactions of OH radicals with propene and isoprene in pulsed laval nozzle expansions. *Journal of Physical Chemistry A*, 2004, **108**(37), pp.7527-7534.
6. TAYLOR, S.E., A. GODDARD, M.A. BLITZ, P.A. CLEARY and D.E. HEARD. Pulsed Laval nozzle study of the kinetics of OH with unsaturated hydrocarbons at very low temperatures. *Physical Chemistry Chemical Physics*, 2008, **10**(3), pp.422-437.
7. S. E. TAYLOR. *Reaction Kinetics at Very Low Temperatures Measured Using a Pulsed Laval Nozzle Apperatus.* thesis, University of Leeds, 2007.
8. ANDREWS, D.L. *Lasers in chemistry.* Berlin ; London: Springer-Verlag, 1986.
9. SMITH, I.W.M. *Low temperatures and cold molecules.* London: Imperial College Press, 2008.
10. D. B. ATKINSON and M. A. SMITH. Radical-molecule kinetics in pulsed uniform supersonic flows: Termolecular association of OH + NO between 90 and 220 K. *J. Phys. Chem.*, 1994, **98**(23), pp.5797 - 5800.
11. MOGER, W.C., D.B. RAMSAY. *Supersonic axisymmetric nozzle design by mass flow techniques utilizing a digital computer.* Defense Technical Information Center, 1964.
12. TAYLOR, S.E. *Reaction Kinetics at Very Low Temperatures Measured Using a Pulsed Laval Nozzle System*. thesis, University of Leeds, 2007.
13. *LIFBASE: Database and spectral simulation* [CD-ROM]. SRI International Report MP 99-009, 1999.
14. ROBERTSON, S.H., GLOWACKI, D. R., LIANG, C.-H.; MORLEY, C., PILLING, M. J.,. MESMER (Master Equation Solver for Multi-Energy Well Reactions), an object oriented C++ program for carrying out ME calculations and eigenvalue-eigenvector analysis on arbitrary multiple well systems. http://sourceforge.net/projects/mesmer. 2008.
15. MILLER, W.H. Tunneling Corrections to Unimolecular Rate Constants, with Application to Formaldehyde. *Journal of the American Chemical Society*, 1979, **101**(23), pp.6810-6814.
16. GARRETT, B.C. and D.G. TRUHLAR. Semi-Classical Tunneling Calculations. *Journal of Physical Chemistry*, 1979, **83**(22), pp.2921-2926.
17. CRAMER, J., CHRISTOPHER. *Essentials of computational chemistry: Theories and models.* Chichester ; New York: Wiley, 2002.

Chapter 4. Low Temperature Rate Coefficients for the Reactions of OH with Acetone and Dimethyl Ether.

The first results presented in this thesis will be for the hydrogen abstraction reactions of dimethyl ether (DME) and acetone with OH. Reactions between the OH radical and oxygenated volatile organic compounds (OVOCS) are ubiquitous in both atmospheric and combustion environments and much of this thesis will concern reactions of this type. The acetone and DME reactions exhibit many similarities with both each other, and the OH + methanol reaction discussed in the subsequent chapter and all three reactions occur over the same generic type of potential energy surface (PES).

4.1. The reaction between OH and acetone

4.1.1. Introduction

Acetone is an important anthropogenic and biogenic emission into the earth's atmosphere and it is removed by two major mechanisms, reaction with the OH radical and photolysis. The amount of acetone in the atmosphere can reach as much 3.3 parts per billion (ppb)(1) and it has been reported that as much as 10 Tg yr^{-1} of acetone could be released into the atmosphere from biomass burning. (2) Although solar photolysis of acetone is the dominant sink, this has been shown to be a source of HOx within the atmosphere and this leaves reaction with OH as the dominant removal mechanism which does not produce HO_2 or OH as a primary product..

The earth's atmosphere is not the only environment in which the OH + acetone reaction plays a role. This reaction has attracted interest from a combustion perspective since in complex combustion systems, the OH + acetone reaction is often an important part of the secondary chemistry. (3) Also acetone has been observed in space in both the interstellar medium (ISM) (4) and also hot cores (5) and as such the OH + acetone reaction is relevant to the very low temperature regime below 100 K.

Given the relevance of the OH + acetone reaction to a variety of complex systems, a number of experimental investigations of the rate coefficients and mechanism of this reaction (6) have been performed over a wide range of temperatures from 69 K (7) to 1300 K. (3) Many of the experimental studies of the OH + acetone reaction have concentrated upon temperatures in the 199 K to 450 K range. The studies from Gierczack (8) and Wollenhaupt (9) are in particularly good agreement in this temperature range and both these studies measured the acetone concentration directly using UV absorption spectroscopy which adds to the precision of these measurements. This temperature range was extended in the study by Yamada where rate coefficients were measured over the (298-832 K) temperature range. (10) The rate coefficients of Yamada agree well with the Gierczack and Wollenhaupt data at lower temperatures. Finally, two studies have measured rate coefficients up to 1300K (3, 11) to probe the reaction further into combustion conditions.

Before considering the very low temperature rate coefficients measured by Taylor, (7) it is worth discussing the mechanism through which the OH + acetone reaction occurs. Cox *et al.* (12) were the first to identify a hydrogen abstraction channel in this reaction (R1) and it has been proposed previously that a second product channel forming acetic acid(9, 13) (R2) is also possible although more recent studies have shown experimentally (14, 15) and theoretically (16-18) that this is a minor channel.

$$OH + CH_3COCH_3 \rightarrow CH_3COCH_2 + H_2O \qquad (R1)$$

$$OH + CH_3COCH_3 \rightarrow CH_3COOH + CH_3 \qquad (R2)$$

For the reaction between OH and acetone (10, 16) there have been a number of *ab initio* potential energy surfaces calculated and a schematic PES is shown in Figure 4.1. with stationary point energies calculated at the different levels of theory. On this PES the two different reaction pathways (R1 and R2) are highlighted and it can be seen, that regardless of level of

theory, the barrier to OH addition is substantially higher than both the barriers for hydrogen abstraction, supporting the conclusion that acetic acid is only a minor channel. The other important feature of this PES, and one that is general to many reactions between the OH radical and VOC species, is the presence of a pre-reaction hydrogen bonded complex. The *ab initio* PES calculated at the MP2/6-31G**//CCSD/6-311G**level of theory by Henon *et al.*(18) found an addition pre-reaction complex bound by 8.3 kJ mol^{-1}, but this complex was not located in the other computational studies and for simplicity and ease of comparison with the DME PES shown later in this chapter, this second pre-reaction complex has not been included in the schematic PES shown in Figure 4.

Interestingly there is some discrepancy between the barrier heights for hydrogen abstraction calculated using different levels of theory. When performing master equation calculation simulations on the system Caralp *et al.* (17) found that the barrier heights of Yamada (6) at CBS-QB3 level of theory gave the best agreement between experiment and theory and that the two papers using CCSD(T) (16, 18) single point calculations both significantly overestimated these barriers. This is surprising since the CCSD(T) energies would be expected to be more reliable than the CBS-QB3 energies and this certainly warrants further investigation.

The OH + acetone rate coefficients in the 199-832 K temperature range display a complicated temperature dependence. Above room temperature Arrhenius behaviour is observed consistent with abstraction over a significant energy barrier. However, at lower temperatures, significant deviation from the Arrhenius behaviour is apparent and the rate coefficients become almost independent of temperature between 200 and 250 K. A number of reasons have been given to rationalize this behaviour. Wallington and Kurylo (19) suggested that the behaviour of the rate coefficient below room temperature could be attributed to stabilization of a hydrogen bonded, pre-reaction complex, though, having performed master equation calculations on the system, Caralp *et al.* (17) showed that the deviation from Arrhenius behaviour could be well described by considering quantum mechanical tunnelling through the barrier to hydrogen abstraction.

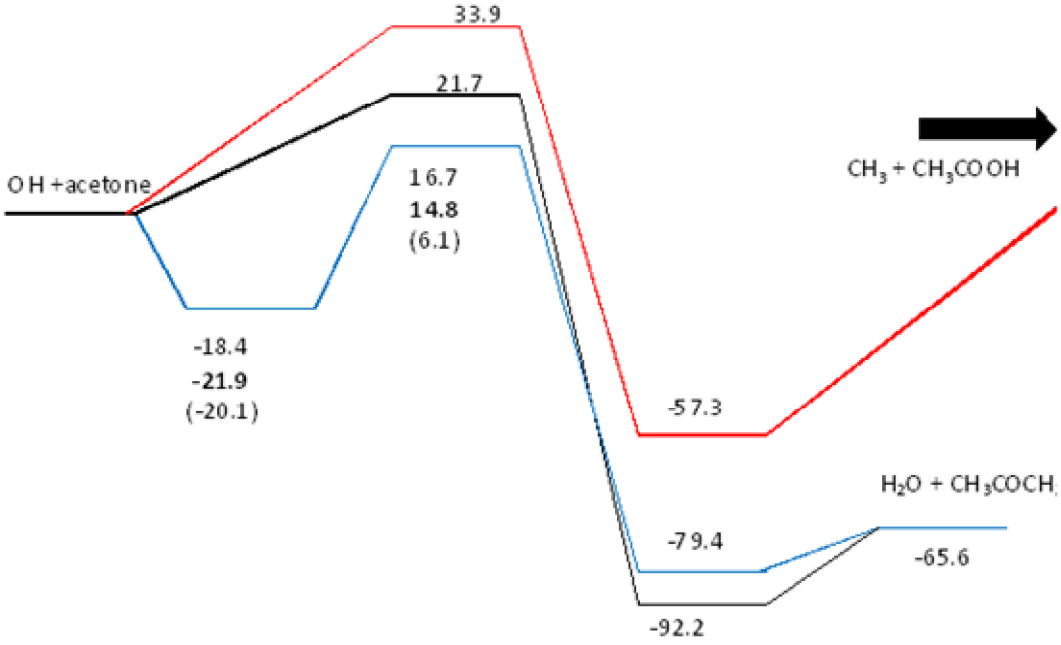

Figure 4.1: Schematic potential energy surface for the reaction between OH and acetone, showing the important stationary points. The reaction path highlighted in blue corresponds to the most energetically favourable path for R1 whilst the reaction path highlighted in red corresponds to reaction R2. The reaction path for R2 is not complete and there are a number of isomerisation steps before the final products are reached. Relative energies for all species include zero point energies (ZPE) are given from the calculations of Henon *et al.* (18) at the MP2/6-31G//CCSD(T)/6-311G** For the important species, energies calculated at the B3LYP-DFT/6-311++G(d,p)//CCSD(T)/ 6-311++G(d,p) by Vandenberk *et al.* (16) are shown in bold and energies calculated at the CBS-QB3 level of theory by Yamada *et al. (6)* are shown in parentheses. Energies are in kJ mol^{-1}**

The temperature dependence of the reaction becomes more complicated when the low temperature rate coefficients measured at 69 and 86 K are considered as shown in Figure 4.2. Here it can be seen that the slight negative temperature dependence between 200 and 250 K is enhanced dramatically by at very low temperatures with an increase by a factor of 1600 between 199 and 69 K. It was postulated that this negative temperature

dependence was due to a change in mechanism in which rather than forming abstraction products, the reaction instead forms a stabilised complex but the possibility of quantum mechanical tunnelling was not considered. To explore the low temperature mechanism further, measurements of the pressure dependence of this reaction at 80 K will be carried out. The tunnelling contribution will then be further explored through measuring the low temperature rate coefficients of the OD + acetone-d6 reaction and performing master equation calculations on the system.

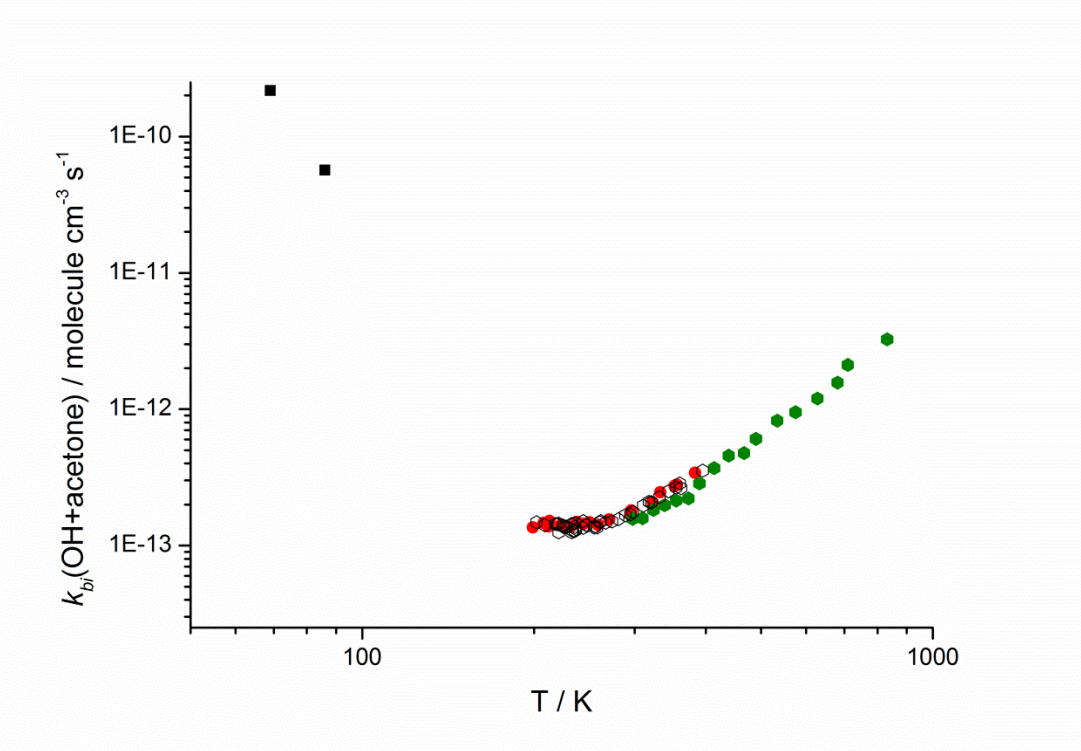

Figure 4.2: Previous measurements of the rate coefficient for the OH + acetone reaction, k_{bi}(OH+acetone), versus temperature. The green hexagons are from Yamada *et al.* (6), the red circles are from Wollenhaupt *et al. (9),* the open circles are from Gierczack *et al. (20)* and the black squares are from Taylor (7).

4.1.2. Methods

4.1.2.1. Experimental details

The rate coefficients for the OH + acetone reaction have been measured at 110, and 93 K using the T110P9E16 and T93P6E16 nozzles respectively. The pressure dependence of the rate coefficients has also been explored though using the T81Pvar nozzle to produce stable expansions with total

gas densities of between 4.6×10^{16} and 1.7×10^{17} at a temperature of 79 K - 83 K. The details of these nozzles are given in Section 3.2.4. In addition to these experiments, rate coefficients have also been measured for the OD + acetone-d6 reaction at 93 K. A detailed description of the experimental method is given in Section 3.3.2 and only the important points will be summarised here.

In order to perform these experiments, it was necessary to produce OH radicals *in situ,* within the reaction chamber and as such a suitable precursor was required which could be used to produce OH radicals upon photolysis. In the current case, the photolysis of acetone itself was used to produce acetyl radicals (CH_3CO) which could then react with O_2 in order to produce OH radicals. The photolysis of acetone (21) and the subsequent reaction between acetyl and O_2 (22) have been studied previously and it has been shown that at low pressures (>20 Torr) (23), this scheme (R3 –R4) provides an effective source of OH radicals(24).

$$CH_3C(O)CH_3 + h\nu \rightarrow CH_3CO + CH_3 \qquad \text{(R3)}$$

$$CH_3CO + O_2 \rightarrow OH + \text{other products} \qquad \text{(R4)}$$

In many other experiments performed in this thesis, tertiary butyl hydrogenperoxide (t-BuOOH) has been used as an OH precursor, but in the current experiments acetone photolysis was preferable for two reasons. First of all, since acetone was also the co-reagent, the only species that it was necessary to add to the system in order to produce OH was oxygen. T-BuOOH is a large molecule, with a propensity to form hydrogen bonded complexes (see chapter 6) and although problems are rarely encountered through using this molecule, oxygen molecules would be expected to interact with the reacting OH and acetone molecules less. Secondly the photolysis cross-section for acetone at 298 K and 248 nm is 2.4×10^{-20} cm^2 (25) which is slightly larger than that for *t*-BuOOH (1.9×10^{-20} cm^2) (26) and in the Laval nozzle system, using acetone as a precursor was observed to produce a larger OH signal, although the magnitude of this increase has not been quantified.

In using acetone as a precursor, the reactive gas mixture consisted of acetone (Fluka, Riedel-deHaėn, analytical grade 99.5%) , oxygen (BOC,

analytical grade) and nitrogen bath gas (BOC, OFN). For the OD experiments acetone-d6 (Aldrich, 99.9%) was used instead of acetone. Oxygen and nitrogen were admitted to the reaction chamber straight from the cylinder via mass flow controllers. Acetone or acetone-d6 were admitted into an empty cylinder using a freeze pump thaw method (~210 Torr) and then the cylinder was diluted with nitrogen up to a total pressure of 5600 Torr, and the cylinder was left overnight for thorough mixing. The resulting acetone, nitrogen mixture was then admitted to the reaction chamber via a mass flow controller. In order to ensure mixing the three gas flows were admitted to a 5L ballast reservoir prior to expansion.

Acetone or acetone-d6 molecules were photolysed at 248 nm using an excimer laser (Lambda Physic LPX 200) with typical pulse energies of 200 mJ. The OH radicals produced were then subsequently probed using a YAG (Spectron Laser Systems SL803) pumped dye laser (Sirah Gmbh-Cobra Stretch) system. In order to induce fluorescence in the target molecules the frequency doubled dye laser output was tuned in order to be resonant with the $A^2\Sigma^+$-$X^2\Pi_i$ (1,0) Q_1(1.5) transition in the OH and OD molecules at ~282 nm and ~288 nm respectively and the resulting fluorescence was collected using a photomultiplier (Thorn EMI 9813QB photocathode voltage -2.1 kV) and the subsequently digitised. The frequency doubled dye laser output at both 282 nm and 288 nm exhibited typical pulse energies of 1 mJ and the relative laser power was collected on a photodiode in order to normalise the laser induced fluorescence (LIF) signal.

The change in the relative OH or OD concentrations was obtained through varying the delay time between photolysis and probe lasers. The maximum delay time Δt was determined by the length of the stable flow resulting from expansion through a particular nozzle and was set to 300 μs for the T93P6E16 nozzle and to 200 μs for the other nozzles. Experimental traces typically consisted of 300 points and each point was averaged 20-30 times. The resulting averaged LIF signal was then normalised with respect to the dye laser power simultaneously measured using a photodiode. In order to analyse these traces obtained in these experiments, the differential equations describing the formation of OH or OD through reactions (R3-R4)

were solved using an integrating factor method to give the following equation:

$$[OH] = \frac{[CH_3CO]_0 k_2^{'}}{k_4^{'} - k_{acetone}} [\exp(-k_4^{'} \cdot t) - \exp(-k_{acetone}^{'} \cdot t)] \qquad \text{(Eq.1)}$$

where $[CH_3CO]_0$ is the initial CH_3CO concentration at t=0 and k'_4 and $k'_{acetone}$ are the pseudo first order rate coefficients for reactions R4 and R1 respectively. Eq. 1 could then be fit to the experimental data in order to extract these rate coefficients.

4.1.2.2. Computational details.

In addition to performing experiments upon the OH + acetone reaction, the rate coefficients were also calculated at low temperatures using the master equation code MESMER. (27) Considering that a number of OH + acetone potential energy surfaces already exist, it was not felt necessary to perform new *ab inito* calculations, to determine the stationary point energies or vibrational frequencies. For these calculations the vibrational frequencies and rotational constants from Henon *et al.* (18) were used and these are given in Table 4.1. Preliminary calculations showed that given the larger barrier height of TS2, abstraction via TS1 dominated under all conditions considered and as such the reduced PES shown in Figure 4.3 was used in the MESMER calculations. It is noted that TS2 (Figure 4.1) may have some influence on the OH + acetone rate coefficient above room temperature, however since the focus of this work is upon the low temperature regime the influence of TS2 was not considered.

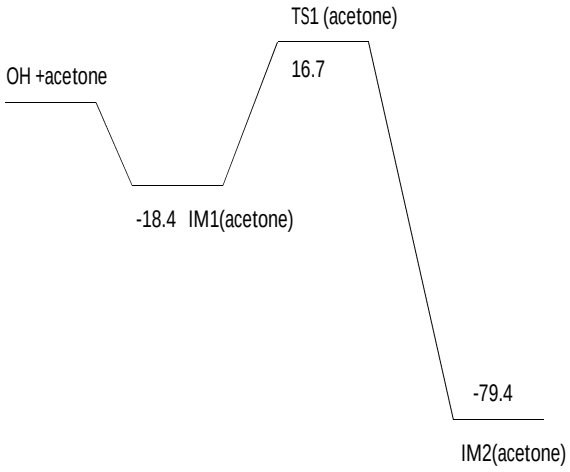

Figure 4.3: Reduced PES for the OH + acetone reaction, used in the MESMER calculations. Energies including zero point correction, are those from Henon et al. in kJ mol^{-1} and these parameters were varied in the fitting routine.

In this reduced PES we have also made use of infinite sink approximation which was described in Section 2.4. Throughout this thesis it has been found that for reactions on the generic type of potential energy surface shown above, the reaction is complete once the post reaction complex is formed and that the reverse reaction from the post reaction complex (IM2) back to the pre reaction complex(IM1) is negligible compared to the forward reaction to bimolecular products. This can be easily rationalised since the bimolecular products are almost 100 kJ mol^{-1} lower in energy than the top of TS1. Preliminary calculations have been performed including the final reaction step to acetonyl and water and it was found that rate coefficients calculated using the infinite sink approximation, differed from those using the full PES by at most 1%.

Species	B / cm^{-1}	ν / cm^{-1}
OH	18.732	3722
acetone	0.328, 0.277, 0.159	105 109 385 484 530 777 877 891 1066 1091 1216 1364 14101426 1450 1454 1731 2963 2972 2937 2937 3019
IM1(acetone)	0.062, 0.075, 0.308	36 45 78 128 166 374 464 522 531 534 782 873 888 1062 1093 1233 1370 1377 1446 1447 1453 1691 1468 2973 2978 3054 3061 3105 3109 3509
TS1(acetone)	0.075, 0.094, 0.318	39 123 173 237 322 429 465 504 688 780 850 890 941 1070 1093 1175 1236 1366 1423 1447 1456 1497 1706 2974 3016 3059 3097 3102 3584 1250i

Table 4.1: Rotational constants, B, and vibrational frequencies, ν, for the stationary points on the OH + acetone potential energy surface employed in the master equation calculations. Frequencies for IM2(acetone) are not required since this species is treated as an infinite sink. All frequencies were calculated at the MP2/6-31G level of theory by Henon *et al.* (18) The frequencies highlighted in red were replaced by hindered rotations.**

Using this reduced PES makes it easier to explore which parameters affect the OH + acetone rate coefficient. As was discussed in Section 4.1.1 there is some discrepancy between previous calculations on the OH + acetone PES

over the barrier height of TS1. The calculated rate coefficients were found to be quite sensitive to this parameter and as such it was varied in order fit the experimental data. It was also found that the low temperature rate coefficients were particularly sensitive to the well depth of IM1 and this was varied as well. In order to perform these fitting calculations, a Levenburg Marquardt fitting routine was used in order to minimise the goodness of fit measure, χ^2 defined below:

$$\chi^2 = \sum \frac{(k_{\text{obs}} - k_{\text{calc}})^2}{\sigma k_{obs}{}^2} \qquad \text{(Eq. 2)}$$

where k_{obs} are experimental rate coefficients for the OH + acetone reaction, k_{calc} are the corresponding calculated rate coefficient and σk_{obs} is the experimental error.

In order to calculate the molecular densities of states a rigid rotor approximation was used for all rotations, and a harmonic oscillator approach was used for most vibrational frequencies. However, there are a number of low frequency vibrational normal modes present in many of the species in the OH + acetone PES which are better described as hindered or free internal rotors. Acetone itself has two vibrational normal modes corresponding to the rotation of each of the CH_3 groups and in IM1 and TS1 there are additional torsional modes corresponding to rotations of the OH moiety about the acetone. The vibrational frequencies corresponding to these hindered rotations are indicated in Table 4.1 and the bonds about which each of these rotations takes place are shown in appendix 1.

In order to calculate the energy levels for the these modes, it was necessary to calculate the change in the potential energy of the molecule as each appropriate bond was rotated. These hindered potential were calculated using the Guassian 03 suite of *ab inito* sotware (28) using the MPW1K/6-31+G(2d,2p) level of theory. The rotational potential was then calculated by incrementing the dihedral angle corresponding to rotation about 360° and at each increment the molecules energy was minimised with respect to all co-ordinates other than the dihedral angle of rotation which is fixed. These relaxed potential energy scans with a constrained geometry optimisation at each step give a more realistic estimation of the true potential barrier to

rotation that a molecule faces since this reflects the fact that whilst a bond is rotating, other atoms may reconfigure themselves so as to minimise the overall energy.

Unfortunately, for some of the hindered rotational modes, these relaxed scans failed to calculate the potential about a full 360°. These modes were observed to be those incorporating the long range hydrogen bonded interaction between the OH and the acetone and the constrained geometry optimisations failed to minimise the geometry for some angles. This has been observed throughout this thesis for rotations of the OH moiety about its co-reactant and is presumably due to the long range nature of these interactions.

In order to approximate the relaxed potentials for these modes the following methodology was used. Rigid potentials for these hindered modes were obtained by incrementing the corresponding dihedral angle in steps of 30° but at each step the MPW1K/6-31+G(2d,2p) energy is calculated without performing a constrained geometry optimisation. Then using these rigid potentials, the dihedral angle was fixed at the value which gave the largest potential energy, and a constrained geometry optimisation was performed at this point only in order to give the relaxed barrier height. The entire rigid potential was subsequently scaled by this relaxed barrier height.

In total 10 hindered rotational modes have been considered and graphical representations of most of these potentials are confined to appendix 1. It was found that internal rotations about C-C bonds in acetone could be treated using fully relaxed calculations. However for rotations involving O-H hydrogen bond interactions the potential was observed to be shallower and the rigid calculations described above needed to be employed. In particular, two hindered rotational modes, one in both IM1(acetone) and TS1(acetone), were found to exhibit barriers of only 2.9 and 5.8 kJ mol^{-1} respectively. These potentials are shown in Figure 4.4 and given the shallow nature of these potentials; these modes would be expected to be particularly poorly described by the harmonic oscillator approximation.

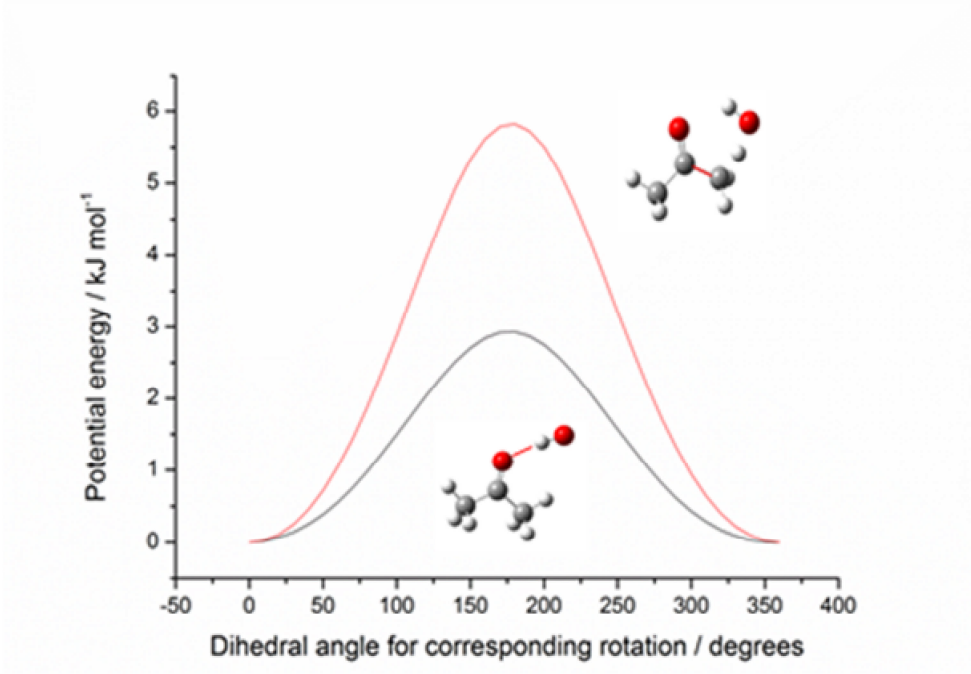

Figure 4.4: Rotation potentials for weakly hindered rotations in IM1(acetone), black, and TS1(acetone) , red. The bonds about which these rotations occur are indicated in red. These potentials consist of 36 energies calculated at the MPW1K/6-31+G(2d,2p) level of theory at intervals of 10 degrees. These rigid energies were then scaled to the optimised energy when the corresponding dihedral was fixed at 180 degrees in order to approximate a true relaxed potential.

Having obtained the molecular density of state for each species microcanonical rate coefficients for the isomerisation reaction were calculated using RRKM theory. Since this reaction involved hydrogen transfer tunnelling transmission coefficients were calculated and the RRKM rate coefficients were corrected for these. Tunnelling was incorporated using two methods. In the first method tunnelling was treated using the imaginary frequency of the transition state according to the method of Miller (29) described in Section 2.4.2.2. Since Henon *et al.* (18) calculated the imaginary frequency at the MP2 level of theory, there is likely to a significant uncertainty in this value and as such the imaginary frequency was treated as an adjustable parameter which was minimised using the Marquardt fitting procedure.

In the second tunnelling approach the semicalssical Wentzel–Kramers–Brillouin (WKB) method (30) was used, and again this method has been described in chapters 2 and 3. In order to perform this type of tunnelling calculation the change in potential energy along the entire reaction path from the reactant complex to the product complex was required and this was obtained through performing an intrinsic reaction co-ordinate (IRC) calculation at the MPW1K/6-31+G(2d,2p) level of theory using the Gaussian 03 suite of programs.(28) Once the fitting procedure had determined which ab initio value for the energy of TS1 gave the best agreement between experiment and theory, the IRC potential was scaled to this barrier height and the WKB method was used to give a more accurate representation quantum mechanical tunnelling than in the method of Miller. (29) The change in potential energy along the reaction path is shown below, and this potential is scaled to give energy difference between IM1(acetone) and TS1(acetone), including zero point energies.

Microcanonical rate coefficients for the barrierless association between OH and acetone to form IM1 were calculated using an inverse Laplace transform method (ILT) (31) as described in Section 2.3.2.2. The ILT A and n parameters were chosen as follows. The ILT A factor can be equated with the high pressure limiting macroscopic rate coefficient for the association and in the case of OH + acetone reaction, this high pressure limit was well defined by fitting to the pressure dependent rate coefficients at 80 K. The n parameter which describes the temperature dependence of the high pressure limit, was less well defined by the experimental data. In this case this parameter was chosen to be zero but a more detailed discussion of this can be found in Section 2.3.2.2.

In order to treat collisional energy transfer, collision frequencies between molecules were calculated assuming a Lennard Jones potential, and energy transfer probabilities were calculated using an exponential down model. This meant that the Lennard Jones parameters ε and σ, needed to be defined for IM1(acetone) as did the parameter ΔE_{down}. These parameters are discussed in greater detail in Section 2.4.2.3 and for the present calculations these parameters were set to 300, 5 and 400 cm^{-1} respectively.

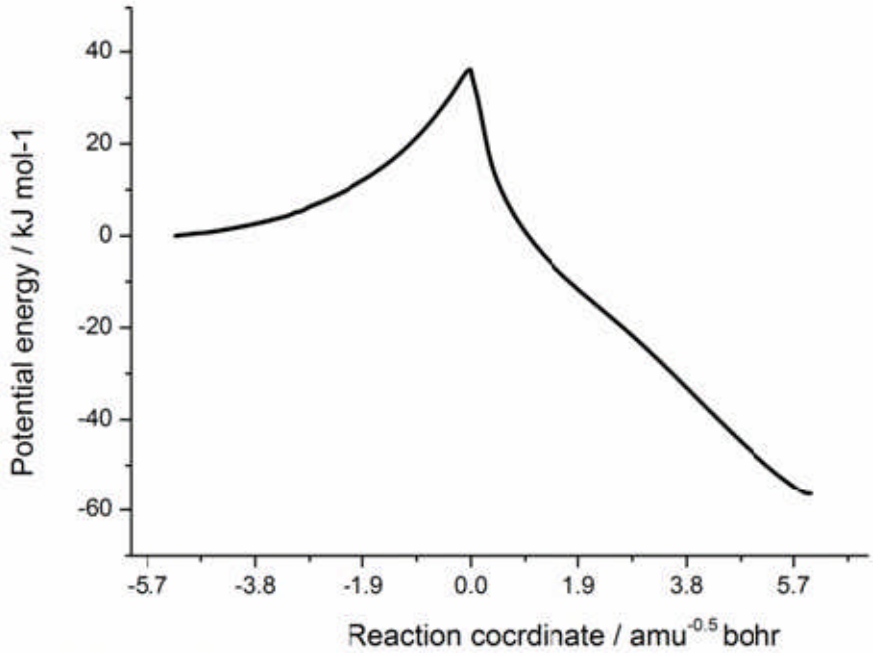

Figure 4.5: Variation in potential energy along the reaction coordinate from IM1(acetone) to IM2(acetone). The *ab initio* calculations were performed using the MPW1K/6-31+G(2d,2p) level of theory and the energy was calculated along the reaction coordinate using a stepsize of 0.1 amu$^{-0.5}$ bohr. These energies were then scaled to the *ab initio* energies of Vanderberk (16)(TS1(actone)-IM1(acetone) = 34.1 kJ mol^{-1}) since these energies were found to give the best agreement between experiment and theory.

Normally ΔE_{down} would be varied in order to fit the experimental data, but in the current case ΔE_{down} and the well depth of IM1(acetone) were so highly coupled that it was necessary to fix one. Measurements and theoretical investigations of ΔE_{down} have only been performed for a limited number of species, and this parameter is poorly understood, particularly at low temperatures.(32-34) The value of 400 cm^{-1} used here is toward the upper end of ΔE_{down} values that appear in the literature (35) but any reduction in ΔE_{down} can be taken up by increasing the well depth of IM1(acetone).

There is also a limited database of experimental values for the Lennard Jones parameters ε and σ and consequently there is a large degree of uncertainty to these values. Below 200 K the master equation calculations are sensitive to these parameters, and increasing either of these parameters

has the same effect as increasing ΔE_{down} or the well depth of IM1(acetone). Since all three of the energy transfer parameters are closely coupled to the well depth, the fitted value for the energy of IM1, is subject to a large degree of uncertainty which is difficult to quantify. However despite this uncertainty in the Lennard Jones parameters and $\Delta E_{down,}$ any change in these parameters can be taken up by a change in the energy of IM1 and a change of 50% in all three of these parameters, is observed to change the fitted well depth by at most 5 kJ mol^{-1}.A grain size of 20cm^{-1} was used for the fitting calculations, though a grain size of 10 cm^{-1} was required in order to perform calculations down to 60K.

4.1.3. Results

4.1.3.1. Experimental

Using the method described in Section 4.1.2.1, bi-exponential, time resolved, OH LIF traces were obtained at a range of acetone concentrations. These plots incorporated both OH formation from reaction R4 and the subsequent loss of OH due to reaction with the acetone and an example trace is shown is Figure 4.6. These traces were well described by Eq.1 and using the standard pseudo first order kinetics methodology (see Chapter 2), the bimolecular rate coefficient for the OH + acetone reaction could be obtained by plotting the first order loss coefficients from fitting the experimental traces versus the concentration of Acetone.

Bimolecular plots were obtained in this manner at both 110 and 93 K and these and an example bimolecular is shown in Figure 4.7. These plots both display good linearity though it was noted that at acetone concentrations > 2×10^{14} molecule cm^3 the bimolecular plots at 93 K displayed a large amount of curvature. This behaviour has been observed previously in the case of the OH + acetone at low temperatures and was attributed to the dimerisation of the acetone monomers. Indeed at 67 K Taylor found that the onset of dimerisation occurred at prohibitively low concentrations of acetone such that no linear portion of the bimolecular plots could be assigned. Consequently the rate coefficient for the OH + acetone reaction could only be obtained through a calculation of the equilibrium constant for acetone

dimerisation and then the subsequent correction of [acetone] in order to account for this. However, at the temperatures used in the current study, it was found that the bimolecular plots showed a sufficiently large linear portion, for rate coefficients to be measured effectively and the high [acetone] data points where clustering was occurring, were simply omitted from the fit.

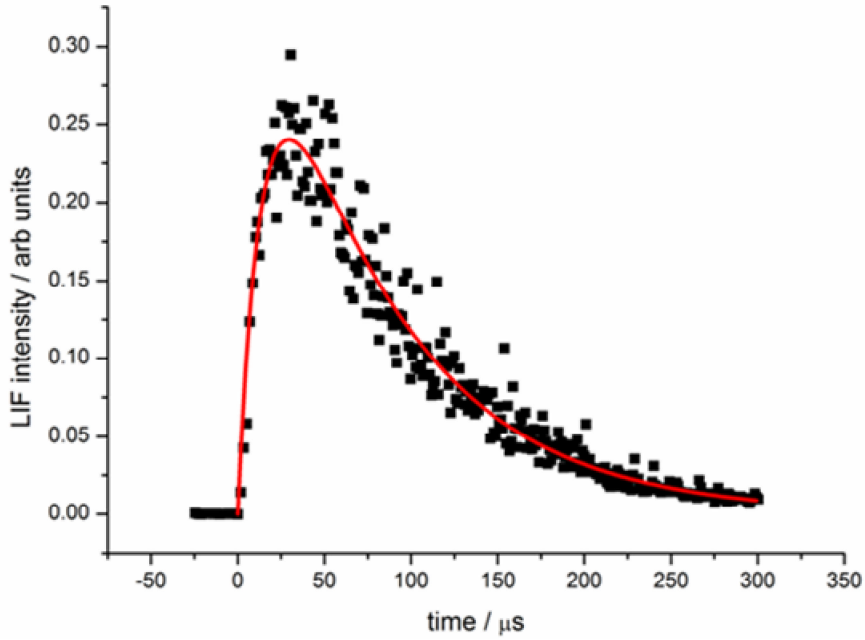

Figure 4.6: Time resolved OH LIF intensity due to OH production from R4 and subsequent reaction with acetone. This scan consists of 300 points and each point was averaged 20 times before being normalised for laser power. The curve in red corresponds to a fit to the experimental data from Eq. 1 which gives a pseudo first order rate coefficient, $k'_{acetone}$ of 13200±1440 s^{-1} Conditions used: Total density = (6.5±0.6)×10^{16} molecule cm^{-3}, [acetone] = (1.4±0.1)×10^{14} molecule cm^{-3} , [O_2] = (2.0±0.2) ×10^{16} molecule cm^{-3} , T = 93±3K.

From the bimolecular plots the bimolecular rate coefficient, k_{bi}(OH+acetone), was determined to be (5.6±0.8)×10^{-11} $molecule^{-1}$ cm^3 s^{-1} and be (5.7±1.2)×10^{-12} $molecule^{-1}$ cm^3 s^{-1} at 93 K and 110 K respectively. These rate coefficients are plotted versus temperature in Figure 4.8 and it can be seen these measurements agree well with those of Taylor and help to highlight the dramatic negative temperature dependence below 200 K. In particular, the measurement at 110 K helps fill in the gap between the high temperature and low temperature experiments and extrapolating the rapid

decrease in rate coefficient between 93 K and 110 K, helps to visualise the link between the two temperature regimes.

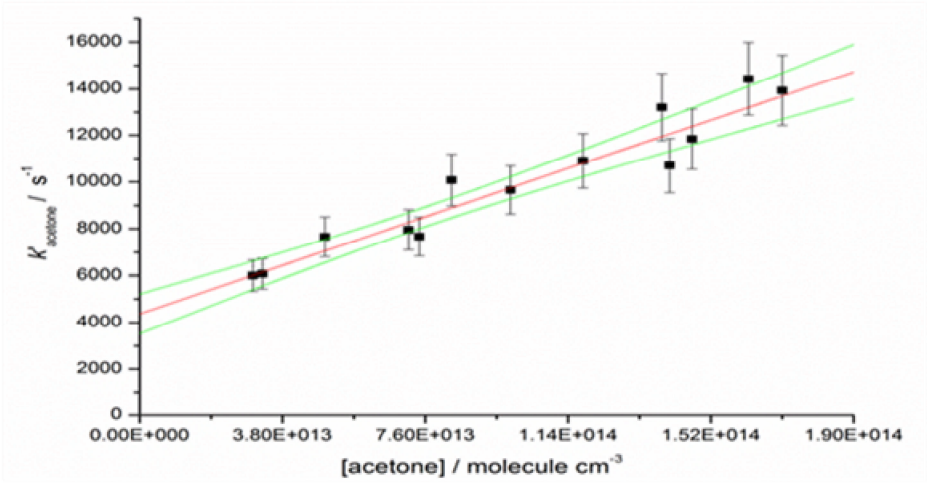

Figure 4.7: Bimolecular plot for the OH + acetone reaction at 93K and a total gas density of 6×10^{16} molecule cm^{-3}. The pseudo first order rate coefficients were obtained from fitting the experimental data with Eq 1 and they incorporate the 2σ errors both from the fitting process and from [acetone]. The bimolecular rate coefficient was obtained from a weighted linear give a k_{bi}(OH + acetone) = $(5.6\pm0.8)\times10^{-11}$ molecule^{-1} cm^3 s^{-1} with errors obtained from the 95% confidence limits of the linear fit.

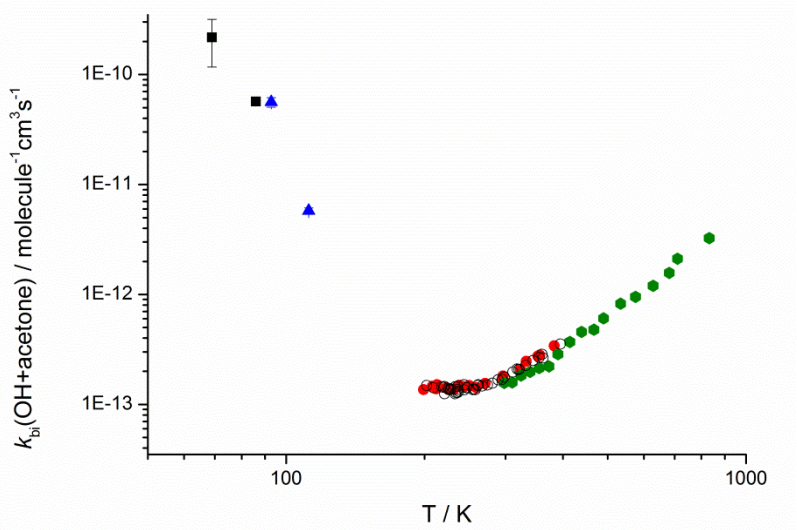

Figure 4.8: Previous measurements of the rate coefficient for the OH + acetone reaction, k_{bi}(OH+acetone), versus temperature together with current results. Both axes are on a logarithmic scale. The green hexagons are from Yamada *et al.* (6), the red circles are from Wollenhaupt *et al. (9),* the open circles are from Gierczack *et al. (20),* the black squares are from Taylor (7) and the blue triangles are from the current work.

Having observed such a dramatic negative temperature dependence to the OH + acetone rate coefficients, it is important to explore the mechanism behind these results. The master equation calculations of Caralp *et al.* (17) show good evidence that in the intermediate temperature regime (300 - 200 K) quantum mechanical tunnelling causes the non-Arrhenius behaviour that is observed. In order to ascertain the extent to which the low temperature reactivity of the OH + acetone system could also be attributed to quantum mechanical tunnelling, the rate coefficient for the reaction between OD and acetone-d6 was measured at 93 K. This system was studied in preference to the OH + acetone-d6 reaction since OD radicals could be produced through the photolysis of acetone-d6 in a method analogous to the production of OH from the photolysis of acetone. This reaction has been the subject of an experimental study previously (20) and above 200 K a primary isotope effect is observed with rate coefficients that are roughly half an order of magnitude smaller than those for OH + acetone.

A bimolecular plot for the OD + acetone-d6 reaction at 93 K is shown in Figure 4.9 and from this bimolecular plot a rate coefficient, k_{bi}(OD+acetone-d6), of (6.8±0.7)×10^{-11} was obtained, agreeing within error with k_{bi}(OH+acetone) measured at the same temperature. The transfer of a deuterium atom would be expected to show a diminished rate of tunnelling, due to its heavier mass. As such, if the dominant mechanism for the OH + acetone reaction at low temperatures was through tunnelling then the corresponding rate coefficient for the deuterated system would be expected to show a large reduction. The comparable low temperature rate coefficients for both the deuterated and non-deuterated systems suggest that the rate determining step for the OH + acetone reaction at low temperatures cannot be attributed to tunnelling.

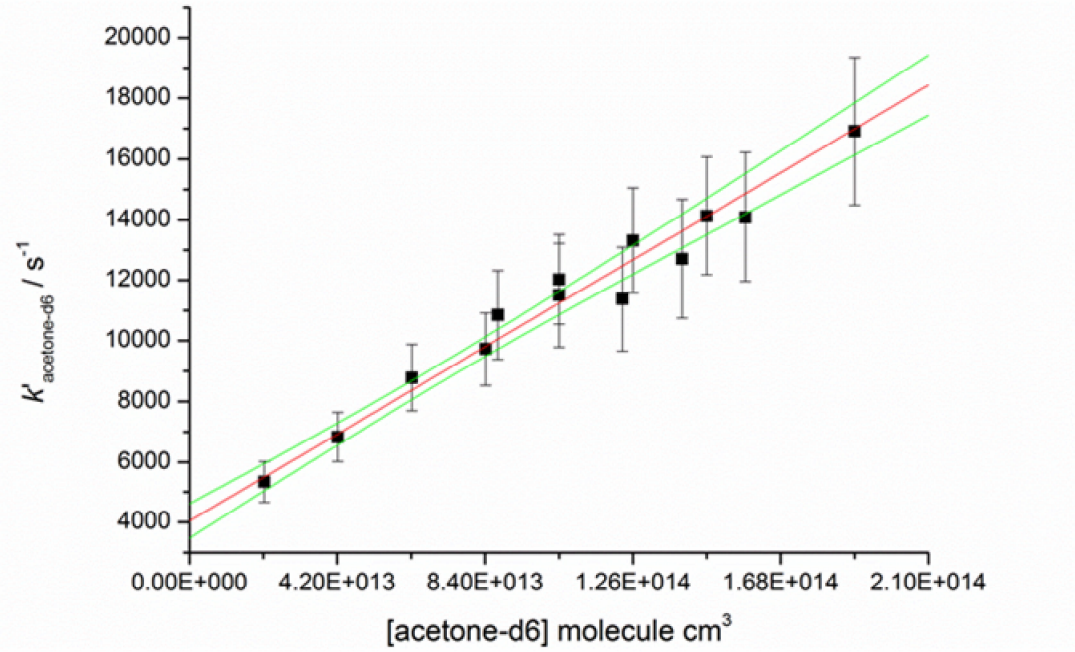

Figure 4.9: Bimolecular plot for the OD + acetone-d6 reaction at 93K and a total gas density of 6×10^{16} molecule cm^{-3}. The pseudo first order rate coefficients were obtained from fitting the experimental data with Eq 1 and they incorporate the 2σ errors both from the fitting process and from [acetone-d6]. The bimolecular rate coefficient was obtained from a weighted linear give a k_{bi}(OH + acetone) = $(6.8\pm0.7)\times10^{-11}$ molecule^{-1} cm^3 s^{-1} with errors obtained from the 95% confidence limits of the linear fit.

Given the results of the deuterated experiments a stabilization mechanism seemed more likely as the rate determining step at low temperatures in which the energised pre-reaction complex IM1(acetone)* is collisionally stabilised to form the stable complex IM1. This mechanism is an example of the Lindemann-Hinshelwood mechanism described in Section 2.1.3 and the rate at which such a complex is stabilized would be proportional to the number of deactivating collisions and therefore the total gas density or pressure. While no pressure dependence has been observed in the rate coefficients for the OH + acetone reaction above 200 K, at the low temperatures used in the current experiments the OH + acetone reaction could have undergone a change in mechanism in which stabilization of the pre-reaction complex had become dominant. To test this the rate coefficients for OH loss in the presence of acetone were measured at five different pressures between 3×10^{16} and 1.7×10^{17} molecule cm^{-3}. Figure 4.10

compares the bimolecular plots obtained at a number of these different densities and Figure 4.11 shows k_{bi}(OH+acetone) versus total gas density. From these results a clear density or pressure dependence can be observed supporting the deuterated experiments in providing evidence that at low temperatures, stabilization of the initial adduct is the dominant mechanism.

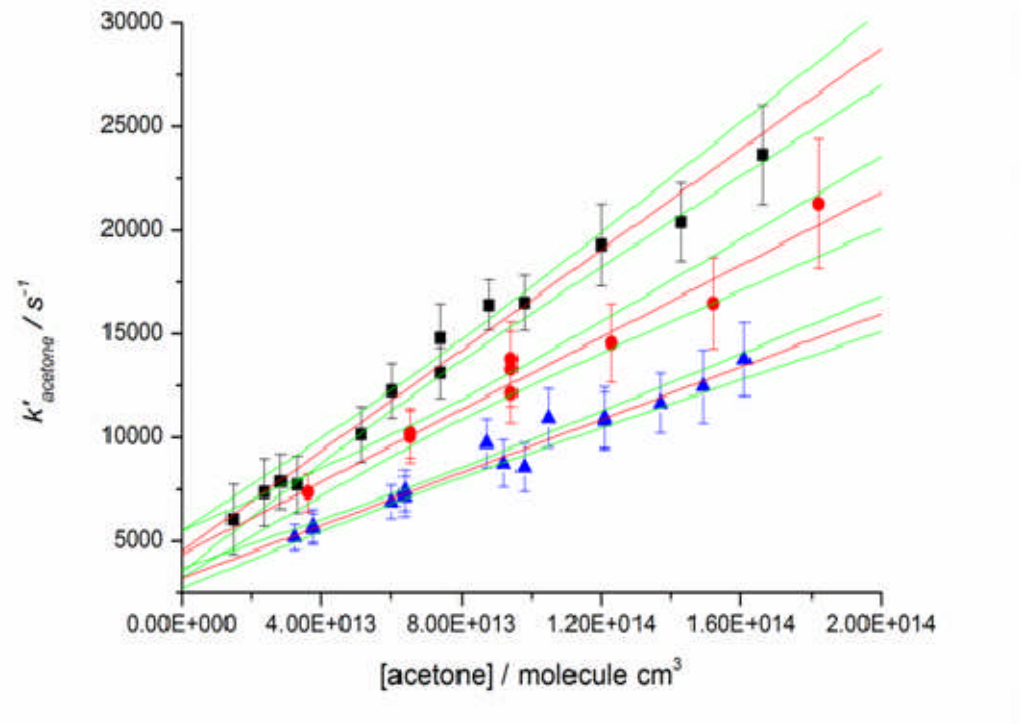

Figure 4.10: Bimolecular plots for the OH + acetone reaction at 80K and total gas densities of 1.7×10^{17} molecule cm^{-3} (black squares), 9×10^{16} molecule cm^{-3} (red circles) and 6×10^{16} molecule cm^{-3} (blue triangles) . The pseudo first order rate coefficients were obtained from fitting the experimental data with Eq. 1 and they incorporate the 2σ errors both from the fitting process and from [acetone]. The bimolecular rate coefficients was obtained from a weighted linear give k_{bi}(OH + acetone) = $(1.0\pm0.1)\times10^{-10}$ molecule^{-1} cm^3 s^{-1}, $(7.6.0\pm0.1)\times10^{-11}$ molecule^{-1} cm^3 s^{-1} and $(5.8\pm0.5)\times10^{-11}$ molecule^{-1} cm^3 s^{-1} respectively with errors (green lines) obtained from the 95% confidence limits of the linear fit.

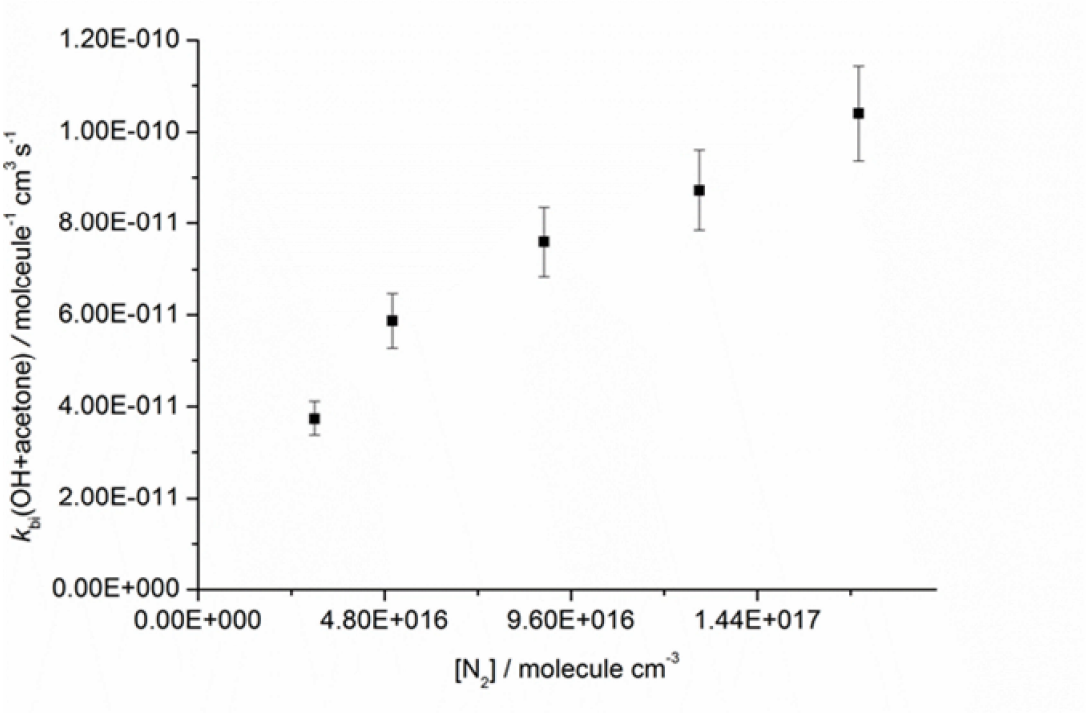

Figure 4.11: Dependence of the rate coefficient for OH loss in the presence of acetone upon total gas density in the Laval nozzle expansion. The temperature in the Laval expansion is between 82±4 K and 79±4K for each point.

4.1.3.2. Master equation calculations

To help interpret the experimental results, master equation simulations were carried out on the OH + acetone reaction. These calculations were performed using the MESMER code as described in section 4.1.2.2. Part of the aim of these calculations was to explore the importance of treating hindered rotations at low temperatures and to explore this, the fitting process was carried out both for the hindered rotor case (model 1) and the harmonic oscillator case (model 2). In addition, there is a CH_3 hindered rotation, which is identical in acetone, IM1(acetone) and TS1(acetone) and in order to explore whether some cancellation of error could be observed for these modes, fitting (model 3) was carried out using a third model in which these three identical modes were replaced with harmonic oscillators, whilst all other hindered rotational modes were used.

Since there have been a large number of studies measuring the OH + acetone rate coefficients at temperatures > 200 K only a subset of the data

in this temperature range was fit to, since the focus of the current work is upon the low temperature regime. This subset of the data consisted of data from both Gierczack (8) and Yamada (10) and contained enough data points to span the 200-800K temperature range with no more than 100 K between points. All of the low temperature data from the current study and the results from Taylor were included to give a total of 13 experimental rate coefficients which were fit to.

Parameter	Model 1	Model 2	Model 3	a	b	c
TS1 / kJ mol^{-1}	13.2	3.6	15.0	16.7	14.6	6.1
IM1 / kJ mol^{-1}	-27.5	-38	-30.3	-18.4	-22.2	-20.1
Imaginary Frequency / cm^{-1}	1018	541	1129	-1250	-1107	-1293
ILT A factor	3.1×10^{-10}	3.1×10^{-10}	3.2×10^{-10}	-	-	-
χ^2 per point	0.9	10.3	2.1	-	-	-

Table 4.2: Optimum MESMER parameters from performing a Levenburg Marquardt fitting procedure to minimise the goodness of fit parameter, χ^2, between experiment and theory. Columns marked a, b and c give *ab intio* values from Henon *et al.* (18), Vanderberk *et al.* (16) and Yamada *et al.* (10) respectively in order to compare with the fitted values. The χ^2 values in the final row are divided by the total number of experimental rate coefficients which were fit to in order to give an average χ^2 per point.

The optimised parameters from these fitting calculations are shown in Table 4.2. This table then shows how the fitted energies of IM1 and TS1 compare to the *ab intio* values from different studies. The first parameter worth consideration, is the well depth of IM1. Using a harmonic oscillator model it is found that the well depth needs to be reduced to 38 kJ mol^{-1}, a change of 16-20 kJ mol^{-1} which is likely to be well outside the error of the *ab initio* calculations. However, it can be seen that by including hindered rotation the fitted well depth is 27 kJ which is within 5 kJ mol^{-1} of *ab initio* well depth of Vanderberk *et al.* (16). It then appears that by increasing the density of

states in IM1 the fitted value for the binding energy of IM1 approaches the *ab initio* values.

The reasons for this change can be understood by considering the equations governing the ILT rate coefficients. In the case of OH + acetone, microcanonical rate coefficients for the re-dissociation of IM1 back to OH and acetone are calculated using the equation :

$$k_d(E) = \frac{CA^{\infty}}{\rho(E)\Gamma(n^{\infty}+1.5)} \int_0^{E^*} \rho_p(x)[(E)-x]^{n^{\infty}+0.5}\,dx \qquad \text{(Eq.4)}$$

where

$$C = \left[\frac{2\pi M_a M_b}{h^2(M_a + M_b)}\right]$$

$$E^* = E - E^{\infty} - \Delta H$$

Γ is the gamma function, $\rho_p(E)$ is the convolved density of states in the bimolecular species (acetone and OH), $\rho(E)$ is the density of states of IM1(acetone), M_a and M_b are the molecular masses of acetone and OH respectively is the mass of molecule a and ΔH is the change in enthalpy during the reaction. From this it can then be seen that by increasing the density of states of IM1, relative to the combined density of states of OH and acetone, the rate coefficient for re-dissociation get smaller and consequently the lifetime of the complex becomes larger. The density of states ratio can be altered by artificially increasing the well depth as has been observed, but by including treating the vibrational modes more correctly it has been shown that this artificial increasing of the well depth can be offset. Moreover IM1 has a number of low frequency bending modes that are poorly described as either an harmonic oscillator or a hindered rotation, and it is likely that a more sophisticated treatment of anharmonicity would bring the fitted well depth even closer to the *ab initio* value.

The effect of including hindered rotations is not confined to the IM1 well depth and the barrier height of TS1 was also found to be very sensitive to addition of hindered rotations. It has been mentioned in earlier sections, that there is some discrepancy between the different *ab initio* barrier heights and

that previous master equation calculations found it necessary to use the lower barrier height of 6 kJ mol^{-1}. In agreement, the fitting results from the harmonic oscillator model give a barrier height within 3 kJ mol^{-1} of this. However, once hindered rotations are included it can be seen from Table 4.2 that the fitted barrier height is much closer to the CCSD (t) barriers of 16.7 and 14.8 kJ mol^{-1}.

Finally it is worth considering the how much the CH_3 hindered rotations contribute to the density of states, since as stated earlier this mode is present in all species on the PES and as such some degree of cancellation would be expected. Considering the fitting results for models 1 and 3 it can be seen that both models which include hindered rotations give fitted values that agree well. It is certainly the case that including all hindered rotations changes the fitted parameters to some extent, but given the uncertainty in identifying rotational modes with harmonic frequencies it is not clear how significant the difference between these models is. However, it is clear that the two hindered rotation models stand distinct from the harmonic oscillator model and these results suggest that the most important hindered rotations, are those involving the OH moiety, which are not present in the acetone molecule itself.

In order to show the agreement between experiment and theory, calculated and experimental rate coefficients for the OH + acetone reaction are shown versus temperature in Figure 4.12. The theoretical rate coefficients shown are taken from the MESMER (27) calculations with all hindered rotations treated, and the agreement between experiment and theory is excellent. For comparison rate coefficients calculated using a WKB tunnelling method are also shown. This second set of theoretical rate coefficients use the *ab intio* energies of Vandenberk *et al.* (16) and minor adjustment of -1 kJ mol^{-1} was made to the energies of IM1(acetone) and TS1(acetone). Although it was necessary to increase ΔE_{down} to 1000 cm^{-1}, these calculations also agree well with the experimental data, showing that even without the extensive fitting process the master equations readily predict a substantial negative temperature dependence. The value of ΔE_{down} is probably unreasonably large in this case but these results show that using *ab initio* data with only very minor adjustments, it is still possible to reproduce the shape of the

temperature dependence of the OH + acetone rate coefficients. Quantitative agreement between experiment and theory at low temperature is only observed in the case of the fitted model, but due to the aforementioned uncertainties in both the molecular density of states and the imaginary frequency, the fitted parameters can be readily rationalised.

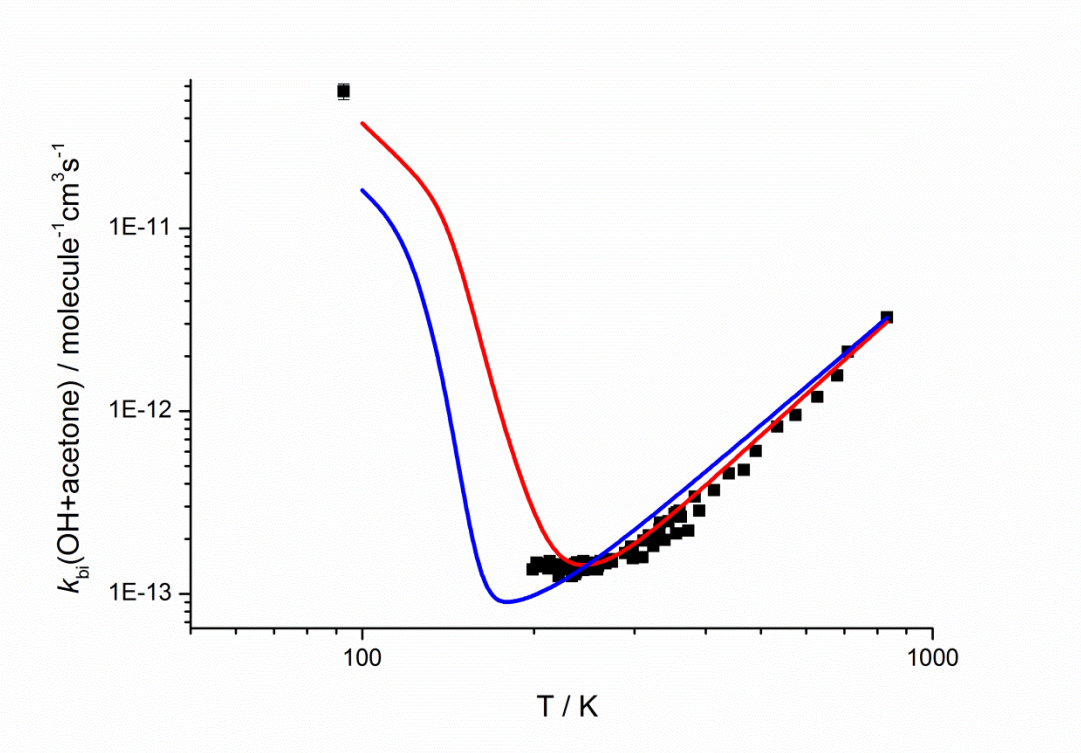

Figure 4.12: Comparison between experimental, and theoretical rate coefficients, k_{bi}(OH+acetone), versus temperature. Experimental measurements (black squares) above 200 K are taken from Yamada *et al.* (6), Wollenhaupt *et al.* (9) and Gierczack *et al.* (20), Whilst at low temperatures only the measurement at 93±6 K and 6×10^{16} molecule cm^{-3} is displayed since the other low temperature measurements are at different positions in their fall off curve due to the pressure dependence observed in k_{bi}(OH+acetone) below 200 K. The two lines show theoretical values for k_{bi}(OH+acetone) from master equation calculations at a total gas density of 6×10^{16} molecule cm^{-3}. The red line corresponds to calculations using model 1 and the corresponding fitted energies whilst the blue line corresponds to calculations using the WKB approach.

In terms of the pressure dependence of k_{bi}(OH+acetone), a comparison between theory (model 3) and experiment versus pressure at 80 K is shown in Figure 4.13. Again the agreement between experiment and theory is excellent and from fitting the master equation ILT A factor to this pressure

dependence, a high pressure limit of 3.1×10^{-10} molecule^{-1} cm^3 s^{-1} is predicted. Interestingly, the master equation calculations appear to predict a non-zero intercept at zero pressure. The value of this rate coefficient is 3.8×10^{-12} molecule^{-1} cm^3 s^{-1} and since there is no stabilisation possible at zero pressure this rate coefficient corresponds to tunnelling through TS1(acetone) to form IM2(acetone).

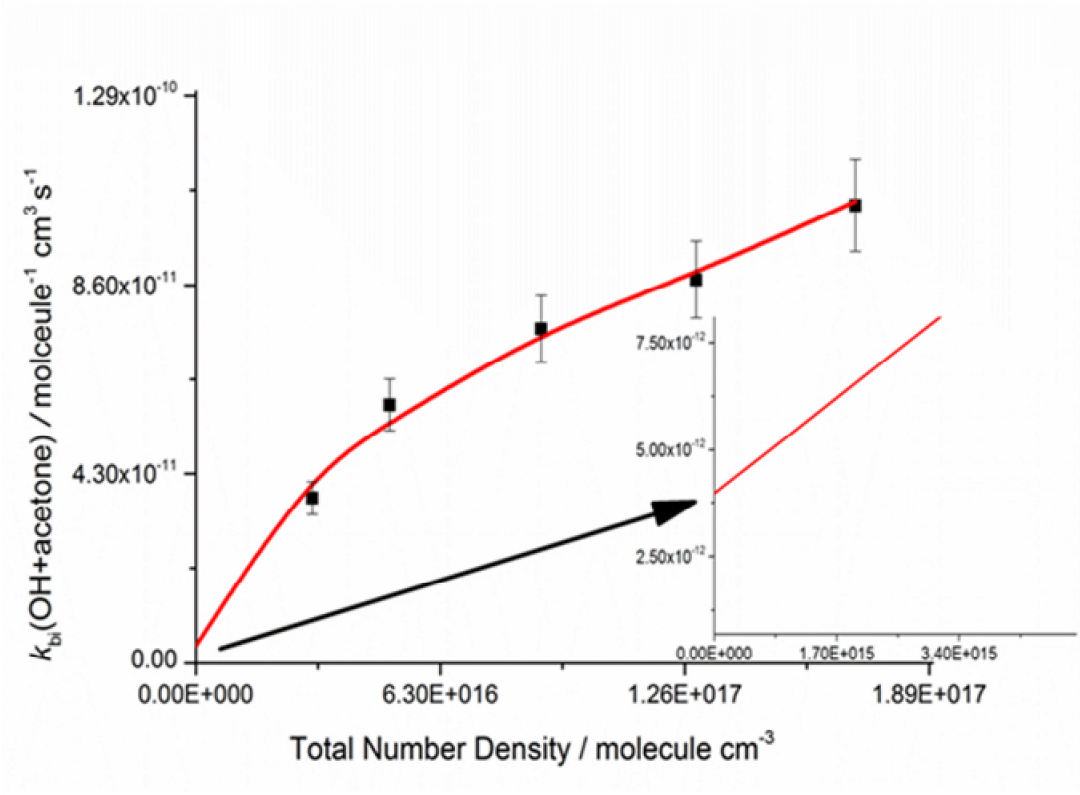

Figure 4.13: Fit of master equation calculations to experimentally determined values of k_{bi}(OH+acetone) at a range of different total gas densities and a temperature of 80 K. Inset shows non zero intercept on this graph which is indicative of tunnelling.

Using the optimum parameters determined fitting routine using model 1, the effect of tunnelling was further considered by comparing master equation calculations with and without a tunnelling correction. From Figure 4.14 it is seen that for the OH + acetone reaction, tunnelling has the largest effect between 200 K and 300 K and quantitative agreement with experiment in this region requires a tunnelling correction to be invoked. This supports the findings of Caralp et al. (17) and it is instructive to look at the time evolution of the populations of both the pre-reaction complex IM1(acetone) and the

post-reaction complex IM2(acetone) at 93 K when tunnelling is considered. These populations are shown in Figure 4.15 and it can be seen that although complex stabilization is the rate determining step, at longer timescales chemical products are being formed in preference to re-dissociation back to reactants

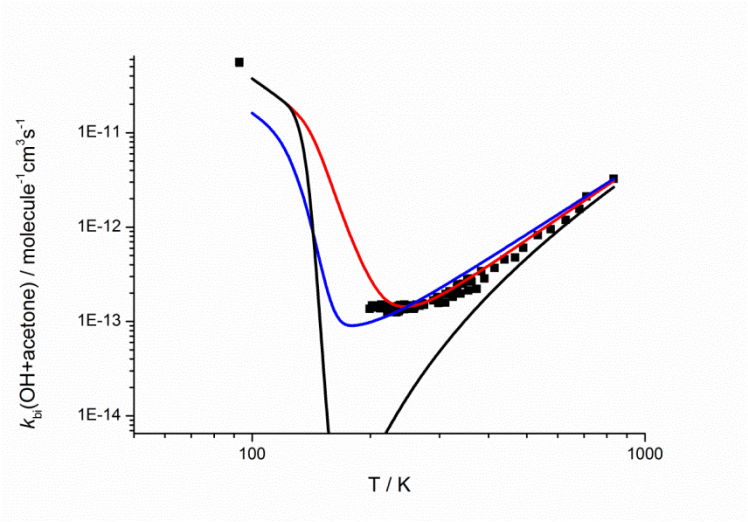

Figure 4.14: Comparison between experimental and master equation rate coefficients for k_{bi}(OH+acetone), versus temperature. The red and blue lines show master equation calculations using model 1 and the WKB model respectively, whilst the black line shows calculated rate coefficients from model 1, without including a tunnelling correction.

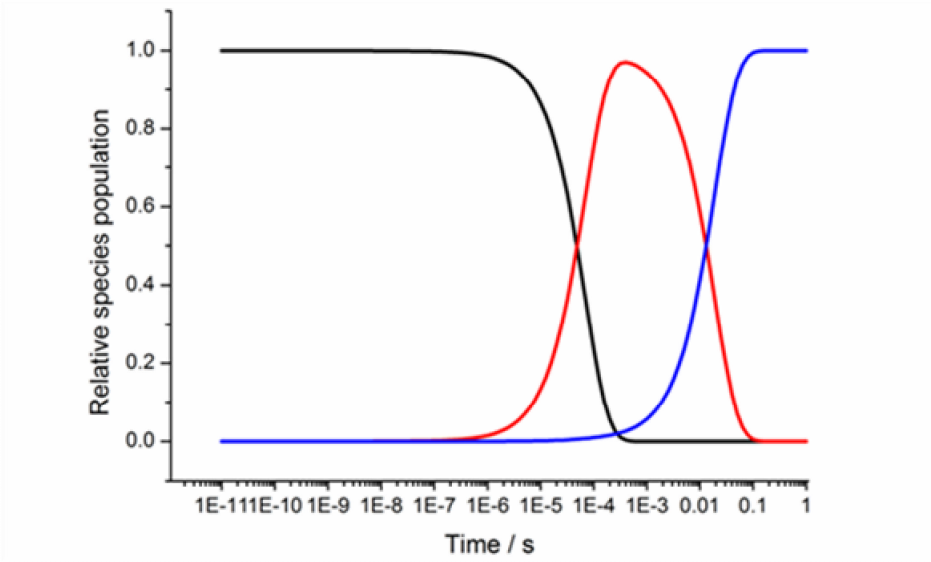

Figure 4.15: Time evolution of the concentrations of OH (black), IM1(acetone) (red) and IM2(acetone) (blue) as calculated by master equation simulations at 80 K and a total gas density of 6×10^{16} molecule cm^{-3}.

In order to explore the possible significance of the OH + acetone reaction in the interstellar medium, it was necessary to extrapolate our master equation simulations to much lower temperatures. Master equations simulations were performed using the parameters from model 1 and transmission coefficients were calculated using the Eckhart method with three different imaginary frequencies and the WKB method with a total gas density of 1×10^{3} molecules cm^{-3} in order to simulate the pressures within the interstellar medium. The simulations were then extrapolated down to 25 K and the results are shown in Figure 4.16 In the limit of zero pressure the master equation simulations predict that a negative temperature dependence to the OH + acetone rate coefficient will still be observed which can be attributed to a direct bimolecular mechanism due to tunnelling. Considering this graph, even if the imaginary frequency of TS1(acetone) is reduced to $1000cm^{-1}$, it can be seen that by 10K, k_{bi}(OH+acetone) has almost reached 10^{-10} molecules^{-1} cm^{3} s^{-1} and these results suggest that even with a 15 kJ mol^{-1} barrier to products, tunneling can lead to low temperature rate coefficients that are approaching the capture limited rate, i.e that rate at which the reacting bimolecular moieties collide.

Interestingly it can be seen that the WKB method predicts much lower rate coefficients than the Eckart methods as seen in Figure 4.16. This is dicussed in greater length in the conclusion section (Section 4.3), however even this method predicts a value for k_{bi}(OH+acetone) at 10 K of 5.2×10^{-11} molecule^{-1} cm^{3} s^{-1}. This is likely to represent a lower limit to the true value of k_{bi}(OH+acetone) at 10 K but even a rate coefficient of 5.2×10^{-11} molecule^{-1} cm^{3} s^{-1} suggests that the OH + acetone reaction may be more important than expected under ISM conditions since currently, this reaction is not present in the kinetic databases used for modelling chemistry in interstellar environments. (36)

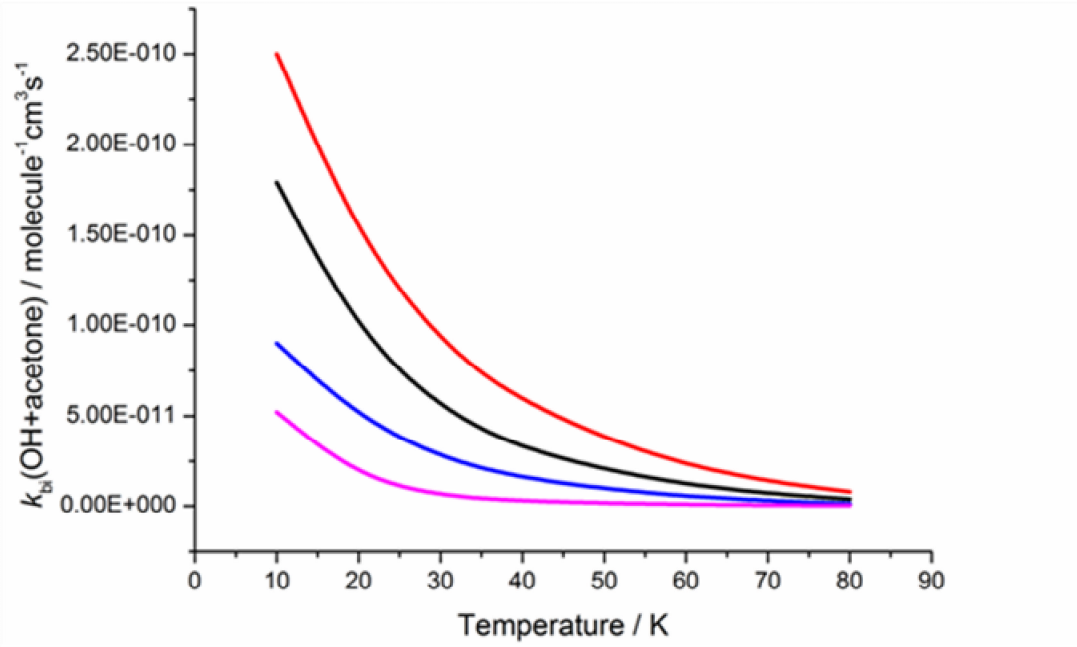

Figure 4.16: Predictions of zero pressure values for k_{bi}(OH+acetone), from MESMER (27) calculations. The red line uses an imaginary frequency of 1200 cm^{-1}, the black uses an imaginary frequency of 1102 cm^{-1}, the blue line uses an imaginary frequency of 1000 cm^{-1} and the purple line uses a WKB method.

4.2. The reaction between OH and DME

4.2.1. Introduction

Unlike the reaction between OH + acetone, the primary motivation for studying the kinetics of the OH + DME reaction has been due to its importance in combustion. Increasingly ethers such as DME are being used as fuel additives (37) and DME has also attracted interest as a potential biofuel. (38, 39) As a consequence of this interest there have been a number of experimental determinations of the rate coefficient for the OH+DME reaction although these studies have been less numerous than in the case of OH + acetone and there are no published rate coefficients below 230K.

The first rate coefficient measurement for the OH + DME reaction was made in 1977 by Perry *et al.* (40) using a flash photolysis – resonance fluorescence method. There have been numerous subsequent studies and the papers of Bonard *et al.* (41) and Arif *et al.* (42) have extended the temperature range to the highest temperatures of 618 and 650 K

respectively. Previous measurements of the OH + DME rate coefficient versus temperature are shown in Figure 4.17 and the agreement between these studies is good.

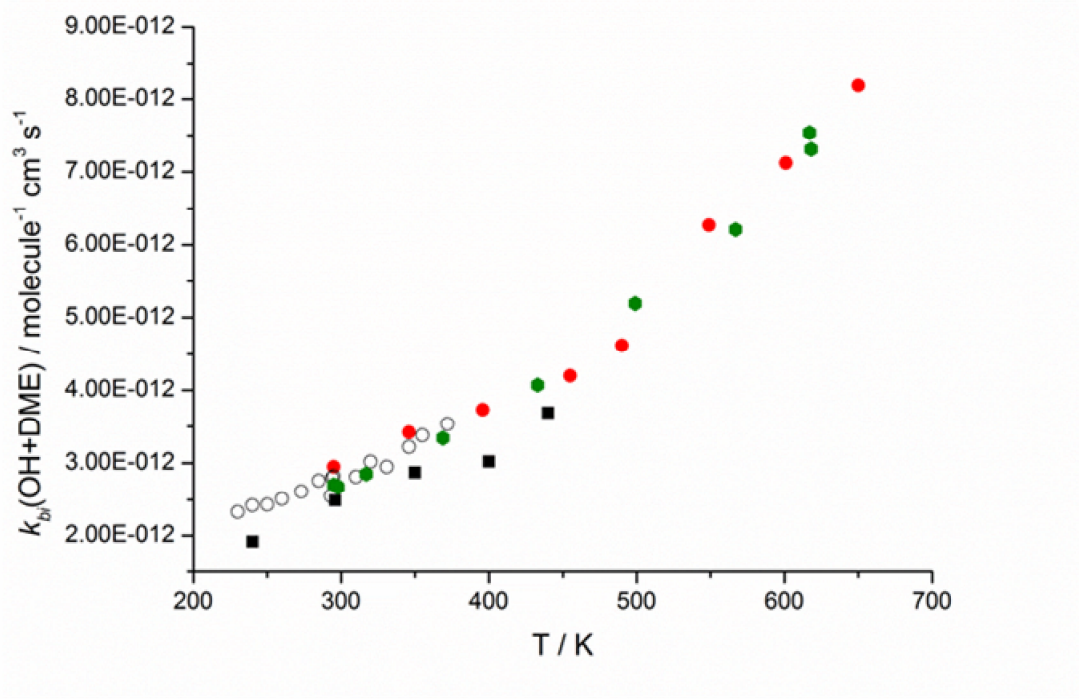

Figure 4.17: Previous measurements of the rate coefficient for the OH + DME reaction, k_{bi}(OH+DME), versus temperature. The green hexagons are from Bonnard *et al.*, (41) the red circles are from Arif *et al., (42)* the open circles are from Melouki *et al.* (43) and the black squares are from Wallington *et al.*. (44)

A potential energy surfaces have also been calculated for the OH + DME reaction by Zhou *et al.* (45) at the MP2/6-311G(d,p)//CCSD(T)/CBS level of theory and a schematic PES from this study is shown in Figure 4.18. From a low temperature perspective, the important feature of this PES is the presence of a hydrogen bonded complex (as in the OH + acetone case) prior to any abstraction transition state and the two complexes vary in their binding energies by at most 3 kJ mol^{-1} depending on level of theory. Given the enhancement in the low temperature rate coefficients of the OH + acetone reaction due to such a complex it may be proposed that the OH + DME reaction might show a similar negative temperature dependence to its rate coefficients at below 200 K. Additionally the lowest abstraction barrier on the OH+DME surface is only 1 kJ mol^{-1}, well below that for acetone and

this could lead to a more pronounced contribution to the low temperature rate coefficients, due to tunnelling.

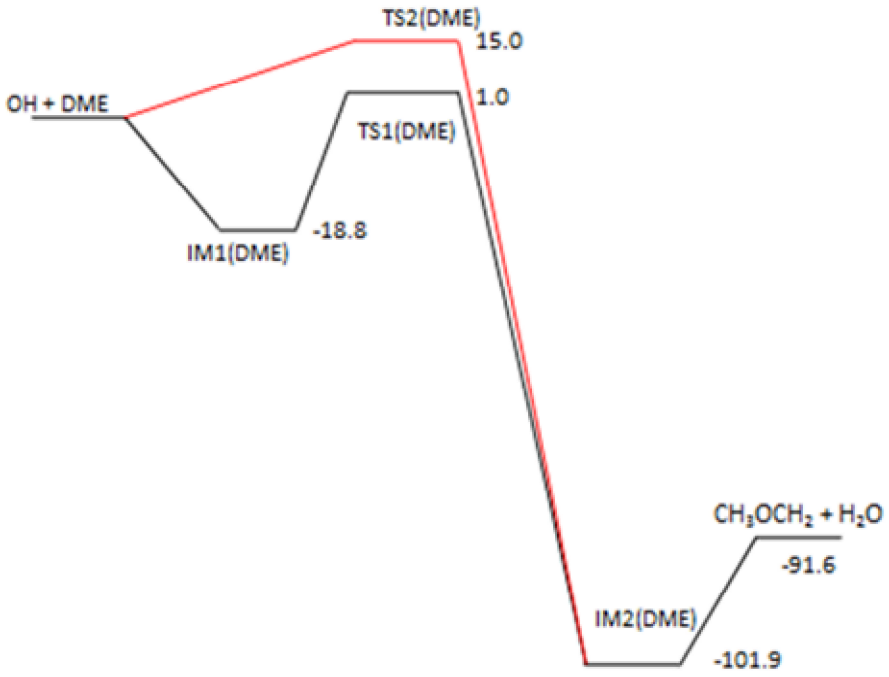

Figure 4.18: Schematic potential energy surface for the OH + DME reaction, calculated at the MP2/6-311G(d,p)//CCSD(T)/CBS level of theory by Zhou *et al.* (45) Relative energies are given in kJ mol^{-1}.

4.2.2. Methods

4.2.2.1. Experimental

The rate coefficients for the OH + DME reaction have been measured at 110, 93 and 63 K using the T110P9E16, T93P6E16 and T63P3E16 nozzles respectively. Rate coefficients have also been measured at total densities of 6×10^{16} molecule cm^{-3} , 9×10^{16} molecule cm^{-3} and 1.7×10^{17} molecule cm^{-3} using the T81Pvar nozzle.

For the OH + DME reaction, OH radicals were produced from the photolysis of t-BuOOH according to reaction R5 below.

$$\text{t-BuOOH} + h\nu \rightarrow \text{OH} + \text{other products} \qquad \text{(R5)}$$

This is the standard method of producing OH radials used throughout this thesis and the advantages of using this precursor are discussed in chapter

3. The reaction mixture then consisted of nitrogen bath gas (BOC, OFN) which was admitted to the system directly from the cylinder, DME (Sigma Aldrich >99%) which admitted to an empty cylinder in a similar way to acetone, and t-BuOOH which was placed in a bubbler through which a small flow of nitrogen was passed. This technique of bubbling nitrogen through a liquid is good way of admitting low vapour pressure species such as t-BuOOH (Sigma Aldrich 70% aqueous) into the reaction chamber. In addition to these three gas flows, oxygen was also added to the reaction chamber for some experiments, and this was used directly from the cylinder. All gas flows were controlled using separate mass flow controllers and these flows were allowed to mix in a 5L ballast reservoir prior to entering the reaction chamber.

The laser systems used were the same as for the OH + acetone reaction. An excimer laser was used to photolyse t-BuOOH at 248nm and the resulting OH radicals were probed using a YAG pumped dye laser system using a rhodamine 6G dye. The OH Q_1(1.5) transition of the A-X(1,0) band, was probed at 282 nm and the resulting fluorescence collected by a PMT.

The time resolved decay of the OH LIF signal was obtained through varying the delay time between photolysis and probe lasers upto a maximum Δt of 300 μs. Each trace consisted of 300 points and each point was generally averaged 20 times. The averaged signal was then normalised for laser power. The normalised traces were then fit with the single exponential decay equation Eq. 5 in order to extract the pseudo first order rate coefficient k'_{DME} :

$$[OH] = [OH]_0 \times \exp(-(k'_{DME} + k_i) \times t) \qquad \text{(Eq.5)}$$

where k_i is the pseudo first order rate coefficient for OH loss due to the sum of diffusion and reaction with the precursor and $[OH]_0$ is the initial population of OH with can be equated with the signal height.

4.2.2.2. Computational

Master equation calculations were performed on the OH + DME system using the MESMER code. The PES used for these calculation was based upon the calculations of Zhou *et al.* (45) As was the case with OH + acetone,

only the lower of the two OH + DME transition states was included, since this channel was expected to be the dominant one at low temperature. Also the infinite sink approximation was used for species IM2(DME) just as it was used for IM2(acetone) and as with the OH + acetone case, using this reduced PES was seen to introduce less than a 1% error to the calculations.

Ro-vibrational densities of states for each stationary point were calculated using the rotational and vibrational frequencies calculate by Zhou *et al.* (45) and these are listed in Table 4.3. All external rotations were treated as rigid rotors and most of the vibrations were treated as harmonic oscillators. However as was observed in the OH + acetone reactions, there were a number of normal modes which were more correctly described as hindered rotations. These modes are indicated in Table 4.3 and the hindered potentials for these modes were calculated at the MPW1K/6-31+G(2d,2p) level of theory using the Gaussian G03 suite of programs (28) with the dihedral angle incremented in steps of 30°. The resulting hindered potentials are shown in appendix 2. It is worth noting that in the case of the OH + DME reaction, only 6 hindered rotations were identified compared to the 10 identified for OH + acetone,

Transmission coefficients for quantum mechanical tunnelling were treated using both the imaginary frequency method of Miller (29) and the semiclassical method. (30) Intrinsic reaction co-ordinate (IRC) calculations were performed at the MPW1K/6-31+G(2d,2p) level of theory and these were scaled to the barrier of TS1. The barrier potential for TS1 from these calculations is shown in Figure 4.19. When using imaginary frequencies, these were fit using the Levenburg Marquardt fitting routine as was the case for OH + acetone.

Species	B / cm^{-1}	ν / cm^{-1}
OH	18.732	3722
DME	1.269 0.333 0.294	204 267 425 980 1147 1183 1220 1232 1288 1486 1500 1511 1515 1525 1548 3017 3026 3080 3085 3183 3184
IM1(DME)	0.318 0.116 0.090	27 66 176 191.5 265 424 484 672 967 1141 1182 1221 1224 1291 1487 1503 1511 1515 1525 1546 3039 3045 3110 3117 3194 3201 3704
TS1(DME)	0.368 0.124 0.103	52 123 210 218 321 357 749 932 1017 1159 1172 1206 1245 1277 1292 1494 1506 1520 1544 1619 3037 3054 3107 3136 3193 800i

Table 4.3: Rotational constants, B, and vibrational frequencies, ν, for the stationary points on the OH + DME potential energy surface employed in the master equation calculations. Frequencies for IM2(DME) are not required since this species is treated as an infinite sink. All frequencies were calculated at the MP2/6-311G(d,p) level of theory by Zhou *et al.* (45) The frequencies highlighted in red were replaced by hindered rotations.

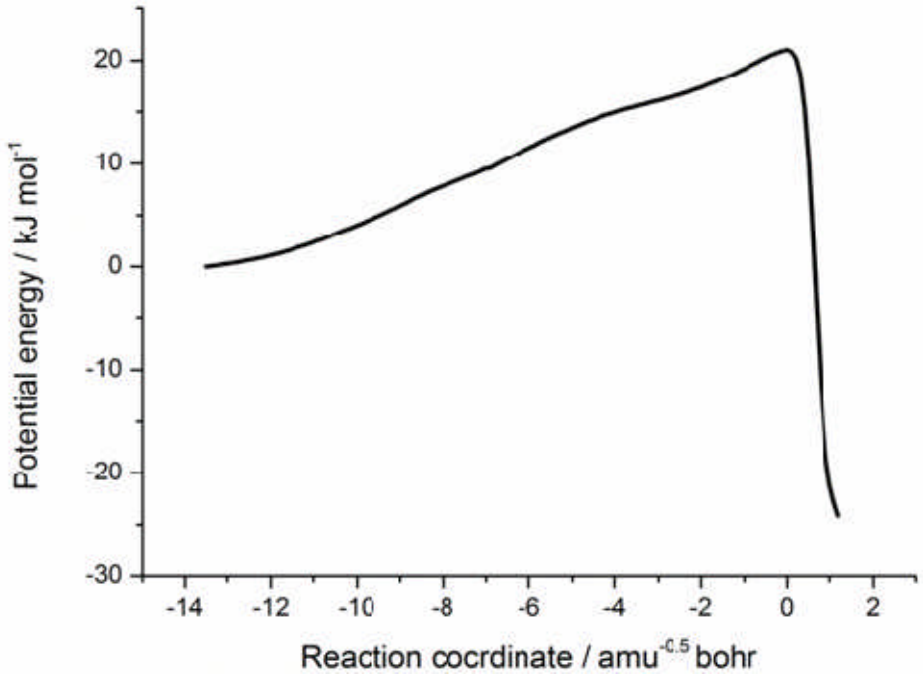

Figure 4.19: Variation in potential energy along the reaction coordinate from IM1(DME) to IM2(DME) via TS1(DME). The *ab initio* calculations were performed using the MPW1K/6-31+G(2d,2p) level of theory and the energy was calculated along the reaction coordinate using a stepsize of 0.1 amu$^{-0.5}$ bohr.

Rate coefficients for the abstraction reaction via TS1 were calculated using RRKM theory and rate coefficients for the barrierless association to form IM1 were calculated using an ILT method. (46) Again the ILT A factor was determined by fitting to the pressured dependent experimental data at 80 K and the ILT n parameter was set to zero. A grain size of 20 cm^{-1} was used for all calculations.

4.2.3. Results

4.2.3.1. Experimental

The first results to be considered concern the temperature dependence of the OH + DME rate coefficients below 200 K. An example, time resolved, OH LIF trace is shown in Figure 4.20 and it can be seen that the experimental data are well described by the exponential decay Eq. 5.

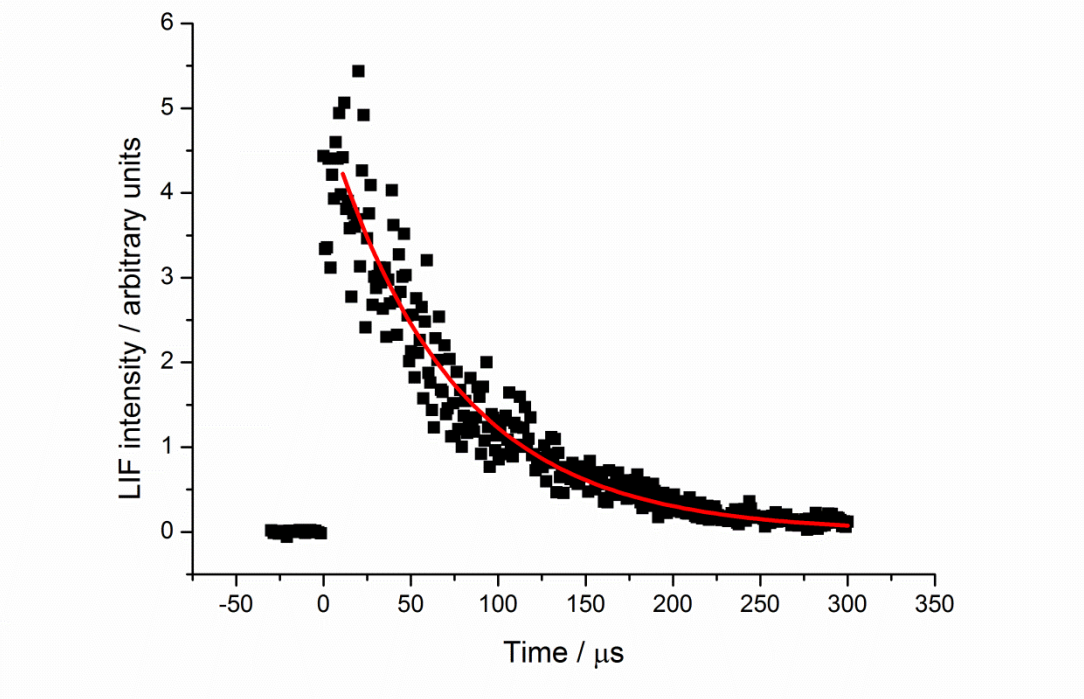

Figure 4.20: Temporal evolution of the LIF signal for OH in the presence of DME. For the current trace [DME] = 2.3×10^{14} molecule cm^{-3}, $[N_2] = 6.3\times10^{16}$ molecule cm^{-3} and [t-BuOOH] ≈ 6×10^{13} and fitting Eq. 5 to the data gives a pseudo first order rate coefficient ($k'_{DME} + k_i$) of 14900 ± 900 s^{-1} This trace consists of a total of 220 points and each point was averaged 10 times. The LIF signal was normalised with respect to the probe laser power on a point-by-point basis.

From these pseudo first order OH decays bimolecular plots were obtained at 110, 93 and 63 K . Unlike acetone, these bimolecular plots displayed good linearity at almost all values of [DME]. At 63 K however, curvature could be observed in the bimolecular plot at value of [DME] > 3×10^{14} and as with acetone this curvature was attributed to clustering of the DME molecules, either with themselves or with the t-BuOOH precursor molecules. Since the clustering effect was only observed at 63 K and high [DME], the linear portion of the bimolecular plots was used to obtain k_{bi}(OH+DME). A typical bimolecular plot is shown in Figure 4.21 and bimolecular rate coefficients, k_{bi}(OH+DME), of $(4.1\pm1.2)\times10^{-12}$ molecule^{-1} cm^3 s^{-1}, $(7.7\pm0.8)\times10^{-12}$ molecule^{-1} cm^3 s^{-1} and $(1.7\pm0.1)\times10^{-11}$ molecule^{-1} cm^3 s^{-1} were obtained at 110 , 93 and 63 K respectively.

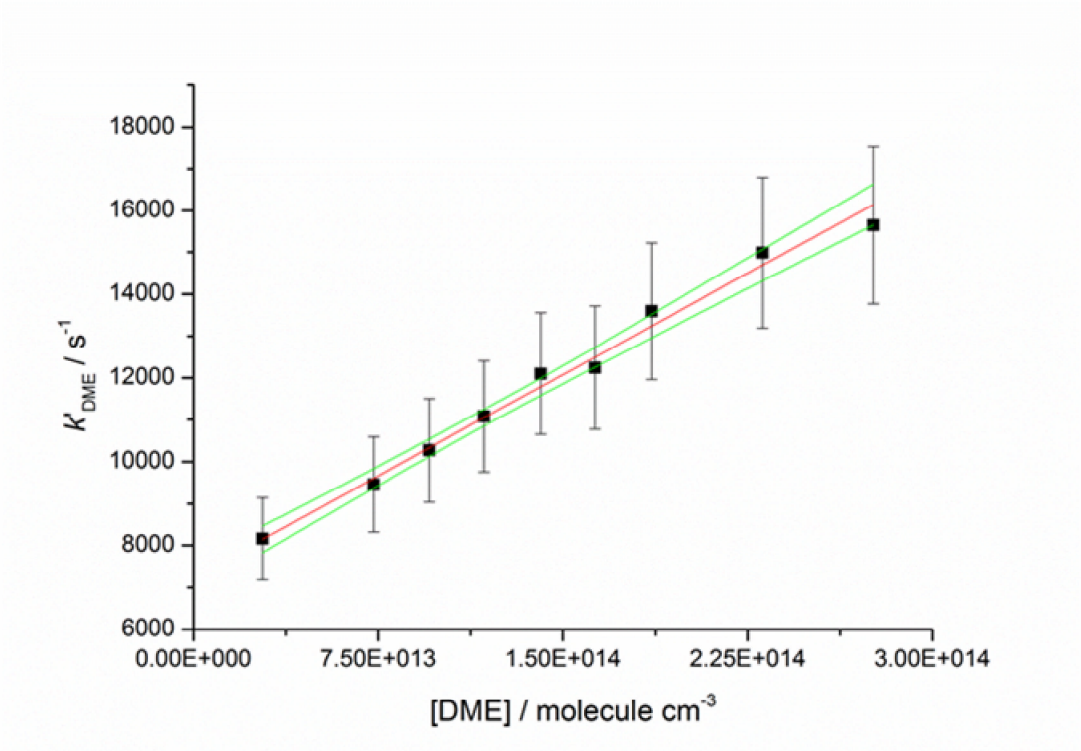

Figure 4.21: Bimolecular plot for the OH + DME reaction at total gas densities of 6.3×10^{16} molecule cm^{-1}. The pseudo first order rate coefficients were obtained from fitting the experimental data with Eq. 5 and they incorporate the 2σ errors both from the fitting process and from [DME]. The bimolecular rate coefficient was obtained from a weighted linear give a value of k_{bi}(OH + DME) = $(7.7\pm0.8)\times10^{-12}$ molecule^{-1} cm^3 s^{-1} with errors obtained from the 95% confidence limits of the linear fit.

The temperature dependence of k_{bi}(OH+DME) is shown in Figure 4.22 and as was observed with OH + acetone, a negative temperature dependence is observed below 200 K. Interestingly however, this negative temperature dependence is much less pronounced than in the OH + acetone case. Part of the reason for this is due to the fact that at in the 200 – 300 K temperature regime, the OH + DME rate coefficients are larger than the OH + acetone rate coefficients by a factor of 20 at room temperature. However it does appear that stabilisation of the OH + DME pre-reaction complex is less facile than for its OH + acetone counterpart.

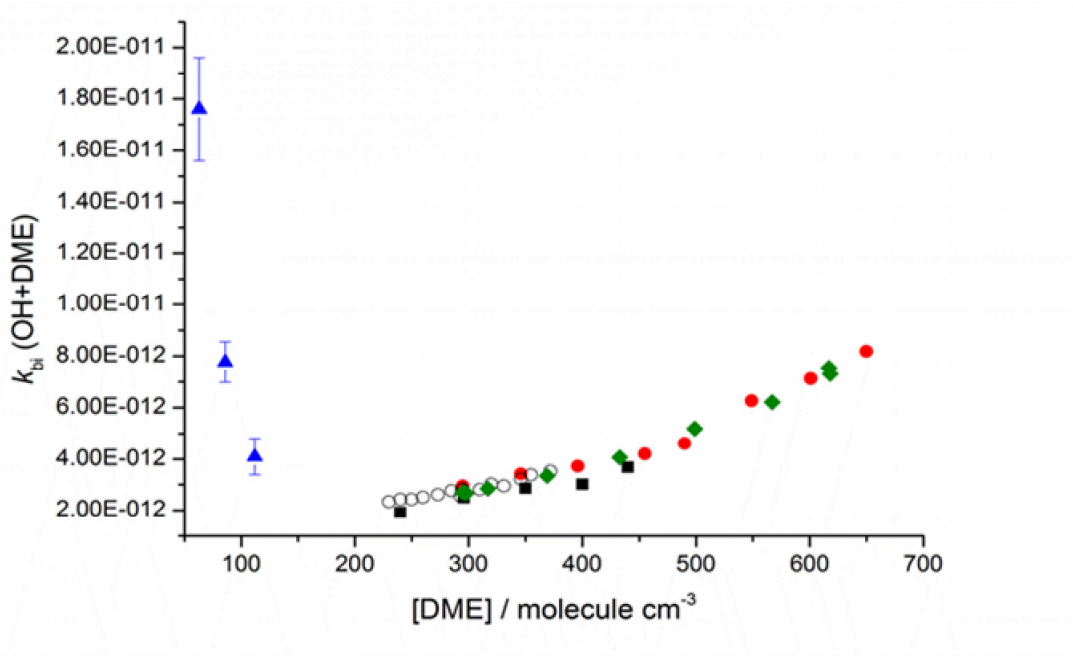

Figure 4.22: Measurements of the rate coefficient for the OH + DME reaction, k_{bi}(OH+DME), versus temperature. The green hexagons are from Bonnard *et al.*, (41) the red circles are from Arif *et al., (42)* the open circles are from Melouki *et al.,* (43) the black squares are from Wallington *et al.* (44) and the blue triangles are taken from the current study.

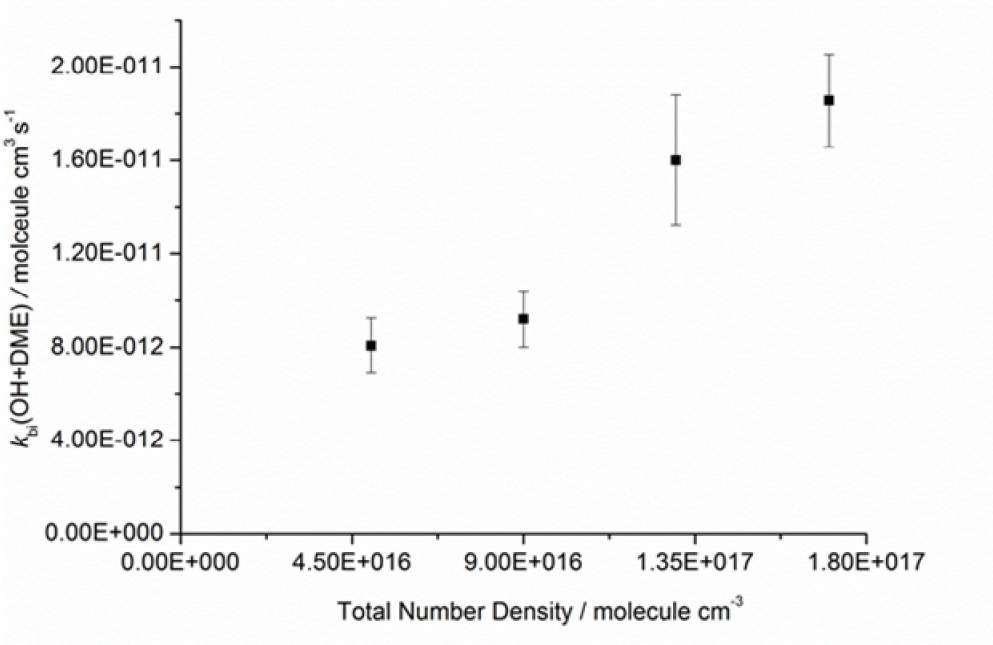

Figure 4.23: Variation in k_{bi}(OH + DME) with total gas density, at an average temperature of 81±4 K.

In order to look further into the possible stabilisation of IM1(DME), bimolecular plots were obtained at total densities of 6.1×10^{16} , 8.9×10^{16} and 1.7×10^{17} molecule cm^{-3} and 80 K. The pressure dependence of k_{bi}(OH + DME) is shown in Figure 4.23 and it can be seen that although a clear pressure dependence can be observed, the stabilisation of IM1(DME) is less pronounced than in the OH +acetone case.

This is the type of behaviour expected considering the density of states arguments which have been discussed in the context of acetone. Although IM1(DME) and IM1(acetone) are bound by a similar energy, IM1(acetone) has one more atom than IM1(DME), and consequently it has 3 more vibrational modes. As the number of atoms in the systems increases, it is generally found that the density of states in the association complex increases relative to the density of states of the separated reactants and from Eq. 4 the rate coefficient for re-dissociation of the complex is therefore decreased.

Although the observation of a pressure dependence suggests that stabilisation is the rate determining step in the OH + DME reaction, the possibility of product formation via tunnelling is worth exploring, particularly due to the very low barrier height of TS1(DME). If hydrogen abstraction were occurring at low temperatures, then one of the products produced would be the methoxymethyl (CH_3OCH_2) radical. This radical then reacts rapidly with O_2 to form the OH radical as a product according to the reaction scheme R6-R7:

$$CH_3OCH_2 + O_2 \leftrightarrows CH_3OCH_2O_2 \qquad \text{(R6)}$$

$$CH_3OCH_2O_2 \rightarrow \text{OH + other products} \qquad \text{(R7)}$$

The reaction between methoxy methyl ($CH_3OCH_2O_2$) and O_2 has been shown to be barrierless and has been shown to display a negative temperature dependence above 200 K. (47) As such it would expected that this reaction will be rapid at low temperatures providing a useful

experimental indicator of product formation in the methoxy methyl formation, from the OH + DME reaction at low temperatures.

Bimolecular plots were obtained for the OH + DME reaction at 63 K and a total gas density of 3×10^{16} molecule cm^3, with and without the addition of 3×10^{15} molecule cm^{-3} oxygen. If methoxy methyl radicals were being created then OH recycling would be expected, and a reduction would then be observed in k_{bi}(OH+DME) upon the addition of oxygen. Figure 4.24 shows these two bimolecular plots, with and without oxygen and when oxygen was present k_{bi}(OH+DME) was reduced to $(8.0\pm0.8)\times10^{-12}$ molecule cm^3 s^{-1} from $(1.7\pm0.1)\times10^{-11}$ molecule cm^3 s^{-1}. This indicates that methoxy methyl radicals are being formed in the OH + DME reaction at low temperatures on the 300 μs timescale, suggesting the influence of tunnelling.

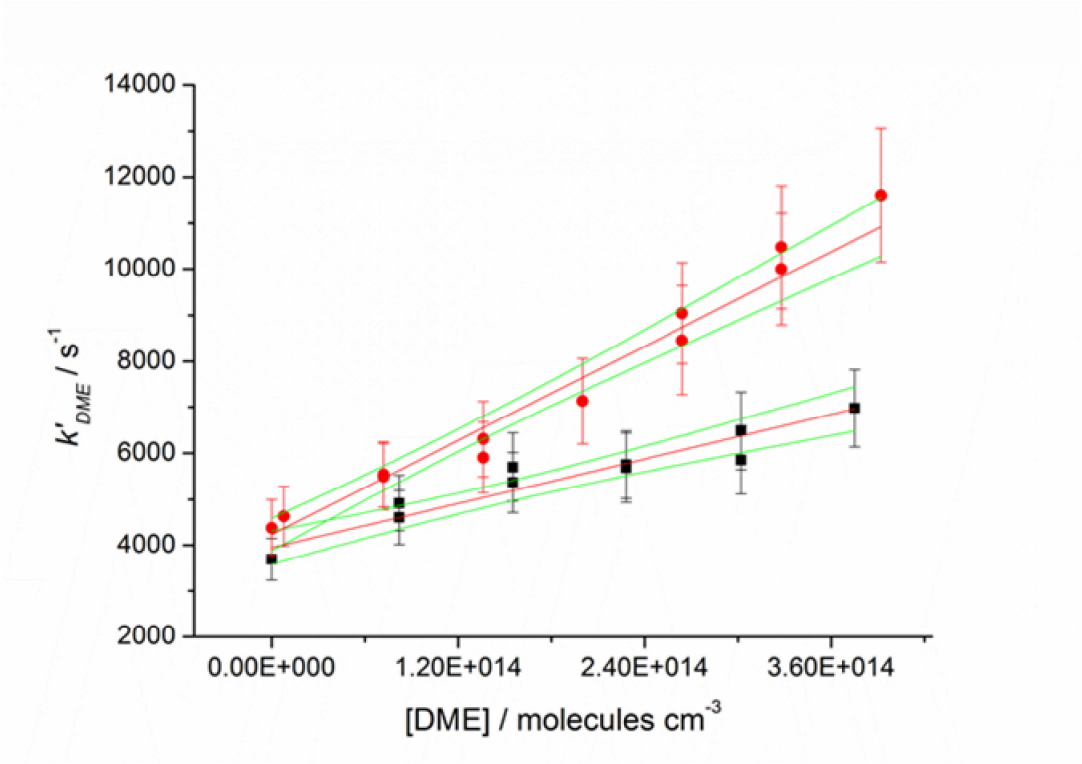

Figure 4.24: Bimolecular plots for the OH + DME reaction, with (black squares) and without (red circles) the addition of 3×10^{15} molecule cm^{-3} oxygen. These plots yield bimolecular rate coefficients, k_{bi}(OH+DME) of $(8.0\pm0.8)\times10^{-12}$ molecule cm^3 s^{-1} and $(1.7\pm0.1)\times10^{-11}$ molecule cm^3 s^{-1} respectively.

4.2.3.2. Master equation calculations

As described in section 4.2.2.2, master equation calculations have also been performed upon the OH + DME reaction, in order to compliment the experiments. As for the OH + acetone system the OH + DME PES was optimised using a Levenburg Marquardt fitting routine. Table 4.4 shows the results from these calculations in which all energies and imaginary frequencies were allowed to vary. When carrying out this fitting procedure, all k_{bi}(OH+DME) obtained in the current work were fit too, including a number of higher temperature measurements to give a total of 10 experimental data points.

Parameter	Harmonic	Hindered	Ab initio values from Zhou (45)
TS1 / kJ mol^{-1}	0.8	2.3	1.0
IM1 / kJ mol^{-1}	-27.1	-26	-18.5
Imaginary Frequency / cm^{-1}	231	464	800
χ^2 per point	32	19	-

Table 4.4: Optimised parameters from fitting the experimental data using a Levenburg Marquardt algorithm implemented within the master equation code MESMER. (48)

Considering these fitted parameters, the effect of hindered rotation, which was so apparent in the case of OH + acetone is less important. As was observed in the case of acetone, including hindered rotation seems to raise the fitted value for the energy of TS1, but in the case of TS1(DME) this change is only 1.5 kJ mol^{-1} compared to the 10 kJ mol^{-1} change in the case of TS1 acetone. It is also found that treating hindered rotations has little effect of the well depth of IM1(DME) and this is likely due to the fact only the two CH_3 rotations which are present in IM1(DME) and these are little changed from their counterparts in DME itself.

A comparison between theoretical and experimental rate coefficients is shown versus temperature and pressure in Figure 4.25 and Figure 4.26 respectively and both cases it can be seen that agreement between the

fitted, hindered rotation, MESMER values and experiment, is good. Also shown in Figure 4.25 are the MESMER rate coefficients from using the *ab initio* parameters of Zhou and the WKB tunnelling method. Here it can be seen that agreement is less good, although theory and experiment do agree to within a factor of 3 at all temperatures.

Much of the disagreement between experiment and theory in the WKB case can be taken up by small adjustments in the energies of IM1 and TS1 as can be observed from the fitting results, although as in the case with acetone, it appears the WKB method underestimates the amount of tunnelling required to fit the experimental data. This is emphasised by considering the rate coefficients k_{bi}(OH+DME), calculated at 10 K and a total gas density of 10^3 molecule cm^{-3}. With the Eckart method of calculating tunnelling, the rate coefficient at 10 K is determined to be 2.0×10^{-10} molecule^{-1} cm^3 s^{-1} whilst using the WKB method the corresponding rate coefficient is determined to be 9×10^{-11} molecule^{-1} cm^3 s^{-1}. However despite the discrepancy between the two methods in both cases the calculated rate coefficient can be seen to be approaching the capture limit.

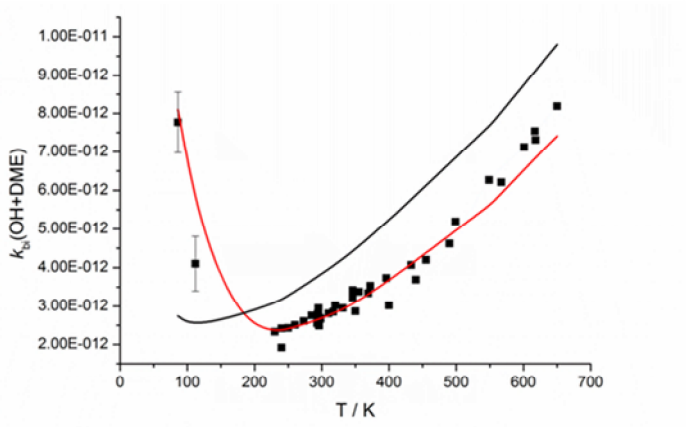

Figure 4.25: Comparison between experimental, and theoretical rate coefficients, k_{bi}(OH+DME), versus temperature. Experimental measurements (black squares) above 200 K are taken from the literature. (41-44) The two lines show theoretical values for k_{bi}(OH+DME) from master equation calculations at a total gas density of 6×10^{16} molecule cm^{-3}. The red line corresponds to calculations using the fitted parameters and whilst the black line corresponds to calculations using the WKB approach and the *ab initio* parameters of Zhou *et al.* (45)

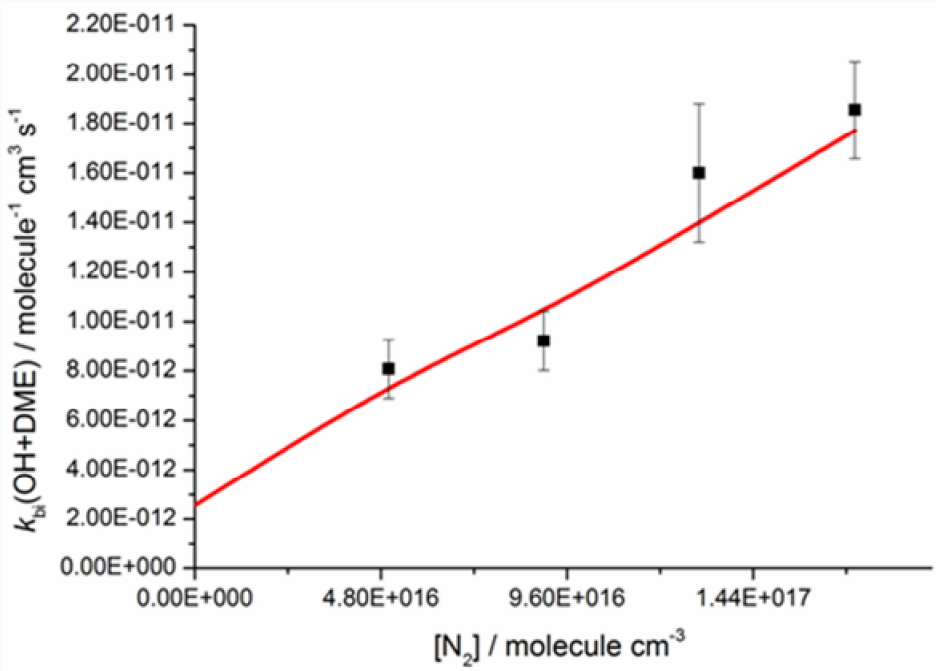

Figure 4.26: Comparison between theoretical and experimental values for k_{bi}(OH+DME) versus total gas density. The theoretical rate coefficients are calculated using MESMER (48) with the fitted parameters and the Eckart tunnelling method.

4.3. Conclusions

In this investigation we have shown that reactions between OH and oxygenated VOC's exhibit large low temperature rate coefficients despite the presence of an overall barrier to products. This behaviour appears generic to this class of reaction and we have shown that the presence of a small 20 kJ mol^{-1} van der Waals well is sufficient to form a complex with an enhanced lifetime which can facilitate either quantum mechanical tunnelling or stabilization at low temperatures. It has also been shown in the case of OH + DME that due to the tunnelling in this type of hydrogen transfer reaction, these reactions can proceed to chemical products rather than the formation of only a stabilized complex and predictions from our modelling studies indicate that these reactions could exhibit zero pressure, bimolecular rate coefficients that are competitive in cold planetary atmospheres and the ISM.

The first thing to note about the OH + oxygenate reactions is the similarity of their kinetic behaviour. The rate coefficients for the reactions between OH and acetone and DME both display the same general shape to the

temperature dependencies of their rate coefficients. At high temperatures above 300 K these systems all exhibit Arrhenius type behaviour consistent with reaction proceeding over an energy barrier but between 300 K and 200 K significant deviations from an Arrhenius extrapolation are observed and the rate coefficients show the beginning of a negative temperature dependence in some cases. Finally, at the lowest temperatures it is shown that in both systems, there is a substantial increase in the rate coefficients compared to the room temperature values.

In order to explain the role of such a complex at low temperatures a two transition state model of the type developed by Greenwald et al. can be used to help rationalize this enhancement to the rate coefficients at low temperatures. This model is mentioned in chapter 2 and although it was originally designed to explain the kinetic behaviour of reactions with a submerged barrier, it is equally applicable to the OH + oxygenate systems studied here.

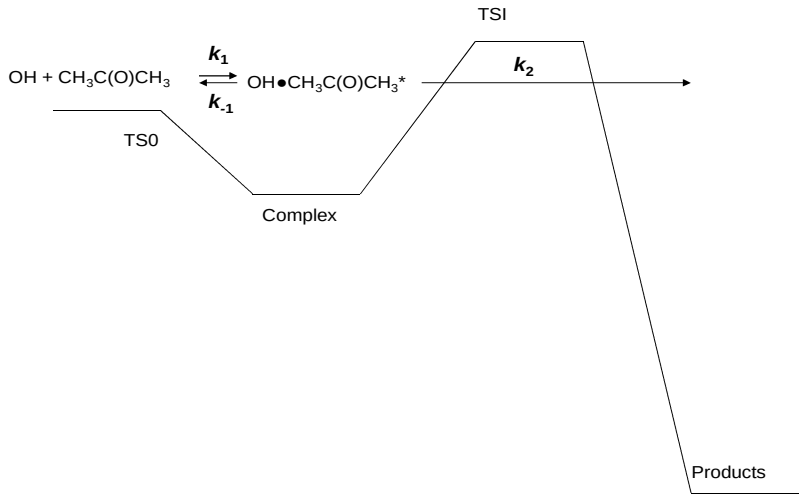

Figure 4.27: Schematic potential energy surface for the OH + acetone reaction demonstrating the two transition state model.

Using this two transition state model we can obtain simple expressions describing the high and low temperature limiting behaviour of system. In the

limit of low temperature, k_{-1} becomes negligible compared to k_1 and the complex exhibits a significant lifetime. Under these conditions the dominant bottleneck to reaction is TSO, the outer transition state, and the observed rate coefficient, k_{obs} is equal to k_1. Conversely in the limit of high temperature the complex rapidly equilibrates and the rate determining step involves crossing the barrier TS1. The observed rate coefficient then reduces to the equilibrium fraction of the complex multiplied by k_2. It should be noted that these expressions describe limiting behaviour only and at intermediate temperatures there will be contributions to the rate coefficient from both TSO and TS1 and rate coefficients may show some dependence upon total pressure [M]. However using these arguments the large increase in the observed rate constant below 200 K can be understood in terms of the controlling transition-state moving from TS1 ($k_{obs} = k_1k_2/k_{-1}$) to TSO, $k_{obs} = k_1$.

This mechanism suggests that at low temperatures these reactions form only a stabilized complex rather than chemical products. However, when reactions involve the transfer of light atoms as is the case here, quantum mechanical tunnelling often becomes important. If tunnelling is considered then k_2 becomes non-negligible, even in energy regimes where classically the forward rate coefficient should be zero. When we consider this in the two transition state model the increased lifetime of the van der Waals complex facilitates product formation via tunnelling.

Under the current experimental conditions it appears the low temperature rate coefficients in the OH + acetone and OH+ DME are dominated by stabilization of the pre reactive complex. The experimental observation of low temperature pressure dependence to the rate coefficients for both of these reactions complemented by the accompanying master equation calculations, shows that despite the weak binding energies of these complexes (5 kcal mol^{-1}) and low total densities at which our experiments were performed at (5×10^{16} molecule cm^{-3}) , it is still found that collisional stabilization of the energized complex occurs readily on our experimental timescale (300 μs).

Concerning the theoretical treatment of stabilisation into such weak wells, it is worthwhile to mention the importance of hindered rotation. The

deficiencies of the harmonic oscillator approximation have long been known but with the very weakly bound hydrogen bonded complexes encountered here, the accurate determination of the molecular density of states is particularly important. It is certainly true that there is a significant amount of uncertainty associating a particular frequency with a vibrational normal mode but the results of the master equation fitting routines show that the more anharmonicty that is introduced the more closely the fitted well depth matches the *ab initio* value. In the current work, even with a full hindered rotor treatment, the fitted well depths are lower than the ab initio values. However more sophisticated treatments of anharmonicty in non-rotor modes have been shown to increase molecular densities of states by up to a factor of four (50) and explicitly treating the coupling between hindered rotors, would also be likely to increase the density of states.

Although it is established that tunnelling is not the rate determining step in the OH acetone or OH + DME reactions, there is evidence to suggest that it still plays a large role in these systems. Indirect observation of products from the OH + DME reaction has been reported and master equation calculations suggest that tunnelling is required in order to model both of these systems successfully. If tunnelling is considered to any extent, our master equation calculations then predict that following stabilization of the complex, product formation occurs on a longer timescale. Furthermore if the zero pressure rate coefficients for OH + acetone calculated using MESMER are extrapolated down to 10K, the rate coefficients due to tunnelling alone can be seen to be approaching the order of 1×10^{-10} molecule cm^3 s^{-1} even when the imaginary frequency of TS1(acetone) is reduced. The master equation calculations for OH + DME predict a zero pressure rate coefficient at 10K of 2.0×10^{-10} $molecule^{-1}$ cm^3 s^{-1} and both these results suggest that under interstellar conditions the OH + acetone and OH + DME reactions could be rapid enough to be important.

Considering the implication of such efficient tunnelling for the ISM, it is worth making a final comment of the two treatments of tunnelling used in the current study. For a given barrier height, the crucial parameter in determining transmission coefficients for tunnelling is the shape of the potential barrier through which the tunnelling occurs. In the tunnelling

method of Miller, the shape of this potential is approximated using the imaginary frequency of the transition state, however in the WKB method, points along the reaction path have been calculated directly using intrinsic reaction coordinate (IRC) calculations.

As discussed in chapter 2, the imaginary frequency of a transition state can be very sensitive to the level of theory used, and in the current work the pragmatic approach of fitting the imaginary frequency has been used, since in the current cases, transmission coefficients are well defined by the available experimental data. However when using the more WKB method, with the directly calculated barrier shape, it has been found for both OH + acetone, and OH + DME, that the tunnelling transmission coefficients under predict the experimental data.

Despite the fact that the WKB method appears to underestimate the available experimental data, this method is likely to be a more reliable representation of one dimensional tunnelling than the Eckart method. However more sophisticated tunnelling treatments, consider tunnelling not only along the reaction co-ordinate, (one dimensional) but also along orthogonal co-ordinates and it has been shown that this can substantially increase tunnelling transmission coefficients.(50) Considering this the WKB method could be underestimating the true transmission coefficients whilst the pragmatic approach of fitting the imaginary frequency could take up any error due to using a one dimensional tunnelling approach.

4.4. References

1. SINGH, H.B., M. KANAKIDOU, P.J. CRUTZEN and D.J. JACOB. High-Concentrations and Photochemical Fate of Oxygenated Hydrocarbons in the Global Troposphere. *Nature*, 1995, **378**(6552), pp.50-54.
2. SINGH, H.B., D. OHARA, D. HERLTH, W. SACHSE, D.R. BLAKE, J.D. BRADSHAW, M. KANAKIDOU and P.J. CRUTZEN. Acetone in the Atmosphere - Distribution, Sources, and Sinks. *Journal of Geophysical Research-Atmospheres*, 1994, **99**(D1), pp.1805-1819.
3. VASUDEVAN, V., D.F. DAVIDSON and R.K. HANSON. High-temperature measurements of the reactions of OH with toluene

and acetone. *Journal of Physical Chemistry A*, 2005, **109**(15), pp.3352-3359.

4. SNYDER, L.E., F.J. LOVAS, D.M. MEHRINGER, N.Y. MIAO, Y.J. KUAN, J.M. HOLLIS and P.R. JEWELL. Confirmation of interstellar acetone. *Astrophysical Journal*, 2002, **578**(1), pp.245-255.
5. FRIEDEL, D.N., L.E. SNYDER, A.J. REMIJAN and B.E. TURNER. Detection of interstellar acetone toward the Orion-KL hot core. *Astrophysical Journal*, 2005, **632**(2), pp.L95-L98.
6. T. YAMADA, P. H. TAYLOR, A. GOUMRI and P. MARSHALL. The reaction of OH with acetone and acetone-d_6 from 298 to 832 K: Rate coefficients and mechanism. *J. Chem. Phys.*, 2003, **119**(20), pp.10600 - 10606.
7. TAYLOR, S.E. *Reaction Kinetics at Very Low Temperatures Measured Using a Pulsed Laval Nozzle System*. thesis, University of Leeds, 2008.
8. GIERCZAK, T., M.K. GILLES, S. BAUERLE and A.R. RAVISHANKARA. Reaction of hydroxyl radical with acetone. 1. Kinetics of the reactions of OH, OD, and (OH)-O-18 with acetone and acetone-d(6). *Journal of Physical Chemistry A*, 2003, **107**(25), pp.5014-5020.
9. WOLLENHAUPT, M., S.A. CARL, A. HOROWITZ and J.N. CROWLEY. Rate coefficients for reaction of OH with acetone between 202 and 395 K. *Journal of Physical Chemistry A*, 2000, **104**(12), pp.2695-2705.
10. YAMADA, T., P.H. TAYLOR, A. GOUMRI and P. MARSHALL. The reaction of OH with acetone and acetone-d(6) from 298 to 832 K: Rate coefficients and mechanism. *Journal of Chemical Physics*, 2003, **119**(20), pp.10600-10606.
11. BOTT, J.F. and N. COHEN. A Shock-Tube Study of the Reactions of the Hydroxyl Radical with Several Combustion Species. *International Journal of Chemical Kinetics*, 1991, **23**(12), pp.1075-1094.
12. COX, R.A., R.G. DERWENT and M.R. WILLIAMS. Atmospheric Photo-Oxidation Reactions - Rates, Reactivity, and Mechanism for Reaction of Organic-Compounds with Hydroxyl Radicals. *Environmental Science & Technology*, 1980, **14**(1), pp.57-61.
13. WOLLENHAUPT, M. and J.N. CROWLEY. Kinetic studies of the reactions CH3+NO2 -> products, CH3O+NO2 -> products, and OH+CH3C(O)CH3 -> CH3C(O)OH+CH3, over a range of temperature and pressure. *Journal of Physical Chemistry A*, 2000, **104**(27), pp.6429-6438.
14. TURPIN, E., C. FITTSCHEN, A. TOMAS and P. DEVOLDER. Reaction of OH radicals with acetone: Determination of the branching ratio for the abstraction pathway at 298 K and 1 Torr. *Journal of Atmospheric Chemistry*, 2003, **46**(1), pp.1-13.

15. TYNDALL, G.R.S., J.J. ORLANDO, T.J. WALLINGTON, M.D. HURLEY, M. GOTO and M. KAWASAKI. Mechanism of the reaction of OH radicals with acetone and acetaldehyde at 251 and 296 K. *Physical Chemistry Chemical Physics*, 2002, **4**(11), pp.2189-2193.
16. VANDENBERK, S., L. VEREECKEN and J. PEETERS. The acetic acid forming channel in the acetone plus OH reaction: A combined experimental and theoretical investigation. *Physical Chemistry Chemical Physics*, 2002, **4**(3), pp.461-466.
17. CARALP, F., W. FORST, E. HENON, A. BERGEAT and F. BOHR. Tunneling in the reaction of acetone with OH. *Physical Chemistry Chemical Physics*, 2006, **8**(9), pp.1072-1078.
18. HENON, E., S. CANNEAUX, F. BOHR and S. DOBE. Features of the potential energy surface for the reaction of OH radical with acetone. *Physical Chemistry Chemical Physics*, 2003, **5**(2), pp.333-341.
19. WALLINGTON, T.J. and M.J. KURYLO. The Gas-Phase Reactions of Hydroxyl Radicals with a Series of Aliphatic-Alcohols over the Temperature-Range 240-440-K. *International Journal of Chemical Kinetics*, 1987, **19**(11), pp.1015-1023.
20. T. GIERCZAK, M. K. GILLES, S. BAUERLE and A. R. RAVISHANKARA. Reaction of the hydroxyl radical with acetone. 1. Kinetics of the reactions of OH, OD, and ^{18}OH with acetone and acetone-d_6. *J. Phys. Chem. A*, 2003, **107**(25), pp.5014 - 5020.
21. M. A. BLITZ, D. E. HEARD and M. J. PILLING. Study of acetone photodissociation over the wavelength range 248 - 330 nm: Evidence of a mechanism involving both the singlet and triplet excited states. *J. Phys. Chem. A*, 2006, **110**(21), pp.6742 - 6756.
22. G. S. TYNDALL, J. J. ORLANDO, T. J. WALLINGTON and M. D. HURLEY. Pressure dependence of the rate coefficients and product yields for the reaction of CH_3CO radicals with O_2. *Int. J. Chem. Kinetics*, 1997, **29**(9), pp.655 - 663.
23. H. HOU, A. LI, H. HU, Y. LI, H. LI and B. WANG. Mechanistic and kinetic study of the $CH_3CO + O_2$ reaction. *J. Chem. Phys.*, 2005, **122**, pp.224304-1 - 224304-11.
24. M. A. BLITZ, D. E. HEARD and M. J. PILLING. OH formation from $CH_3CO + O_2$: a convenient experimental marker for the acetyl radical. *Chem. Phys. Lett.*, 2002, **365**, pp.374 - 379.
25. GIERCZAK, T., J.B. BURKHOLDER, S. BAUERLE and A.R. RAVISHANKARA. Photochemistry of acetone under tropospheric conditions. *Chemical Physics*, 1998, **231**(2-3), pp.229-244.
26. BAASANDORJ, M., D.K. PAPANASTASIOU, R.K. TALUKDAR, A.S. HASSON and J.B. BURKHOLDER. (CH(3))(3)COOH (tert-butyl hydroperoxide): OH reaction rate coefficients between 206

and 375 K and the OH photolysis quantum yield at 248 nm. *Physical Chemistry Chemical Physics*, 2010, **12**(38), pp.12101-12111.

27. ROBERTSON, S.H., GLOWACKI, D. R., LIANG, C.-H.; MORLEY, C., PILLING, M. J.,. MESMER. *(Master Equation Solver for Multi-Energy Well Reactions), 2008; an object oriented C++ program for carrying out ME calculations and eigenvalue-eigenvector analysis on arbitrary multiple well systems.* http://sourceforge.net/projects/mesmer.
28. Gaussian. Gaussian 03, Revision C.02, M. J. Frisch, G. W. Trucks, H. B. Schlegel, G. E. Scuseria, M. A. Robb, J. R. Cheeseman, J. A. Montgomery, Jr., T. Vreven, K. N. Kudin, J. C. Burant, J. M. Millam, S. S. Iyengar, J. Tomasi, V. Barone, B. Mennucci, M. Cossi, G. Scalmani, N. Rega, G. A. Petersson, H. Nakatsuji, M. Hada, M. Ehara, K. Toyota, R. Fukuda, J. Hasegawa, M. Ishida, T. Nakajima, Y. Honda, O. Kitao, H. Nakai, M. Klene, X. Li, J. E. Knox, H. P. Hratchian, J. B. Cross, V. Bakken, C. Adamo, J. Jaramillo, R. Gomperts, R. E. Stratmann, O. Yazyev, A. J. Austin, R. Cammi, C. Pomelli, J. W. Ochterski, P. Y. Ayala, K. Morokuma, G. A. Voth, P. Salvador, J. J. Dannenberg, V. G. Zakrzewski, S. Dapprich, A. D. Daniels, M. C. Strain, O. Farkas, D. K. Malick, A. D. Rabuck, K. Raghavachari, J. B. Foresman, J. V. Ortiz, Q. Cui, A. G. Baboul, S. Clifford, J. Cioslowski, B. B. Stefanov, G. Liu, A. Liashenko, P. Piskorz, I. Komaromi, R. L. Martin, D. J. Fox, T. Keith, M. A. Al-Laham, C. Y. Peng, A. Nanayakkara, M. Challacombe, P. M. W. Gill, B. Johnson, W. Chen, M. W. Wong, C. Gonzalez, and J. A. Pople, Gaussian, Inc., Wallingford CT, 2004.
29. MILLER, W.H. Tunneling Corrections to Unimolecular Rate Constants, with Application to Formaldehyde. *Journal of the American Chemical Society*, 1979, **101**(23), pp.6810-6814.
30. GARRETT, B.C. and D.G. TRUHLAR. Semi-Classical Tunneling Calculations. *Journal of Physical Chemistry*, 1979, **83**(22), pp.2921-2926.
31. ROBERTSON, S.H., M.J. PILLING, D.L. BAULCH and N.J.B. GREEN. Fitting of Pressure-Dependent Kinetic Rate Data by Master Equation Inverse Laplace Transform Analysis. *Journal of Physical Chemistry*, 1995, **99**(36), pp.13452-13460.
32. BAER, T. and W.L. HASE. *Unimolecular reaction dynamics: theory and experiments.* New York: Oxford University Press, 1996.
33. BARKER, J.R., L.M. YODER and K.D. KING. Vibrational energy transfer modeling of nonequilibrium polyatomic reaction systems. *Journal of Physical Chemistry A*, 2001, **105**(5), pp.796-809.
34. JASPER, A.W. and J.A. MILLER. Collisional Energy Transfer in Unimolecular Reactions: Direct Classical Trajectories for CH4

reversible arrow CH3 + H in Helium. *Journal of Physical Chemistry A*, 2009, **113**(19), pp.5612-5619.

35. PILLING, M.J. and S.H. ROBERTSON. Master equation models for chemical reactions of importance in combustion. *Annual Review of Physical Chemistry*, 2003, **54**, pp.245-275.
36. WOODALL, J., M. AGUNDEZ, A.J. MARKWICK-KEMPER and T.J. MILLAR. The UMIST database for astrochemistry 2006. *Astronomy & Astrophysics*, 2007, **466**(3), pp.1197-U203.
37. JIANG, T., C.J. LIU, M.F. RAO, C.D. YAO and G.L. FAN. A novel synthesis of diesel fuel additives from dimethyl ether using dielectric barrier discharges. *Fuel Processing Technology*, 2001, **73**(2), pp.143-152.
38. LUQUE, R., L. HERRERO-DAVILA, J.M. CAMPELO, J.H. CLARK, J.M. HIDALGO, D. LUNA, J.M. MARINAS and A.A. ROMERO. Biofuels: a technological perspective. *Energy & Environmental Science*, 2008, **1**(5), pp.542-564.
39. ARCOUMANIS, C., C. BAE, R. CROOKES and E. KINOSHITA. The potential of di-methyl ether (DME) as an alternative fuel for compression-ignition engines: A review. *Fuel*, 2008, **87**(7), pp.1014-1030.
40. PERRY, R.A., R. ATKINSON and J.N. PITTS. Rate Constants for Reaction of Oh Radicals with Dimethyl Ether and Vinyl Methyl-Ether over Temperature-Range 299 Degreesk 427 Degreesk. *Journal of Chemical Physics*, 1977, **67**(2), pp.611-614.
41. BONARD, A., V. DAELE, J.L. DELFAU and C. VOVELLE. Kinetics of OH radical reactions with methane in the temperature range 295-660 K and with dimethyl ether and methyl-tert-butyl ether in the temperature range 295-618 K. *Journal of Physical Chemistry A*, 2002, **106**(17), pp.4384-4389.
42. ARIF, M., B. DELLINGER and P.H. TAYLOR. Rate coefficients of hydroxyl radical reaction with dimethyl ether and methyl tert-butyl ether over an extended temperature range. *Journal of Physical Chemistry A*, 1997, **101**(13), pp.2436-2441.
43. MELLOUKI, A., S. TETON and G. LEBRAS. Kinetics of OH Radical Reactions with a Series of Ethers. *International Journal of Chemical Kinetics*, 1995, **27**(8), pp.791-805.
44. WALLINGTON, T.J. and M.J. KURYLO. Flash-Photolysis Resonance Fluorescence Investigation of the Gas-Phase Reactions of Oh Radicals with a Series of Aliphatic-Ketones over the Temperature-Range 240-440-K. *Journal of Physical Chemistry*, 1987, **91**(19), pp.5050-5054.
45. ZHOU, C.W., J.M. SIMMIE and H.J. CURRAN. An ab initio/Rice-Ramsperger-Kassel-Marcus study of the hydrogen-abstraction reactions of methyl ethers, H_3COCH_3-x(CH_3)(x), x=0-2, by (OH)-O-center dot; mechanism and kinetics. *Physical Chemistry Chemical Physics*, 2010, **12**(26), pp.7221-7233.

46. ROBERTSON, S.H. and D.M. WARDLAW. The Unimolecular Dissociation of the Isopropyl Radical. *Chemical Physics Letters*, 1992, **199**(3-4), pp.391-396.
47. ESKOLA, A.J., S.A. CARR, M.A. BLITZ, M.J. PILLING and P.W. SEAKINS. Kinetics and yields of OH radical from the CH_3OCH_2 + O_{-2} reaction using a new photolytic source. *Chemical Physics Letters*, 2010, **487**(1-3), pp.45-50.
48. ROBERTSON, S.H., GLOWACKI, D. R., LIANG, C.-H.; MORLEY, C., PILLING, M. J.,. MESMER (Master Equation Solver for Multi-Energy Well Reactions), an object oriented C++ program for carrying out ME calculations and eigenvalue-eigenvector analysis on arbitrary multiple well systems. http://sourceforge.net/projects/mesmer. 2008.
49. NGUYEN, T.L. and J.R. BARKER. Sums and Densities of Fully Coupled Anharmonic Vibrational States: A Comparison of Three Practical Methods. *Journal of Physical Chemistry A*, 2010, **114**(10), pp.3718-3730.
50. PU, J.Z. and D.G. TRUHLAR. Tests of potential energy surfaces for H+CH4 <-> CH3+H-2: Deuterium and muonium kinetic isotope effects for the forward and reverse reaction. *Journal of Chemical Physics*, 2002, **117**(23), pp.10675-10687.

Chapter 5. The reaction between OH and methanol

In this chapter, the low temperature kinetics of the OH + methanol reaction will be explored in detail. This system has many similarities with the OH + acetone and OH + DME reactions considered in chapter 4. It occurs over the same type of generic PES that is observed in both the reactions studied in the previous chapter, however, the OH + methanol system is smaller than the previous two in terms of the number of atoms. Here both the pressure dependence and product formation in the OH + methanol reaction, will be explored at ~80K and below.

5.1. Introduction

The reaction between OH and methanol is important in both combustion environments and the earth's atmosphere and consequently there have been numerous studies of the kinetics of this reaction over the past 34 years. (1) The importance of OH + OVOC reactions with the Earth's atmosphere has been mentioned (Section 4.1) in the context of acetone, and methanol is one of the more abundant OVOC species with mixing ratios of between 500 and 1000 ppt (2). Sources of atmospheric methanol include anthropogenic emission during biomass burning and biogenic emission during the decay of flora (3) and like many OVOCS reaction with the OH radical is the major sink in the upper troposphere. From a combustion perspective the OH + methanol reaction has attracted attention in the context of car fuel cells. (4) More commonly methanol is used as a fuel additive and the oxidation of methanol by OH is an important addition to many combustion models. (5)

The first measurement of the rate coefficient for the OH + methanol reaction was performed in 1978 by Overend and Paraskevopoulos (6) using a flash photolyisis – resonance fluorescence, technique and there have been a number of similar measurements performed around 298K.(7-9)There are a number of additional studies that explore the temperature dependence of the

OH + methanol rate coefficients. Most of these are confined to the 200K to 450 K (10-12) temperature range more relevant to atmospheric conditions. A study by Hess and Tully (13) performed measurements up to 800 K and a shock tube study of the OH + methanol reaction by Bott and Cohen (5) was able to obtain a rate coefficient at 1200 K. These studies extend the available experimental data to temperatures more relevant to combustion but there are no previous studies below 200 K probing the low temperature behaviour of this reaction. Rate coefficients from the studies by Wallington, (11) Crowley, (10) Jimenez (12) and Hess (13) are shown versus temperature in Figure 5.1 and the agreement is very good between these studies. From this figure it can also be seen that there is substantial deviation from Arrhenius behaviour below 300 K perhaps indicative of quantum mechanical tunnelling playing a role.

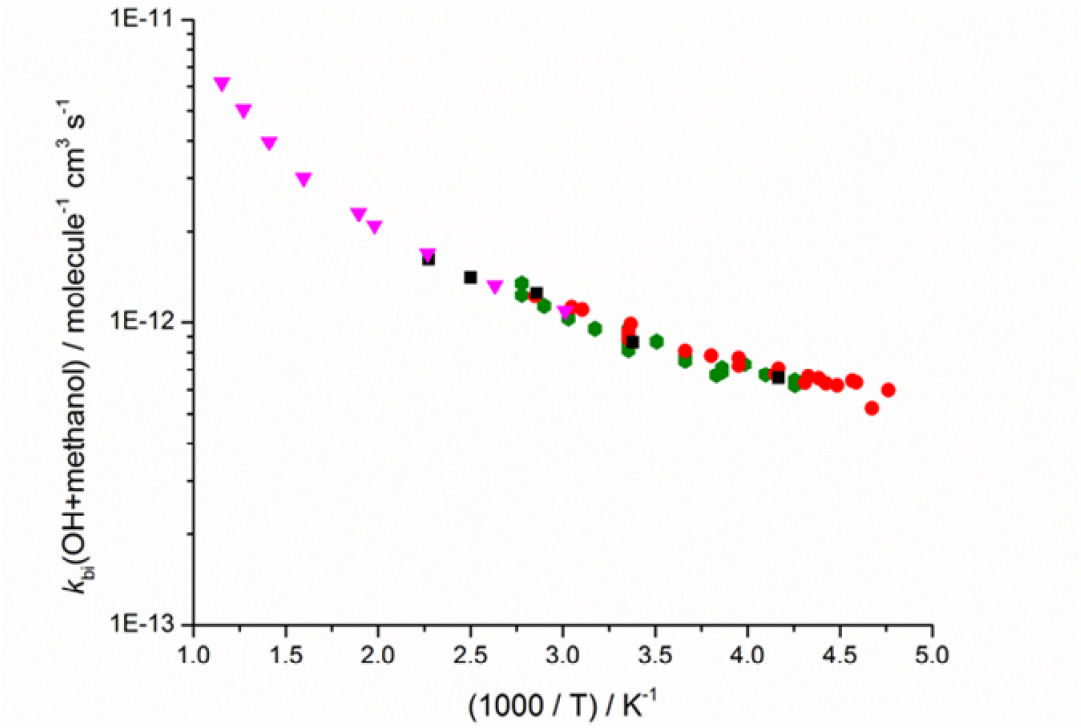

Figure 5.1: Arrhenius plot showing the rate coefficients for the OH + methanol reaction, k_{bi}(OH+methanol), versus reciprocal temperature in Kelvin. The abscissa is on a natural logarithmic scale. Rate coefficients are taken from previous studies as follows. Pink triangles are measurements from Hess and Tully, (13) black squares are from Wallington, (11) green hexagons are from Jimenez *et al.* (12) and red circles are from Crowley *et al.*. (10)

Very low temperature rate coefficients for the OH + methanol reaction are also desirable from a fundamental point of view. Both the OH radical and methanol have been directly observed in dense cloud environments of circumstellar envelopes. The OH radical has been observed to exhibit a fractional abundance of 1×10^{-7} with respect to H_2 (14, 15) and fractional abundances of methanol of between 1×10^{-9} to 1×10^{-7} (16) have been reported. As such there is a very practical application, for the study of the kinetics of the OH + methanol reaction at very low temperatures.

The OH + methanol reaction proceeds by hydrogen abstraction and there are two possible abstraction sites corresponding to either a methyl or the hydroxyl hydrogen. These two reaction paths form the CH_2OH (hydroxyl methyl radical) or the CH_3O (methoxy radical) respectively along with water as a co-product as shown in reactions R1a and R1b.

$$OH + CH_3OH \rightarrow H_2O + CH_2OH \qquad (R1a)$$

$$OH + CH_3OH \rightarrow H_2O + CH_3O \qquad (R1b)$$

The branching ratios for these two channels have been experimentally determined at some temperatures. Direct measurements of the branching ratio for R1a have been performed by Meier *et al.* (17) using mass spectrometry and a value of 0.83±0.13 was measured at room temperature. However, there have been no direct measurements of the temperature dependence of this branching ratio. In a separate study, by Hess and Tully (13), rate coefficients for CD_3OH + OH were measured in addition to those for OH + methanol and the kinetic isotope effect was determined at a number of different temperatures between 290 and 860 K. At room temperature a substantial kinetic isotope effect was observed consistent with methyl hydrogen abstraction being the dominant channel. However this kinetic isotope effect was seen to become less substantial as the temperature was increased, as shown in Figure 5.2. Since only the methyl hydrogen's are deuterated, no kinetic isotope effect would be expected from channel R1b and consequently one interpretation of these deuterated studies is that the branching ratio for hydroxyl hydrogen abstraction, via R1b,

increases with temperature, although direct product studies would be required in order to confirm this.

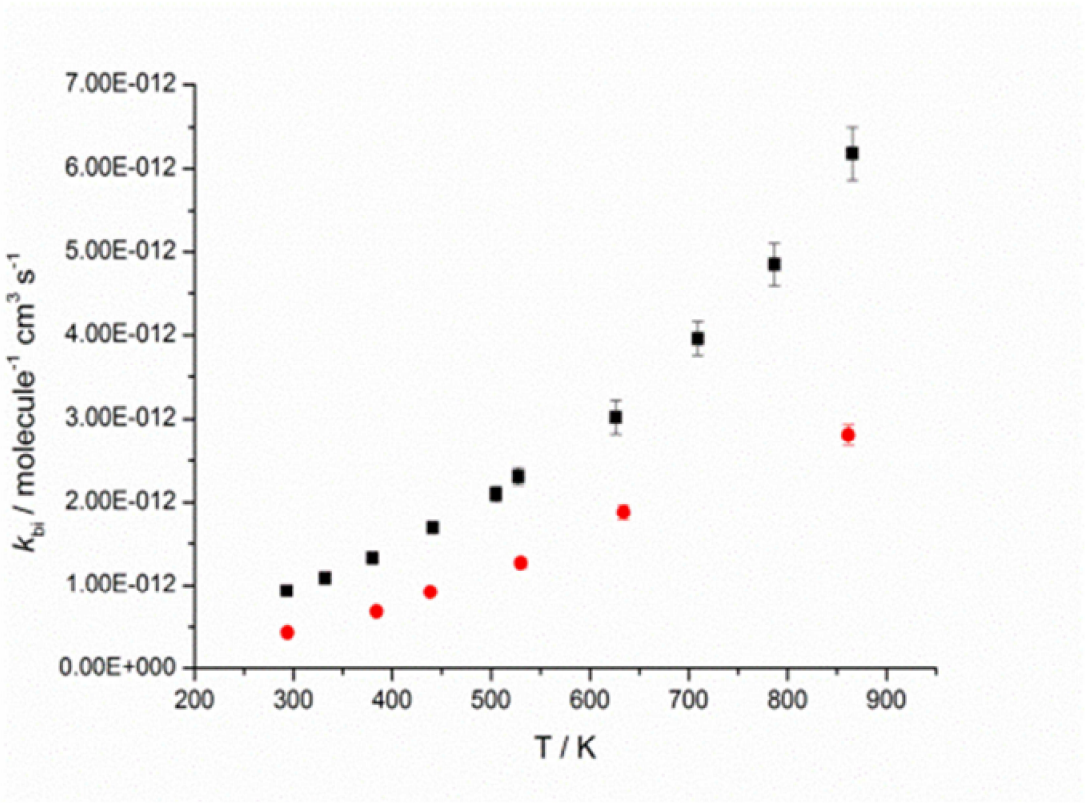

Figure 5.2: Rate coefficients for the OH + methanol (black squares) and the OH + CD_3OH (red circles) versus temperature. The measurements were performed by Hess and Tully. (13)

Complementing the numerous experimental studies there have been several *ab intio* studies upon the OH + methanol reaction. The two most recent studies by Xu and Lin (18) and Galano *et al.* (19) have characterised the stationary points on the potential energy surface (PES) using geometry optimisations at the MP2/6-311 + G(3df,2p) and BHandHLYP/6-311G(d,p) levels of theory. In each case the relative energies of each stationary point were refined through performing single point calculations at the CCSD(T) level of theory with the same basis sets that were used in the geometry optimisations. The PES's calculated in each study agree well and a schematic diagram of the PES is shown in Figure 5.3 below with the relative energies obtained from each study. This PES is of the same form as the generic PES's for the OH + acetone and OH + DME reactions with a weakly bound hydrogen bonded complex preceding one or more transition state for hydrogen abstraction. In the OH + methanol reaction there are two transition

states corresponding to hydrogen abstraction from the two different abstraction sites and both computational studies determine the barrier height for methyl hydrogen abstraction to be considerably smaller than the barrier height for hydroxyl hydrogen abstraction. This is in agreement with the experimental yield measurements and transition state theory calculations based upon these two OH + methanol PES's have shown good agreement with the experimental rate coefficients. However, neither of the theoretical studies predict the branching ratio of methoxy radicals to increase at higher temperatures, as suggested by the deuterated experiments of Hess and Tully. (13)

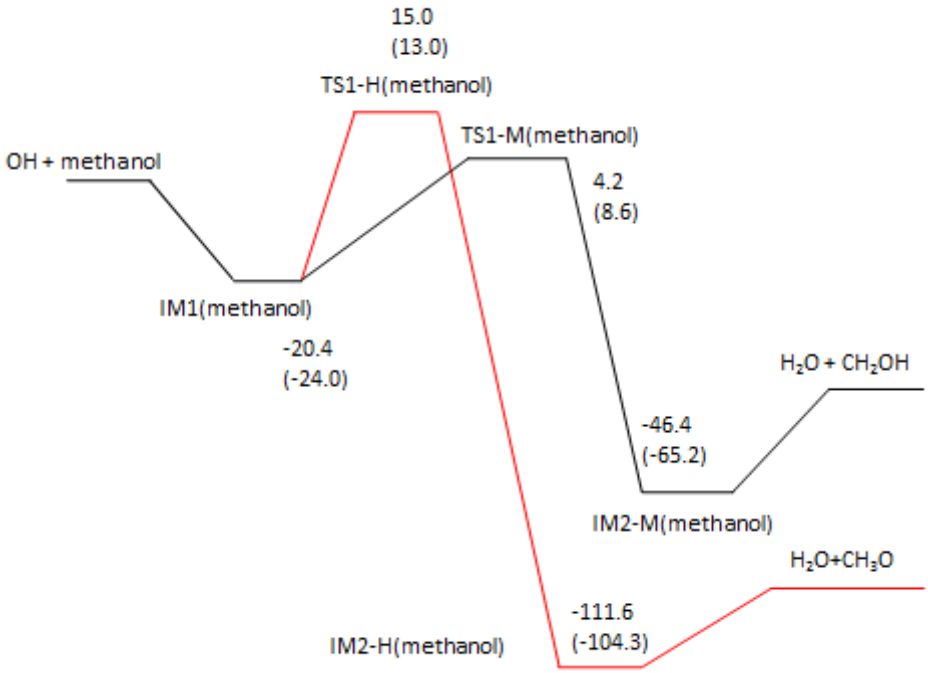

Figure 5.3: Schematic potential energy surface for the OH + methanol reaction with stationary point energies calculated by Xu and Lin(18) and Galano (19) (energies in parentheses). The reaction path shown in red corresponds to hydrogen abstraction from the hydroxyl group of methanol, whilst the reaction path in black corresponds to abstraction from the methyl group of hydrogen. All energies are in kJ mol^{-1}.

5.2. Methods

5.2.1. Experimental

The rate coefficients for the OH + methanol reaction were measured using the Leeds pulsed Laval nozzle apparatus in the manner described in chapter 3. The rate coefficients for OH loss in the presence of methanol were measured at 83 and 63 K using the T81Pvar and T63P3E16 nozzles and the rate coefficient for methoxy formation was measured at 83 K. The dependence of the OH + methanol rate coefficient upon total gas density was also explored through performing measurements at total gas densities of 6.1×10^{16} molecule cm^3, 8.9×10^{16} molecule cm^3 and 1.7×10^{17} molecule cm^{-3}.

For the experiments looking at the loss of OH in the presence of methanol, tertiary butyl hydroperoxide (t-BuOOH) was used as an OH precursor. As was discussed in the case of OH + DME, making OH radicals through the photolysis of t-BuOOH requires only the addition of t-BuOOH radicals to the reactive gas mixture, whilst using acetone as a precursor requires the addition of both oxygen and acetone to the reaction mixture. In addition, analysis of the experimental data produced from acetone photolysis, is complicated by the growth in OH due to the $CH_3CO + O_2$ reaction whilst in the case of t-BuOOH, OH radicals are produced instantaneously upon laser photolysis. However in order to confirm, that no systematic error was introduced through using t-BuOOH as an OH precursor, the OH + methanol rate coefficient was also measured at 83 K and 6.1×10^{16} molecule cm^{-3} using acetone as an OH precursor.

For all experiments nitrogen (BOC, OFN) was used as a bath gas and this was admitted to the reaction chamber from the cylinder. Methanol (Sigma Aldrich, technical grade) co-reagent was admitted to empty cylinders using a freeze pump thaw method and these cylinders were subsequently diluted up to a total pressure of 7.6 bar with nitrogen. These cylinders were left to mix overnight before the methanol, nitrogen mixture could be admitted to the reaction chamber. In order to get t-BuOOH (Sigma Aldrich 70% aqueous) or acetone (Fluka, Riedel-deHaėn, analytical grade 99.5%) into the gas phase, a small flow of nitrogen was passed through a bubbler containing the

precursor prior to being admitted to the reaction chamber. Oxygen (BOC, analytical grade) for use in the acetone precursor experiments was admitted to the reaction chamber directly from the cylinder. All gas flows were admitted to a 5 L ballast reservoir prior to entering the reaction chamber, in order to ensure thorough mixing

For the studies of methoxy radical formation rate coefficients the OH radicals were produced using the $O(^1D) + H_2$ reaction using the photolysis of ozone to produce the $O(^1D)$ radicals. Ozone has a large absorption cross section (1.00×10^{-17} cm^2 $molecule^{-1}$ at 247 nm (20)), much larger than that for t-BuOOH (1.9×10^{-20} cm^2 $molecule^{-1}$) (21), and this precursor was used since t-BuOOH did not produce enough OH radicals for methoxy radical formation to be observed. The OH loss rate coefficient in the presence of methanol, was also measured at 83 K using the $O(^1D) + H_2$ reaction as a precursor in order to check for consistency.

For these experiments ozone (estimated at 5% in O_2) was introduced to an empty cylinder through flowing oxygen through an ozone generator. This ozone oxygen mixture was then diluted with nitrogen and the cylinders were left overnight to mix. Hydrogen (BOC) was introduced to the reaction mixture straight from the cylinder. In order to ensure that methoxy radicals were being observed, methyl nitrite, a known methyl precursor was also used in order to produced methoxy radical directly, such that the laser induced fluorescence signals from both methods could be compared . In these experiments, methyl nitrite (0.3 bar) was admitted to an empty cylinder and diluted with nitrogen before being left overnight to mix

In all experiments the OH precursors were photolysed at 248 nm using an excimer laser (Lambda Physic LPX 200) with typical pulse energies of 200 mJ. The radicals produced were then subsequently probed using a YAG (Spectron Laser Systems SL803) pumped dye laser (Sirah Gmbh-Cobra Stretch) system. In order to induce fluorescence in the OH molecules the frequency doubled dye laser output was tuned in order to be resonant with the $A^2\Sigma^+$-$X^2\Pi_i$ (1,0) $Q_1(1.5)$ transition in OH at 282 nm. In the case of the methoxy radical, an excitation spectrum of the $\tilde{A}^2A_1$-$\tilde{X}^2E$ band ($\nu_3 = 3 \leftarrow 0$ and overlapping combination bands), was recorded, using methyl nitrite as a

precursor, through varying the laser wavelength between 297 nm and 299 nm and recording the resulting fluorescence. This spectrum is shown in Figure 5.4 and a broad band can be observed containing a large amount of rotational fine structure. Figure 5.5 shows a small part of this spectrum, comparing rotationally resolved transitions using both methyl nitrite, and the OH + methanol reaction to produce the methoxy radical. By comparing these two spectra it can be observed that the peaks match up well. When probing methoxy radicals for the kinetic studies, the peak at 297.63 nm was probed.

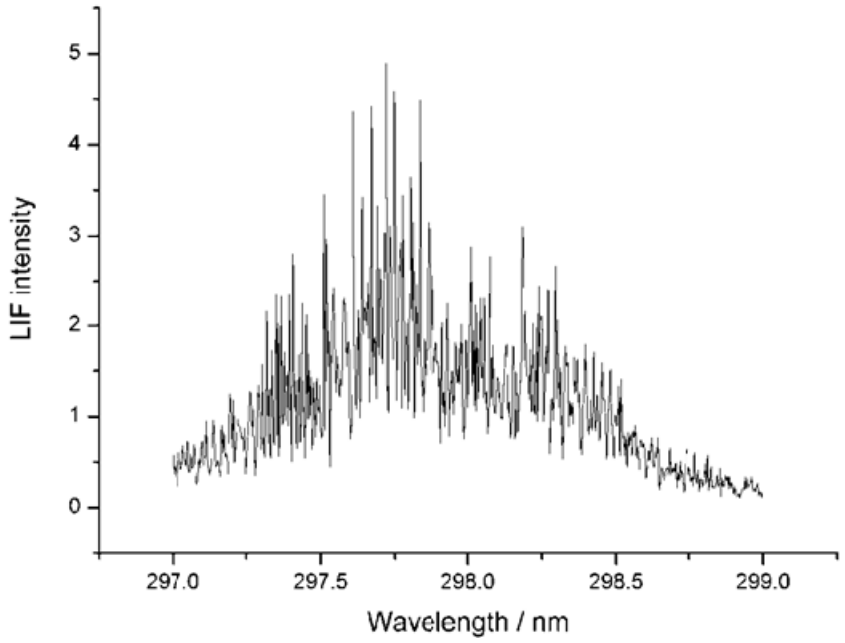

Figure 5.4: Laser excitation spectrum of the methoxy (CH_3O) radical at 82±4 K and (5.1±0.7)×10^{16} molecule cm^{-3}.This spectrum is obtained from the photolysis of methyl nitrite (4×10^{-13} molecule cm^{-3}) at 248 nm . In order to obtain the fluorescence spectrum the doubled probe output was scanned between 297 and 299 nm in increments of 0.001 nm and each point was averaged twice.

Laser induced fluorescence from either OH radicals or methoxy radicals, was collected using a PMT and then digitised on an oscilloscope. A delay generator was then used in order to vary the delay time Δt between photolysis and probe lasers in order to build up a time resolved, decay or growth. For the 63 K experiments the maximum Δt was 300 μs whilst for the 83 K data it was 200 μs. These delay times were determined by the length of stable flow resulting from each nozzle. OH decay traces typically consisted of 300 points with each point averaged 20 times, whilst due to the poorer

signal to noise when probing methoxy, its formation traces typically consisted of 150 points, averaged 60 times. The averaged LIF signal was then normalised with respect to the relative probe laser power, measured simultaneously using a photodiode, prior to analysis.

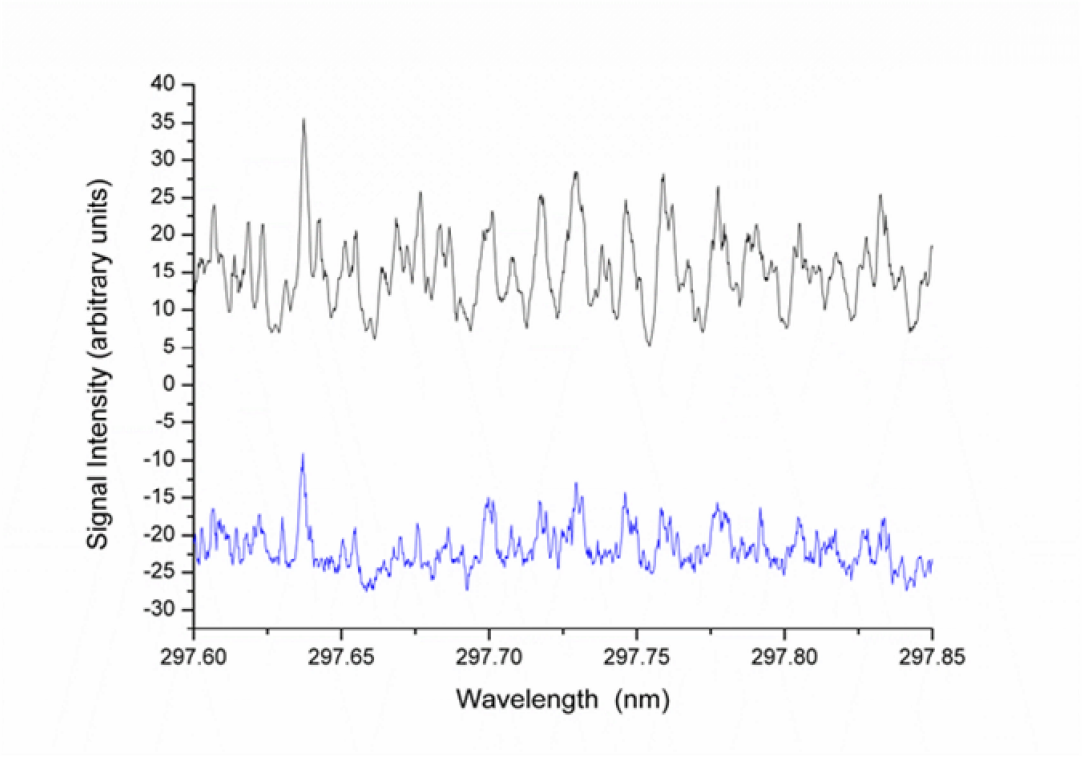

Figure 5.5: Comparison of LIF emission spectra of the $\tilde{A}^2A_1$-$\tilde{X}^2E$ band of the methoxy (CH_3O) radical at 83±4 K and (5.1±0.7)×10^{16} molecule cm^{-3} with methoxy produced using two different methods. The top spectrum is from methoxy radicals produced from methyl nitrite photolysis while the bottom spectrum is from methoxy radicals produced from the OH + methanol reaction. The bottom spectrum has been scaled by a factor of 50 and offset in order to provide a good comparison. In order to obtain the excitation spectrum the doubled, probe laser, output was scanned between 297.6 and 297.85 nm in increments of 0.0002 nm and each point was averaged four times.

For typical decay and growth traces, the experimental data were analysed using the fitting equations Eq. 1 and Eq. 2 respectively:

$$[OH] = [OH]_0 \, e^{(-(k'_{methanol} + k_d)t)} \qquad \text{(Eq. 1)}$$

$$[CH_3O] = \frac{k'_{methanol}\,[OH]_0}{k_{dm} - k'_{methanol} - k_d}\left(e^{-(k_d + k'_{methanol})\times t} - e^{-k_{dm}\times t}\right) \qquad \text{(Eq. 2)}$$

where $[OH]_0$ is the concentration of OH at time zero, $k'_{methanol}$ is the pseudo first order rate coefficient for OH loss through reaction with methanol (this is the pseudo first order rate coefficient for reaction R1 and it is assumed that this is equal to the pseudo first order rate coefficient for methoxy formation), k_d is the rate coefficient for loss of OH by reaction with the *t*-BuOOH precursor and by diffusion, k_{dm} is the rate coefficient for first order loss of CH_3O including any possible reactive pathways and diffusion. In this case Eq. 2 is obtained by solving the rate equations (Eq. 3 / Eq. 4) given below using an integrating factor method:

$$\frac{d[CH_3O]}{dt} = k'_{methanol}[OH] - k_{dm}[CH_3O] \qquad \text{(Eq.3)}$$

$$\frac{d[OH]}{dt} = k'_{methanol}[OH] - k_d[OH] \qquad \text{(Eq. 4)}$$

The case of using acetone as an OH precursor has been described in chapter 4 and in this case the following fitting equation was used:

$$[OH] = \frac{[CH_3CO]_0 k'_{methanol}}{k'_{o2} - k_{methanol}}[\exp(-k'_{o2} \cdot t) - \exp(-k'_{methanol} \cdot t)] \qquad \text{(Eq. 5)}$$

where $[CH_3O]_0$ is the initial CH_3O concentration at t=0 and k'_{o2} and $k'_{methanol}$ are the pseudo first order rate coefficients OH formation due to the $CH_3CO + O_2$ reaction, and the subsequent loss due to reaction with methanol.

5.2.2. Computational

In addition to performing experiments, both electronic structure theory and master equation simulations have been performed upon the OH + methanol system. Given the small number of atoms involved in the reaction, it was possible to perform high level ROHF-UCCSD(t)/aug-cc-pvdz//ROHF-UCCSD(t)/aug-ccpvtz, calculations. (22) These calculations were performed for species OH, methanol, IM1, TS1_H and TS1_M using the Molpro (23) suite of *ab initio* software, and these calculations, should be more reliable than those of Xu (18) and Galano (19), particularly since the UCCSD(t) geometries and vibrational frequencies calculated here would be expected to offer an improvement upon the MP2 and BHandHlyp geometries of Xu (18)

and Galano, (19) respectively. The calculated energies and frequencies are given in Table 5.1. In addition, the T1 (24) and D1 (25) (see Section 2.2.4) diagnostic values are also shown for IM1, TS-M and TS-H in order to explore any multi-reference effects in these species.

In these calculations, the geometries of all species were optimised successfully apart from the calculations upon TS1-H which failed to locate a stable geometry. However the T1 and D1 diagnostics performed at the geometry at which TS1_H was located in the calculations of Xu give values of 0.051 and 0.228 . A T1 diagnostic of > 0.02 Indicates that there may be substantial multireference effects (at this geometry the species is poorly described by a single dominant electronic configuration) and a ratio T1/D1 > $2^{-0.5}$ is also a strong indicator of multireference character. In the vicinity of TS1_H, both these criteria are met, possibly suggesting a low lying electronic excited state in the region. Referring to Table 5.1 it can also be seen that the multireference criteria are also met for TS_M, although in this case the diagnostics are less conclusive than for TS_H.

All calculations performed on the OH + methanol reaction, including those described in the previous paragraph, have been carried out using single reference calculations. However, the main difference in the CCSD calculations present here, is the fact that a restricted Hartree Fock wavefuction is used, whereas the previous calculations have both employed unrestricted Hartree Fock wave functions. Unrestricted calculations can cause errors in calculations due to spin contamination and for many cases, the ROHF-UCCSD(t) calculations offer a more reliable alternative to the completely unrestricted calculations employed with other *ab intio* software packages. In cases where multireference effects are important though, unrestricted calculations can go some way to accounting for the these multireference effects whilst still using a single reference level of theory and this could explain why TSH(methanol) could not be located using the ROHF-UCCSD(T) level of theory.

Species	E_{elec} + ZPE / kJ mol^{-1}	ν / cm^{-1}	T1	D1
IM1	-22.1	53 66 197 317 444 643 1026 1068 1160 1368 1457 1479 1491 3021 3095 3144 3543 3820	0.011	0.027
TS1_M	0.3	72 136 226 418 755 1015 1056 1124 1325 1357 1399 1444 1512 3038 3145 3689 3799	0.031	0.125

Table 5.1: Stationary points in the OH + methanol reaction with vibrational frequencies calculated at the ROHF-UCCSD(t) / aug –cc- pvdz and relative energies calculated at the ROHF-UCCSD(t) / aug –cc- pvtz level of theory using the Molpro (23) suite of *ab initio* software.

To explore these issues further, calculations were carried out using multireference perturbation theory (rs2) (26) calculations. In these calculations, a 7 electron, 7 orbital, (7,7) complete active space was used and the calculations were performed using the aug-cc-pvtz basis set. Each orbital included in the active space exhibited an occupation number of between 0.98 and 0.02. The main species of interest with regards to these multireference calculations are TS1_H and TS1_M, but although multi-reference effects are not important for IM1, rs2/aug-cc-pvdz// rs2/aug-cc-pvtz calculations were also performed for this species in order to obtain the relative barrier height of TS1_H at the rs2/aug-cc-pvdz// rs2/aug-cc-pvtz level of theory. Using this multireference level of theory, a second Van-der Waals complex (IM1b(methanol)) was also located, the structure of which is shown in Figure 5.6. Calculations at the MP2/6-31++G** and CCSD(t)/aug-cc-pvdz level of theory using the Gaussian (27) and Molpro (23) *ab initio* programs respectively, were unable to locate this species. However, geometrically the structure of this complex is more closely related to the structure of TS1-H than IM1 and it is likely that hydroxyl hydrogen

abstraction in the OH + methanol reaction occurs from this newly discovered complex rather than IM1. In order to confirm this however, IRC calculations would be required using a multireference method. Unfortunately such calculations are non-trivial using a multireference method and attempts at calculating the reaction path at the rs2 level have been unsuccessful.

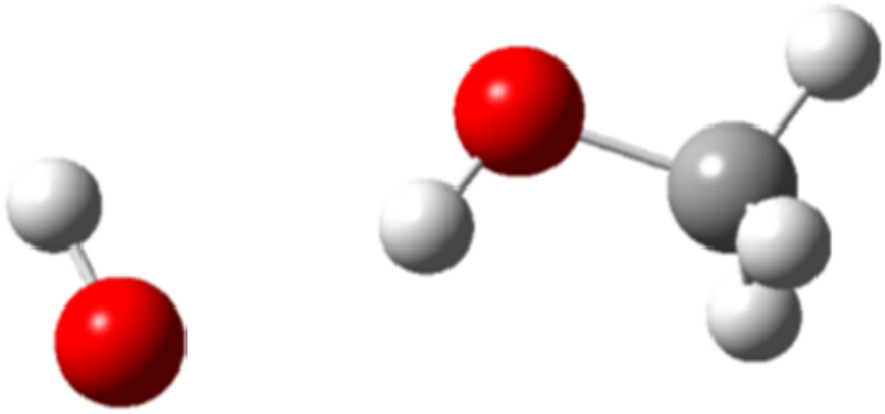

Figure 5.6: Structure of hydrogen bonded complex IM1b from a geometry optimisation at the rs2(7,7)/aug-cc-pvdz level of theory using the Molpro software. (23)

The results from these multireference calculations are summarised in Table 5.2 . Surprisingly, assuming the rs2/aug-cc-pvdz// rs2/aug-cc-pvtz calculations give the correct binding energy for IM1, these calculations predict a barrier height for TS1-H of 16.6 kJ mol^{-1} in good agreement with the value of 15 kJ mol^{-1} calculated by Xu and Lin. (18) This could be fortuitous but suggests that a multirefence method is not essential to give the correct energy for TS1-H. However since single reference calculations are unable to locate IM1b, it could be that multireference calculations are required in order to give the correct minimum energy path in the vicinity of TS1-H. For TS1_M the multireference calculations give a barrier height of 9.2 kJ mol^{-1} which is in good agreement with the calculations of Galano *et al.* (19) (8.6 kJ mol^{-1}) but much higher than the barrier calculated at the ROHF-UCCSD(t) level of theory in current study.

Species	E_{elec} + ZPE / kJ mol^{-1}	B / cm^{-1}	ν / cm^{-1}
TS1_H	16.5	0.95 0.18 0.16	120 186 222 393 794 1017 1107 1164 1275 1442 1469 1489 1509 3063 3158 3172 3705
TS1_M	9.2	1.22 0.21 0.18	80 149 233 406 233 755 966 1055 1117 1330 1363 1400 1456 1512 3099 3211 3678 3831
IM1b	-7.7	1.19 0.17 0.15	56 95 132 160 319 409 1054 1099 1168 1408 1466 1494 1508 3049 3123 3181 3647 3779

Table 5.2: Vibrational frequencies and energies for IM1b TS1-H and TS1- M optimisation at the rs2(7,7)/aug-cc-pvdz level of theory using the Molpro software. (23) Frequencies in red correspond to internal rotations of the CH_3 group in methanol and frequencies in blue correspond to internal rotations of the OH moiety.

Having performed these detailed calculations, the potential energy surface for the OH + methanol reaction was created as follows. First of all a reduced potential energy surface was used as discussed in chapter 4, and the infinite sink approximation was used on species IM2-H and IM2-M. Calculations including the final reaction step to bimolecular products showed that this approximation introduced less than 1% error to the calculations. The relative energies of all species were taken from the ROHF-UCCSD(T) calculations, apart from for TS1-H. Given the substantial multireference character of TS1-H, the barrier height of TS1-H was determined from the difference in the energies of TS1-H and IM1 at the rs2/aug-cc-pvtz level of theory. Vibrational frequencies and rotational constants for all species were taken from the ROHF-UCCSD(T) level of theory again apart from for species TS1-H for which the ro-vibrational parameters were obtained from the rs2/aug-cc-pvdz calculations. In addition, although the connectivity was not confirmed using

ab initio calculations, TS1-H was connected to species IM1b rather than IM1. The potential used in MESMER (28) calculations is shown below in Figure 5.7

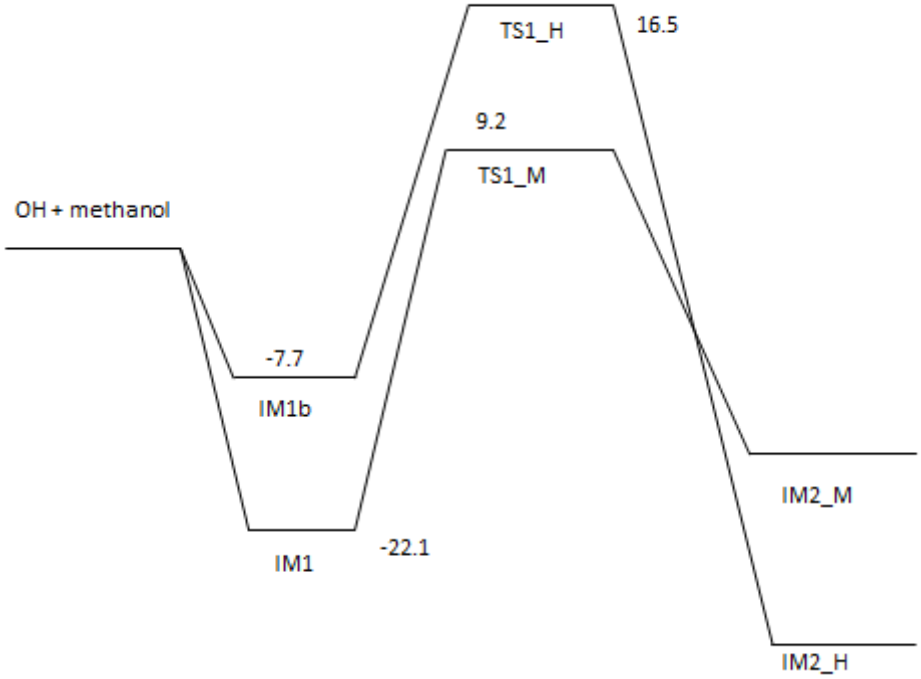

Figure 5.7: Potential energy surface used in master equation calculations. The energy of IM1 is calculated at the ROHF-CCSD(t) / aug-cc-pvtz level of theory and all other energies are given at rs2(7,7) / aug-cc-pvtz level of theory. All energies are given in kJ mol^{-1}.

Using this potential energy surface master equation calculations were carried out for the OH + methanol reaction. Within the master equation calculations the molecular densities of states for each species were calculated using a rigid rotor approximation and the vibrational frequencies were treated as harmonic oscillators unless otherwise stated. However there were a number of hindered rotational motions that needed to be considered. The hindered rotations included are as follows. In all species there exists a vibrational normal mode that corresponds to rotation of the CH_3 group. These frequencies are highlighted in blue in Table 5.2 and potentials for these modes were obtained at the MPW1K/6-31+G** level of theory. In addition both TSH(methanol) and TSM(methanol) had a vibrational normal mode which corresponded to the rotation of the OH moiety about the rest of the methanol molecule. These frequencies are highlighted in red in Table 5.2

and the potentials were obtained using the rigid methodology described in chapter 4 at the MPW1K/6-31+G** level of theory. Details of these modes are given in appendix 3.

Rate coefficients for the barrierless association of OH and methanol to form IM1 and IM1b were calculated using an ILT method. In this case the ILT *A* factor was set to 1.5×10^{-10} molecule^{-1} cm^3 s^{-1} for each, and the ILT *n* factor was set to 0 in order to represent a temperature independent, near gas kinetic high pressure limit for the association reaction. The value of 1.5 for each association was chosen to give a combined high pressure limit for the association reaction, of 3×10^{-10} molecule^{-1} cm^3 s^{-1} as has been used throughout this thesis, and as supported by the proxy method measurements in chapter 7. Rate coefficients for all other reaction steps were calculated using RRKM theory.

To incorporate a tunnelling correction to the RRKM rate coefficients, transmission coefficients were calculated using the approach suggested by Miller, (29) in which the shape of the barrier potential is approximated as an asymmetric Eckart potential using the imaginary frequency of the transition state. Ideally transmission coefficients would be calculated by using the true shape of the barrier as calculated using *ab initio* energies, but in the current case reaction path potentials could not be obtained using the multireference levels of theory required. Although direct calculations of the reaction path would be preferable, in the current case, the imaginary frequencies are obtained at the same level of theory as the barrier heights and as such these imaginary frequency should be more accurate than those from the calculations by Xu (18) and Galano.(19)

Collisional energy transfer was modelled using an exponential down model with collision frequencies determined assuming a Lennard Jones potential. In the current case the Lennard Jones parameters ε and σ were chosen to be 300 Å and 5 K whilst ΔE_{down} was chosen to be 300 cm^{-1}. However, in the case of OH + methanol, the rate coefficients were found to be determined by tunnelling rather than stabilisation at low temperatures, and as such the values chosen for the collisional energy transfer parameters were unimportant for most calculations.

The OH + methanol master equations were performed using double precision at all temperatures. For calculations above 300 K a grain size of 50 cm^{-1} was used, however as the temperature was decreased it was found necessary to reduce the grain size and grain sizes as low as 10 cm^{-1} were used at the lowest temperatures.

5.3. Results

5.3.1. Experimental studies of OH loss kinetics

Bimolecular rate coefficients (k_1) for the OH + methanol reaction were obtained using the general method described in Section 3.3.3. For each temperature (83 K and 63 K) a number of pseudo first order decays were obtained with various concentrations of excess reagent ([CH_3OH]). An example decay trace is shown in Figure 5.8 with experimental details given in the caption. Each decay trace was fit with equation Eq.1 and the experimental data were observed to be well described by a single exponential function.

Having fit the experimental traces values of $k'_{methanol}$ versus [CH_3OH] were plotted at 83 K and 63 K and k_1 could be obtained from the gradient of a linear fit to the data. An example bimolecular plot at 83 K is shown in Figure 5.9 and from bimolecular plots such as this rate coefficients, k_{bi}(OH+methanol), of $(3.4 \pm 0.5)\times10^{-11}$ molecule^{-1} cm^3 s^{-1} and $(4.2 \pm 0.4)\times10^{-11}$ molecule^{-1} cm^3 s^{-1} were obtained at 83 ± 2 K and 63 ± 2 K respectively.

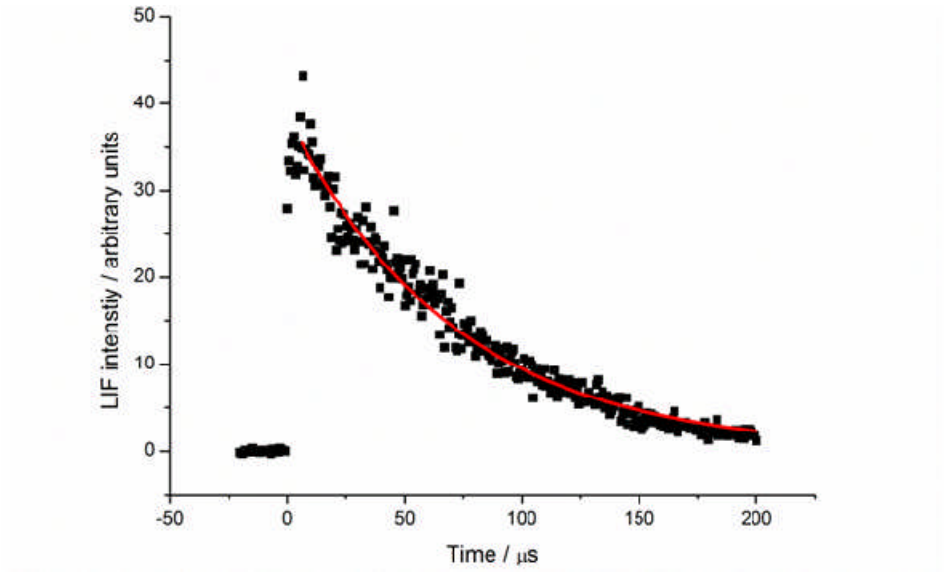

Figure 5.8: Time resolved OH LIF intensity showing OH decay in the presence of methanol. This scan consists of 300 points and each point was averaged 20 times before being normalised for laser power. The curve in red corresponds to a fit to the experimental data from Eq. 1 which gives a pseudo first order rate coefficient, $k'_{methanol}$ of 14060 ± 260 s^{-1}. Conditions used: Total density = (6.1±0.5)×10^{16} molecule cm^{-3}, [methanol] = (2.4±0.2)×10^{14} molecule cm^{-3} , T = 83±3 K.

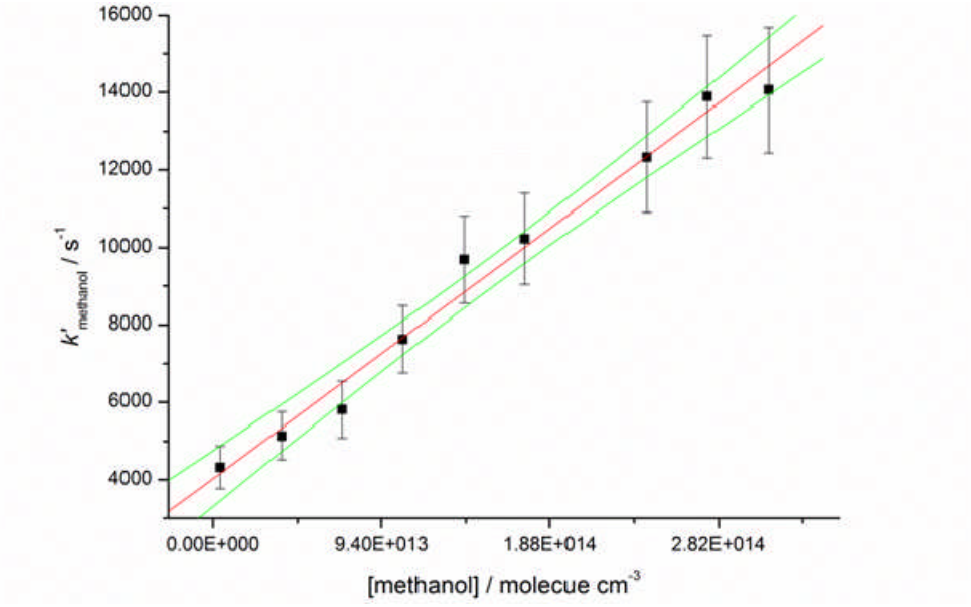

Figure 5.9: Bimolecular plot for the reaction between OH and methanol at 82±4 K and a total gas density of (6.1±0.5) ×10^{16} molecule cm^{-3}. The pseudo first order rate coefficients were obtained from fitting the experimental data with Eq. 1 and they incorporate the 2σ errors both from the fitting process and from [methanol]. The bimolecular rate coefficient was obtained from a weighted linear give a k_{bi}(OH + methanol) = (3.4±0.5)×10^{-11} molecule^{-1} cm^3 s^{-1} with errors obtained from the 95% confidence limits of the linear fit.

It should be noted that in order to confirm that the t-BuOOH precursor was not catalysing the OH + methanol reaction in some way k_{bi}(OH+Methanol) was also measured using the photolysis of acetone as an OH precursor as described in chapter 4. This check was necessary considering the results obtained in chapter 6 of this thesis where t-BuOOH was found to catalyse the OH + ammonia reation. A first order decay trace and the resulting bimolecular plot from this precursor are shown in Figure 5.10 and Figure 5.11 and a rate coefficient, k_{bi}(OH + methanol), of (3.2±0.7)×10^{-11} molecule^{-1} cm^3 s^{-1} was obtained at 83 K, in good agreement with the results using t-BuOOH as a precursor.

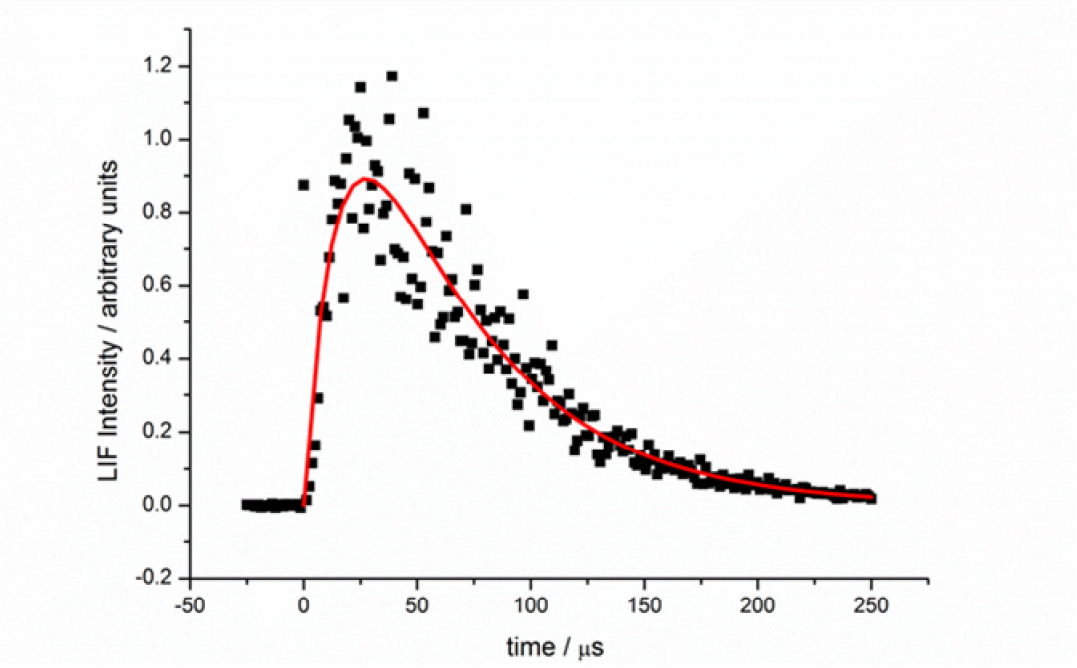

Figure 5.10: Time resolved OH LIF intensity showing OH decay in the presence of methanol using acetone as an OH precursor. This scan consists of 300 points and each point was averaged 20 times before being normalised for laser power. The curve in red corresponds to a fit to the experimental data from Eq. 3 which gives a pseudo first order rate coefficient, $k'_{methanol}$ of 11209 ± 1060 s^{-1}. Conditions used: Total density = (6.1±0.6)×10^{16} molecule cm^{-3}, [methanol] = (1.7±0.2)×10^{14} molecule cm^{-3} , T = 83±3K.

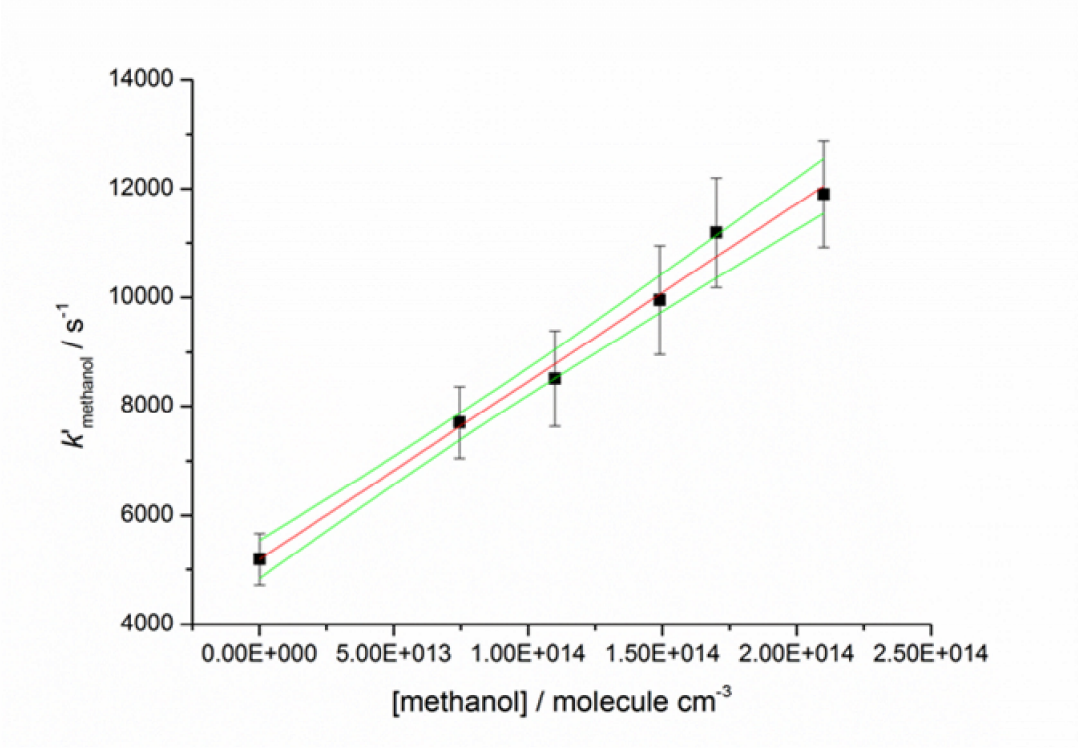

Figure 5.11: Bimolecular plot for the reaction between OH and methanol at 83±3 K and a total [N2] of (6.1±0.5) ×10^{16} molecule cm^{-3}. The pseudo first order rate coefficients were obtained from fitting the experimental data with Eq. 3 and they incorporate the 2σ errors both from the fitting process and from [methanol]. The bimolecular rate coefficient was obtained from a weighted linear give a k_{bi}(OH + methanol) = (3.2±0.7)×10^{-11} molecule^{-1} cm^3 s^{-1} with errors obtained from the 95% confidence limits of the linear fit.

The rate coefficients measured here are shown in relation to the higher temperature literature data in Figure 5.12. Here it can be observed that as is the case with OH + acetone and OH + DME reactions, a large increase in the OH + methanol rate coefficients can be observed below 200 K with $k_{1,T=63K}$ / $k_{1,T=210\ K}$ = 72. In the previous chapter the substantial negative temperatures dependencies observed, were attributed primarily to stabilisation of the excited pre-reaction complex. However the OH + methanol complex has fewer degrees of freedom than both the OH + acetone and OH + DME reactions, and densities of states arguments (see chapter 4) would suggest that the rate coefficients for the OH + methanol would be closer to the low pressure limit.

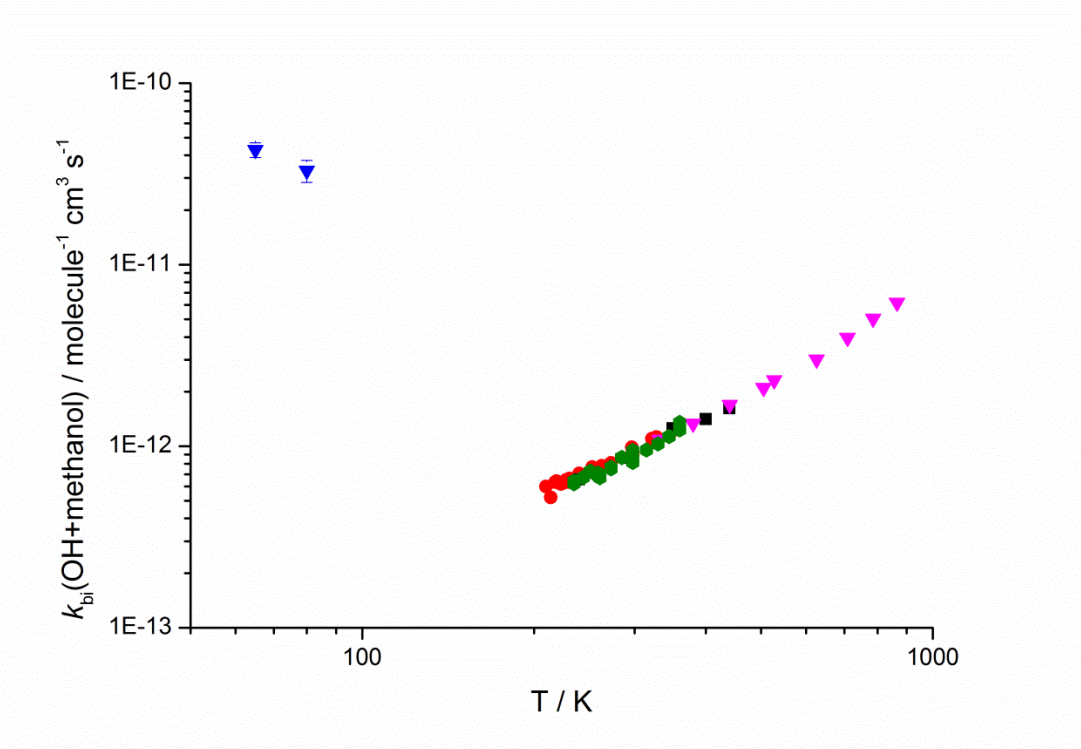

Figure 5.12: The rate coefficients for the OH + methanol reaction, k_{bi}(OH+methanol), versus temperature in Kelvin. Both axes are on a logarithmic scale. Rate coefficients are taken from previous studies as follows. Pink triangles are measurements from Hess and Tully (13), black squares are from Wallington,(11) green hexagons are from Jimenez *et al.*, (12) red circles are from Crowley *et al.* (10) and blue triangles are measurements from the current study.

To explore the possibility of stabilisation and therefore pressure dependence the OH + methanol reaction was explored at three different densities using the T81Pvar nozzle. Figure 5.13 shows the variation in bimolecular rate coefficient with density. Here it can be seen that k_1 exhibits very little dependence upon total gas density and this suggests that some mechanism other than stabilisation of the hydrogen bonded complex, causes the negative temperature dependence observed in the OH + methanol reaction. If the OH + methanol reaction does not form a stabilised hydrogen bonded complex at low temperatures then the only other possible reaction pathway is through hydrogen abstraction, via either of the transition states shown in Figure 5.7. However, considering the significant energy barriers associated with each transition state, the proportion of reactant molecules with sufficient energy to reach products would decrease with temperature and considering

this argument, going over either of the two transition states, cannot account for the negative temperature dependence to the OH + methanol rate coefficients observed below 200 K. The remaining possibility is that highly efficient quantum mechanical tunnelling occurs through one or both of the two transition states. It should be noted that even with extremely efficient quantum mechanical tunneling, it is not possible to go through a barrier faster than over it and hence tunnelling alone cannot account for the negative temperature observed. However, although it appears stabilisation of the complexes IM1 and IM1b, is not significant under the current experimental conditions, the transient lifetime of this complex with respect to re-dissociation will increase as the temperature is lowered. When this is considered along with the possibility of tunnelling, the negative temperature dependence observed can be rationalised as the increase in the population of the hydrogen bonded complexes at low temperatures offsets the decrease in the rate coefficient for hydrogen abstraction.

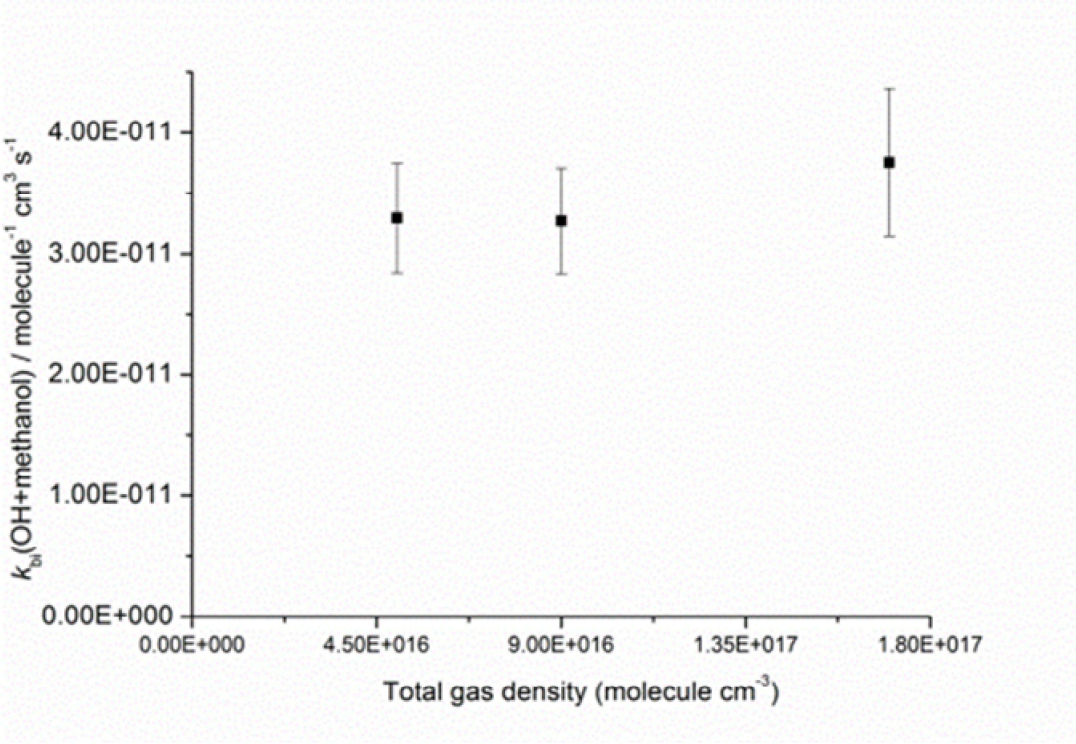

Figure 5.13: Rate coefficients k_{bi}(OH+methanol), measured at total pressures of (6.1±0.5)×10^{16} molecule^{-1} cm^3 s^{-1} (83 K), (8.9±0.6)×10^{16} molecule^{-1} cm^3 s^{-1} (83 K) and (1.7±0.2)×10^{-17} molecule^{-1} cm^3 s^{-1} (79 K).

5.3.2. Master equation studies of OH loss kinetics

In order to explore the mechanism of the OH + methanol reaction the *ab initio* and master equation calculations will now be considered. First of all, master equation calculations were performed without considering tunnelling, in order to confirm that a stabilisation mechanism could not produce the observed low temperature rate coefficients. These calculated rate coefficients are shown in Figure 5.14 versus total pressure. Contrary to the experimentally measured rate coefficients under the same conditions, (Figure 5.13) the theoretical rate coefficients are observed to depend linearly upon total pressure and the theory underpredicts the experimental measurements by almost 3 orders of magnitude. The theoretical rate coefficients could be increased by a more accurate description of anharmonicity in the complexes or increasing the energy transfer parameters, but the magnitude of the discrepancy between experiment and theory makes it very hard to rationalise, that stabilisation in the OH + methanol reaction, could lead to the large low temperature rate coefficients observed.

Master equation calculations were then performed including transmission coefficients calculated from the *ab initio* imaginary frequencies. These calculated rate coefficients are shown Figure 5.15 versus temperature. From this graph it can be seen that the master equation calculations agree reasonably well with the experimental measurements above 200 K. The master equation calculations also readily predict a sharp increase in the rate coefficients between 200 K and 83 K although at 83 K and 63 K, the theoretical rate coefficients still substantially under predict the experimental ones. In order to show how sensitive the theoretical rate coefficients are to the *ab initio* barrier heights, Figure 5.15 also shows theoretical rate coefficients with the energies of both TS1_H and TS1_M reduced by 2 kJ mol^{-1}. Although these calculations slightly over predict experimental rate coefficients at higher temperatures, it can be seen that this small adjustment

in the energies, predicts low temperature rate coefficients at 83 K and 63K which are in much better agreement with experiment.

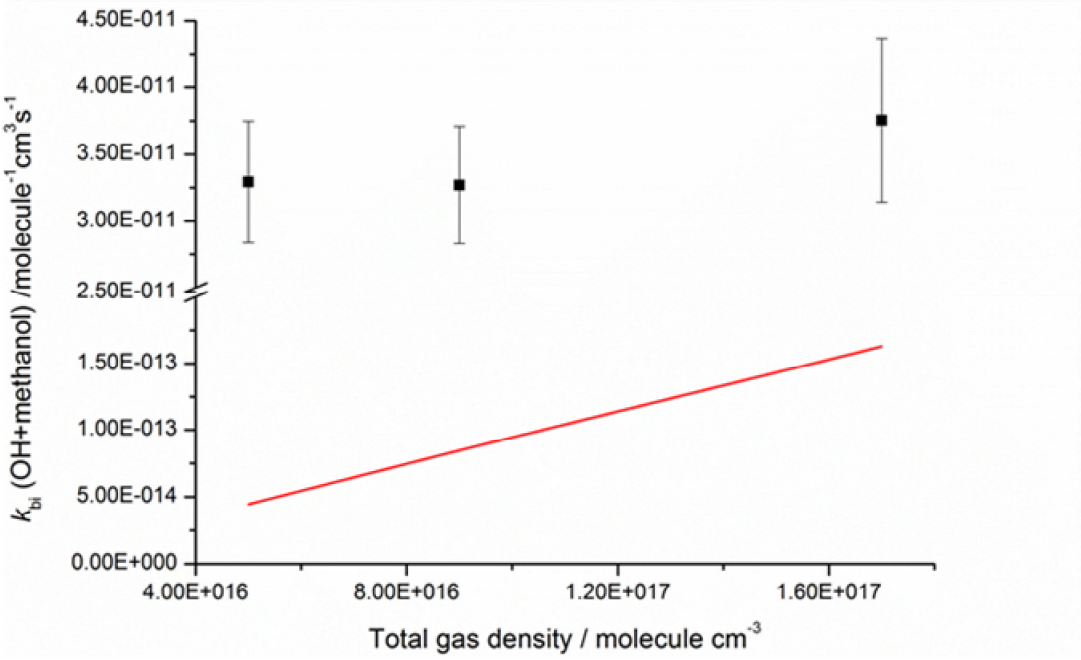

Figure 5.14: Variation in k_{bi}(OH+methanol) with the total gas density. The black squares are experimental data points, with error bars at the 2σ level. The red line corresponds to theoretical calculations considering only the association of OH + CH_3OH to form IM1 and IM1b with an energy transfer parameter. Note the break in the *y*-axis at 2×10^{-11} molecule^{-1} cm^3 s^{-1}.

Considering the complicated temperature dependence of the OH + methanol rate coefficients, these calculations agree well with experiment without any adjustment of the *ab initio* parameters. Although the agreement is not quantitative at low temperatures it has also been shown that small adjustments in the *ab initio* energies can substantially change the calculated rate coefficients. However even if the *ab initio* parameters are altered in ordered to fit the experiment, it is found that in order to give quantitative agreement at 83 and 63 K, the theoretical rate coefficients over predict the rate coefficients in the 200-300 K region. The reason for this disparity is likely to be due to the relatively crude tunneling calculations performed and more sophisticated, multidimensional tunneling calculations are necessary to explore this further.

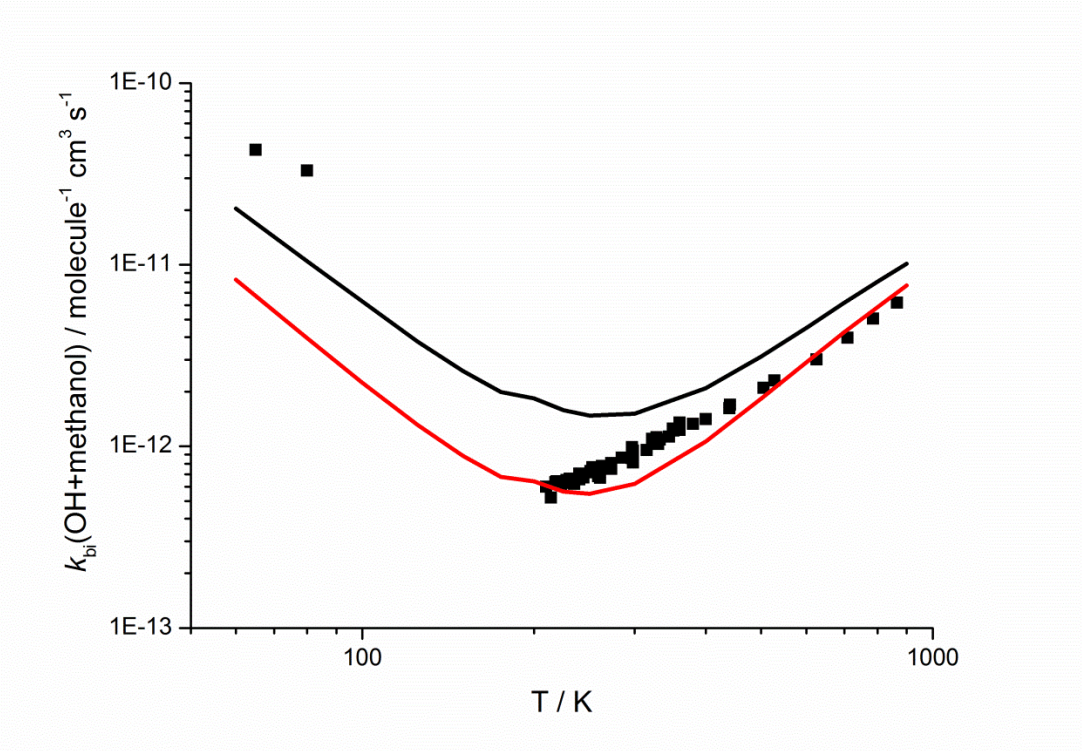

Figure 5.15: Comparison between experimental (black squares), values for k_{bi}(OH+methanol) and theoretical master equation calculations performed using the MESMER code. The red line shows rate coefficients calculated using the *ab initio* parameters and the black line corresponds to calculations with the energies of both TS_H and TS_M reduced by 2 kJ mol^{-1}.

From these master equation calculations, the mechanism through which tunnelling leads to a negative temperature dependence in the rate coefficients can be visualised. Figure 5.16 shows the microscopic rate coefficients k_3 and k_5 versus energy as calculated by MESMER. Also shown on this plot is the initial Boltzmann distribution of energies within the complex C formed for OH + methanol at both 300 K and 63 K . These Boltzmann distributions are offset by 1715 cm^{-1} which is the energy of the bimolecular reagents relative to the bottom of IM1, and as such these distributions represent the initial distribution in IM1/IM1b prior to any energy transfer via collisions.

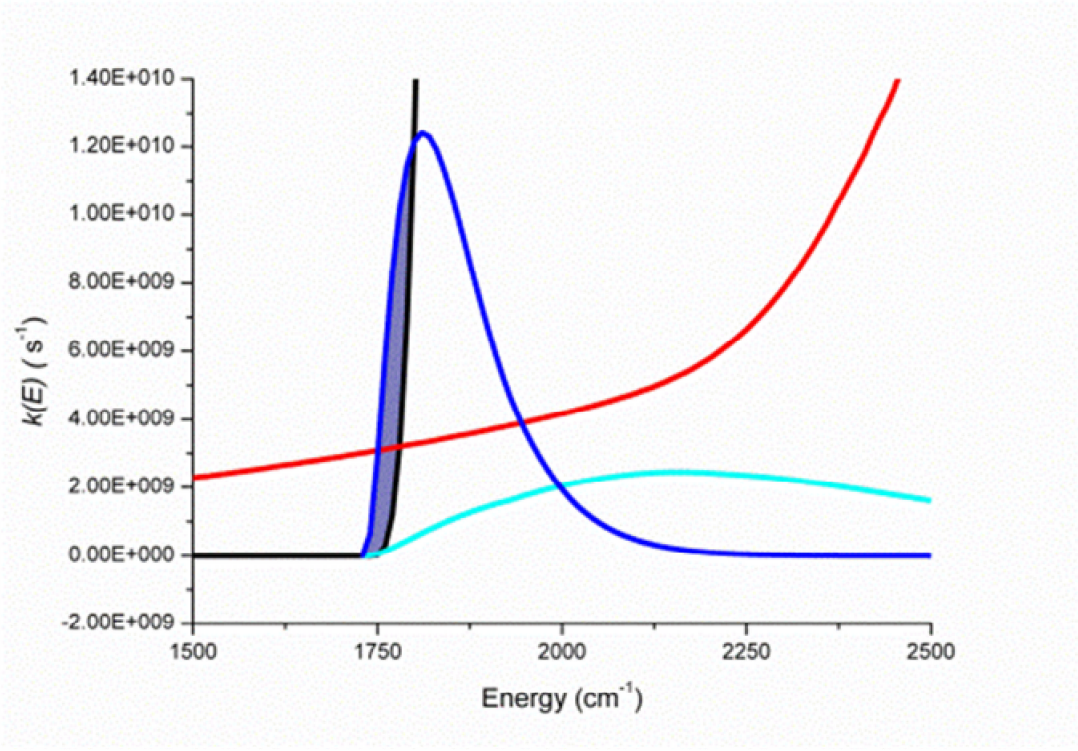

Figure 5.16: Microcanonical rate constants for the dissociation of IM1b back to OH + methanol (k_{rev}) (black) and for abstraction via either TS_M or TS_H (k_{for}) (red) calculated as a function of energy within IM1 and IM1b using the chemical master equation. Also shown are the initial relative Boltzmann distribution of energies of the complex at 300 K (cyan) and 63 K (blue) (values not shown on axis for clarity). The shaded portion shows the population that have energies for which k5 > k3 and only the 63 K Boltzmann distribution has a significant population in this region. The energy scale is shown relative to the bottom of the hydrogen bonded complex IM1, which is bound by 1715 cm-1.

An important point to notice in this figure is the crossover of the rate constants k_{rev} and k_{for} at ~1750 cm^{-1}, below which tunnelling becomes more favourable than re-dissociation of the complex. At 300 K, the Boltzmann energy distribution has a negligible population of molecules below the k_3 and k_5 crossing point, however, at 63 K, the Boltzmann energy distribution has a significant population below this crossing point. In Figure 5.16, the shaded area shows the fraction of the 63 K Boltzmann distribution for which $k_{for} > k_{rev}$. It is this increase in the population of the complex below the k_{rev} and k_{for} crossing point as the temperature is lowered that brings about the increase in the overall rate constant, k_{bi}(OH+methanol).

At this point it is worth exploring how the branching ratios for R1a and R1b, change with temperature. As mentioned in section 5.1, experimentally measured product yields show that methyl hydrogen abstraction dominates at room temperature, consistent with the lower barrier height of TS1_M. However considering the imaginary frequencies of the two transition states, TS_H has an imaginary frequency of 2291 cm^{-1} compared to an imaginary frequency of 923 cm^{-1} for TS1_M and this suggests that tunnelling could be more facile through TS_H, despite the larger barrier height. The yields calculated from the master equation calculations are shown in Figure 5.17 and it can be seen that although TS1_M dominates at room temperature, as shown experimentally, at low temperatures the branching ratio of the hydroxyl abstraction channel increases due to quantum mechanical tunnelling. Remarkably, at 63 K, despite the 16 kJ mol^{-1}, these calculations predict a branching ratio of over 0.8 for the hydroxyl abstraction channel producing the methoxy radical.

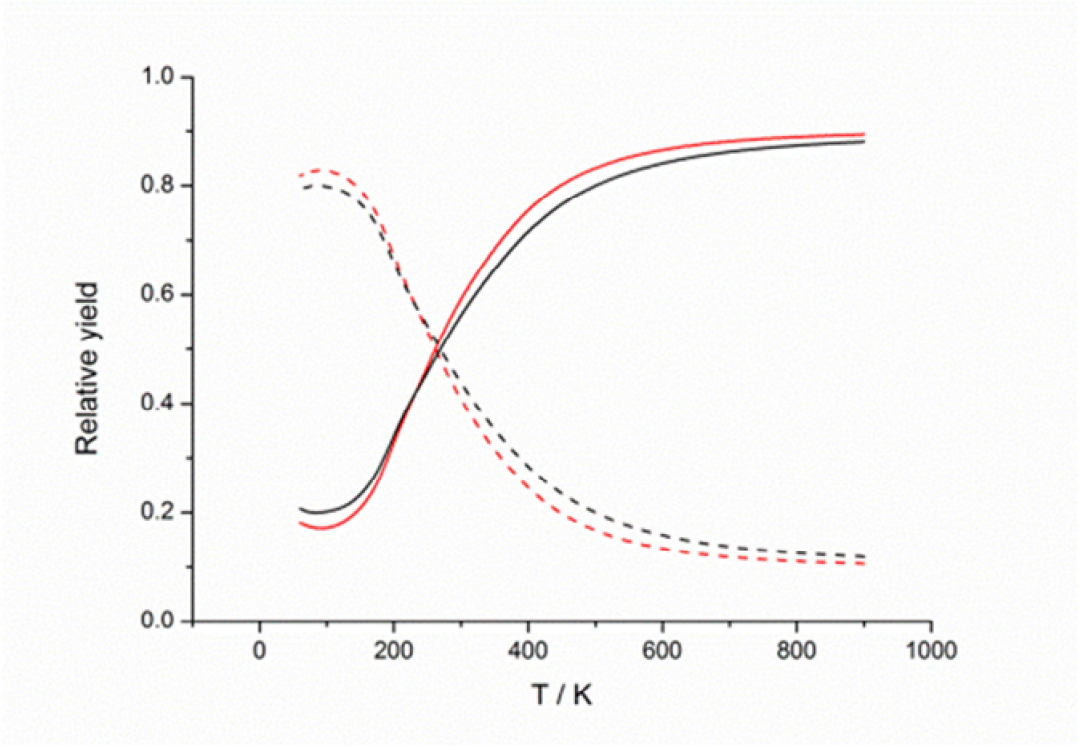

Figure 5.17: Branching ratios for abstraction via TS_M (line) and TS_H (dashed line) as calculated using MESMER. The red lines correspond to calculations using the *ab initio* parameters whilst the black lines correspond to calculations with the energies of TS1_H and TS_M reduced by 2 kJ mol^{-1}.

Finally the theoretical calculations were extrapolated down to 10 K to explore the reactivity of OH in the presence of methanol under interstellar conditions. These calculations are shown in Figure 5.18 and since both the theoretical models used, under predict the OH + methanol rate coefficients at 83 K, these calculations are likely to represent a lower limit to the true rate coefficients. Considering Figure 5.18 it can be seen that both theoretical models predict that by 10 K the rate coefficient is greater than 2×10^{-10} molecule^{-1} cm^3 s^{-1} and these results suggest in very low temperature environments, the OH + methanol reaction is likely to be limited only by the rate at which the OH and methanol moieties collide.

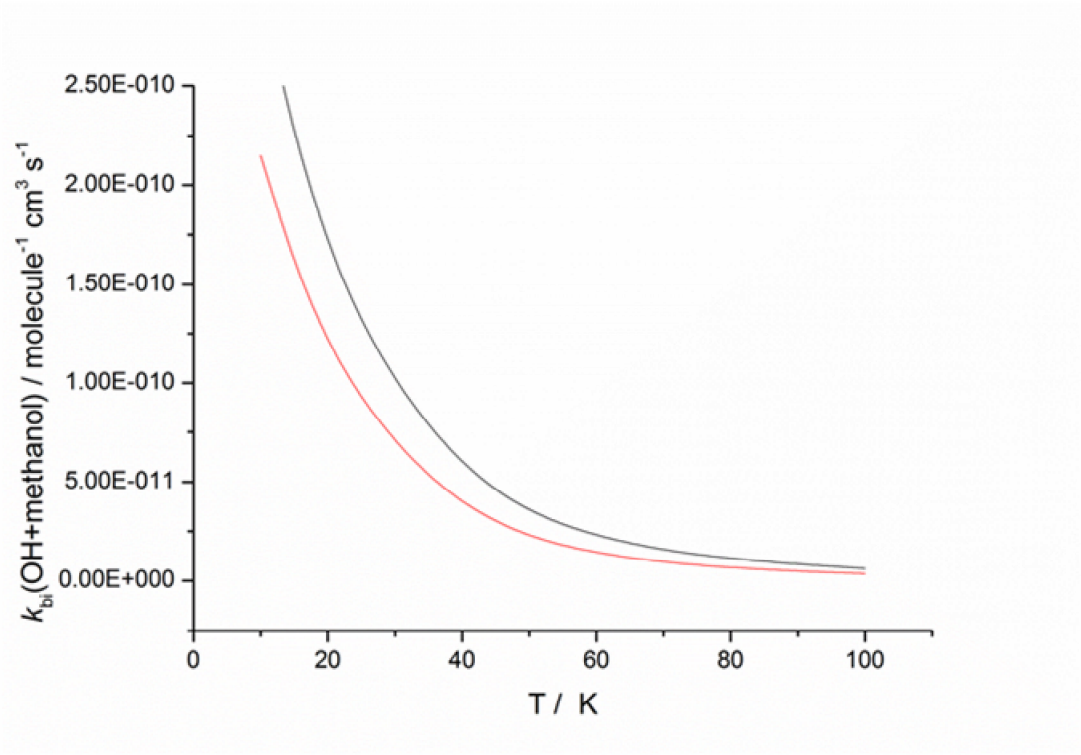

Figure 5.18: k_{bi}(OH+methanol) calculated at a total gas density of 1×10^6 using MESMER. Red line corresponds to calculations using the *ab initio* energies and the black line corresponds to calculations with the energies of TS_M and TS_H reduced by 2 kJ mol^{-1}.

5.3.3. Experimental studies of methoxy radical formation kinetics.

From the master equation calculations, it was predicted that at low temperatures, the dominant abstraction product in the OH + methanol reaction is the methoxy radical, which is produced via the larger of the two abstraction barriers TS1-H. Channel switching at low temperatures due to quantum mechanical tunnelling, has been observed previously, (30) and all ab *initio* studies on TS1-H and TS1-M, predict that TS-H has the larger

imaginary frequency, leading to greater transmission coefficients for this transition state.

To support these theoretical predictions, it was necessary to observe methoxy radical formation experimentally. As has been described in section 5.2.1, the methoxy radical is known to exhibit an LIF spectrum (31, 32) and such a spectrum has been obtained experimentally using the Leeds Laval apparatus (Figure 5.5). Pseudo first order growth traces for methoxy radicals where then obtained by monitoring a single LIF transition within the $\tilde{A}^2A_1$-$\tilde{X}^2E$ band and taking time resolved measurements of the intensity. Such a growth trace is shown in Figure 5.19 and an OH decay trace, at the same [methanol] is also shown for comparison, clearly showing that both OH loss and methoxy growth, occur on a similar timescale.

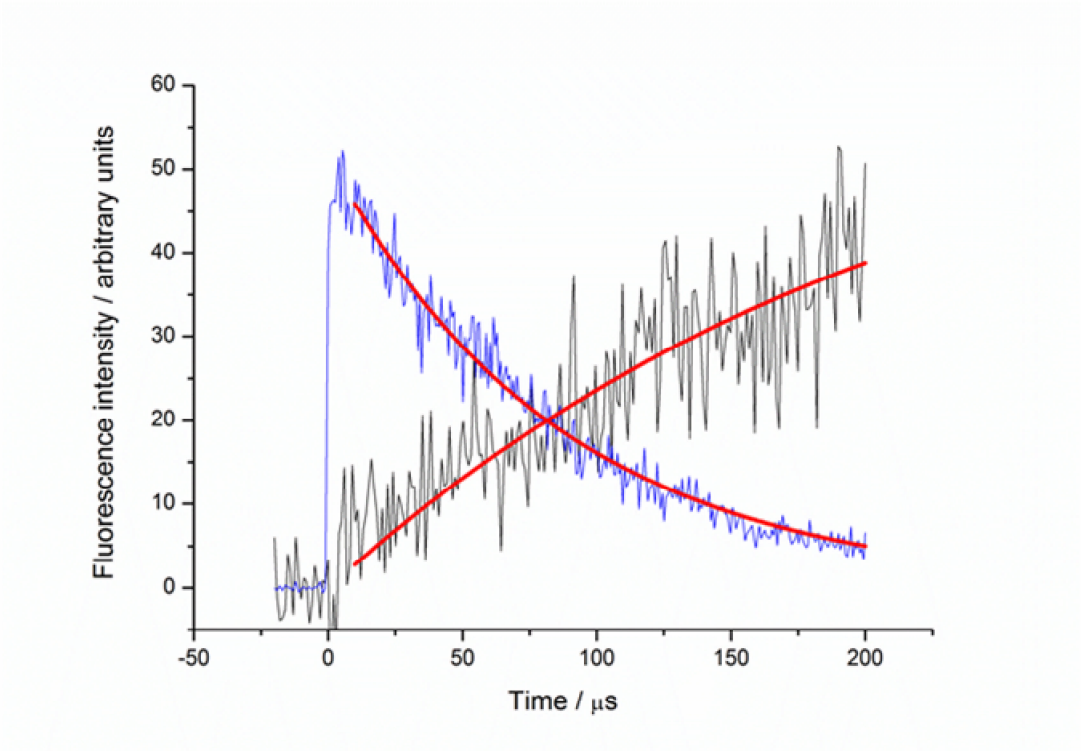

Figure 5.19: Experimental traces showing the growth of methoxy radicals (CH_3O) and the decay of OH radicals at 82 ± 4 K, a total gas density of 5×10^{16} molecule cm^{-3} and [CH_3OH] = 2.06×10^{14} molecule^{-1} cm^3. These two traces give values for the pseudo-first-order rate constant *k′* of 8870 ± 2800 s^{-1} (growth-black) and 8600 ± 580 s^{-1} (decay-black) from fits with Eq. 2 and Eq. 1 respectively, (red lines). The growth trace for CH_3O is scaled by a factor of 20 to aid comparison.

Pseudo first order growth traces were fit with Eq. 2 in order to obtain k'methanol from the methoxy growth data. When fitting these growth traces it was noted that the parameters kd and kdm were poorly defined by the experimental traces and it was found necessary to fix the values of these parameters. This was largely due to the fact that since the methoxy growth could only be collected over 200 μs the traces were too short to properly observe the much slower decay at long times due to the diffusion of the methoxy radical out of the laser detection region. The first order diffusional loss of the OH, k_d was well defined by the OH loss experiments. The intercepts in these experiments varied between 4000 s^{-1} and 5000 s^{-1} and the portion of these intercepts due to reaction between OH + t-BuOOH was estimated to be 1900 s^{-1} from low temperature rate coefficients for OH + t-BuOOH measured by Taylor et al. (33) With these considerations kd was fixed at 3100 s^{-1}. The rate of diffusional loss is proportional to $\sqrt{m}$, where m is the molecular mass, and as such k_{dm} was assigned a value of 2000 cm^{-1}. The resulting bimolecular plot from fitting the methoxy growth traces is shown in Figure 5.20 and yields a bimolecular rate coefficient k_{bi} of (3.6±1.4)×10^{-11} molecule^{-1} cm^3 $s^{-1.}$ In order to explore the error introduced through fixing the values of k_d and k_{dm} these parameters were varied by ± 1000 s^{-1} and new values for k_{bi}(OH+methanol) were determined. The value of k_{bi}(OH+methanol) was found to vary by as much as 1.5×10^{-11} molecule^{-1} cm^3 s^{-1} .

Importantly, even with this large variation, the values of k_{bi}(OH+methanol) obtained though monitoring OH loss and through monitoring methoxy growth still agree within error. The large error on k_{bi}(OH+methanol) measured from methoxy formation, of 1.4×10^{-11} molecule^{-1} cm^3 is understandable considering the poor LIF signal produced by methoxy radicals and this coupled with the uncertainty in the parameters $k_{d,}$ and k_{dm} leads to a relatively inaccurate determination of k_{bi}(OH+methanol) using the methoxy product. However, more accurate values of k_{bi}(OH+methanol) have already been obtained from the OH decay data and the experiments probing methoxy formation show that OH loss and methoxy formation, occur on similar time scales, supporting the arguments presented earlier in this

chapter in showing that even at low temperatures, the OH + methanol reaction proceeds by direct abstraction.

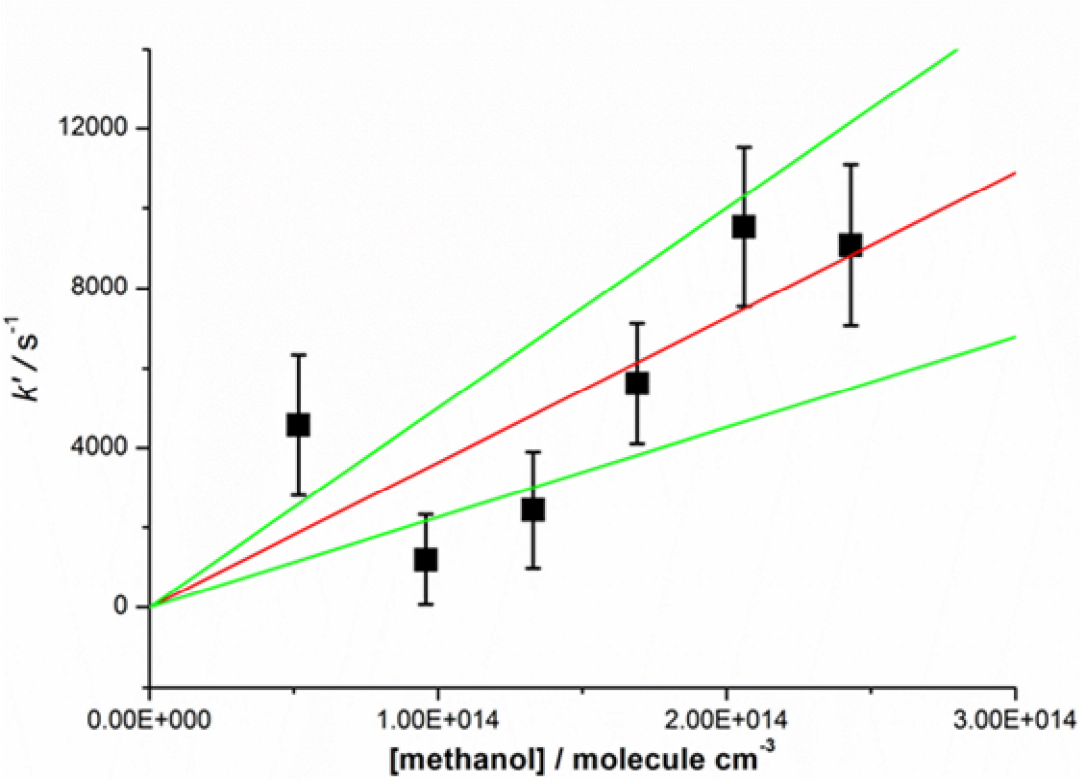

Figure 5.20: Bimolecular plot for methoxy formation from the reaction between OH and methanol at 82±4 K and a total [N_2] of (5.1±0.7) ×10^{16} molecule cm^{-3}. The pseudo first order rate coefficients were obtained from fitting the experimental data with Eq. 3 and they incorporate the 2σ errors both from the fitting process and from [methanol]. The bimolecular rate coefficient was obtained from a weighted linear give a k_{bi}(OH + methanol) = (3.6±1.4)×10^{-11} molecule^{-1} cm^3 s^{-1} with errors obtained from the 95% confidence limits of the linear fit and incorporating the uncertainty in [methanol].

There is one more complication to the methoxy formation data that will be discussed briefly. As will be discussed in Chapter 6, the use of ozone as an OH precursor produces significant populations of OH(v=1,2,3…). (34) The important thing to note in this context, is that in Chapter 6 the rate coefficients for OH (v=1,2,3) + methanol have all been determined to be > 10^{-10} molecule^{-1} cm^3 s^{-1} and the different values of k_{bi}(OH+methanol) from

methoxy formation are all significantly lower than this and in good agreement with k_{bi}(OH+methanol) as measured from the OH loss data.

5.4. Discussion and Conclusions

In this chapter the OH + methanol reaction has been shown to proceed via a novel mechanism involving a hydrogen bonded complex and quantum mechanical tunnelling. This mechanism shows that even with significant energy barriers to products, a bimolecular, zero pressure channel to products can be dramatically enhanced at low temperatures. Similar behaviour was with regards to the OH + acetone, and OH + DME reactions discussed in chapter 4 and it is proposed that such a mechanism is general to any reaction involving both a pre-reaction complex and transfer of a hydrogen atom.

There are two features of the OH + methanol reaction which are particularly interesting. First of all, due in part to both the small number of atoms involved in the OH + methanol reaction, and the extremely efficient quantum mechanical tunnelling, the negative temperature dependence in this reaction is due to an entirely bimolecular abstraction channel, with no stabilisation component at all. This mechanism is confirmed by both the lack of pressure dependence to k_{bi}(OH+methanol) at 83 K and also the observation of methoxy radical formation on the same timescale as OH loss. Secondly, as observed in a recent paper,(34) the majority of the tunnelling at low temperatures, appears to occur through the larger of the two abstraction barriers. Unfortunately, due to the poor signal from measuring methoxy, it has not been possible to assign the yield of methoxy experimentally in the current work, however the fact that methoxy radicals have been observed suggests that this product channel must have a relatively large yield at 83 K, as supported by the master equation analysis.

While both methanol and OH are present with relatively large abundances in the ISM, it is beyond the scope of this study to comment upon the importance of the OH + methanol reaction. However, the true significance of the results presented here and in the preceding chapter, is in highlighting the

generality of the low temperature behaviour of reactions involving both a pre-reaction complex and hydrogen transfer. Two previous studies have shown that tunneling combined with a pre-reaction complex can lead to a negative temperature dependence. (35, 36) However in both these studies the observed negative temperature dependence is modest and no studies have shown that such a mechanism can produce rate coefficients, approaching the capture limit at very low temperatures. It is still accepted that reactions with an overall barrier to products will be unimportant in very low temperature environments, (37) and the results presented here show that this is not the case.

Master equation studies on all three of the OH reactions studies in these two chapters, have been extrapolated down to 10 K, and in all cases, zero pressure rate coefficients on the order of 10^{-10} molecule^{-1} cm^3 s^{-1} have been predicted. Of course, since these are extrapolations, there is some large degree of uncertainty to these predictions. However many of these master equation models can be seen to under predict the negative temperature dependencies observed experimentally and as such, extrapolation of these models can if anything , be viewed as a lower limit to the true rate coefficients for the systems at 10 K. In summary, while the specific reactions studied here show fascinating negative temperature dependencies to their rate coefficients, from these results we would propose that a great number of similar reactions, which occur over a barriered PES, would exhibit similar behaviour under ISM conditions.

5.5. References

1. ATKINSON, R., D.L. BAULCH, R.A. COX, J.N. CROWLEY, R.F. HAMPSON, R.G. HYNES, M.E. JENKIN, M.J. ROSSI and J. TROE. Evaluated kinetic and photochemical data for atmospheric chemistry: Volume I - gas phase reactions of Ox, HOx, NOx and SOx species. *Atmospheric Chemistry and Physics*, 2004, 4, pp.1461-1738.

2. SINGH, H.B., L.J. SALAS, R.B. CHATFIELD, E. CZECH, A. FRIED, J. WALEGA, M.J. EVANS, B.D. FIELD, D.J. JACOB, D. BLAKE, B. HEIKES, R. TALBOT, G. SACHSE, J.H. CRAWFORD, M.A. AVERY, S. SANDHOLM

and H. FUELBERG. Analysis of the atmospheric distribution, sources, and sinks of oxygenated volatile organic chemicals based on measurements over the Pacific during TRACE-P. *Journal of Geophysical Research-Atmospheres*, 2004, 109(D15).

3. HEIKES, B.G., W.N. CHANG, M.E.Q. PILSON, E. SWIFT, H.B. SINGH, A. GUENTHER, D.J. JACOB, B.D. FIELD, R. FALL, D. RIEMER and L. BRAND. Atmospheric methanol budget and ocean implication. *Global Biogeochemical Cycles*, 2002, 16(4).

4. THOMAS, C.E., B.D. JAMES, F.D. LOMAX and I.F. KUHN. Fuel options for the fuel cell vehicle: hydrogen, methanol or gasoline? *International Journal of Hydrogen Energy*, 2000, 25(6), pp.551-567.

5. BOTT, J.F. and N. COHEN. A Shock-Tube Study of the Reactions of the Hydroxyl Radical with Several Combustion Species. *International Journal of Chemical Kinetics*, 1991, 23(12), pp.1075-1094.

6. OVEREND, R. and G. PARASKEVOPOULOS. Rates of Oh Radical Reactions .4. Reactions with Methanol, Ethanol, 1-Propanol, and 2-Propanol at 296-K. *Journal of Physical Chemistry*, 1978, 82(12), pp.1329-1333.

7. RAVISHANKARA, A.R. and D.D. DAVIS. Kinetic Rate Constants for Reaction of Oh with Methanol, Ethanol, and Tetrahydrofuran at 298-K. *Journal of Physical Chemistry*, 1978, 82(26), pp.2852-2853.

8. MCCAULLEY, J.A., N. KELLY, M.F. GOLDE and F. KAUFMAN. Kinetic-Studies of the Reactions of F and Oh with Ch3oh. *Journal of Physical Chemistry*, 1989, 93(3), pp.1014-1018.

9. NELSON, L., O. RATTIGAN, R. NEAVYN, H. SIDEBOTTOM, J. TREACY and O.J. NIELSEN. Absolute and Relative Rate Constants for the Reactions of Hydroxyl Radicals and Chlorine Atoms with a Series of Aliphatic-Alcohols and Ethers at 298-K. *International Journal of Chemical Kinetics*, 1990, 22(11), pp.1111-1126.

10. CROWLEY, J.N., T.J. DILLON, D. HOLSCHER, V. SIVAKUMARAN and A. HOROWITZ. Kinetics of the reactions of HO with methanol (210-351 K) and with ethanol (216-368 K). *Physical Chemistry Chemical Physics*, 2005, 7(2), pp.349-355.

11. WALLINGTON, T.J. and M.J. KURYLO. The Gas-Phase Reactions of Hydroxyl Radicals with a Series of Aliphatic-Alcohols over the Temperature-Range 240-440-K. *International Journal of Chemical Kinetics*, 1987, 19(11), pp.1015-1023.

12. JIMENEZ, E., M.K. GILLES and A.R. RAVISHANKARA. Kinetics of the reactions of the hydroxyl radical with CH3OH and C2H5OH between 235 and 360 K. *Journal of Photochemistry and Photobiology a-Chemistry*, 2003, 157(2-3), pp.237-245.

13. HESS, W.P. and F.P. TULLY. Hydrogen-Atom Abstraction from Methanol by Oh. *Journal of Physical Chemistry*, 1989, 93(5), pp.1944-1947.

14. WEINREB, S., A.H. BARRETT, J.C. HENRY and M.L. MEEKS. Radio Observations of Oh in Interstellar Medium. *Nature*, 1963, 200(490), pp.829-&.

15. HARJU, J., A. WINNBERG and J.G.A. WOUTERLOOT. The distribution of OH in Taurus Molecular Cloud-1. *Astronomy and Astrophysics*, 2000, 353(3), pp.1065-1073.

16. HERBST, E. Methanol in Space and in the Laboratory. *Atoms, ions and molecules: New results in spectral line astrophysics, ASP Conference Series (ASP: San Francisco)*, 1991, 16, p.313.

17. MEIER, U., H.H. GROTHEER and T. JUST. Temperature-Dependence and Branching Ratio of the Ch3oh+Oh Reaction. *Chemical Physics Letters*, 1984, 106(1-2), pp.97-101.

18. XU, S. and M.C. LIN. Theoretical study on the kinetics for OH reactions with CH3OH and C2H5OH. *Proceedings of the Combustion Institute*, 2007, 31, pp.159-166.

19. GALANO, A., J.R. ALVAREZ-IDABOY, G. BRAVO-PEREZ and M.E. RUIZ-SANTOYO. Gas phase reactions of C-1-C-4 alcohols with the OH radical: A quantum mechanical approach. *Physical Chemistry Chemical Physics*, 2002, 4(19), pp.4648-4662.

20. ATKINSON, R., D.L. BAULCH, R.A. COX, R.F. HAMPSON, J.A. KERR, M.J. ROSSI and J. TROE. Evaluated kinetic and photochemical data for atmospheric chemistry: Supplement VI - IUPAC subcommittee on gas kinetic data evaluation for atmospheric chemistry. *Journal of Physical and Chemical Reference Data*, 1997, 26(6), pp.1329-1499.

21. BAASANDORJ, M., D.K. PAPANASTASIOU, R.K. TALUKDAR, A.S. HASSON and J.B. BURKHOLDER. (CH(3))(3)COOH (tert-butyl hydroperoxide): OH reaction rate coefficients between 206 and 375 K and the OH photolysis quantum yield at 248 nm. *Physical Chemistry Chemical Physics*, 2010, 12(38), pp.12101-12111.

22. KNOWLES, P.J., C. HAMPEL and H.J. WERNER. Coupled-Cluster Theory for High-Spin, Open-Shell Reference Wave-Functions. *Journal of Chemical Physics*, 1993, 99(7), pp.5219-5227.

23. MOLPRO IS A PACKAGE OF AB INITIO PROGRAMS WRITTEN BY H.-J. WERNER, P.J.K., G. KNIZIA, F. R. MANBY, M. SCHÜTZ, P. CELANI, T. KORONA, R. LINDH, A. MITRUSHENKOV, G. RAUHUT, K. R. SHAMASUNDAR, T. B. ADLER, R. D. AMOS, A. BERNHARDSSON, A. BERNING, D. L. COOPER, M. J. O. DEEGAN, A. J. DOBBYN, F. ECKERT, E. GOLL, C. HAMPEL, A. HESSELMANN, G. HETZER, T. HRENAR, G. JANSEN, C. KÖPPL, Y. LIU, A. W. LLOYD, R. A. MATA, A. J. MAY, S. J. MCNICHOLAS, W. MEYER, M. E. MURA, A. NICKLAß, D. P. O'NEILL, P. PALMIERI, K. PFLÜGER, R. PITZER, M. REIHER, T. SHIOZAKI, H. STOLL, A. J. STONE, R. TARRONI, T. THORSTEINSSON, M. WANG, A. WOLF . .

24. LEE, T.J. and P.R. TAYLOR. A Diagnostic for Determining the Quality of Single-Reference Electron Correlation Methods. *International Journal of Quantum Chemistry*, 1989, pp.199-207.

25. LEE, T.J. Comparison of the T-1 and D-1 diagnostics for electronic structure theory: a new definition for the open-shell D-1 diagnostic. *Chemical Physics Letters*, 2003, 372(3-4), pp.362-367.

26. WERNER, H.J. Third-order multireference perturbation theory - The CASPT3 method. *Molecular Physics*, 1996, 89(2), pp.645-661.

27. Gaussian. Gaussian 03, Revision C.02, M. J. Frisch, G. W. Trucks, H. B. Schlegel, G. E. Scuseria, M. A. Robb, J. R. Cheeseman, J. A. Montgomery, Jr., T. Vreven, K. N. Kudin, J. C. Burant, J. M. Millam, S. S. Iyengar, J. Tomasi, V. Barone, B. Mennucci, M. Cossi, G. Scalmani, N. Rega, G. A. Petersson, H. Nakatsuji, M. Hada, M. Ehara, K. Toyota, R. Fukuda, J. Hasegawa, M. Ishida, T. Nakajima, Y. Honda, O. Kitao, H. Nakai, M. Klene, X. Li, J. E. Knox, H. P. Hratchian, J. B. Cross, V. Bakken, C. Adamo, J. Jaramillo, R. Gomperts, R. E. Stratmann, O. Yazyev, A. J. Austin, R. Cammi, C. Pomelli, J. W. Ochterski, P. Y. Ayala, K. Morokuma, G. A. Voth, P. Salvador, J. J. Dannenberg, V. G. Zakrzewski, S. Dapprich, A. D. Daniels, M. C. Strain, O. Farkas, D. K. Malick, A. D. Rabuck, K. Raghavachari, J. B. Foresman, J. V. Ortiz, Q. Cui, A. G. Baboul, S. Clifford, J. Cioslowski, B. B. Stefanov, G. Liu, A. Liashenko, P. Piskorz, I. Komaromi, R. L. Martin, D. J. Fox, T. Keith, M. A. Al-Laham, C. Y. Peng, A. Nanayakkara, M. Challacombe, P. M. W. Gill, B. Johnson, W. Chen, M. W. Wong, C. Gonzalez, and J. A. Pople, Gaussian, Inc., Wallingford CT, 2004.

28. ROBERTSON, S.H., GLOWACKI, D. R., LIANG, C.-H.; MORLEY, C., PILLING, M. J.,. MESMER. *(Master Equation Solver for Multi-Energy Well Reactions), 2008; an object oriented C++ program for carrying out ME calculations and eigenvalue-eigenvector analysis on arbitrary multiple well systems.* *http://sourceforge.net/projects/mesmer*.

29. MILLER, W.H. Tunneling Corrections to Unimolecular Rate Constants, with Application to Formaldehyde. *Journal of the American Chemical Society*, 1979, 101(23), pp.6810-6814.

30. SCHREINER, P.R., H.P. REISENAUER, D. LEY, D. GERBIG, C.H. WU and W.D. ALLEN. Methylhydroxycarbene: Tunneling Control of a Chemical Reaction. *Science*, 2011, 332(6035), pp.1300-1303.

31. LIU, X.M., C.P. DAMO, T.Y.D. LIN, S.C. FOSTER, P. MISRA, L. YU and T.A. MILLER. Free Jet-Cooled Laser-Induced Fluorescence-Spectrum of Methoxy Radical .2. Rotational Analysis of the A2a1 [--] X2e Electronic-Transition. *Journal of Physical Chemistry*, 1989, 93(6), pp.2266-2275.

32. FOSTER, S.C., P. MISRA, T.Y.D. LIN, C.P. DAMO, C.C. CARTER and T.A. MILLER. Free Jet Cooled Laser-Induced Fluorescence-Spectrum of Methoxy .1. Vibronic Analysis of the a-State and X-State. *Journal of Physical Chemistry*, 1988, 92(21), pp.5914-5921.

33. TAYLOR, S.E., A. GODDARD, M.A. BLITZ, P.A. CLEARY and D.E. HEARD. Pulsed Laval nozzle study of the kinetics of OH with unsaturated hydrocarbons at very low temperatures. *Physical Chemistry Chemical Physics*, 2008, 10(3), pp.422-437.

34. AKER, P.M., J.J.A. OBRIEN and J.J. SLOAN. Energy Partitioning in O(1D) Reactions .1. O(1D)+H2->OH(V')+H. *Chemical Physics*, 1986, 104(3), pp.421-427.

35. HERBST, E. Tunneling in the C2h-H2 Reaction at Low-Temperature. *Chemical Physics Letters*, 1994, 222(3), pp.297-301.

36. XIA, W.S. and M.C. LIN. A multifacet mechanism for the OH+HNO3 reaction: An ab initio molecular orbital/statistical theory study. *Journal of Chemical Physics*, 2001, 114(10), pp.4522-4532.

37. SABBAH, H., L. BIENNIER, I.R. SIMS, Y. GEORGIEVSKII, S.J. KLIPPENSTEIN and I.W.M. SMITH. Understanding reactivity at very low temperatures: The reactions of oxygen atoms with alkenes. *Science*, 2007, 317(5834), pp.102-105.

Chapter 6. Enhanced Low Temperature Reactivity Due to Weak Van der Waals Complexes on Low Temperature Reactivity. The Reactions Between the OH Radical and Acetylene and Ammonia

In the previous two chapters the reactions between the OH radical and the various OVOC's studied, all involved the formation of a hydrogen bonded complex. The presence of this pre-reaction complex was then shown to have dramatic consequences on the rate coefficients as the temperature was reduced. From this work it is clear that even in the low (≈1–10 Torr) pressures of the Laval expansion, such complexes can exhibit significant lifetimes but, these hydrogen bonded complexes have significantly larger binding energies (≈20 kJ mol^{-1}) than a typical van der Waals complex.

In this chapter, two OH radical reactions are considered in which only dipole – dipole or dipole – induced dipole attractions are present between the OH moiety and the co-reagent. The pre-reaction complexes involved in these reactions are consequently much more weakly bound and the extent to which even these weakly bound complexes affect the kinetics at low temperatures will be explored.

6.1. The OH + acetylene (C_2H_2) reaction.

6.1.1. Introduction

The reaction between OH and acetylene is important in a number of environments. (1) (2) Primarily, previous studies have focussed on the role of this reaction under either combustion or atmospheric conditions. However, acetylene is also interesting from a low temperature point of view since it has been observed in large abundances in the atmospheres of some of the outer planets such as Saturn (3) and in particular Saturn's moon Enceladus. (4) In the atmosphere of Enceladus, acetylene has been observed in plumes of water vapour, originating from cracks in Enceladus' icy surface. (5) These plumes are attracting scientific interest in the field of astrobiology (6) and

acetylene is one of the more abundant chemical species in these plumes with a mixing ratio of (3.3±2) $\times 10^{-3}$. (4)

The OH + acetylene reaction has been studied extensively (7) in the literature and the previous studies can be split broadly into two categories focussing on either the temperature dependence of the rate coefficients of this system up to high temperatures relevant to combustion (T>450 K) (8-12) or upon the reaction at 295 K, more relevant to the Earth's atmosphere. (13, 14) The OH + acetylene reaction proceeds via two different mechanisms in different temperature regimes. To help elucidate the reaction mechanism theoretical studies have extensively studied the stationary points on the OH + acetylene potential energy surface (15, 16) and the potential energy surface (PES) calculated by McKee *et al.* (15) is shown in Figure 6.1 in order to illustrate this.

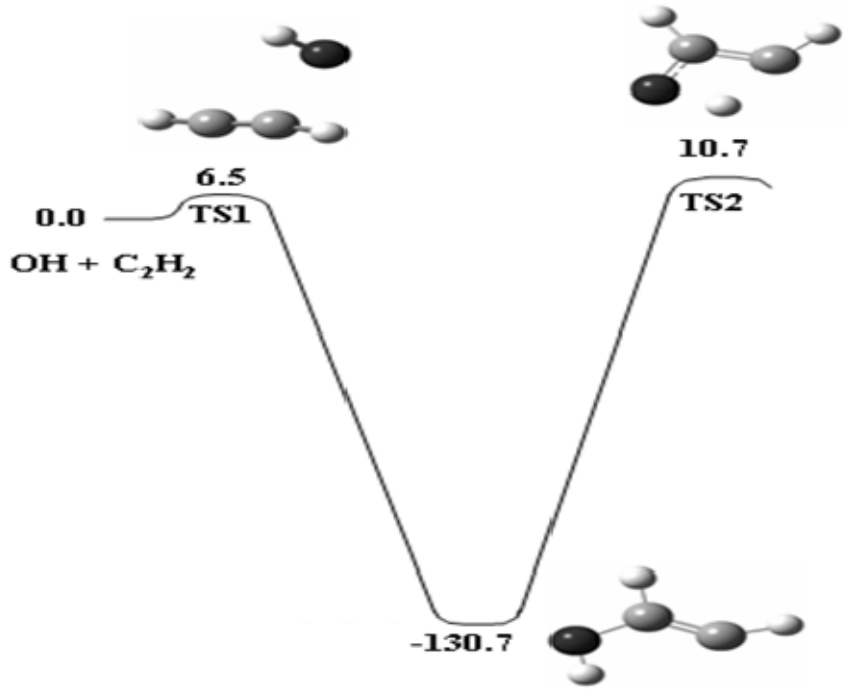

Figure 6.1: Stationary points on the OH + acetylene potential energy surface taken from McKee et al. (15). The energy values show the electronic and zero point energies for each species relative to the OH + acetylene reagents and these were calculated at the CBS-QCI/APNO//B3LYP/6-311+G(3df,2p) level of theory. The structures show the geometries of each stationary point and these were also taken from calculations performed by McKee et al. (15)

At high temperatures (T>1000 K) relevant to combustion conditions, the reaction proceeds via direct abstraction over TS2 to form a number of different bimolecular products (R1-R5) via exothermic channels.

$$OH + C_2H_2 \rightarrow H_2O + C_2H \quad (R1)$$

$$\rightarrow H + HCCOH \quad (R2)$$

$$\rightarrow H_2 + HCCO \quad (R3)$$

$$\rightarrow H + CH_2CO \quad (R4)$$

$$\rightarrow CH_3 + CO \quad (R5)$$

At lower temperatures relevant to the Earth's atmosphere the higher barrier TS2 becomes energetically inaccessible and TS1 becomes the dominant bottleneck to reaction. Under these conditions the reaction mechanism is as follows.

$$OH + C_2H_2 \leftrightarrows C_2H_2OH^* \quad (R6)$$

$$C_2H_2OH^* + M \rightarrow C_2H_2OH \quad (R7)$$

The mechanism above is in the form of a Lindemann type mechanism and the rate coefficients for the OH + acetylene reaction have been shown to display pressure dependence up to 800 K. (17) However there is a 6.5 kJ mol^{-1} (15) barrier to the formation of the C_2H_2OH adduct and as such this channel is likely to be inoperable at the low temperatures of a Laval nozzle expansion. Although it is not shown in the simplified PES above, there is however a van der Waals complex prior to TS1. The complex has been characterised both spectroscopically and theoretically (18) and its binding energy has been determined to be 13.3 kJ mol^{-1} relative to the separated OH and acetylene reactants at the RCCSD(t) level of theory extrapolated to the complete basis set (CBS) limit. (18)

This then raises the question of whether at low temperatures it is possible to collisionally stabilise the excited van der Waals complex. There is some discrepancy over this in the literature. In a review paper by Hansmann *et al.* (19) a graph was presented, showing measurements of the OH + acetylene rate constant at 70 K and a total gas density 9×10^{16} molecule cm^{-3}. This

graph indicated a bimolecular rate coefficient for OH+ acetylene of ≈ 3×10^{-12} molecule^{-1} cm^3 s^{-1}.

Contrary to this measurement Taylor *et al.* (20) have studied this reaction at 69 K and 3.7×10^{16} molecule cm^{-3} and were unable to observe any reaction and instead assigned an upper limit to the rate coefficient of 1×10^{-12} molecule^{-1} cm^3 s^{-1}. If empirical arguments based upon ionisation energies are used (21), as described in section 2.1.2, it is found that for OH + acetylene, I.E-Ea = 9.57 eV (21) and it would therefore be predicted that this reaction should be slow at room temperature. However, the two previous experimental measurements are not necessarily contradictory since at the substantially higher total gas densities used by Hansmann *et al.* (20) it is possible that they were able to observe complex stabilisation that Taylor *et al.* (19) were not.

6.1.2. Methods

6.1.2.1. Experimental

The rate coefficient for the reaction between OH + acetylene was measured at 79±3 K and a total gas density of $(1.7\pm0.2)\times10^{17}$ molecule cm^{-3} using the T81Pvar nozzle. These experiments were carried out as described in chapter 3. For these experiments neat acetylene (BOC >99.5%) was introduced to the reaction chamber directly from the cylinder and N_2 (BOC OFN) was used as the bath gas. Tertiary butyl hydroperoxide (t-BuOOH) (Sigma Aldrich 70% aqueous) was used as an OH precursor and this was admitted to the system via a bubbler through which a small flow (~300 sccm) of N_2 was passed. Pseudo first order conditions $[C_2H_2]$ >> [OH] were used throughout.

OH radicals were produced through the photolysis of t-BuOOH at 248 nm using excimer laser radiation (Lambda Physic LPX 200) according to reaction shown below.

$$\text{t-BuOOH} + h\nu \rightarrow \text{OH} + \text{other products} \qquad \text{(R8)}$$

A YAG (Spectron Laser Systems SL803) pumped dye laser system (Sirah Gmbh-Cobra Stretch) was then used to generate 282 nm light which was

resonant with the $Q_1(1.5)$ transition in the (1,0) vibrational band of the A-X transition in the OH radical, and the resulting fluorescence was digitised and recorded following integration using an oscilloscope.

To record a pseudo first order kinetic decay, the delay time of the probe laser after the photolysis laser was varied up to 200 μs. Each trace typically consisted of 300 points with each point averaged 20 times and the probe power measured on a photodiode was recorded simultaneously. The resulting LIF signal was then normalised with respect to probe laser power and the decay was fit to the single exponential decay equation Eq .1, in order to obtain the pseudo first order rate coefficient $k'_{acetylene}$:

$$[OH] = [OH]_0 \times \exp(-(k'_{acetylene} + k_i) \times t) \qquad \text{(Eq.1)}$$

where

$$k_i = k_d + k'_{t-BuOOH}$$

$[OH]_0$ is the concentration of OH at time zero, $k'_{acetylene}$ is the pseudo first order rate coefficient for the loss of OH in the presence of acetylene and k_d is the first order loss due to diffusion and $k'_{t\text{-}BuOOH}$ is the pseudo first order rate coefficient for reaction between OH and the t-BuOOH precursor.

6.1.2.2. Computational

In addition to experiments, *ab initio* and master equation calculations have also been performed upon the OH + acetylene reaction. Given the small number of atoms involved in this system, geometry optimisations for the van der Waals complex, acetylene and OH could be carried out using the ROHF-UCCSD(t)/aug-cc-pvdz (22, 23) level of theory using the Molpro suite of *ab inito* software, (24) to calculate the ro-vibrational properties of these species. The calculated and experimental frequencies are shown in Table 6.1. In order to calculate a more accurate binding energy for the van der Waals complex, single point calculations were performed at each stable geometry using the ROHF-UCCSD(t)/aug-cc-pvtz level of theory.

Species	E_{elec} + ZPE / kJ mol^{-1}	Rotational constant / cm^{-1}	Ab inito ν / cm^{-1}
OH	0	19.2	3722
acetylene	0	1.2	366 366 690 690 1968 3384 3378
Vdw complex	-9.0	1.1 0.2 0.1	71 100 213 390 662 687 778 792 2057 3411 3514 3631

Table 6.1: Ro-vibrational and energetic properties of stationary points on the OH + acetylene potential energy surface. Vibrational and rotational frequencies were obtained from ab initio calculations at the ROHF-UCCSD(t)/aug-cc-pvdz level of theory and relative energies were obtained from single ROHF-UCCSD(t)/aug-cc-pvtz calculations on the located minima.

Using these *ab initio* data, master equation simulations using MESMER, (25) were carried out on the association of OH + C_2H_2 to form the Van der Waals complex. For these calculations ro-vibrational densities of state were calculated using a rigid rotor-harmonic oscillator approximation for all modes. The rate coefficients for the association were the calculated using an inverse laplace transform (ILT) (26) method in which the ILT A factor was set 3×10^{-10} $molecule^{-1}$ s^{-1} as has been discussed in previous chapters and the parameter n describing the temperature dependence of the OH+acetylene high pressure limit was set to zero. Energy transfer was described using an exponential down model and the parameter ΔE_{down} was varied in order to maximise agreement with the low temperature experimental results. Lennard Jones parameters for the complex were estimated by using the Lennard Jones σ and for C_2H_2 of 2.5 Å and 5 K respectively. (27) In all master equation simulations, a grain size of 10 cm^{-1} was sufficiently small for the results to be converged with respect to a reduction in the grain size.

6.1.3. Results and analysis.

A typical OH decay due to reaction with acetylene is shown in Figure 6.2. The resulting bimolecular plot for the OH + acetylene reaction is shown in Figure 6.3 with experimental conditions given within the caption. This plot gives a rate coefficient of $(2.5 \pm 0.6)\times10^{-12}$ molecule^{-1} cm^3 s^{-1} where the quoted errors are at the 2σ level incorporating the 95% confidence limits shown in green. The measured rate coefficient agrees well with the measurements of Hansmann *et al.* (19) and provides good evidence that even stabilisation into a weak van der Waals well can be significant as the temperature is lowered.

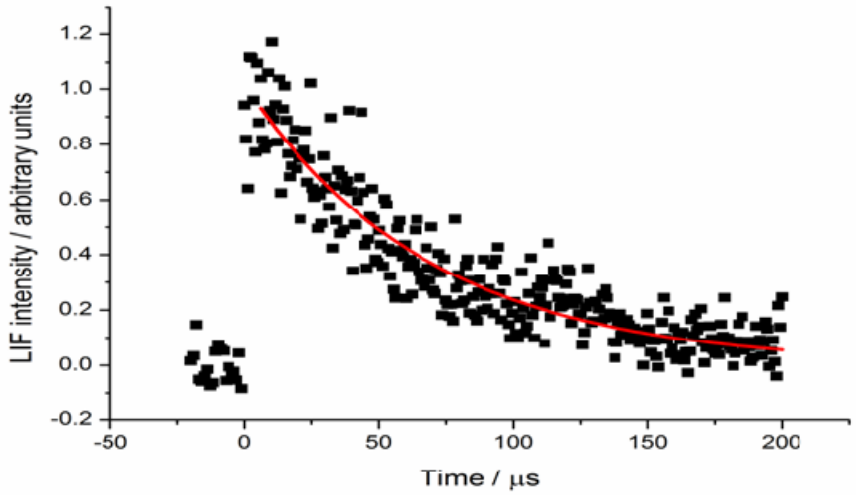

Figure 6.2: Temporal evolution of the LIF signal for OH in the presence of acetylene. For the current trace [acetylene] = 2.9×10^{15} molecule cm^{-3}, [N_2] = 1.7×10^{17} molecule cm^{-3} and [t-BuOOH]≈ 3.1×10^{14} and fitting Eq.1 to the data gives a pseudo first order rate coefficient $k'_{acetylene} + k_i$ of 14900 ± 1100 s^{-1} This trace consists of a total of 220 points and each point was averaged 10 times. The LIF signal was normalised with respect to probe laser power on a point-by-point basis.

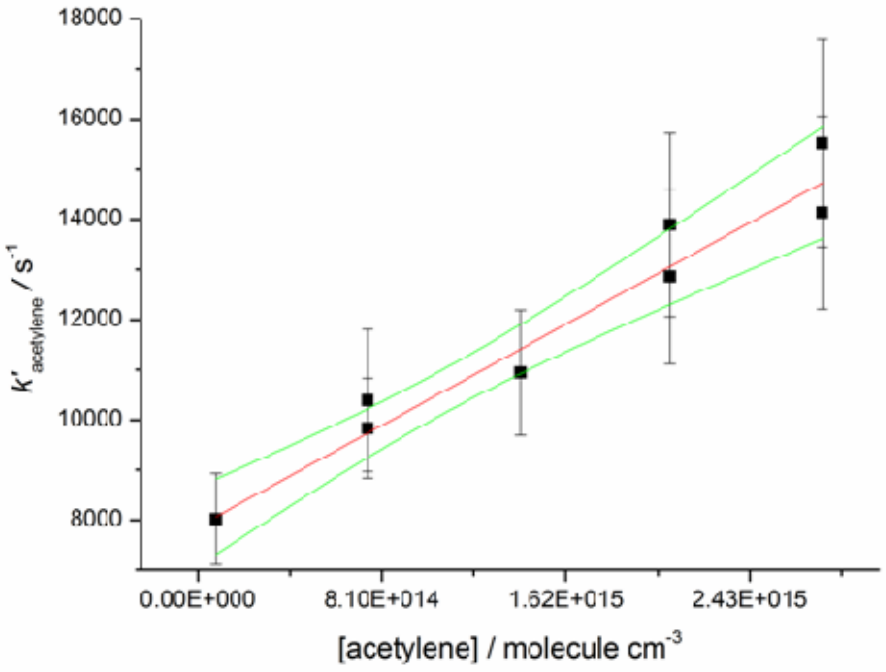

Figure 6.3: Bimolecular plot for the OH + acetylene reaction at 79K and a total gas density of 1.7×10^{17} molecule cm^{-3}. The pseudo first order rate coefficients were obtained from fitting Eq. 1 to the data and they incorporate the 2σ errors both from the fitting process and from [acetylene]. The bimolecular rate coefficient obtained from a weighted linear is k_{bi}(OH + acetylene) = $(2.5\pm0.6)\times10^{-12}$ molecule^{-1} cm^3 s^{-1} with errors obtained from the 95% confidence limits of the linear fit.

It is easy to rationalise why Taylor *et al.* (20) could not observe a measurable loss of OH. Although the current experiments are performed at higher temperatures, 79 K rather than 67 K, the total gas density is almost a factor of 6 larger in the current study and this is likely to promote the rate of stabilisation of the complex significantly. In the current experiments there is also the advantage that due to the larger total densities a large [acetylene] could be added without altering the conditions of the stable flow and as such a larger pseudo first order decays rates could be obtained, leading to a more accurate bimolecular plot.

To support the experimental results a master equation simulation was carried out upon the OH+C_2H_2 reaction at 79K and a total gas density of 1.7×10^{17} molecule cm^{-3} . The rate coefficients obtained from these calculations are plotted versus ΔE_{down} in Figure 6., and from these

calculations it can be seen that regardless of the value for ΔE_{down} chosen, the master equation rate coefficients significantly under predict the experimental value.

A similar effect was observed in sections 4.1.3 and 4.2.3 and in the case of OH + acetone the well depth had to be increased by at least 6 kJ in order to correctly predict the experimentally observed rate coefficients and when hindered rotors were not accounted for the well depth in the OH + acetone case had to be reduced by 16 kJ mol^{-1}. Although in the OH+ acetylene van der Waals complex, there are no obvious modes corresponding to hindered internal rotations, there are still a number of low frequency modes which are likely to be highly anharmonic, and poorly described by a harmonic oscillator approximation. Also shown on Figure 6.4 are theoretical rate coefficients for the case where the well depth of the OH + acetylene complex has been lowered by 4 kJ mol^{-1} and 8 kJ mol^{-1} respectively and it can be seen that by increasing the well depth, the agreement between experiment and theory is improved.

The results from these master equation calculations were then extended up to 6 bar total pressure in order to gain an insight in the rates at which weakly bound adducts are stabilised in extra-terrestrial atmospheres. These results are not necessarily, particularly relevant to the OH + acetylene reaction itself, since Enceladus has only a trace atmosphere. However, such an extrapolation does give an insight into the rate at which similarly weakly bound association adducts may be stabilised in the atmospheres of extra-terrestrial planets. In these calculations the extrapolation is performed using two well depths for the van der Waals complex, the *ab initio* well depth of 9 kJ mol^{-1} and an increased well depth of 17 kJ mol^{-1}. The rate coefficients calculated using the well depth of 17 kJ mol^{-1} are likely to give a more accurate representation of the true rate coefficients since this model was shown to yield the best agreement between experiment and theory in Figure 6.4. With a well depth of 9 kJ mol^{-1}, Figure 6.4 shows that the calculated rate coefficients underpredict the experiments by over an order of magnitude so the extrapolated rate coefficients using this model are likely to represent a lower bound to the true rate coefficients.

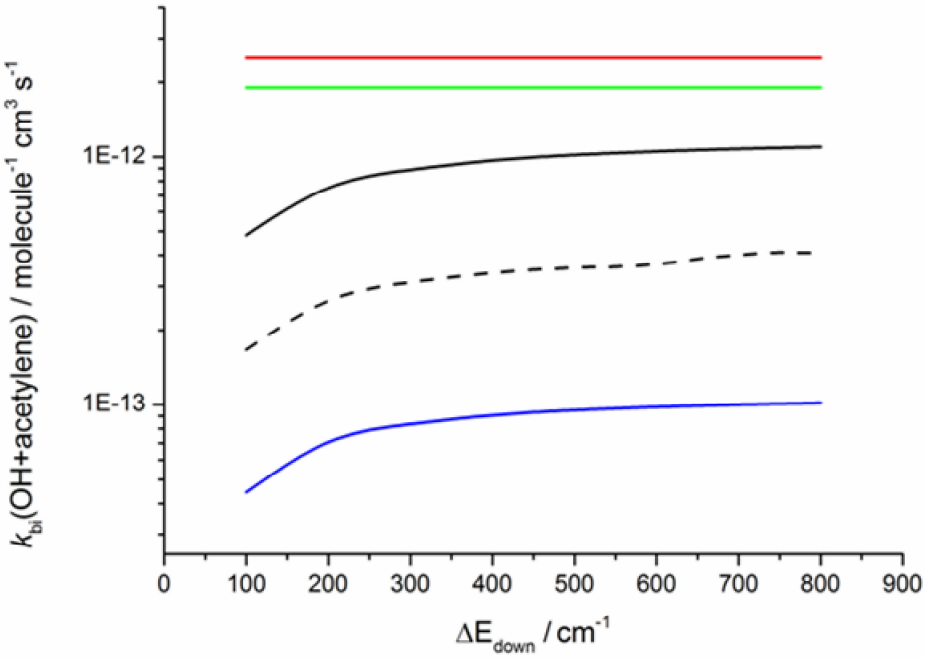

Figure 6.4: Variation in k_{bi} (OH + acetylene) calculated by MESMER (25) with different values of ΔE_{down}. These calculations were performed at 79 K and a total gas density of 1.7 × 10^{17} molecule cm^{-3} using the potential energy surface described in section 6.1.2.2. Different values were used the the well depth of the van der Waals complex, 9 kJ mol^{-1} (blue line), 13 kJ mol^{-1} (black dashed line) and 17 kJ mol^{-1} (solid black line) A grain size of 10 cm^{-1} was used in these calculations. The red line represents the experimental value measured at 79 K whilst the green line shows the lower error on this value at the 2σ level.

Figure 6.5 shows the variation in the calculated rate coefficient with pressure. These calculations were performed at 79 K using a value of 500 cm^{-1} for ΔE_{down}. These calculations predict that under conditions relevant to the atmosphere of Titan the rate coefficient for OH loss in the presence of acetylene will have reached 1.3×10^{-10} molecule^{-1} cm^3 s^{-1} and 3.7×10^{-11} molecule^{-1} cm^3 s^{-1} with a van der Waals well depth of 17 kJ mol^{-1} and 9 kJ mol^{-1}. Although the OH + acetylene reaction may not be relevant to the atmosphere of Titan, these results hint that weakly bound association adducts which are generally not considered in reactive potential surfaces, could be a significant sink for separated reactants in many types of reaction.

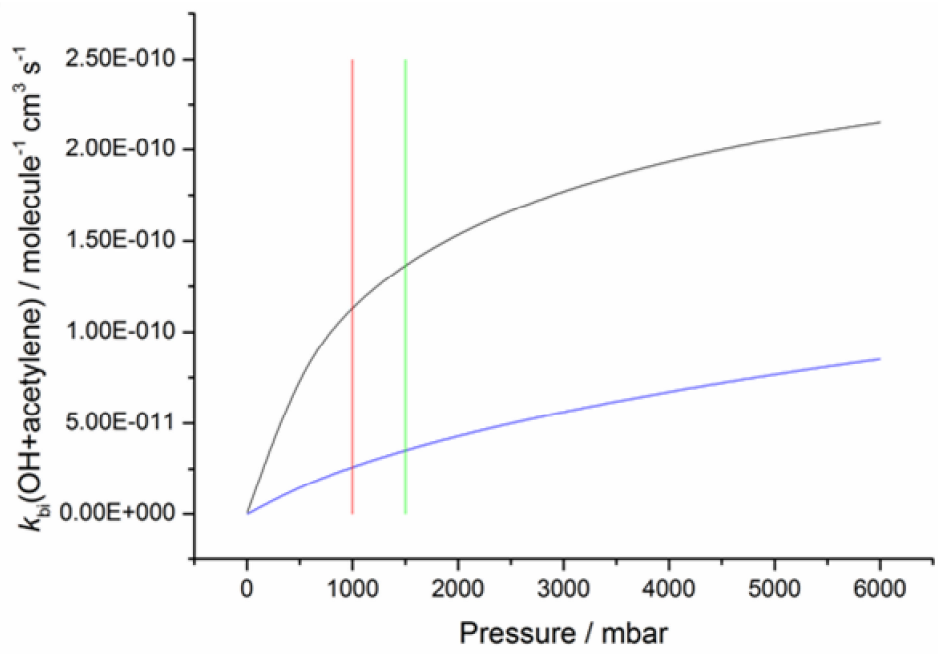

Figure 6.5: Variation in k_{bi} (OH + acetylene) with pressure as calculated using MESMER (25) using van der Waals well depths of 17 kJ mol^{-1} (black line) and 9 kJ mol^{-1} (blue line) . These calculations were performed at a temperature of 79 K and ΔE_{down} was set to 500 cm^{-1}. Details of these calculations are given in section 6.1.2.2. Here the red line marks the surface pressure of Earth whilst the green line marks the surface pressure of Titan

6.2. The OH + ammonia (NH_3) reaction.

6.2.1. Introduction

In the context of low temperature environments, ammonia is an important species. Like acetylene, there have been observations of ammonia in the water plumes of Enceladus (4) and ammonia has also been observed in star forming regions within the ISM (28). Compared to the reactions between OH and small VOC molecules that have been mentioned thus far, the reaction between OH and ammonia has been the subject of only a few studies, and no studies have investigated the kinetics of either NH_3 or indeed any other amines at low temperatures.

Most of the experimental studies of the OH + NH_3 rate coefficient have been confined to the 273-500K (29-33) regime but studies by Silver and Kolb (34) and Jeffries and Smith (35) have extended this range up to 1425 K. Relative

to the other reactions studied in this thesis, the OH+NH_3 reaction is slow, with a rate coefficient of between 1.4×10^{-13} and 1.7×10^{-13} at 300K. These results indicate the presence of a substantial barrier to products. However, it can also be seen that the OH + NH_3 rate coefficients display a slight deviation from Arrhenius behaviour at low temperatures, perhaps indicating an effect from quantum mechanical tunnelling.

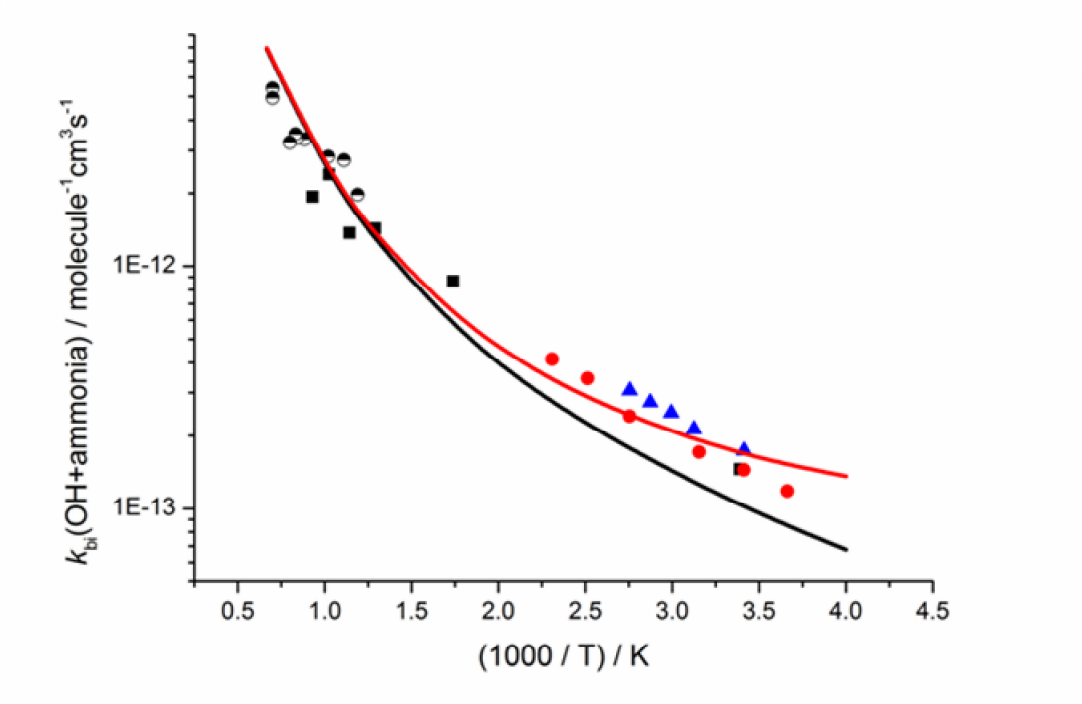

Figure 6.6: Comparision between previous experimental and theoretical studies of the OH + ammonia reaction. Individual data points correspond to experimentally measured rate coefficients. Black and white circles are measurements by Jeffries and Smith(35), black squares are measurments by Silver and Kolb(34), red circles are measurements by Diau et al. (29) and blue triangles are measurements by Stephens (31). The black and red lines correspond to calculations by Corchado et al. (36) using the small-curvature tunnelling and microcanonical optimised multidimensional tunnelling methods respectively.

Only one study has performed *ab initio* calculations upon the OH + NH_3 system. These calculations were performed by Corchado *et al.* (36) using a number of different levels of theory in order to build a potential energy surface upon which reaction path dynamics could be performed. This study also calculated the rate coefficients for the reaction using canonical variational transition state theory. These calculations included sophisticated

tunnelling calculations in the form of small-curvature tunnelling (SCT), (37) and a microcanonical optimised multidimensional tunnelling approach (μOMT). (38) The SCT method is a one dimensional method, which assumes that the dominant tunnelling effect occurs along the reaction co-ordinate, whereas the μOMT method is a multi dimensional tunnelling approach which incorporates tunnelling along paths orthogonal to the reaction coordinate. (39) Figure 6.6 shows a comparison between rate coefficients calculated using these two methods, and the experimental data available in the literature, and it is observed that the μOMT method is required to give qualitative agreement to the experimental rate coefficient at low temperatures, suggesting that OH + NH_3 rate coefficients are affected substantially by tunnelling.

6.2.2. Methods

6.2.2.1. Experimental

The rate coefficient for the reaction between OH + ammonia was measured at 81 and 79 K with total gas densities of 1.7×10^{17} molecule cm^{-3} and 6.1×10^{16} molecule cm^{-3}. These experiments were carried out as described in Section 3.3.2. For these experiments ammonia (BOC, 99.98% purity) was admitted to an empty cylinder and diluted with N_2 (BOC, OFN) before being left over night to mix. OH radicals were produced using two different methods, photolysis of t-BuOOH (Sigma Aldrich 70% aqueous) and photolysis of acetone (Fluka, Riedel-deHaėn, analytical grade 99.5%) in the presence of O_2 (BOC, analytical grade) as used for the acetone experiments in Chapter 4. Both of these precursors were admitted to the reaction chamber via a bubbler through which N_2 was flowed. For the experiments using acetone as a precursor O_2 was added to the system directly from the cylinder. Pseudo first order conditions $[NH_3] >> [OH]$ were used throughout.

OH radicals were produced through excimer photolysis of acetone (R9-10) or t-BuOOH (R8) at 248nm.

$$CH_3C(O)CH_3 + h\nu \rightarrow CH_3CO + CH_3 \qquad \text{(R9)}$$

$$CH_3CO + O_2 \rightarrow OH + CH_2OO \qquad \text{(R10)}$$

The OH radicals were subsequently probed at 282 nm using a YAG pumped dye laser.

Using these two different precursors, time resolved OH decays were obtained. For both precursors the experimental traces typically consisted of 300 points and the traces were recorded up to a maximum delay time between the lasers of 200 μs. Traces were typically averaged 20 times per point and normalised with respect to the laser power measured on a photodiode before analysis. Fitting equations where then used to extract $k'_{ammonia} + k_i$. For the t-BuOOH case Eq. 3 was fit to the experimental data and for the acetone case, Eq. 2 was used:

$$[OH] = \frac{[CH_3CO]_0 k'_{10}}{k'_{10} - k'_{ammonia} + k_d}[\exp(-((k'_{ammonia} + k_i)\cdot t) - \exp(-k'_{10}\cdot t)] \quad \text{(Eq. 2)}$$

$$[OH] = [OH]_0 \times \exp(-(k'_{ammonia} + k_i)\times t) \quad \text{(Eq. 3)}$$

where $[CH_3CO]_0$ is the initial concentration of CH_3CO produced from reaction R9, k'_{10} is the pseudo first order rate coefficient for R10 (i.e $k'_{10} = k_{10}[O_2]$), $k'_{ammonia}$ is the pseudo first order rate coefficient for OH loss in the presence of ammonia, k_i is the pseudo first order rate coefficient for OH loss due to the sum of diffusion and reaction with the precursor.

6.2.2.2. Computational details

In addition to experiments, *ab initio*, and master equation calculations have also been performed upon the OH + ammonia reaction. As was the case with OH + acetylene, the stationary points on the OH + ammonia PES were carried out at the accurate RHF-CCSD(T)/aug-cc-pvdz// RHF-CCSD(T)/aug-cc-pvtz (22, 23) using the Molpro (24) suite of *ab initio* software. The results from these calculations are shown in Table 6.2, and a schematic potential energy surface is shown in Figure 6.7. From these results it can be observed that the OH + ammonia PES displays the same standard features as the other abstraction reactions studied in this thesis with hydrogen bonded complexes (IM1 and IM2) on either side of a hydrogen abstraction transition state (TS1). From IM2 the reaction continues to produce H_2O and NH_2 as products however as was the case in other master equation

calculations performed in this thesis preliminary master equations showed the reaction to be complete once the product complex had been formed and an infinite sink approximation was used for this species (see Chapter 2) . For this reason, high level calculations were not performed upon the H_2O and NH_2 products and the potential in Figure 6.7 was used for all master equations calculations.

In order to increase the accuracy of the master equations calculations for the OH + ammonia reaction, further calculations were performed using the Gaussian 03 suite of *ab initio* programs. (40) Both IM1 and TS exhibited a vibrational mode which could be more correctly described as a hindered rotation corresponding to an internal rotation about the O-N bond in each species. The harmonic frequencies for these modes are indicated in Table 6.2 and in order to more accurately describe the molecular densities of states these modes were treated using the one dimensional hindered rotor treatment implemented in MESMER. (25)

Ideally, potential energy curves for these hindered rotational modes should be calculated using a relaxed scan as was described in chapter 4. As has been found in a number of cases in this thesis, these relaxed calculations, failed to calculate the full potential. A more detailed discussion of such potentials is presented in chapter 4. The OH + ammonia hindered potentials, were obtained using the same methodology as has been used in chapter 4 and 5. Briefly, for each mode, rigid potential energy surfaces, were obtained at the mp2/6-311+G(3d,2p) level of theory through incrementing the corresponding dihedral angle 36 times by 10˚. Once the barrier height had been obtained for the rigid potential, a constrained geometry optimisation was performed, with the corresponding dihedral angle fixed at the value for the rigid barrier, and this optimised energy was used to estimate the barrier height for the relaxed calculation. The rigid potential was then scaled to this reduced barrier height in order to approximate the whole relaxed potential around 360˚ and these potentials are shown in Figure 6.8.

Species	E_{elec} + ZPE / kJ mol^{-1}	B / cm^{-1}	ν / cm^{-1}
OH	0		3722
NH3	0		366, 366, 690 690 1968 3384 3378
IM1	-6.6	0.61 0.06 0.05	118, 191, 237, 316 498, 873 1637, 1638 3500, 3635 3650, 3765
TS	12.9	0.59 0.1 0.08	146, 411, 493 813, 861, 1461, 1514 1633, 3427 3527, 3734 1610*i*
IM2	-74.2		50, 134, 164 197, 383 597, 1527 1661, 3348 3451, 3696 3872

Table 6.2: Rovibrational and energetic properties for the stationary points on the OH + ammonia potential energy suface shown in Figure 6.7. Those frequencies which were replaced with hindered rotational modes are highlighted in red.

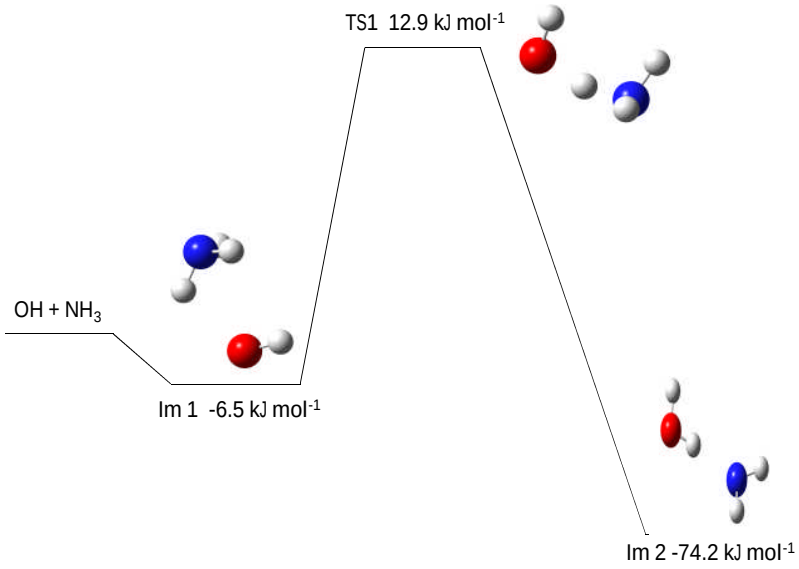

Figure 6.7: Schematic potential energy surface for the OH + ammonia reaction. Geometries and energies were obtained from calculations at the ROHF-UCCSD(t)/aug-cc-pvdz// ROHF-UCCSD(t)/aug-cc-pvtz level of theory.

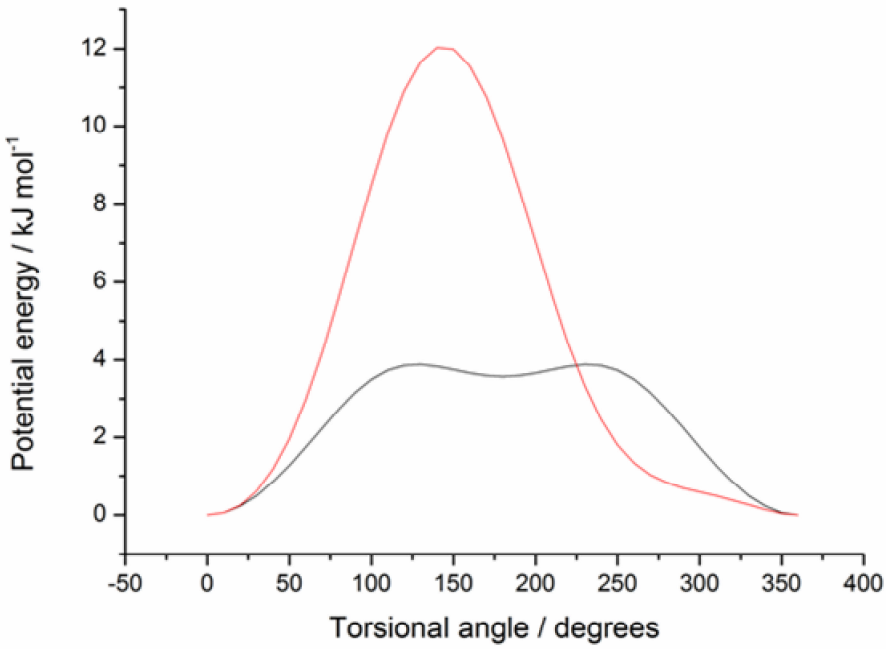

Figure 6.8: Variation in potential energy with rotation of the OH moiety about NH_3 in thre transition state TS (red) and the complex IM1 (black). These potentials were calculted at the MP2/6-311+G(3d,2p) level of theory and each scan consisted of 32 points with the corresponding dihedral angle incremented by 10˚ each time

Previous rate coefficients measured by Corechado *et al.* (36), found tunnelling to be important in the OH + NH_3 reaction and tunnelling was considered in the current calculations in two ways. In the first method tunnelling was treated using the imaginary frequency of the transition state according to the method of Miller (10) described in Section 2.4.2.2. In the current case the small number of atoms involved in the OH + NH_3 reaction has meant that it was possible to perform frequency calculations at the RHF-CCSD(T)/aug-cc-pvdz level of theory and as such the imaginary frequency calculated here should be more accurate than that calculated by Corechado *et al.*. (36) In the second tunnelling approach the semicalssical WKB method (11) was used, and again this method has been described in Section 2.4.2.2. In order to perform this type of tunnelling calculation the change in potential energy along the entire reaction path from the reactant complex to the product complex was required and this was obtained through performing an intrinsic reaction co-ordinate (IRC) calculation at the mp2/6-311+G(3d,2p) level of theory using the Gaussian 03 suite of programs. (40) The resulting potential was then scaled to the RHF-CCSD(T)/aug-cc-pvtz barrier height and the resulting potential is shown in Figure 6.9.

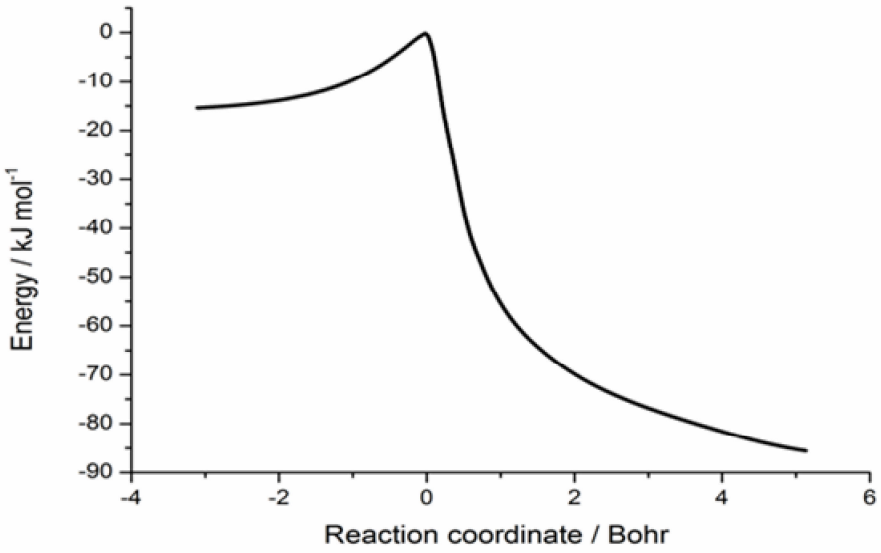

Figure 6.9: Change in potential energy along the reaction co-ordinate in going from IM1 to IM2 via TS. This was obtained through performing an intrinsic reaction co-ordinate (IRC), calculation at the mp2/6-311+G(3d,2p)

The other master equation details are as follows. The OH + NH_3 association step was treated using an ILT method (41) as described in Section 2.3.2.2, and the parameters for this were chosen to be identical to those used for the OH + acetylene reaction decribed above. The subsequent abstraction step was then treated using RRKM theory. Molecular densities of states were calculated using the rigid rotor / harmonic oscillator approximation apart from for the hindered rotational modes described above.

Energy transfer within the pre-reaction complex was considered using an exponential down model though in the current case stabilisation was found to be unimportant and therefore the calculated rate coefficients were independent of ΔE_{down} and the Lennard Jones parameters. All calculations were performed using a grain size of 10 cm^{-1} and this was found to be sufficiently small for the calculated rate coefficients to be converged.

6.2.3. Results and analysis.

A typical first order decay trace obtained using t-BuOOH as the OH precursor is shown in Figure 6.10. From repeated traces such as these bimolecular plots were assembled as shown in Figure 6.11 and from these rate coefficients, k_{bi}(OH+ammonia) were determined to be (1.3±0.2) $\times 10^{-11}$ molecule^{-1} cm^3 s^{-1} and (1.9±0.2)$\times 10^{-11}$ molecule^{-1} cm^3 s^{-1} at 6.1$\times 10^{16}$ molecule cm^{-3} (83 K) and 1.7$\times 10^{17}$ molecule cm^{-3} (79 K),respectively. The errors for these rate coefficients were obtained from the 95% confidence limits from a weighted linear least squares fit to the bimolecular plot data.

By comparison with the OH + acetylene reaction, it would be expected that for the OH + NH_3 reaction, stabilisation of the energised van der Waals complex would be less facile. This is largely due to density of states type arguments since although in both systems the pre-reaction complex is bound by a similar energy, the number of atoms and hence of vibrational modes, is lower in the OH + ammonia reaction. However the k_{bi}(OH+ammonia) measured for the OH + NH_3 reaction at both densities are more than a 5 times greater than for the OH + acetylene reaction.

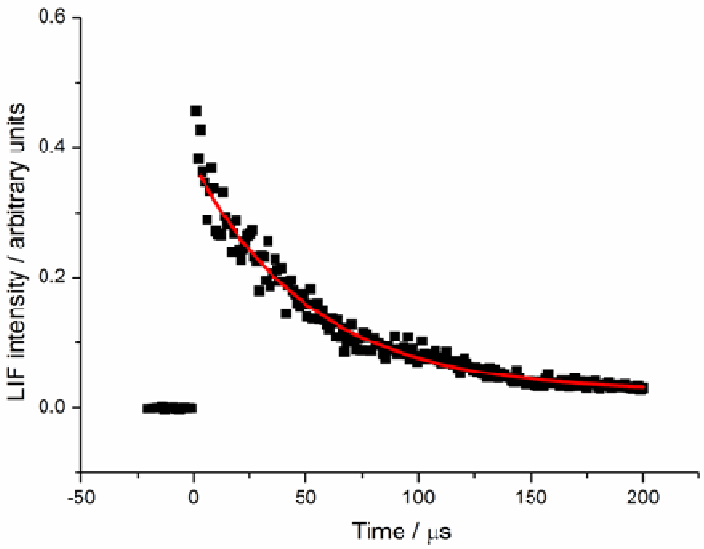

Figure 6.10: Temporal evolution of the LIF signal for OH in the presence of ammonia. For the current trace [NH_3] = 4.4×10^{14} molecule cm^{-3}, [N_2] = 1.7×10^{17} molecule cm^{-3} and [t-BuOOH]≈ 1.1×10^{14} and fitting Eq.2 to the data gives a pseudo first order rate coefficient ($k'_{ammonia}$ + k_d) of 14200 ± 900 s^{-1} This trace consists of a total of 220 points and each point was averaged 10 times. The LIF signal was normalised with respect to the probe laser power on a point-by-point basis.

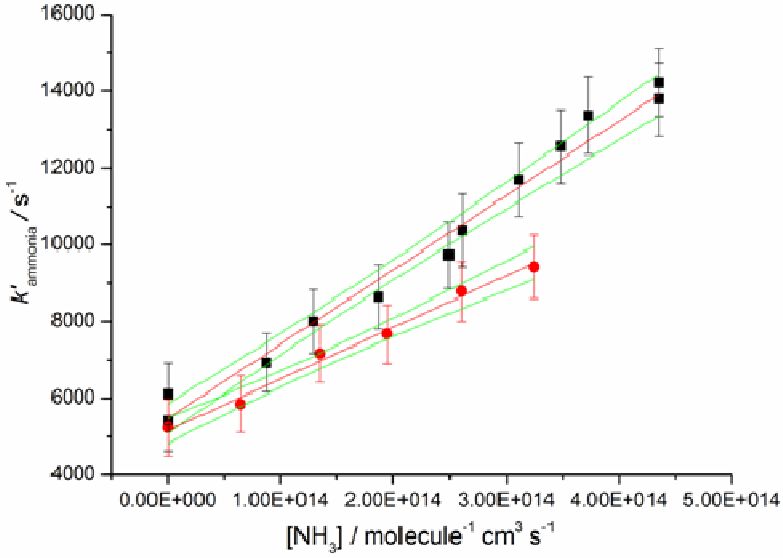

Figure 6.11: Bimolecular plots for the OH + ammonia reaction at total gas densites of 1.7×10^{17} molecule cm^{-3} (black squares) and 6×10^{16} molecule cm^{-3} (red circles). The pseudo first order rate coefficients were obtained from fitting the experimental data with Eq. 2 and they incorporate the 2σ errors both from the fitting process and from [NH_3]. The bimolecular rate coefficient was obtained from a weighted linear give a k_{bi}(OH + NH_3) = (1.9±0.2) ×10^{-11} molecule^{-1} cm^3 s^{-1} and (1.3±0.2) ×10^{-11} molecule^{-1} cm^3 s^{-1} with errors obtained from the 95% confidence limits of the linear fit.

One possible explanation for this result could be due to the influence of quantum mechanical tunnelling. The OH + NH_3 reaction proceeds via a hydrogen abstraction and the imaginary frequency of 2190 cm^{-1} calculated by Corechado *et al.* (36) is large compared to many of the imaginary frequencies encountered in this thesis suggesting that tunnelling may be efficient. If the enhancement in the rate OH + NH_3 rate coefficient were due to tunnelling, as is the case with OH + methanol, then little or no pressure dependence would be expected, yet in the OH + NH_3 reaction the rate coefficient is shown to display a dependence upon total gas density as seen in Figure 6.11 and this is suggestive of a considerably greater degree of stabilisation in the OH + NH_3 reaction, than would be predicted.

In order to check these results the same experiments were performed using acetone as the OH precursor. The bimolecular plot from these experiments is shown in Figure 6.12 and it can be seen that by removing t-BuOOH from the system, the OH+NH_3 rate coefficients are reduced by almost an order of magnitude.

From these results it appeared that t-buOOH enhances the OH + NH_3 reaction in some way. Pulsed Laval nozzle measurements from Vohringer-Martinez *et al.* (42, 43) have shown that at low temperatures, water molecules can catalyse a reaction through forming a complex with the co-reagent. The reactions studied by Vohringer-Martinez and co-workers were barrierless reactions and in these cases catalysis occurred due to the fact that the submerged barrier to reaction products is lowered when the co-reagent forms and complex with a water molecule. If t-BuOOH_NH_3 complexes were being formed in current experiments, these complexes could have a similar catalytic effect, not through lowering the energy barrier to hydrogen abstraction, but rather through forming a three way t-BuOOH_NH_3_OH complex which due to the large number of atoms, would be expected to stabilise efficiently.

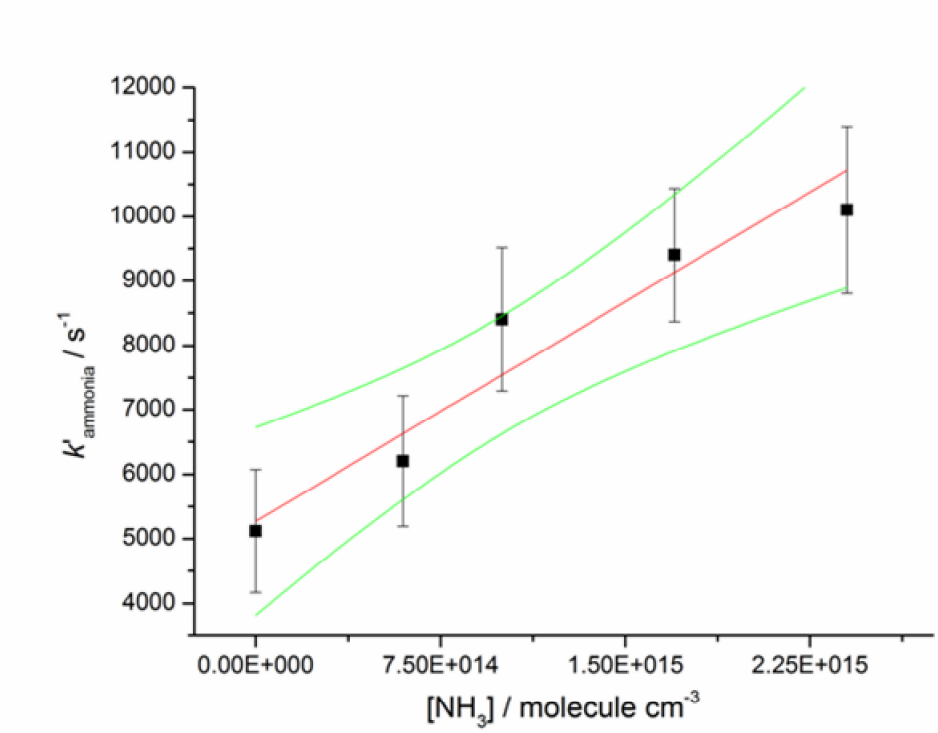

Figure 6.12 : Bimolecular plot for the OH + ammonia reaction at 79K and a total gas density of 1.7×10^{17} molecule cm^{-3}. The pseudo first order rate coefficients were obtained from fitting the experimental data with Eq. 3 and they incorporate the 2σ errors both from the fitting process and from [NH_3]. The bimolecular rate coefficient was obtained from a weighted linear give a k_{bi}(OH + ammonia) = $(2.3\pm1.7)\times10^{-12}$ molecule^{-1} cm^3 s^{-1} with errors obtained from the 95% confidence limits of the linear fit.

This hypothesis was supported by the observation that the measured rate coefficients for the OH + NH_3 reaction, varied with [t-BuOOH]. Figure 6.13 shows two contour plots of the pseudo first order rate coefficients versus both [t-BuOOH] and [NH_3]. And from this graph a clear trend can be observed in that as [t-BuOOH] is increased, the gradient $\partial k/\partial[NH_3]$ also increases. This is what would be expected in the proposed scenario since at high [t-BuOOH], [t-BuOOH_NH_3] would also be larger.

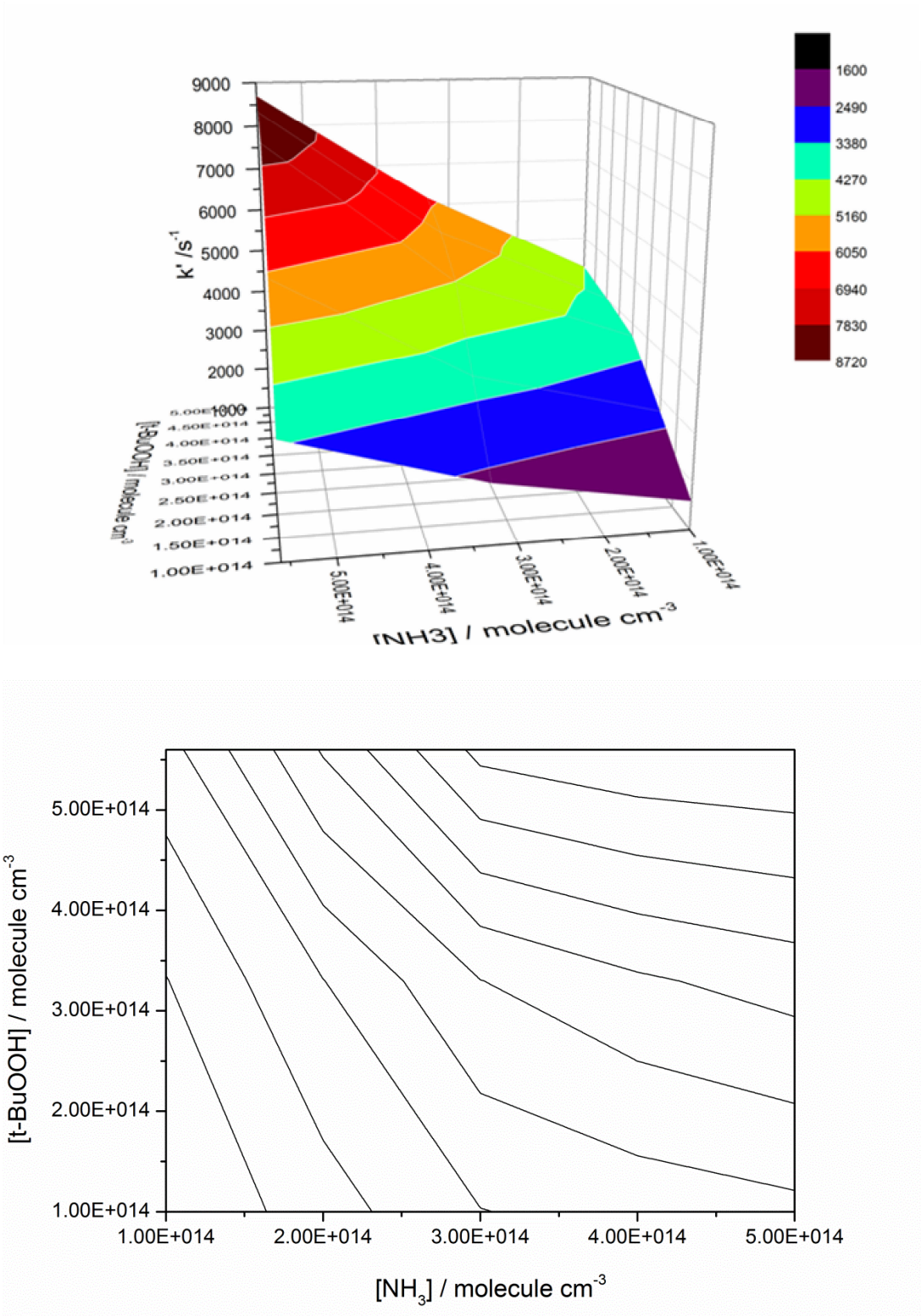

Figure 6.13: Two different representations of the same three dimensional plot. These plots show the variation is the experimental value of $k'_{ammonia}$ with both [t-BuOOH] and [NH_3].

The proposed mechanism in which OH reacts with a t-BuOOH_NH_3 complex is given by the reactions R9 and R10 below.

$$\text{t-BuOOH} + NH_3 \leftrightarrows \text{t-BuOOH-}NH_3 \qquad \text{(R11)}$$

$$\text{t-BuOOH-}NH_3 + OH \leftrightarrows \text{t-BuOOH-}NH_3\text{-OH} \qquad \text{(R12)}$$

In order to obtain the bimolecular rate coefficient for reaction R12, (k_{12}) it would be necessary to plot $k'_{ammonia}$ versus [t-BuOOH_NH_3] rather than [t-BuOOH] or [NH_3]. This concentration is unknown but assuming equilibrium has been reached, it can be related to the equilibrium constant for reaction R12 given by Eq. 4.

$$K_c = \frac{[\text{t-BuOOH} - \text{NH}_3]}{[\text{t-BuOOH}][\text{NH}_3]} \qquad \text{(Eq. 4)}$$

In order to calculate this equilibrium constant*, ab initio* calculations were performed at the MPW1K/6-31+G(d,p) level of theory. Given the large number of heavy atoms involved in this system, high level MP2 or CCSD calculations, were not possible and the MPW1K density functional was used. Using this level of theory the stable geometries were located for the t-BuOOH_NH_3 complex and the t-BuOOH_NH_3_OH complex. Energies, vibrational frequencies and thermodynamic properties of these species are given in Table 6.3. The structure of the t-BuOOH_NH_3_OH complex obtained from these calculations is shown in Figure 6.14.

Complex	ΔH_f^θ **/ kJ mol^{-1}**	ΔS_f^θ **/ J K^{-1} mol^{-1}**	ΔG_f^θ **/ kJ mol^{-1}**	**K_c / molecule^{-1} cm^3**
T-BuOOH_NH_3_OH	-12.2	-123.2	-22.1	3.8×10^{-19}
T-BuOOH_NH3	-25.2	-107.8	-160.8	8.1×10^{-10}

Table 6.3: Thermodynamic properties of the two hydrogen bonded complexes between t-BuOOH and NH_3 and between t-BuOOH, NH_3 and OH, calculated at the MPW1K/6-31+G(d,p).

In order to calculate K_c from the ab inito data, it was necessary to first calculate the Gibbs change in forming the t-BuOOH_NH_3 complex from the separated molecules:

$$\Delta G_f^\theta = \Delta H_f^\theta - T\Delta S_f^\theta \qquad \text{(Eq . 5)}$$

where ΔH_f^θ is the change in enthalpy upon formation of the complex and ΔS_f^θ and is the change entropy upon formation of the complex. The Gibbs free energy can then be used to calculate the equilibrium coefficient in terms of partial pressures, from the following equation:

$$K_p = \exp(-\Delta G / \mathrm{R}T) \qquad \text{(Eq.6)}$$

$$K_c = K_p \mathrm{R}T \qquad \text{(Eq. 7)}$$

From this approach the equilibrium constant for formation of the t-BuOOH_NH_3 complex was determined to be 8.1×10^{-10} molecule^{-1} cm^3 at 79 K although given that this value is based purely upon calculation, this value is likely to subject to a significant amount of uncertainty which is difficult to quantify.

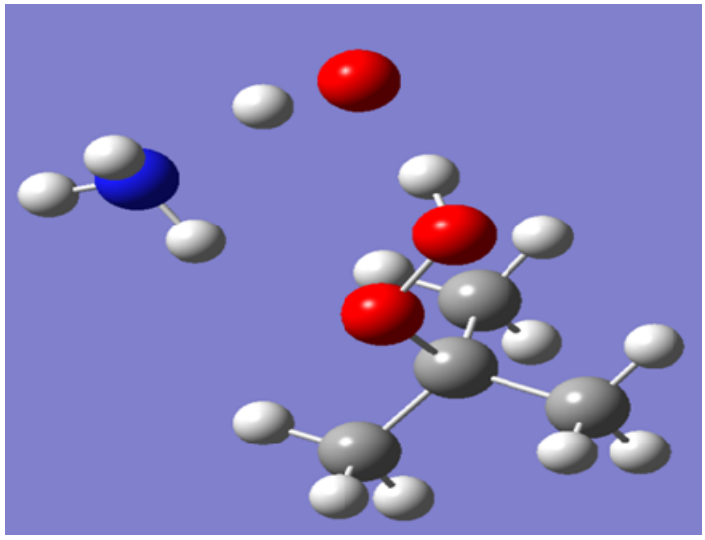

Figure 6.14: Structure of the T_BuOOH_NH_3_OH complex located at the MPW1K/6-31+G(d,p) level of theory. At this level of theory the binding energy of this complex relative to the separated t-BuOOH_NH_3 and OH molecules was determined to be -12.2 kJ mol^{-1} and the equilibrium coefficient K_c for the formation of this complex was determined to be 8.1×10^{-10} molecule^{-1} cm^3 at 79K.

Using this equilibrium coefficient the pseudo first order decays could be reanalysed for both the 6×10^{16} molecule cm^{-3} and 1.7×10^{17} molecule cm^{-3} Laval nozzle data, taking into account the formation of complexes. As can be observed in Figure 6.15 some of the pseudo first order traces appeared to exhibit a non-zero baseline at long reaction times. There are a number of possible reasons for this. Given the short 200 μs timescale over which reaction could be observed (due to the length of the stable flow), and the relatively low [NH_3], the reaction does not proceed to completion and so the true baseline of the data was rarely observed. This coupled with the poor signal to noise ratios of many traces due to t-BuOOH_NH_3 formation, means that these apparent non zero baselines could just be an experimental artefact. Alternatively, the pseudo first order decays could be exhibiting real bi-exponential behaviour due to re-dissociation of the t-BuOOH_NH_3_OH complex back to OH. This re-dissociation is accounted for in R12 and the kinetic scheme given in R11 and R12 is captured by the fitting equation Eq.8 below:

$$[OH] = A\left(\frac{(\alpha 1 - k_{-12})\exp(-\alpha 1 * t) + (k_{-12} - \alpha 2)\exp(-\alpha 2 * t)}{\alpha 1 + \alpha 2}\right) \quad \text{(Eq. 8)}$$

where

$$\alpha 1 = p + q$$

$$\alpha 2 = p + q$$

$$p = k'_{12} + k'_d + k'_{t-BuOOH} + k_{-12}$$

$$q = \sqrt{p^2 - 4k_{-12}k'_d k_{t-BuOOH}}$$

A is a scaling factor related to the initial [OH], k'_{12} is the pseudo first order rate coefficient for the reaction R12, k_{-12} is the first order rate coefficient for the reverse of reaction R12, k'_d is the pseudo first order rate coefficient for diffusional loss of ammonia out of the supersonic expansion, and $k'_{t\text{-}Bu\text{-}OOH}$ is the pseudo first order rate coefficient for the reaction between OH and the t-BuOOH precursor.

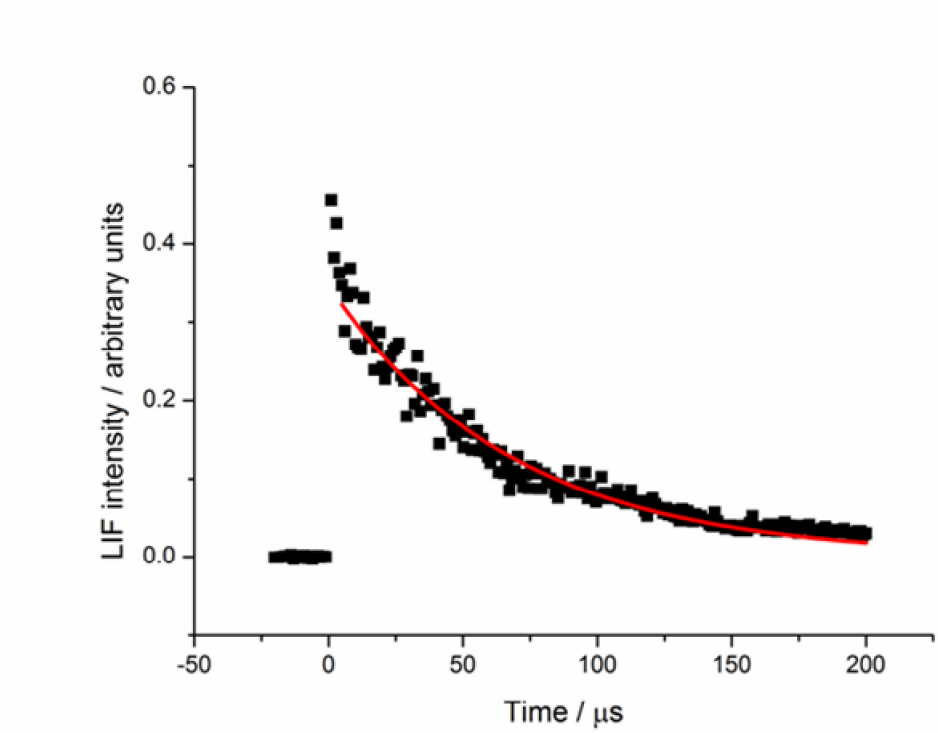

Figure 6.15: Temporal evolution of the LIF signal for OH in the presence of ammonia. A discrepancy can be observed between the fitting equation and the experimental data at long times indicating a non-zero baseline. For the current trace [NH_3] = 2.1×10^{14} molecule cm^{-3}, [N_2] = 1.7×10^{17} molecule cm^{-3} and [t-BuOOH]≈ 1.1×10^{14} and fitting Eq.2 to the data gives a pseudo first order rate coefficient $k'_{ammonia} + k_i$ of 10400 ± 1100 s^{-1} This trace consists of a total of 220 points and each point was averaged 10 times. The LIF signal was normalised with respect to probe laser power on a point-by-point basis.

Using this fitting equation the experimental data was analysed in Microsoft excel using the solver functionality. For each time point in an experimental trace, the LIF intensity was compared to the corresponding fitted LIF intensity from Eq. 8 at the same time point. A χ^2 goodness of fit indicator:

$$\chi^2 = \sum \frac{(k_{obs} - k_{calc})^2}{k_{obs}^2} \qquad \text{(Eq. 9)}$$

where k_{obs} are experimental data points in each trace and k_{calc} are the corresponding data points calculated using the fitting equation Eq. 8, was used and these χ^2 values were then summed for each time point in order to give a value of chi squared per trace. The equilibrium constant K_c was

defined globally for each trace, and the pseudo first order rate coefficients k'_{12} and $k'_{t\text{-}BuOOH}$ were also determined from the corresponding bimolecular rate coefficients which were globally defined for each trace. This was done as follows. For each trace [NH_3] and [t-BuOOH] was recorded and [t-BuOOH_NH_3] was then calculated using the ab initio equilibrium constant K_c according to Eq. 8. The rate coefficients k'_{12} and $k'_{t\text{-}BuOOH}$ were then defined for each trace using the corresponding bimolecular rate coefficients k_{bi}(R12) and k_{bi}(OH+t-BuOOH) according the relationship $k_{bi} = k'$ [x] where [x] is either [t-BuOOH_NH_3] or [t-BuOOH]. The first order rate coefficients k_d and k_{-12} were also defined globally. Locally the parameter A, was defined separately for each individual trace.

For a given total density, the χ^2 values for each trace were summed and this total χ^2 was minimised with respect to the various fitting parameters. All parameters were allowed to float other than K_c which was fixed at the *ab inito* value. This fitting procedure was performed for both the 6×10^{16} and 1.7×10^{17} molecule cm^{-3} data and the results are presented in Table 6.4.

The first thing that is noticed from these results, is that when allowed to float, the rate coefficient for re-dissociation of the NH_3_t-BuOOH_OH complex (k_{-12}) is determined to be 0 suggesting that the experimental traces collected did not display true bi-exponential behaviour and that re-dissociation of the complex was not observed on our experimental timescale.

The results presented here are extremely sensitive to the *ab initio* equilibrium constant which is in turn very sensitive to the change in enthalpy in the formation of the T-BuOOH_NH_3 complex. Changing the binding energy from 25 kJ mol^{-1} to 20 kJ mol^{-1} reduces K_c by over three orders of magnitude and such a change in the binding energy is likely to be well within the error of the MPW1K level of theory. It was noted that for K_c values of > 5×10^{-15} the equilibrium value of [t-BuOOH_NH_3] was equal to the lower of the two [NH_3], [t-BuOOH] (at equilibrium, each pair of NH_3 and t-BuOOH monomers has formed a t-BuOOH_NH_3 complex) and as such the fitting results with K_c set at the *ab initio* value, represent an upper limit of [t-BuOOH_NH_3] and therefore a lower limit of k_{bi}(R12). Values of $K_c < 5\times10^{-15}$ $molecule^{-1}$ cm^3 were observed to increase the fitted value of k_{12} but in this

case a reduction in the overall χ^2 was observed indicating a slightly better fit to the data. A value for K_c of 1×10^{-15} molecule^{-1} cm^3 gave the lowest value for χ^2 and the fitting results from using this value are also shown in Table 6.4.

	Fitting the 6×10^{16} data with $K_c = 8\times10^{-10}$	**Fitting the 1.7×10^{17} data.with $K_c = 8\times10^{-10}$**	**Fitting the 6×10^{16} data.with $K_c = 1\times10^{-15}$**	**Fitting the 1.7×10^{17} data.with $K_c = 1\times10^{-15}$**
k_{bi}(R12) / molecule^{-1} cm^3 s^{-1}	4.1×10^{-11}	6.0×10^{-11}	1.4×10^{-10}	1.5×10^{-10}
k_{bi} (OH + t-BuOOH) / molecule^{-1} cm^3 s^{-1}	4.7×10^{-11}	3.3×10^{-11}	4.2×10^{-11}	1.5×10^{-11}
k_d / s^{-1}	714	1670	812	2100
k_{-12} /s^{-1}	0	0	0	0
c^2	82	188	69	142

Table 6.4: Fitted rate coefficients using the solver functionality in Microsoft excel. The first two columns show the results from using the *ab inito* K_c whilst the final two columns show the results obtained using a lower K_c .

Although there is a large amount of uncertainty in the equilibrium constant K_c and hence also in k_{bi}(R12), the results in Table 6.4 still offer important information on the kinetics of reaction R12. As discussed, using the *ab inito* K_c gives a lower limit to k_{bi}(R12) and considering that the hydrogen bonded complexes encountered thus far have been bound by ~20 kJ mol^{-1} rather than the 25 kJ mol^{-1} calculated for the t-BuOOH_NH_3 complex, the *ab initio* value of K_c is likely to be an overestimate. Even if K_c is correct, the analysis performed here assumes that equilibrium is attained instantaneously whereas in actual fact the rate at which equilibrium is attained in the t-BuOOH + NH_3 reaction is likely to be competitive with the rate at which OH

reacts with the t-BuOOH_NH_3 complex. Considering these arguments and the lack of any significant pressure dependence observed for k_{bi}(R12), it is likely that this reaction is approaching is capture controlled limit despite the weak binding energy of the complex of -12 kJ mol^{-1}.

Without the catalytic effect of the t-BuOOH molecules it has been found experimentally that the rate coefficients for OH + NH_3 are relatively small compared to many of the other reactions in this thesis. Because of this only one rate coefficient has been obtained experimentally, and there are large uncertainties associated with this value. In order to explore this reaction further, master equation calculations have therefore been performed on the system. The change in calculated rate coefficients for the OH + ammonia reaction with temperature is shown in Figure 6.16 using both Eckhart tunnelling (10), and the more sophisticated semi-classical method (11) which have been described in Section 2.4.2.2. Here it can be seen that both methods yield a good agreement with the available experimental data though as was observed in the case of OH + acetone and OH + DME, the semiclassical method appears to underpredict the amount of tunnelling required. The very small well depth of the OH + ammonia association complex, coupled with the low number of atoms in the system makes it very hard to rationalise that any stabilisation of this adduct could be observed experimentally and the master equation results predict that the OH + ammonia rate support this, suggesting that the OH + ammonia reaction proceeds via a similar mechanism to the OH + methanol reaction as discussed in Chapter 5.

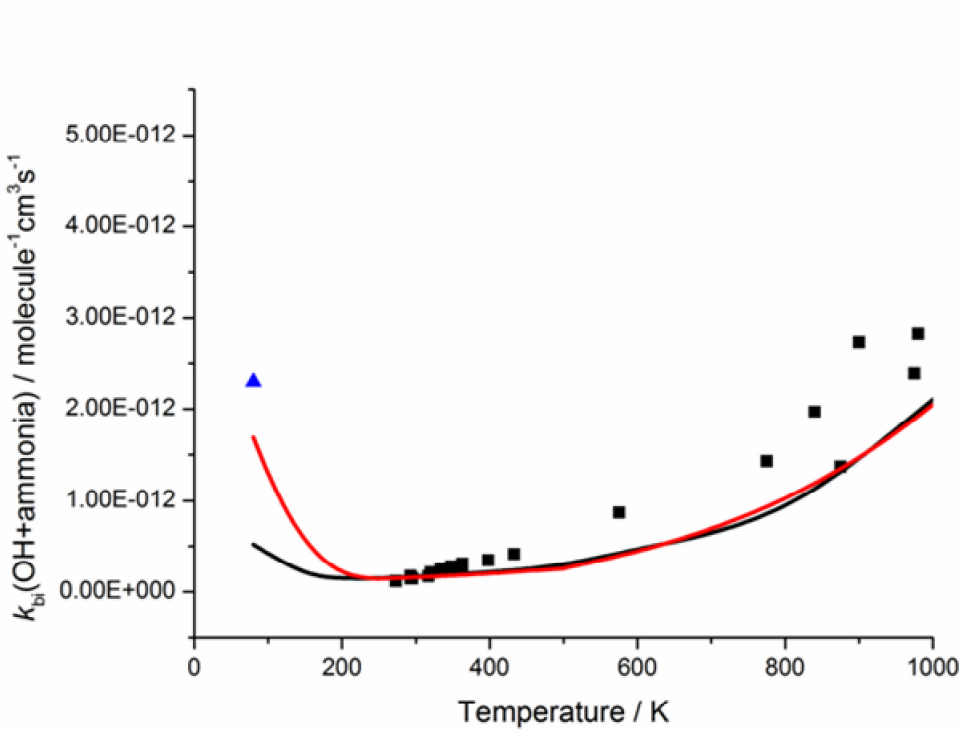

Figure 6.16: Comparison between experimental and theoretical rate coefficients for the OH + ammonia reaction. The black squares are data from previous literature studies (29, 31, 34, 35), the blue triangle is the rate coefficient measured in the current work at 79 K. The two lines correspond to theoretical rate coefficients calculated using the MESMER software (25) using both the Eckart method (10) (red) and the semiclassical method (11) (black) to calculate transmission coefficients.

From these results it then appears that the OH + ammonia reaction proceeds through an identical mechanism to the OH + methanol system. It would then be expected that under ISM conditions, the OH + ammonia reaction would efficiently form the abstraction products H_2O and NH_2. In order to explore this, the master equation calculations were extended down to 20 K and these results are shown in Figure 6.17.

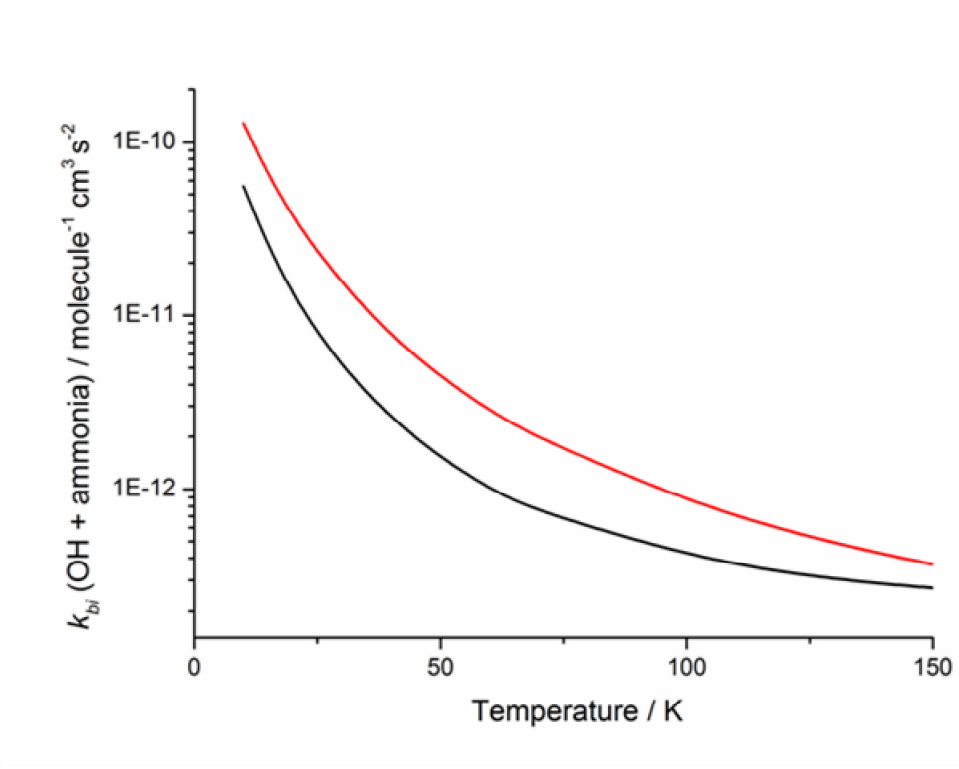

Figure 6.17 Rate coefficients for the OH + ammonia reation calculated by MESMER (25) using both the Eckart method (10) (red) and the semiclassical method (11) (black) to calculate transmission coefficients.Calculations have been performed at temperatures between 80 and 20 K and at a total gas density of 1×10^6 molecule cm^{-3}

6.3. Conclusions

Since the previous two chapters have considered reactions with relatively strongly bound hydrogen bonded complexes the aim of this chapter was to explore the significance of more weakly bound of van der Waals adducts at low temperatures. Two reactions, OH + acetylene and OH + ammonia have been studied with association complex well depths of 9.0 kJ mol^{-1} and 6.6 kJ mol^{-1} and is has been shown that despite the weakly bound nature of these adducts, they still enhance the rate coefficients for these reaction as the temperature is lowered.

The low temperature rate coefficients for the OH + acetylene reaction, demonstrate that even at 79 K and a total gas density of 1.7×10^{17} molecules cm^{-3}, the association complex is stabilised with a rate coefficient of 2.5×10^{-12} molecule^{-1} cm^3 s^{-1}, raising the possibility that at the higher gas densities of extraterrestrial planetary atmospheres such as Saturn's or Titan's, many

gaseous species could be bound in weak complexes with each other. However, since this reaction does not proceed via hydrogen abstraction, it is unlikely to be significant in the interstellar medium.

There is also further evidence for the propensity of separated gas molecules to form complexes at low temperatures, through the observation of an interference in the OH + ammonia experiments due to the formation of a t-BuOOH_NH_3_OH complex. That such a complex exists is supported by calculations at the MPW1K/6-31+G(d,p) level of theory and these calculations predict that it is bound by only 12.2 kJ mol^{-1}. The rate coefficient for the OH + BuOOH_NH_3 has been estimated using an equilibrium constant derived from the *ab inito* calculation and although it is difficult to quantify the error on such calculations, the results certainly suggest that stabilisation of this complex occurs with a rate coefficient on the order of 10^{-10} $molecule^{-1}$ cm^3 s^{-1}.

The pre-reaction complex in the OH + ammonia reaction is even more weakly bound than the OH + acetylene analogue and the theoretical results obtained here suggest that given the small well depth and the small number of atoms involved it is unlikely that the rate coefficients observed for this reaction are the result of stabilisation. It is true that rate coefficients were only measurable for this reaction at the highest total density of 1.7×10^{17} molecule cm^{-3} but given the small rate coefficient and the consequently large errors on this measurement, this is far from conclusive evidence of pressure dependence.

It is clear that the OH + ammonia system requires further experimental study at low temperatures, but from the theoretical calculations it appears that the 6.6 kJ mol^{-1} bound pre reaction complex is sufficient to promote the type of tunnelling mechanism which was used to explain the methanol + OH rate coefficients in Chapter 5. Extrapolation of the MESMER calculations down to 20K suggests that this reaction is approaching the capture limit just like the OH + methanol reaction. These results thus give a further evidence to the generality of this efficient tunnelling mechanism for the hydrogen transfer reactions in the ISM.

In summary, these results show that not only hydrogen bonded complexes, but weaker van der Waals complexes also can enhance rate coefficients at very low temperatures. At 80 K the negative temperature dependencies observed are not as dramatic for the van der Waals case as those observed in chapter 4 and 5. However considering the OH + ammonia modelling it still appears that under ISM conditions this reaction could be approaching the capture controlled limit and if this is the case for OH + methanol then this is likely to hold for many other systems.

6.4. References

1. HERBST, E. Chemistry of star-forming regions. *Journal of Physical Chemistry A*, 2005, **109**(18), pp.4017-4029.
2. SMITH, I.W.M., E. HERBST and Q. CHANG. Rapid neutral-neutral reactions at low temperatures: a new network and first results for TMC-1. *Monthly Notices of the Royal Astronomical Society*, 2004, **350**(1), pp.323-330.
3. NOLL, K.S., R.F. KNACKE, A.T. TOKUNAGA, J.H. LACY, S. BECK and E. SERABYN. The Abundances of Ethane and Acetylene in the Atmospheres of Jupiter and Saturn. *Icarus*, 1986, **65**(2-3), pp.257-263.
4. WAITE, J.H., W.S. LEWIS, B.A. MAGEE, J.I. LUNINE, W.B. MCKINNON, C.R. GLEIN, O. MOUSIS, D.T. YOUNG, T. BROCKWELL, J. WESTLAKE, M.J. NGUYEN, B.D. TEOLIS, B. NIEMANN, R.L. MCNUTT, M. PERRY and W.H. IP. Liquid water on Enceladus from observations of ammonia and (40)Ar in the plume. *Nature*, 2009, **460**(7254), pp.487-490.
5. SPENCER, J. and D. GRINSPOON. Planetary science - Inside Enceladus. *Nature*, 2007, **445**(7126), pp.376-377.
6. PARKINSON, C.D., M.C. LIANG, Y.L. YUNG and J.L. KIRSCHIVNK. Habitability of Enceladus: Planetary conditions for life. *Origins of Life and Evolution of Biospheres*, 2008, **38**(4), pp.355-369.
7. ATKINSON, R., D.L. BAULCH, R.A. COX, J.N. CROWLEY, R.F. HAMPSON, R.G. HYNES, M.E. JENKIN, M.J. ROSSI and J. TROE. Evaluated kinetic and photochemical data for atmospheric chemistry: Volume I - gas phase reactions of O(x), HO(x), NO(x) and SO(x) species. *Atmospheric Chemistry and Physics*, 2004, **4**, pp.1461-1738.
8. ATKINSON, R., D.L. BAULCH, R.A. COX, R.F. HAMPSON, J.A. KERR, M.J. ROSSI and J. TROE. Evaluated kinetic and photochemical data for atmospheric chemistry: Supplement VI - IUPAC subcommittee on gas kinetic data evaluation for atmospheric chemistry. *Journal of Physical and Chemical Reference Data*, 1997, **26**(6), pp.1329-1499.

9. XU, S. and M.C. LIN. Theoretical study on the kinetics for OH reactions with CH3OH and C2H5OH. *Proceedings of the Combustion Institute*, 2007, **31**, pp.159-166.
10. MILLER, W.H. Tunneling Corrections to Unimolecular Rate Constants, with Application to Formaldehyde. *Journal of the American Chemical Society*, 1979, **101**(23), pp.6810-6814.
11. GARRETT, B.C. and D.G. TRUHLAR. Semi-Classical Tunneling Calculations. *Journal of Physical Chemistry*, 1979, **83**(22), pp.2921-2926.
12. PU, J.Z. and D.G. TRUHLAR. Validation of variational transition state theory with multidimensional tunneling contributions against accurate quantum mechanical dynamics for H+CH4 -> H-2+CH3 in an extended temperature interval. *Journal of Chemical Physics*, 2002, **117**(4), pp.1479-1481.
13. PERRY, R.A. and D. WILLIAMSON. Pressure and Temperature-Dependence of the Oh Radical Reaction with Acetylene. *Chemical Physics Letters*, 1982, **93**(4), pp.331-334.
14. SORENSEN, M., E.W. KAISER, M.D. HURLEY, T.J. WALLINGTON and O.J. NIELSEN. Kinetics of the reaction of OH radicals with acetylene in 25-8000 Torr of air at 296 K. *International Journal of Chemical Kinetics*, 2003, **35**(5), pp.191-197.
15. MCKEE, K.W., M.A. BLITZ, P.A. CLEARY, D.R. GLOWACKI, M.J. PILLING, P.W. SEAKINS and L.M. WANG. Experimental and master equation study of the kinetics of OH+C2H2: Temperature dependence of the limiting high pressure and pressure dependent rate coefficients. *Journal of Physical Chemistry A*, 2007, **111**(19), pp.4043-4055.
16. SENOSIAIN, J.P., S.J. KLIPPENSTEIN and J.A. MILLER. The reaction of acetylene with hydroxyl radicals. *Journal of Physical Chemistry A*, 2005, **109**(27), pp.6045-6055.
17. FULLE, D., H.F. HAMANN, H. HIPPLER and C.P. JANSCH. The high pressure range of the addition of OH to C2H2 and C2H4. *Berichte Der Bunsen-Gesellschaft-Physical Chemistry Chemical Physics*, 1997, **101**(10), pp.1433-1442.
18. DAVEY, J.B., M.E. GREENSLADE, M.D. MARSHALL, M.I. LESTER and M.D. WHEELER. Infrared spectrum and stability of a pi-type hydrogen-bonded complex between the OH and C2H2 reactants. *Journal of Chemical Physics*, 2004, **121**(7), pp.3009-3018.
19. HANSMANN, B. and B. ABEL. Kinetics in cold laval nozzle expansions: From atmospheric chemistry to oxidation of biomolecules in the gas phase. *Chemphyschem*, 2007, **8**(3), pp.343-356.
20. TAYLOR, S.E., A. GODDARD, M.A. BLITZ, P.A. CLEARY and D.E. HEARD. Pulsed Laval nozzle study of the kinetics of OH with unsaturated hydrocarbons at very low temperatures. *Physical Chemistry Chemical Physics*, 2008, **10**(3), pp.422-437.
21. SMITH, I.W.M., A.M. SAGE, N.M. DONAHUE, E. HERBST and D. QUAN. The temperature-dependence of rapid low temperature reactions: experiment, understanding and prediction. *Faraday Discussions*, 2006, **133**, pp.137-156.
22. KNOWLES, P.J., C. HAMPEL and H.J. WERNER. Coupled-Cluster Theory for High-Spin, Open-Shell Reference Wave-Functions. *Journal of Chemical Physics*, 1993, **99**(7), pp.5219-5227.

23. WATTS, J.D. and R.J. BARTLETT. Triple Excitations in Coupled-Cluster Theory - Energies and Analytical Derivatives. *International Journal of Quantum Chemistry*, 1993, pp.51-66.
24. MOLPRO IS A PACKAGE OF AB INITIO PROGRAMS WRITTEN BY H.-J. WERNER, P.J.K., G. KNIZIA, F. R. MANBY, M. SCHÜTZ, P. CELANI, T. KORONA, R. LINDH, A. MITRUSHENKOV, G. RAUHUT, K. R. SHAMASUNDAR, T. B. ADLER, R. D. AMOS, A. BERNHARDSSON, A. BERNING, D. L. COOPER, M. J. O. DEEGAN, A. J. DOBBYN, F. ECKERT, E. GOLL, C. HAMPEL, A. HESSELMANN, G. HETZER, T. HRENAR, G. JANSEN, C. KÖPPL, Y. LIU, A. W. LLOYD, R. A. MATA, A. J. MAY, S. J. MCNICHOLAS, W. MEYER, M. E. MURA, A. NICKLAß, D. P. O'NEILL, P. PALMIERI, K. PFLÜGER, R. PITZER, M. REIHER, T. SHIOZAKI, H. STOLL, A. J. STONE, R. TARRONI, T. THORSTEINSSON, M. WANG, A. WOLF
25. ROBERTSON, S.H., GLOWACKI, D. R., LIANG, C.-H.; MORLEY, C., PILLING, M. J.,. MESMER. *(Master Equation Solver for Multi-Energy Well Reactions), 2008; an object oriented C++ program for carrying out ME calculations and eigenvalue-eigenvector analysis on arbitrary multiple well systems. http://sourceforge.net/projects/mesmer*.
26. SEAKINS, P.W., S.H. ROBERTSON, M.J. PILLING, I.R. SLAGLE, G.W. GMURCZYK, A. BENCSURA, D. GUTMAN and W. TSANG. Kinetics of the Unimolecular Decomposition of Iso-C3h7 - Weak Collision Effects in Helium, Argon, and Nitrogen. *Journal of Physical Chemistry*, 1993, **97**(17), pp.4450-4458.
27. HIPPLER, H., J. TROE and H.J. WENDELKEN. Collisional Deactivation of Vibrationally Highly Excited Polyatomic-Molecules .2. Direct Observations for Excited Toluene. *Journal of Chemical Physics*, 1983, **78**(11), pp.6709-6717.
28. CHEUNG, A.C., D.M. RANK, C.H. TOWNES, D.D. THORNTON and W.J. WELCH. Detection of NH_{3} Molecules in the Interstellar Medium by Their Microwave Emission. *Physical Review Letters*, 1968, **21**(25), pp.1701-1705.
29. DIAU, E.W.G., T.L. TSO and Y.P. LEE. Kinetics of the Reaction OH + NH_3 in the Range 273-433-K. *Journal of Physical Chemistry*, 1990, **94**(13), pp.5261-5265.
30. PERRY, R.A., R. ATKINSON and J.N. PITTS. Rate Constants for Reaction of Oh Radicals with Normal-Butane over Temperature-Range 297-420 Degreesk. *Journal of Chemical Physics*, 1976, **64**(12), pp.5314-5316.
31. STEPHENS, R.D. Absolute Rate Constants for the Reaction of Hydroxyl Radicals with Ammonia from 297-K to 364-K. *Journal of Physical Chemistry*, 1984, **88**(15), pp.3308-3313.
32. STUHL, F. Absolute Rate Constant for Reaction Oh+Nh3-]Nh2+H2o. *Journal of Chemical Physics*, 1973, **59**(2), pp.635-637.
33. ZELLNER, R. and I.W.M. SMITH. Rate Constants for Reactions of Oh with Nh3 and Hno3. *Chemical Physics Letters*, 1974, **26**(1), pp.72-74.
34. SILVER, J.A. and C.E. KOLB. Rate-Constant for the Reaction Nh3+Oh-]Nh2+H2o over a Wide Temperature-Range. *Chemical Physics Letters*, 1980, **75**(1), pp.191-195.
35. JEFFRIES, J.B. and G.P. SMITH. Kinetics of the Reaction Oh + Nh3. *Journal of Physical Chemistry*, 1986, **90**(3), pp.487-491.

36. CORCHADO, J.C., J. ESPINOSAGARCIA, W.P. HU, I. ROSSI and D.G. TRUHLAR. Dual-Level Reaction-Path Dynamics (the ///-Approach to Vtst with Semiclassical Tunneling) - Application to Oh+Nh3-]H2o+Nh2. *Journal of Physical Chemistry*, 1995, **99**(2), pp.687-694.
37. LIU, Y.P., G.C. LYNCH, T.N. TRUONG, D.H. LU, D.G. TRUHLAR and B.C. GARRETT. Molecular Modeling of the Kinetic Isotope Effect for the [1,5] Sigmatropic Rearrangement of Cis-1,3-Pentadiene. *Journal of the American Chemical Society*, 1993, **115**(6), pp.2408-2415.
38. LIU, Y.P., D.H. LU, A. GONZALEZLAFONT, D.G. TRUHLAR and B.C. GARRETT. Direct Dynamics Calculation of the Kinetic Isotope Effect for an Organic Hydrogen-Transfer Reaction, Including Corner-Cutting Tunneling in 21 Dimensions. *Journal of the American Chemical Society*, 1993, **115**(17), pp.7806-7817.
39. GARRETT, B.C., T. JOSEPH, T.N. TRUONG and D.G. TRUHLAR. Application of the Large-Curvature Tunneling Approximation to Polyatomic-Molecules - Abstraction of H or D by Methyl Radical. *Chemical Physics*, 1989, **136**(2), pp.271-283.
40. Gaussian. Gaussian 03, Revision C.02, M. J. Frisch, G. W. Trucks, H. B. Schlegel, G. E. Scuseria, M. A. Robb, J. R. Cheeseman, J. A. Montgomery, Jr., T. Vreven, K. N. Kudin, J. C. Burant, J. M. Millam, S. S. Iyengar, J. Tomasi, V. Barone, B. Mennucci, M. Cossi, G. Scalmani, N. Rega, G. A. Petersson, H. Nakatsuji, M. Hada, M. Ehara, K. Toyota, R. Fukuda, J. Hasegawa, M. Ishida, T. Nakajima, Y. Honda, O. Kitao, H. Nakai, M. Klene, X. Li, J. E. Knox, H. P. Hratchian, J. B. Cross, V. Bakken, C. Adamo, J. Jaramillo, R. Gomperts, R. E. Stratmann, O. Yazyev, A. J. Austin, R. Cammi, C. Pomelli, J. W. Ochterski, P. Y. Ayala, K. Morokuma, G. A. Voth, P. Salvador, J. J. Dannenberg, V. G. Zakrzewski, S. Dapprich, A. D. Daniels, M. C. Strain, O. Farkas, D. K. Malick, A. D. Rabuck, K. Raghavachari, J. B. Foresman, J. V. Ortiz, Q. Cui, A. G. Baboul, S. Clifford, J. Cioslowski, B. B. Stefanov, G. Liu, A. Liashenko, P. Piskorz, I. Komaromi, R. L. Martin, D. J. Fox, T. Keith, M. A. Al-Laham, C. Y. Peng, A. Nanayakkara, M. Challacombe, P. M. W. Gill, B. Johnson, W. Chen, M. W. Wong, C. Gonzalez, and J. A. Pople, Gaussian, Inc., Wallingford CT, 2004.
41. ROBERTSON, S.H., M.J. PILLING, D.L. BAULCH and N.J.B. GREEN. Fitting of Pressure-Dependent Kinetic Rate Data by Master Equation Inverse Laplace Transform Analysis. *Journal of Physical Chemistry*, 1995, **99**(36), pp.13452-13460.
42. VOHRINGER-MARTINEZ, E., B. HANSMANN, H. HERNANDEZ, J.S. FRANCISCO, J. TROE and B. ABEL. Water catalysis of a radical-molecule gas-phase reaction. *Science*, 2007, **315**(5811), pp.497-501.
43. VOHRINGER-MARTINEZ, E., E. TELLBACH, M. LIESSMANN and B. ABEL. Role of Water Complexes in the Reaction of Propionaldehyde with OH Radicals. *Journal of Physical Chemistry A*, 2010, **114**(36), pp.9720-9724.

Chapter 7. The proxy method at low temperatures. Approximating the high pressure limit for the formation of weak pre-reaction complexes in reactions between the OH radical and various hydrocarbons

7.1. Introduction

In the previous two chapters, a number of radical-neutral reactions with barriers to products have been shown to display large enhancements in their rate coefficients below 100 K. It has been firmly established that this behaviour can be attributed to the presence of a pre-reaction complex be it a strongly bound hydrogen bonded complex (≈20 kJ mol^{-1}) or a weaker van der Waals complex (<10 kJ mol^{-1}) and even at the low total gas densities used in Laval nozzle experiments, collisional stabilisation of these weak adducts is remarkably facile.

The OH + acetone and OH + DME reactions both displayed a marked pressure or gas density dependence to their rate coefficients at ≈ 80 K and even with the weaker interactions present in the OH + acetylene reaction, the rate coefficient was measurable at the highest total densities only. The notion of collisional stabilisation of an energised adduct is mature and both the Lindemann Hinshelwood mechanism and the more sophisticated master equation approach have been explained in detail in Chapter 2.

Through performing master equation calculations on the systems studied in this thesis, the pressure dependencies observed can be readily rationalised. In the reaction kinetics theory of pressure dependent reactions there are two regimes that are referred to as the low pressure limit and the high pressure limit. In the low pressure limit, the overall rate coefficient is limited by the number of stabilising collisions with a bath gas molecule and the reaction rate coefficient is shown to increase linearly with increasing pressure. Conversely at the high pressure limit it is assumed that upon formation of an energised association adduct, a stabilising collision occurs immediately and the rate coefficient is therefore limited only by the rate at which the

associating form an energised adduct. From both the experimental and theoretical work performed in this thesis, it is clear that none of the reactions studied here are at this high pressure limit. Master equation modelling shows the OH + C_2H_2 (Chapter 6), and OH + methanol (Chapter 5) reactions are at the low pressure limit in the pulsed Laval nozzle experiments. The rate coefficients for the OH + acetone and OH + DME reactions (Chapter 4) exhibit a certain amount of curvature with pressure, but even with these reactions, it is clear that they are still far from reaching the high pressure limit.

In this chapter the aim is twofold, first to estimate experimentally the high pressure limit for the reactions already studied, and secondly to explore the validity of the proxy method at low temperatures. In all the master equation calculations performed, barrierless steps have been described using an inverse Laplace transform (ILT) method. (1) As has been described in section 2.3.2.2 the ILT method requires the user to fit the high pressure limiting rate coefficients for this association step to the following Arrhenius form:

$$k^{\infty}(T) = A^{\infty}\left(\frac{T}{T^{\infty}}\right)^{n\infty}\exp(-E^{\infty}/\mathrm{R}T) \qquad \text{(Eq.1)}$$

where A^{∞} is the pre-exponential factor, E^{∞} is the activation energy and n^{∞} accounts for any temperature dependence in the observed $k^{\infty}(T)$'s. When possible, the ILT *A* factor has been fit to experimental data, but for reactions where the experimental data are in the low pressure limit, this ILT parameter is ill defined by fitting to experiments. In such cases the ILT *A* factor has been set to 3×10^{-10} molecule^{-1} cm^3 s^{-1}, representative of capture theory values. Further discussion of the justification of this can be found in Section 2.3.2.2 but to confirm the validity of this choice of *A* factor it is desirable to obtain an estimate of the high pressure limits of these reactions to both validate our master equation simulations and help extrapolate our data to higher pressures relevant to planetary atmospheres.

7.1.1. The Proxy method

The proxy method was first by proposed jointly by Quack and Troe (2) and Smith and co-workers (3) as a method of obtaining the high pressure limit in cases where it is not experimentally feasible to raise the total pressure sufficiently. In this method the high pressure limit for a given reaction:

$$A + B \rightarrow AB \qquad (R1)$$

is obtained not by measuring the loss of A in an excess of B but by instead measuring the loss of A (v=1,2,3...) in an excess of B, where the reagent A now has some degree of vibrational excitation. There are two assumptions implicit in this method. The first assumption is that the interaction potential between A and B is identical to the interaction potential between A (v=1,2,3) and B and therefore that the capture rate between the two reacting moieties and therefore the rate of formation of the energised adduct is independent of vibrational excitation. The second assumption is that the rate of intramolecular vibrational redistribution (IVR) of the vibrationally excited AB adduct is fast compared to the timescale for re-dissociation such that A is no longer vibrationally excited once the adduct dissociates.

A schematic of this scheme is shown in Figure 7.1. If the assumptions listed above hold then the rate for the loss of A(v=1) is equal to the rate of complex formation between A(v=1) and B which is in turn equal to the rate of complex formation between A and B and this by definition gives the high pressure limiting rate coefficient for the A + B reaction.

This method has been used successfully on a number of occasions. Jaffer and Smith (4) measured the rate coefficients for the loss of OH(v=1) in the presence of NO and NO_2 and showed that these rate coefficients agreed within error with the high pressure limiting rate coefficients for these reactions. In another study Silvente *et al.* (5) studied the reaction of OH(v=1,2,3) with a number of different co-reactants. For the reactions between OH and CS_2 and CH_3SH it was found that all three vibrational levels gave the same rate coefficient, however for other systems studied this was not the case and rate coefficient for OH loss was observed to increase with vibrational level.

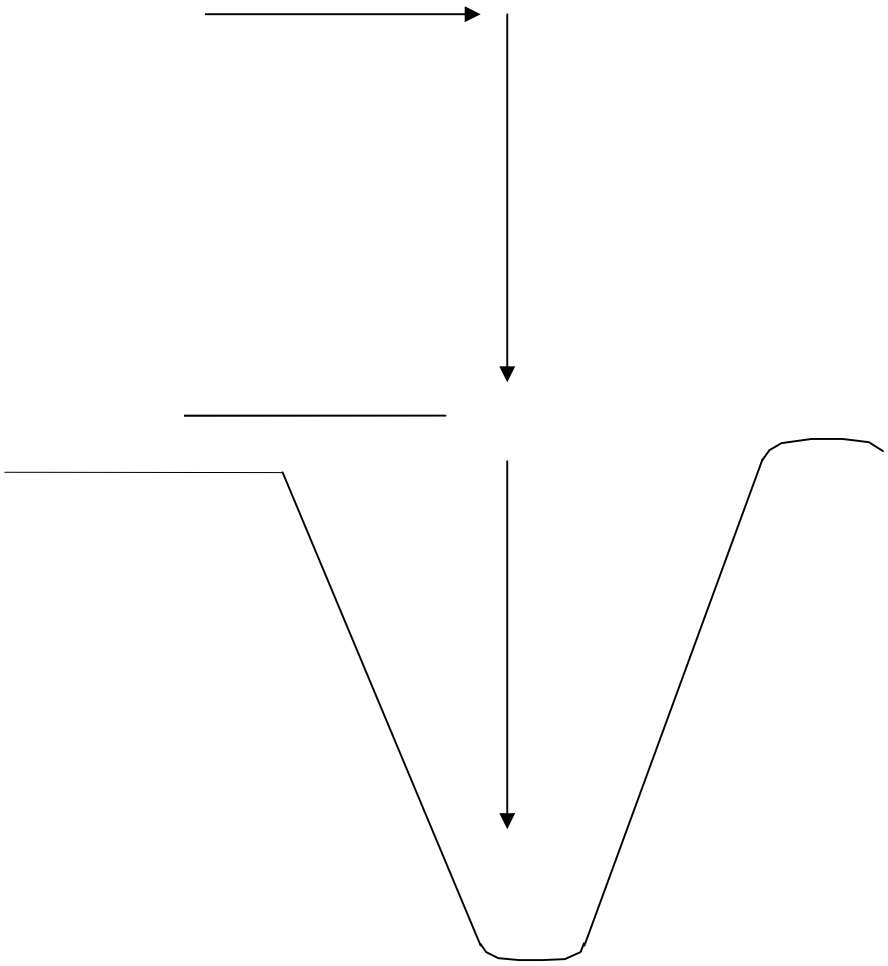

Figure 7.1: Schematic diagram showing the assumptions of the proxy method for the A+B reaction. Here the A(v=1) + B collision forms the highly excited adduct AB which undergoes rapid intermolecular vibrational energy transform to form the partially stabilised adduct AB* which then dissociates to give ground state A + B molecules.**

As was shown in the study by Silvente *et al.* (5) there are many situations where simply measuring the rate coefficient for A(v=1) + B does not give the desired high pressure limit. In a study looking at the high pressure limit of the OH + acetylene reaction McKee et al. (6) created OH in the v=1,2 energy levels and then measured the rate coefficient for the reaction between each vibrationally excited species. It was then found that the rate coefficient for OH(v=2) was larger than the rate coefficient for OH (v=1). In this case the high pressure limit could still be extracted but a large amount of analysis of the data was required. In another study Talukdar *et al.* (7) measured the rate coefficient for the reaction between OH (v=1) and acetone at 298K in

order to estimate the high pressure limit for formation of the hydrogen bonded complex. A rate coefficient of 2.7×10^{-11} molecule^{-1} cm^{3} s^{-1} was measured but considering the low temperature rate coefficients measured in this thesis, this would appear a significant underestimate of the true high pressure limit. While it is true that these experiments were at a significantly higher temperature than those in this thesis, the rate coefficients of barrierless association reactions to form an energised adduct are generally found to be relatively independent of temperature. (8-10) There are other studies which have also look at vibrationally excited reactants in order to infer association rate coefficients and many of these are discussed in a review by Smith. (11)

In such cases where the proxy method does break down it is the assumption of efficient IVR that does not always hold. The underlying theory of vibrational energy transfer will be presented in more detail in section 7.1.2 but for now it suffices to say that as the amount of vibrational excitation in a molecule is increased, the rate of IVR will also increase. This can be observed in the results of Mckee (6) where the measured rate coefficient for the reaction between OH and acetylene is seen to increase with increasing vibrational excitation in the OH. If assumption one of the proxy method holds, the measured rate coefficient for a vibrationally excited reaction can never be faster than the high pressure limit for the ground state reaction. It can then be postulated that as the OH molecule is taken to increasingly large amounts of vibrational excitation , the measured rate coefficients should converge to the desired high pressure limit.

It is not often practical to create and probe highly vibrationally excited species and an alternative to speeding up the rate of IVR is to instead decrease the rate at which the association complex dissociates. Cases where the proxy method appears to work will henceforth be referred to as being at the proxy limit, and it can be observed that for systems shown to be at the proxy limit at room temperature, the stabilisation energy of the association complex is large. For the species investigated in this thesis the association complex is simply a weak van der Waals well and as such these complexes have extremely short lifetimes at room temperature (1.59×10^{-10} s as predicted by master equation calculations on OH + acetone system

performed in Chapter 4). It is proposed however that by reducing the temperature and thus increasing the lifetime of the van der Waals complexes, the proxy limit can be promoted. This chapter will aim to test this and by measuring the rate of loss OH (v=1,2 and 3) and the extent to which the results approximate the true high pressure limit can be inferred from the convergence of the rate coefficients for the loss of each of these levels.

7.1.2. Energy transfer and SSH theory

Although no detailed energy transfer calculations are performed in this chapter, the proxy method relies upon efficient redistribution of vibrational energy. As such a brief discussion of the theory behind energy transfer will be given here. This discussion will be confined to vibrational and translational energy transfer for simplicity.

Before touching upon the rigorous mathematical details of the energy transfer, to give an overview of such processes in the context of the proxy method. Although in the current case we are interested in the vibrational energy transfer within an excited AB* complex, for the purpose of the energy transfer theories presented here it is necessary to start with the collisional event between A(v=i) and B. The lifetime of the complex AB* with respect to dissociation can then be described as the lifetime of the collision and theories of energy transfer aim to quantify the probability of a particular vibrational energy change occurring within the collision lifetime. The premise of the current work is, that by reducing the temperature, the collision lifetime between A and B can be increased, which raises the probability that vibrational energy will be removed from A prior to the dissociation of AB*.

The simplest picture of vibrational energy transfer is given by the Ehrenfest adiabatic principle (12) which classifies processes in terms of being adiabatic (no energy transfer) or non-adiabatic (energy transfer). In vibrational energy transfer, whether or not the collisional process is adiabatic or non-adiabatic, depends upon the change in force during the collision, compared to the vibrational period. Mathematically this can be described using an adiabacity parameter:

$$\xi = \frac{\tau_c}{t_v} \qquad \text{(Eq. 2)}$$

where τ_c is the duration of the collision and t_v is the period of oscillation in the vibrational mode which undergoes energy transfer. Using the adiabacity parameter, a adiabatic collision can then be classified as one, for which $\zeta < 1$.

There are different theoretical models used to quantify energy transfer and as with many fields of science, there is a particular nomenclature which is used in the theory of energy transfer. The quantity desired from any energy transfer calculation or experiment is the parameter P_{ab} which is the probability per collision of an a→ b vibrational transition occurring in a particular vibrational mode. The most elementary theory of vibrational energy transfer is the Landau-Teller (13) theory however for the present purposes the more sophisticated SSH theory of Schwartz and Slawsky and Herzfeld (14) will be described. All theories describing energy transfer require the definition of a potential between the two colliding atoms. In reality intermolecular collisions are most accurately described using a Lennard Jones potential which was described in section 2.4.2.3. However the use of such a potential complicates the mathematical solutions energy transfer equations and in order to give analytical solutions, a potential function based upon exponentials is often used. (13) SSH theory is no different and the intermolecular potential used in this model is given by:

$$V(r) = \mathrm{U}\exp(-\alpha r) - \varepsilon \qquad \text{(Eq. 3)}$$

Where *r* is the internuclear separation between the two colliding molecules and the other parameters are fitted in order to approximate a known Lennard Jones potential for the two species. Another important quantity is ΔE, the energy transferred upon collision:

$$\Delta E = h\nu_a(i - j) - h\nu_b(k - l) \qquad \text{(Eq. 4)}$$

Where a vibrational mode a with frequency ν_a changes from quantum state *i* to *j* and simultaneously another mode b either in the same molecule or the colliding molecule with frequency ν_b changes from quantum state *k* to *l*. The quantity ΔE then determines the amount of energy which must be taken up

as translational energy in one of the colliding molecules and if *k* = *l* then this corresponds to purely vibrational-translational energy transfer. In the limiting cases ΔE > 200 cm^{-1} and ΔE < 50 cm^{-1} the SSH equations have simpler analytical forms (15) and these are given in equations Eq. 5 and Eq. 6 respectively.

$$P_{k-l(b)}^{i-j(a)} = P_0(a)P_0(b)(\frac{r_c^*}{\sigma})^2[V^{i-j}(a)]^2[V^{k-l}(b)]^2 8(\frac{\pi}{3})^{\frac{1}{2}} \times[\frac{8\pi^3\mu\Delta E}{\alpha^{*2}h^2}]\xi^{\frac{1}{2}}\exp[-3\xi+\frac{\Delta E}{2kT}+\frac{\varepsilon}{kT}] \quad \text{(Eq.5)}$$

$$P_{k-l(b)}^{i-j(a)} = P_0(a)P_0(b)[V^{i-j}(a).V^{k-l}(b)]^2(\frac{64\pi^2\mu kT}{\alpha^{*2}h^2})\exp(\frac{-\varepsilon}{kT}) \quad \text{(eq.6)}$$

where

$$\xi = (\frac{\Delta E^2\mu\pi^2}{2\alpha^{*2}\hbar^2 kT})^{\frac{1}{3}} \quad \text{(eq.7)}$$

Here a vibrational mode a undergoes a transition from quantum state *i* to *j*, whilst simultaneously a vibrational mode b undergoes a transition from state *k* to *l*. The P_0 are steric factors, σ is the fitted Lenard Jones parameter in the intermolecular potential, r_c^* refers to the classical turning point in the intermolecular potential, the [*V*] are vibration factors given by the matrix element for the vibrational transition, α and ε are the parameters from the fitted potential in Eq. 3 and μ is the reduced mass of the collision

From these equations the manner in which transition probability changes with ΔE and the amount of vibrational energy in mode a, *i* , can be explore. The dependence of the transition probability upon ΔE is the most apparent and from Eq. 8 it can be seen that the transition probability decreases exponentially as the energy gap gets larger. Resonant vibrational energy transfer, where ΔE = 0 is particularly efficient and since Eq. 6 shows no dependence upon ΔE all near resonant transitions with ΔE < 50 cm^{-1} act as if resonant. (13)

It is also found that the transition probability increases with vibrational excitation, so as proposed, OH(v=3) would be expected to relax faster than OH(v=2) which would in turn be expected to relax faster than OH(v=1). This dependence arises from the vibrational factor $[V^{i-j}(a)]$ which for single quanta transition is given by the formula:

$$[V^{(i+1)-i}]^2 = \alpha^2 (A^2)(i+1)/2\gamma \qquad \text{(Eq. 8)}$$

where

$$\gamma = \frac{4\pi^2 \nu}{h} \qquad \text{(Eq. 9)}$$

Here A is the vibrational amplitude coefficient and ν is the frequency of the vibrational mode. Neglecting anharmonicity, it is then found that $[V^{3-2}]^2 \approx 3$ $[V^{2-1}]^2/2 \approx 2[V^{1-0}]^2$ and since the transition probability is directly proportional to $[V^{i-j}(a)]$ this would be expected to increase with increasing vibrational excitation, according to the same ratios.

Referring back to the A (v=1,2,3) + B reaction, when the lifetime, τ of the pre-reaction complex AB* is greater than the relaxation time of the vibrational energy in A then according to the proxy method it should be found that $k_{bi(A(v=3))} = k_{bi(A(v=2))} = k_{bi(A(v=1)} = k_{bi}^{\infty}{}_{(A(v=0).}$ This has been defined as the proxy limit for a reaction. However if the converse is true and relaxation time >> than τ then given the SSH arguments it would be expected that $k_{bi(A(v=3))} = 3\, k_{bi(A(v=2))}/2 = 2k_{bi(A(v=1)}$ and this shall be referred to as the SSH limit for the reaction.

There are other general arguments that can be made from the SSH equations. The dependence of the transition probability upon μ the reduced mass of the collision, and temperature is complex in Eq.5 and it is difficult to make generic statements regarding this. However given that in the current work, vibrational energy levels of OH are being considered with $\nu = 3$ it is likely that some combination of modes in the co-reactant will produce a resonant or near resonant transition. From Eq.6 it can be seen that the transition probability is proportional to μ. The T dependence in this equation is more complicated but it can be seen that although the transition probability is proportional to T in the pre-exponential factor, there is an exponential

dependence upon the inverse of *T* and this is likely to produce an overall negative temperature dependence. It would then be predicted that increasing the mass of the co-reagent and decreasing the temperature would promote the proxy limit and this will be explored in the current chapter.

7.1.3. The $O(^1D) + H_2$ reaction.

In order to perform proxy method experiments on the reactions of the last two chapters, it was necessary to create the OH radical with significant amounts of vibrational excitation. In order to do this ozone was photolysed within the supersonic laval flow to produce $O(^1D)$ atoms. These $O(^1D)$ atoms then react with H_2 in order to produce OH radicals in vibrational levels of up to v=4. (16) This method was used to produce ground state OH when probing methoxy radical formation in Chapter 5 but here the reaction shall be looked at in a little more detail.

The $O(^1D) + H_2$ reaction is relevant to both combustion (17) and chemical lasers (18) but it has attracted the most attention due to its importance in the earth's atmosphere. (19) O (^1D) atoms are produced in the earth's atmosphere though the photo dissociation of ozone at wavelengths < 340 nm as shown in R2.

$$O_3 + h\nu \rightarrow O_2 + O(^1D) \qquad \text{(R2)}$$

The absorption of radiation by ozone is a key process in the stratosphere, preventing harmful UV radiation reaching the surface and the $O(^1D)$ radicals produced readily reacting with water methane or hydrogen to produce the OH radical as shown in R(3-5).

$$O(^1D) + H_2O \rightarrow 2OH \qquad \text{(R3)}$$

$$O(^1D) + CH_4 \rightarrow OH + CH_3 \qquad \text{(R4)}$$

$$O(^1D) + H_2 \rightarrow OH + H \qquad \text{(R5)}$$

The $O(^1D) + H_2$ reaction is thus relevant to two of the most important process in the earth's atmosphere, absorption of UV radiation by ozone and production of the OH radical (though only in the stratosphere not the troposphere), and consequently this reaction has been studied extensively,

both theoretically (20, 21) and experimentally. (22, 23) Given the many experimental and theoretical studies a full review of the literature is beyond the scope of this thesis, though it is noted that there are a number of review articles which summarise the various studies on this reaction. (24, 25)

There are two reaction paths whereby the OH radical can be formed from this reaction. (26) The first corresponds to the barrierless insertion of the $O(^1D)$ radical perpendicular to the H-H bond followed by isomerisation and dissociation to form OH. The second channel corresponds to a direct abstraction mechanism with a barrier of 17 kJ mol^{-1}. Rate coefficients for the overall reaction have been measured and were determined to be 1.2×10^{-10} $molecule^{-1}$ cm^3 s^{-1} at 298 K (27) . For the current temperature regime it is expected that only the barrierless channel will be important and since this rate coefficient is approximately gas kinetic at 298 K, the rate coefficients measured are likely to be a good approximation to the overall rate coefficient at 93 K, the temperature of the studies in the current work

From the current perspective it is the vibrational distribution in the OH products that is particularly important. The most comprehensive experimental study of the relative distributions was performed by Aker and Sloan. (16) In this study significant populations were observed in vibrational levels up to v=4 and a population inversion was seen be vibrational levels 1 and 2 The relative populations of v=1,2,3 and 4 were determined to be 0.29:0.32:0.25:0.13 and many other studies have observed or predicted similar amount of vibrational excitation.

7.2. Methodology

The rate coefficients for the reactions between OH(v=1,2 and 3) with acetone, DME, methanol, acetylene and were measured at 93 K using the T93P6E16 nozzle and in addition the OH(v=1,2 and 3) + methanol reaction was also studied at 63K using the T63P3E16 nozzle. Ozone (~4% in O_2) was created by flowing oxygen (BOC) through an ozone generator. The resulting O_3 / O_2 mixture was then admitted to an empty cylinder and diluted further with N_2 (BOC, OFN) to give ~ 0.5 % O_3 overall. For the co-reagents,

acetone (Fluka, Riedel-deHaėn, analytical grade 99.5%), methanol (Aldrich, 99.9%) and DME (Aldrich, 99.9%) were admitted to a separate cylinder (~1-2 %) and subsequently diluted with N_2 (BOC, OFN) as described in chapter 3. For experiments with acetylene (BOC) as the co-reagent, these were admitted to the gas line straight from the cylinder. The hydrogen (BOC) necessary for the $O(^1D) + H_2$ reaction was also added directly from the cylinder.

In these experiments the ozone was photolysed as before using an excimer laser (Lambda Physic LPX 200) at 248 nm, however in order to probe the excited vibrational levels of OH, a separate excimer (Lambda Physic LPX 300) pumped dye laser (Lambda Physic FL3002E) system was used. The rotationally resolved fluorescence excitation spectra for the (1,1), (2,2) and (3,3) bands for the OH $A^2\Sigma^+$-$X^2\Pi_{3/2}$ electronic transition, were simulated using the LIFBASE (28) software and they are shown below in Figure 7.2. Here the Q1(1.5) transition was probed for each vibronic band at wavelengths of 313.4 nm, 319.7 nm and 326.4 nm for the (1,1), (2,2) and (3,3) bands respectively. The resulting fluorescence was collected using a PMT (Thorn EMI 9813QB photocathode voltage -2.1 kV) and an interference filter (Barr Associates Inc., 50 mm diameter, λ_{centre} = 308.5 nm, FWHM = 5 nm) was used such that only the (0,0) off resonance was collected. A simple energy level diagram for the excitation and emission processes is shown in Figure 7.3.

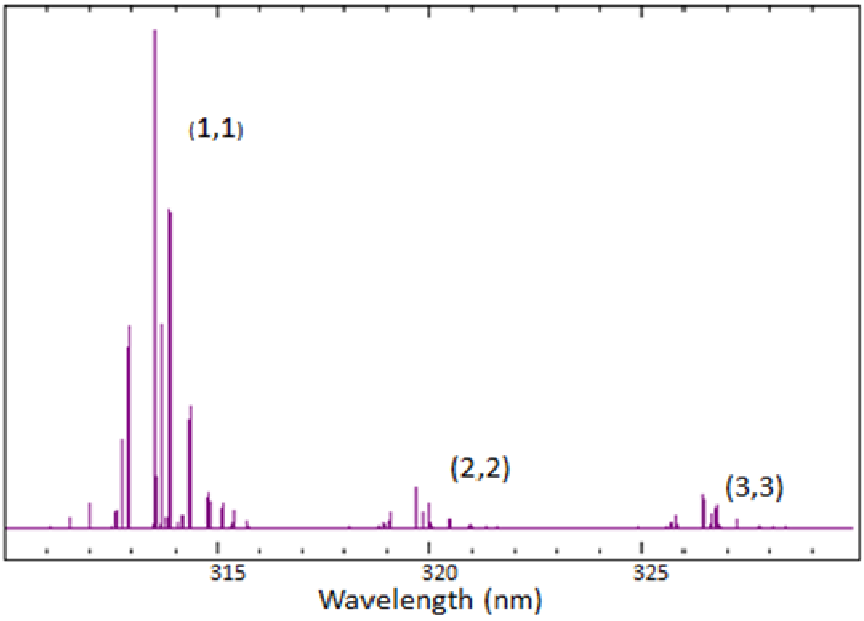

Figure 7.2: LIF excitation spectra for the (1,1), (2,2) and (3,3) bands of the OH $A^2\Sigma^+$-$X^2\Pi_{3/2}$ transition. These have been simulated using LIFBASE with a rotational temperature of 93K and a resolution of 0.01 nm . The intensity of the $A^2\Sigma^+$-$X^2\Pi_{3/2}$ (3,3) band has be scaled by three orders of magnitude in order to present all three transitions levels on the same figure.

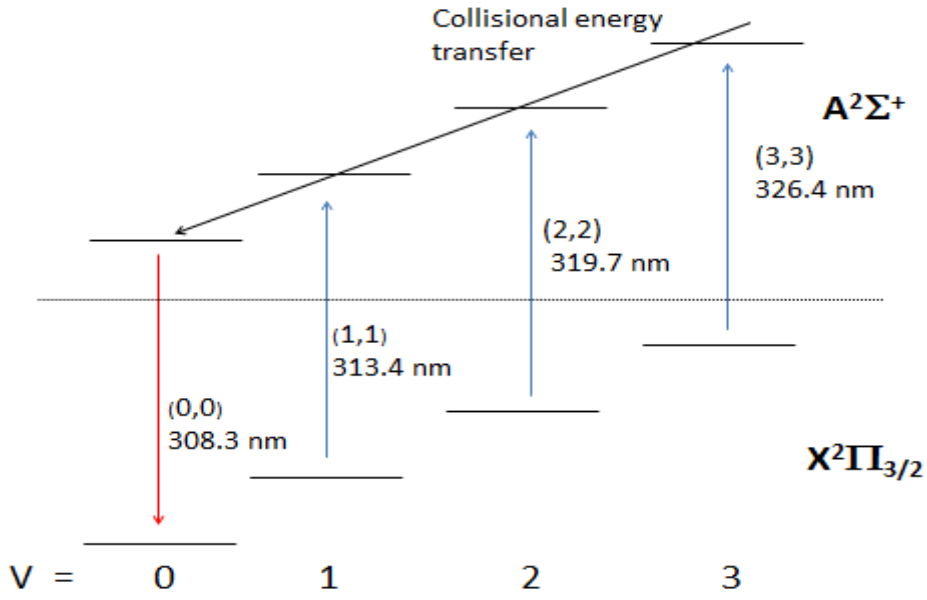

Figure 7.3: LIF excitation and emission scheme used in the current work. For each vibrational level V the $A^2\Sigma^+$-$X^2\Pi_{3/2}$ (V,V) band is excited and following collisional energy transfer in the $A^2\Sigma^+$ state, fluorescence is collected off resonantly from the (0,0) emission.

In order to analyse the pseudo first order temporal traces obtained from these experiments, it was necessary to solve the rate equations for the system. The kinetic scheme may be written out as follows:

$O(^1D) + H_2$	→	OH(v=(i)) + H	(k_{v1})	(R6)
$O(^1D) + H_2$	→	OH(v=(i+1)) + H	(k_{v2})	(R7)
OH (v=(i+1)) + B	→	OH(v=i) + B	(k_{c2})	(R8)
OH (v=(i+1)) + B	→	products	(k_{r2})	(R9)
OH (v=i) + B	→	OH(v=(i-1)) + B	(k_{c1})	(R10)
OH (v=i) + B	→	products	(k_{r1})	(R11)

This scheme considers two OH vibrational levels reacting with some co-product B. Rate coefficients with the subscript v (R6 and R7) correspond to the formation of OH in some vibrational level, rate coefficients with subscript c (R8 and R10) correspond to cascade from one vibrational level to a lower one, and rate coefficients with the subscript r (R9 and R11) represent the vibrationally excited OH reacting with B to form chemical products (ie abstraction products). The subscripts 2 and 1 for the rate coefficients represent the higher and lower of the two OH vibrational levels respectively. It should also be noted that reactions R8-R11 all occur via the formation of some association complex OH(v=*i*)--B though this step has not been shown explicitly. This scheme can then be formulated by the following rate equation:

$$\frac{d[\mathrm{OH}(v=i)]}{dt} = k_{c2}[\mathrm{OH}(v=i+1)] + k_{v1}[\mathrm{H}_2] - (k_{c1} + k_{r1})[\mathrm{OH}(v=i)]$$

(Eq. 10)

where the rate coefficients *k* are the pseudo first order for reactions R6-R11. In these equations, only changes in energy of 1 quanta (OH(*v*=*i*+1) → OH(*v*=*i*)) were considered. This is an approximation, however it was necessary in order to reduce the number of parameters in the resulting fitting equation. The differential equations were solved using an integrating factor method and the following fitting equation was obtained :

$$[\mathrm{OH}(v=i)] = A1\exp(-(k_{v1}+k_{v2})t) + A2\exp(-((k_{v2}+k_{v1})t) - A3\exp(-(k_{c2}+k_{r2})t) + A4\exp(-(k_{r1}+k_{c1})t)) + b$$

(Eq. 11)

where

$$A1 = \frac{k_{v1}\,\mathrm{O1D}}{(k_{r1} + k_{c1} - k_{v1} - k_{v2})}$$

$$A2 = \frac{k_{c2}\,k_{v2}\,\mathrm{O1D}}{(k_{c2} + k_{r2} - k_{v1} - k_{v2})(k_{r1} + k_{c1} - k_{v2} - k_{v1})}$$

$$A3 = \frac{k_{c2}\,k_{v2}\,\mathrm{O1D}}{(k_{c2} + k_{r2} - k_{v1} - k_{v2})(k_{r1} - k_{c2} - k_{r2})}$$

$$A4 = A3 - A1 - A2$$

and *O*1D is the initial relative population in OH(v=i) given by the LIF signal height.

7.3. Results and analysis

An example of a pseudo first order OH decay is show below for v =1, 2 and 3 in Figure 7.4, Figure 7.5 and Figure 7.6 respectively. The simplest trace of the three is that corresponding to the decay of OH (v=3) and it can be seen from the fit and the corresponding residuals that these data are well described a single exponential decay equation. The reasons for this can be readily understood by referring to the relative vibrational level distributions, for OH radicals formed through the $O(^1D) + H_2$ reaction. The population produced in v=4 is relatively small (0.13 of the total OH population compared to 0.25 for v=3) and many of these v=4 radicals could be stabilised in multiple quanta transitions, causing growths in the population of OH(v=2,1) rather than OH(v=3). In comparison to the OH(v=3) experimental traces, the decays for OH(v=1) and OH(v=2) displayed growth in the LIF signal at early times consistent with cascade from upper vibrational levels. This growth persists for up to 50 μs and a single exponential decay could only reproduce the experimental data at times > 75 μs.

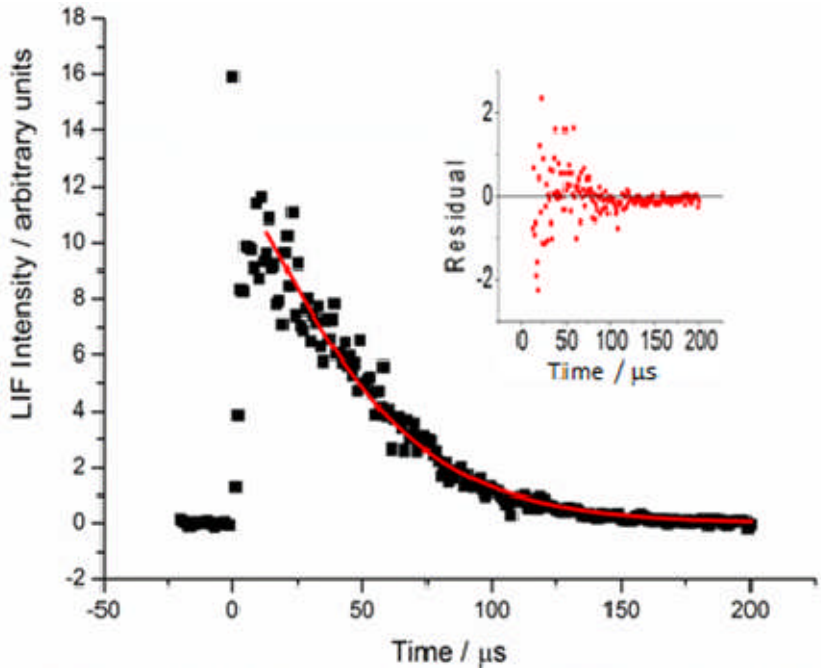

Figure 7.4: Temporal evolution of the LIF signal for OH(v=3) in the presence of methanol. For the current trace [methanol] = 1.2×10^{14} molecule cm^{-3}, $[H_2] = 1.2\times10^{16}$ molecule cm^{-3}, $[O_3] = \sim4\times10^{13}$ molecule cm^{-3}, $[N_2] = 5.1\times10^{16}$ molecule cm^{-3} and T = 93±4 K. Fitting Eq. 12 to the data gives a pseudo first order rate coefficient $k_{c1} + k_{r1}$ of 31400 ± 1300 s^{-1}. This trace consists of a total of 220 points and each point was averaged 20 times. The LIF signal was normalised with respect to probe laser power on a shot-by-shot basis. The inset shows the residuals of the fit of Eq. 12 (below) to the data.

It was clear that the OH(v=1) and OH(v=2) traces required the full fitting equation (Eq. 11) in order to describe, however using this equation was found to be highly non- trivial given the number of fitting parameters. In order to constrain some of the parameters, the following approach was used. Given that the v=3 data showed no obvious growth at early times, these traces were fit with the single exponential decay equation:

$$[\mathrm{OH}(v=i)] = [\mathrm{OH}(v=i)]_0 \times \exp(-(k_{c1} + k_{r1}) \times t) \qquad \text{(Eq. 12)}$$

where $[OH\ (v=i)]_0$ corresponds to the relative OH(v=3) population at time zero which is given by the signal height Then using the bimolecular rate coefficient obtained for OH(v=3) + methanol from this fitting the k_{c2} parameter from Eq. 11 was fixed for the OH(v=2) data Using the bimolecular rate coefficient for OH(v=2) + methanol obtained in this manner, k_{c2} could

then be fixed for the OH (v=1) data. In each case k_{r2} is set to the value of the intercept of the bimolecular plot for the level above. For each trace k_{v2} and k_{v1} where assigned according to the ratio of vibrational levels produced from the $O(^1D) + H_2$ reaction (16) given in section 7.1.3. Given the $[H_2]$ concentrations used in the current experiments of 1.2×10^{16} molecule cm^{-3} and the rate coefficient for the $O(^1D) + H_2$ reaction measured at 298 (27) it was assumed that the the OH (v=i) molecules would be formed at a rate of 1000000 molecule cm^{-3} s^{-1}. This overall rate coefficient was then multiplied by the respective ratios for the different vibrational levels in order to give k_{v2} and k_{v1} . Finally the baseline *b* was fixed at zero for each trace, and the O^1D parameter was allowed to float, being well defined by the signal height for each trace.

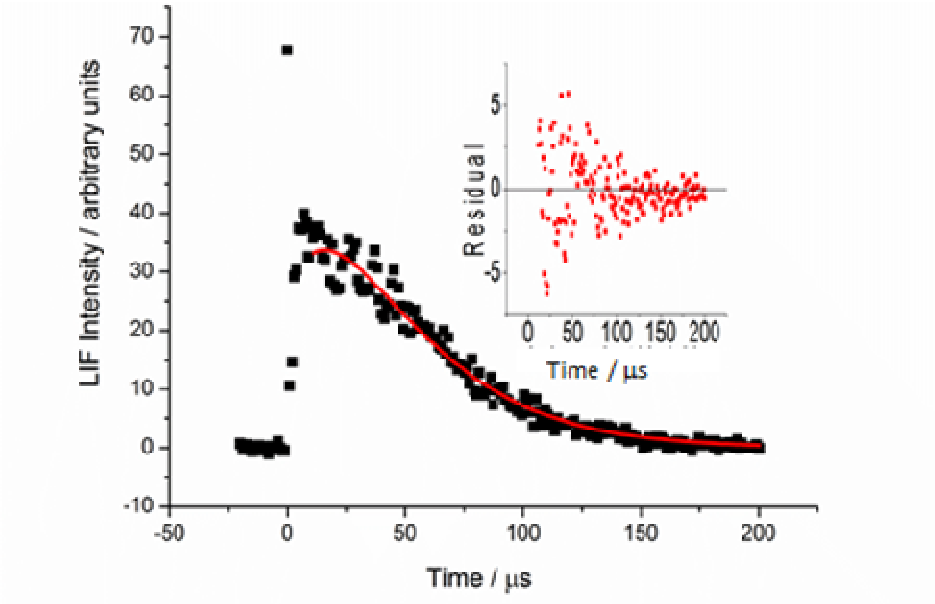

Figure 7.5: Temporal evolution of the LIF signal for OH(v=2) in the presence of methanol. For the current trace [methanol] = 1.7×10^{14} molecule cm^{-3} $[H_2] = 1.2\times10^{16}$ molecule cm-3, $[O_3] = \sim4\times10^{13}$ molecule cm^{-3}, $[N_2] = 5.1\times10^{16}$ molecule cm^{-3} and T = 93±4 K. Fitting with Eq. 11 gives a pseudo first order rate coefficient $k_{c1} + k_{r1}$ of 33400 ± 1300 s^{-1} This trace consists of a total of 220 points and each point was averaged 10 times. The LIF signal was normalised with respect to probe laser power on a shot-by-shot basis. The inset shows the residuals of the fit of Eq. 11 to the data.

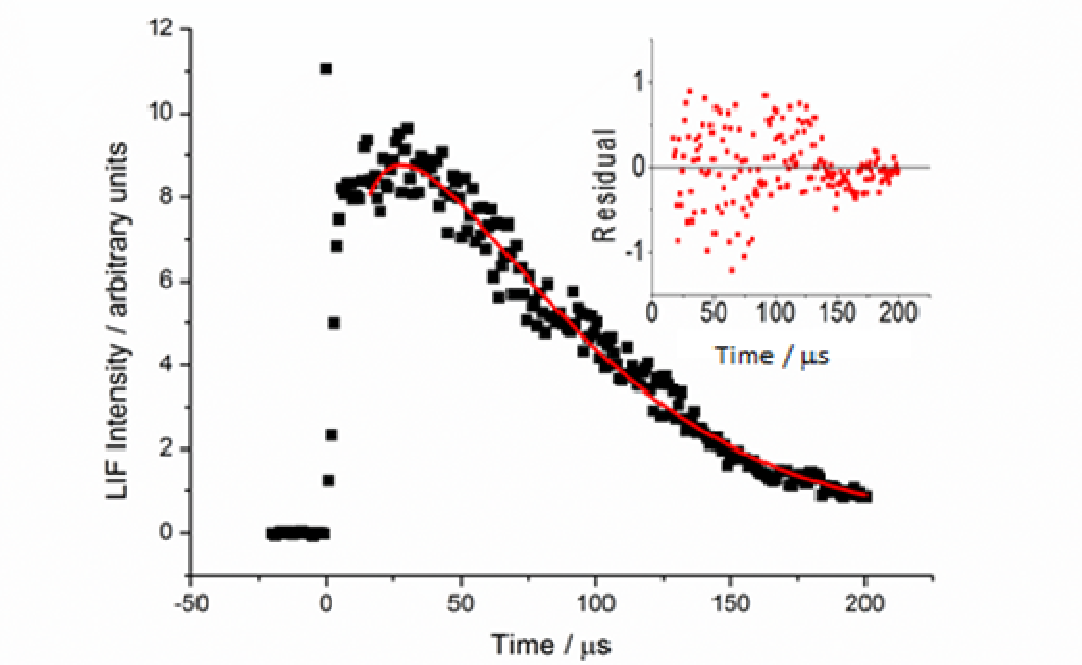

Figure 7.6: Temporal evolution of the LIF signal for OH(v=1) in the presence of methanol. For the current trace [methanol] = 1.3×10^{14} molecule cm^{-3} , [H_2] = 1.2×10^{16} molecule cm-3, [O_3] = ~4×10^{13} molecule cm-3, [N_2] = 5.1×10^{16} molecule cm^{-3} and T = 93±4 K. Fitting with Eq. 11 gives a pseudo first order rate coefficient, k_{c1} + k_{r1}, of 19800± 1100. This trace consists of a total of 220 points and each point was averaged 10 times. The LIF signal was normalised with respect to probe laser power on a shot-to-shot basis. The inset shows the residuals of the fit of Eq 11 to the data.

As a check it was also shown that the rate coefficients obtained in this method agreed with rate coefficients obtained when the OH(v=1,2) decays were fit with the single exponential equation Eq. 12 starting 75 μs into the trace. Since it was the decay component of these traces that was required, Eq. 12 would be expected to give a reasonable approximation to the true decay coefficient k_c+k_r providing that the fitting was started at a sufficiently long delay time after the start of the trace such any growth component was no longer significant. This approach would not be expected to give answers with the same accuracy as the full equation Eq. 11 but it provided a good check to ensure that the fitting methodology employed was giving realistic answers. A comparison between rate coefficients obtained for the OH(v=1,2) + methanol reaction at 93 K using the two different fitting methods is shown in Table 7.1.

In order to further explore the errors associated with fixing parameters in the full equation, the parameters $k_{v2}$and k_{1i} were varied by an order of magnitude and the change in the bimolecular rate coefficient k_{bi} (OH(v=i) + methanol) was observed to be at most 5%. The parameter k_{c1} was also allowed to vary by upto 10% and the change in the bimolecular rate coefficient k_{bi} (OH(v=i) + methanol) was again observed to be < 5%. This fitting approach using Eq. 11 was then adopted for all other data analysis within this chapter.

OH vibrational level	k_{bi} (OH(v=i)+methanol) / molecule^{-1} cm^3 s^{-1} (equation Eq. 11)	k_{bi} (OH(v=i)+methanol) / molecule^{-1} cm^3 s^{-1} (equation Eq. 12)
2	(1.9±0.7) ×10^{-10}	(2.2±0.8) ×10^{-10}
1	(8.9±0.7) ×10^{-11}	(7.2±0.6) ×10^{-11}

Table 7.1: Comparison of bimolecular rate coefficients for the OH(v=1) and OH(v=2) reactions with methanol at 93±4 K obtained using two different fitting methods. The errors correspond to the 95% confidence limits of the linear fits to the bimolecular plots.

Bimolecular plots for all three OH vibrational levels are shown in Figure 7.7 for the OH (v=1,2,3) + methanol reaction at 93 K. From this graph it is apparent that the rate coefficient increases with increased vibrational level, though even the rate coefficient for OH(v=1) + methanol ((8.9±0.3)×10^{-11} molecule^{-1} cm^3 s^{-1}) is 2.6 times larger that the rate coefficient for OH(v=0) + methanol at 83K ((3.4±0.5)×10^{-11} molecule^{-1} cm^3 s^{-1}). How close a given reaction is to the proxy limit is determined by the ratio of the rate of cascade compared to the inverse lifetime of the energised adduct. SSH theory predicts that the rate coefficient for cascade to lower vibrational levels (k_c), increases with vibrational energy and from the methanol results it is clear that the increase in k_c outcompetes any reduction in the complex lifetime as the vibrational level is increased.

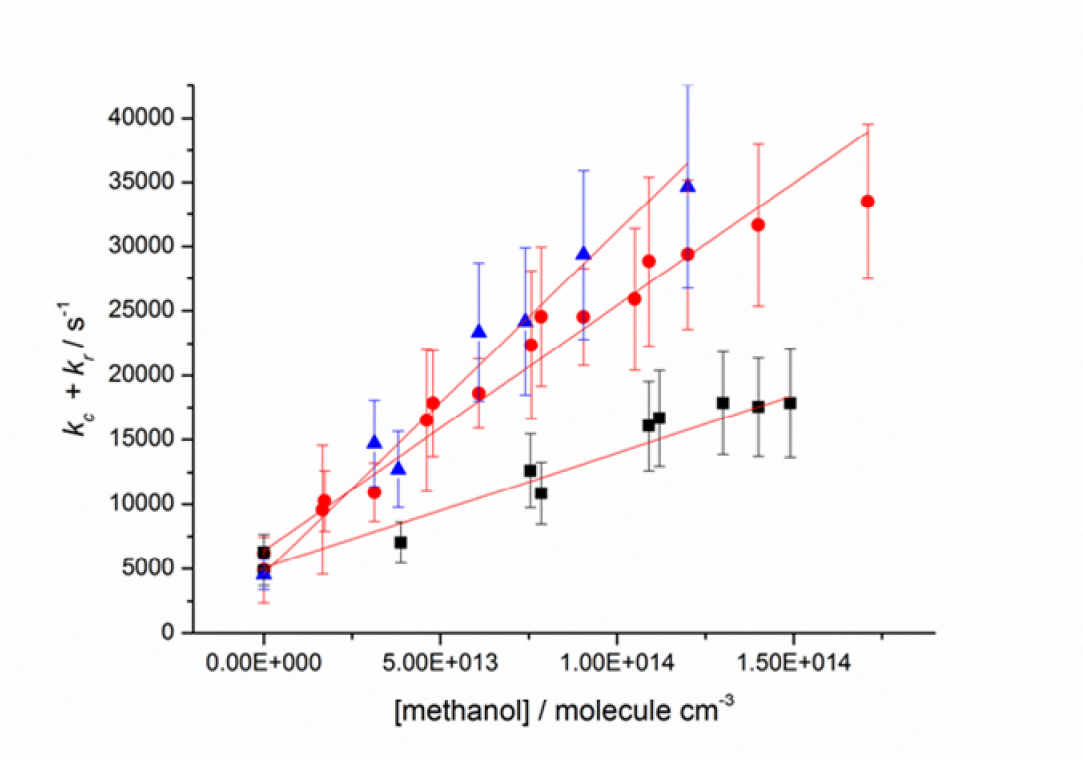

Figure 7.7: Bimolecular plots for the OH(v=3) (blue) OH(v=2) (red) and OH(v=1) (black) reactions with methanol at 93±4 K. The pseudo first order rate coefficients were obtained from fitting the experimental data with Eq 11 and they incorporate 2σ error both from the fitting process and [methanol]. Bimolecular rate coefficients were obtained from a weight linear fit and value are given in Table 7.2. The errors were obtained from the 95% confidence limits of the linear fits.

One of the assumptions of the proxy method is that the collision rate between the two reacting species is unchanged when vibrational excitation is added. As has been stated this assumption appears to be a good one. This can be seen from considering the gas kinetic collision rate given below :

$$Z = 2n\sigma^2(\pi kT/m)^{\frac{1}{2}} \qquad \text{(Eq. 13)}$$

where n is the number density of molecules, σ is the Lennard Jones parameter and m is the mass of the molecule. Only σ could possibly change in going from v=0 to v=1,2,3 and since the overall bond length would be expected to change only marginally on going from v=0 to v=3 σ would be expected to change by a similarly small amount.

Given the above arguments, the high pressure limit of the OH(v=3) + methanol reaction, can be assumed to be identical to that for the OH(v=0)

reaction and consequently, the OH(v=3) + methanol rate coefficient of (2.6±1.7) $\times 10^{-10}$ molecule^{-1} cm^3 s^{-1} at 93 K can be considered a lower limit to the true high pressure limiting rate coefficient for the OH + methanol reaction. However since the OH + methanol rate coefficient can be observed to be increasing with each quanta of vibrational energy, then this suggests that the reaction is still not at the proxy limit and that the OH(v=3) + methanol rate coefficient is likely to be an underestimate of the overall high pressure limit.

Using the same approach as for the OH + methanol reaction, rate coefficients were measured at 93 K using DME and acetone as co-reagents and bimolecular plots for each OH vibrational level are shown in Figure 7.8 and Figure 7.9 respectively. In each of these plots it is again evident that the observed OH loss coefficient increases with the amount of vibrational excitation in the OH bond but it can be seen that in both the DME and acetone cases the v=3 and v=2 bimolecular rate coefficients are closer in magnitude than the methanol case. It should be noted however, that given the large error bars on the bimolecular plots even in the OH + methanol case the v=2 and v=3 rate coefficients are not statistically different. With this consideration it is worth exploring difference between OH v=3 and OH v=1 rate coefficients instead and it is found that $k_{(OH(v=1))}/k_{(OH(v=3))}$ increases in the order acetone > DME > methanol, with ratios of 0.59, 0.42 and 0.34 respectively. According to SSH theory, this ratio would be expected to be 0.33 and it can be seen that these results would predict that the OH + methanol system is near the SSH limit, whilst the OH + DME and OH + acetone reactions are converging towards the proxy limit.

It would be expected that the OH + acetone and OH + DME reactions would be closer to the proxy limit than the OH + methanol reaction. The results obtained in chapters 4 and 5 showed that theoretically the rate of dissociation of the association complex decreases with the size of the molecule and experimentally the OH(v=0) + acetone rate coefficient were observed to be higher in the fall off regime than the OH + DME rate coefficients which were in turn higher than those for OH + methanol reaction.

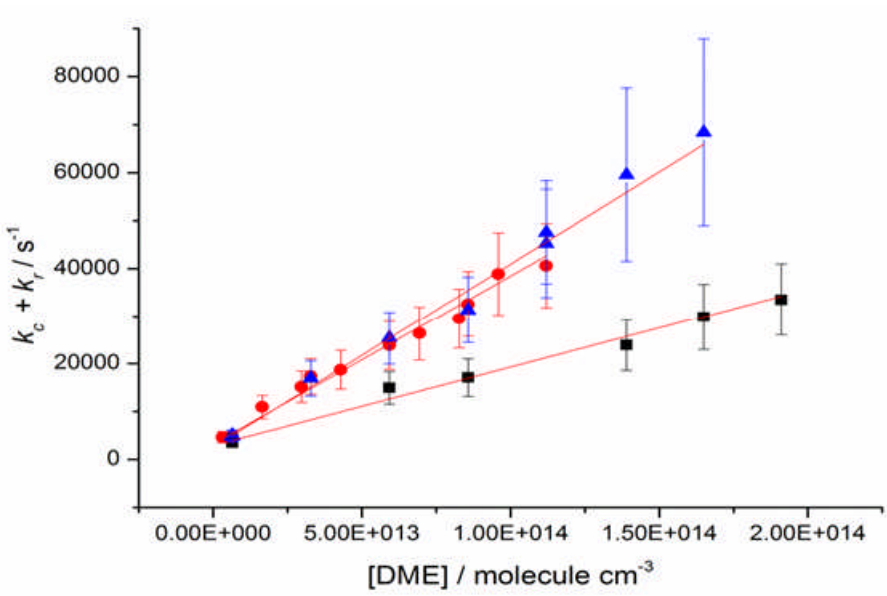

Figure 7.8: Bimolecular plots for the OH(v=3) (blue) OH(v=2) (red) and OH(v=1) (black) reactions with DME at 93±4 K. The pseudo first order rate coefficients were obtained from fitting the experimental data with Eq 12 and they incorporate 2σ errors both from the fitting process and in [DME]. Bimolecular rate coefficients were obtained from a weight linear fit to each dataset and the results are given in Table 7.2. The errors were obtained from the 95% confidence limits of the linear fits.

All the OH(v=1,2,3) rate coefficients measured in the current chapter are given in Table 7.2 and using the OH(v=3) rate coefficients as lower limits to the high pressure limiting rate coefficients, these results would suggest that the high pressure limiting rate coefficients for the OH + methanol, OH+acetone and OH + DME reactions, are all > 3×10^{-10} molecule^{-1} cm^3 s^{-1} , consistent with a gas kinetic collision rate. Interestingly, at 93K it is the OH + DME reaction which exhibits the largest rate coefficient rather than the OH + acetone reaction but since all the OH (v=3) rate coefficient agree within error, it is unclear how much significance should be placed upon this.

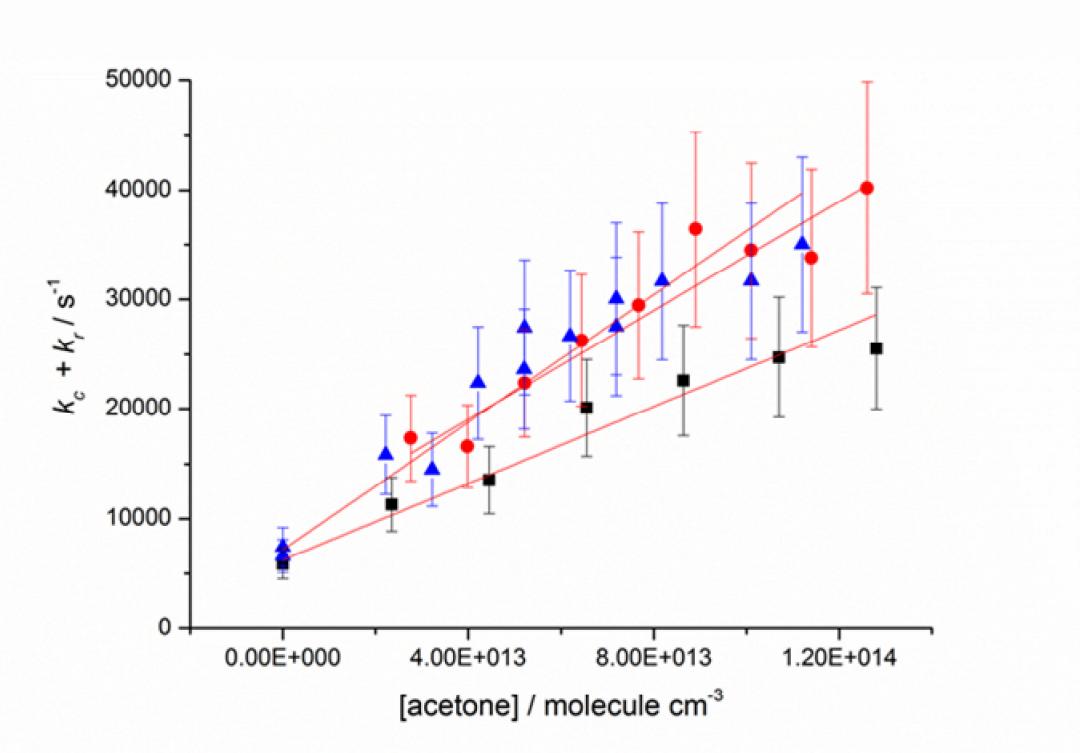

Figure 7.9: Bimolecular plots for the OH(v=3) (blue) OH(v=2) (red) and OH(v=1) (black) reactions with acetone at 93K. The pseudo first order rate coefficients were obtained from fitting the experimental data with Eq 12 and they incorporate 2σ errors both from the fitting process and in [acetone]. Bimolecular rate coefficients were obtained from a weight linear fit to each data set and the results are given in Table 7.2. The errors were obtained from the 95% confidence limits of the linear fits.

The three systems considered so far all form hydrogen bonded pre reaction complexes bound by around 20 kJ mol^{-1}, and the v=3 rate coefficients for each of these systems are all tending to the gas kinetic collision value. However the OH + acetylene reaction forms a much weaker Van der Waals complex bound by 8 kJ mol^{-1} and it would be expected that at 93 K the system would be further away from the proxy limit than the other three reactions. Rate coefficients for OH(v=1,2 and 3) + acetylene were measured at 93K and the resulting bimolecular plots are shown in Figure 7.10.

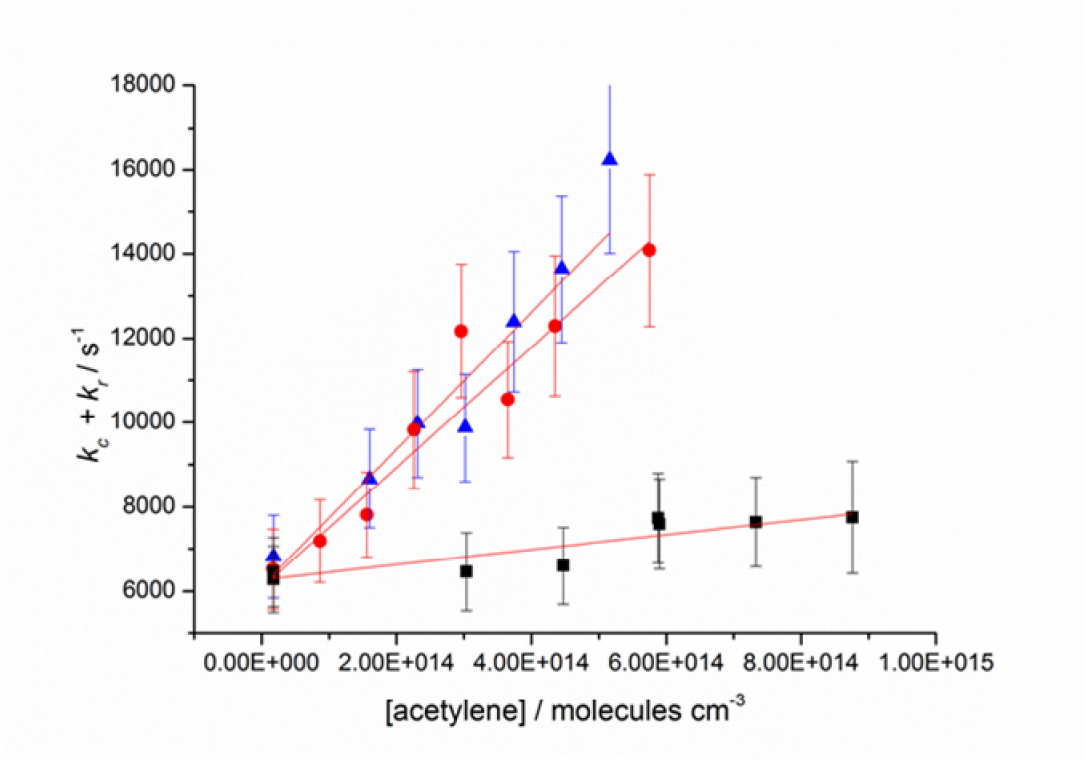

Figure 7.10 Bimolecular plots for the OH(v=3) (blue) OH(v=2) (red) and OH(v=1) (black) reactions with acetylene at 93K. The pseudo first order rate coefficients were obtained from fitting the experimental data with Eq 12 and they incorporate the 2σ both from the fitting process and [acetylene]. Bimolecular rate coefficients were obtained from a weight linear fit to each data set and the results are given in Table 7.2. The errors were obtained from the 95% confidence limits of the linear fits.

Given the weaker well in the OH + acetylene reaction and the consequently shorter lifetime of the energised complex, it would be expected that the OH + acetylene reaction would be closer to the SSH limit. The rate coefficients would then be expected to be further from the true high pressure limit for OH(v=0) + acetylene and to increase substantially with vibrational energy. It is immediately apparent that the rate coefficients are about an order of magnitude lower than for the other three systems considered. It is also evident that the v=1 reaction gives a much smaller rate coefficient than the other two vibrational levels, and both of these results would be expected given the substantially weaker well in the OH + acetylene system. However surprisingly the v=2 and v=3 data give rate coefficients that agree well within error and are almost converged. Contrary to this, the ratio $k_{(OH(v=1))}$ /$k_{(OH(v=3))}$

for the OH + acetylene reaction is 0.10 which is much lower than the proposed ratio of 0.33 at the SSH limit. To some extent both of these observations could be due in part to the large uncertainties in the OH + acetylene rate coefficients. These rate coefficients are much lower than the rate coefficients for the other three systems and particularly in the case of the OH(v=1) data, an increase of only 1000 s^{-1} is observed in the pseudo first order rate coefficient over the full experimental range of [acetylene] and this coupled with the large intercept in the bimolecular plot leads to a very large uncertainty in this number.

Co-reagent	Temperature / K	$k_{bi\ (v=1)}$ / molecule^{-1} cm^3 s^{-1}	$k_{bi\ (v=2)}$ / molecule^{-1} cm^3 s^{-1}	$k_{bi\ (v=3)}$ / molecule^{-1} cm^3 s^{-1}
methanol	93±4	(8.9±0.6) ×10^{-11}	(1.9±0.7) ×10^{-10}	(2.6±1.7) ×10^{-10}
	63±2	(1.4±0.5) ×10^{-10}	(2.6±0.4) ×10^{-10}	(2.8±0.5) ×10^{-10}
acetone	93±4	(1.7±0.6) ×10^{-10}	(2.4±0.6) ×10^{-10}	(2.9±0.7) ×10^{-10}
DME	93±4	(1.6±0.9) ×10^{-10}	(3.5±1.0) ×10^{-10}	(3.8±1.4)×10^{-10}
acetylene	93±4	(1.7±2.4)×10^{-12}	(1.6±0.4)×10^{-11}	(1.4±0.5)×10^{-11}

Table 7.2: Bimolecular rate coefficients for all the systems studied in this chapter.

The OH + acetylene reaction, is complex in that there are two possible adducts that could be stabilised. The potential energy surface for this reaction is shown below in Figure 7.11. The previous proxy method studies of Mckee *et al.* (6) measured the high pressure limit for stabilising the C_2H_2OH adduct bound by 131 kJ mol^{-1} and determined a high pressure limit of 1.1×10^{-12} molecule^{-1} cm^3 s^{-1} for this. (6) The rate coefficients measured in the current work are much larger than this, and it is likely that stabilisation of the van der Waals adduct is instead being observed. If this is the case, it would be expected that at sufficiently low temperatures, the high pressure limiting rate coefficient for this process should approach the gas kinetic limit as observed for the other three reactions, however the current experimental

data are insufficient to make any definite claims and further experiments and theoretical studies are needed for the OH + acetylene reaction.

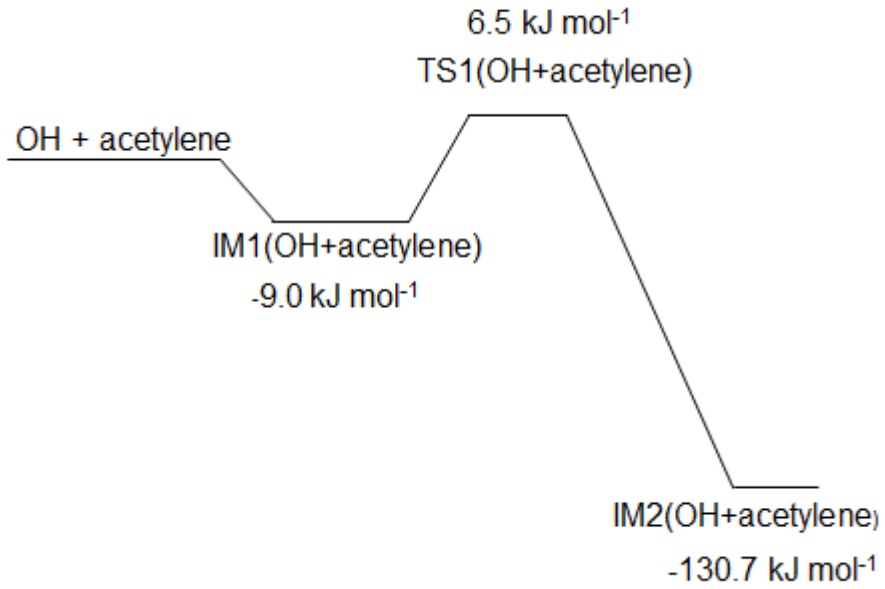

Figure 7.11: Stationary points on the OH + acetylene potential energy surface taken from McKee et al. (6) and the calculations presented in Section 6.2.2.2. The energy values show the electronic and zero point energies for each species relative to OH + acetylene and these were calculated at the CBS-QCI/APNO//B3LYP/6-311+G(3df,2p) level of theory apart from for IM1(OH+acetylene) for which the energy was calculated at the RHF-CCSD(T)/aug-cc-pvtz level of theory.

In order to compare the four systems fully, Table 7.3 gives the lifetimes of the pre-reaction complexes for each system as calculated using MESMER. (29) These were obtained from the calculations described in chapters 4, 5 and 6 by taking the inverse of the rate coefficient for re-dissociation. Here it can be seen that theoretical calculations predict that the lifetime for the acetylene complex with respect to re-dissociation is the lowest as has been proposed in this chapter. The calculated lifetimes are given at 298 K and 93 K. The lifetimes of the complexes formed with vibrational energy in the OH bond, will undoubtedly be shorter than the 93K lifetimes given here, however the relative lifetimes show the expected trend.

Reaction	t (298K) / s	t (93K) / s
OH+acetylene	2.33×10^{-14}	2.88×10^{-10}
OH+methanol	6.81×10^{-13}	2.05×10^{-7}
OH+DME	5.55×10^{-11}	1.11×10^{-4}
OH+acetone	1.59×10^{-10}	1.18×10^{-3}

Table 7.3: Association complex lifetimes at 298 K and 90 K as predicted from master equation calculations on the OH+acetylene, OH+methanol, OH+DME and OH+acetone reactions. The details of these master equation calculations have been described in sections 4.1.2.2, 4.2.2.2, 5.2.2 and 6.1.2.2.

Finally, in order to explore the effect of reducing the temperature upon promoting the proxy limit, experiments have also been performed at 63±2 K for the OH + methanol reaction only. Further studies of the temperature dependence of the proxy limit are needed for other systems, in particular the OH + acetylene reaction. However, the OH + acetylene reaction appears more complex , possibly due to contributions from the second, deeper well, and this system warrants more detailed investigation than will be given here. The OH + methanol reaction is the next closest reaction to the SSH limit and this reaction will be used to explore the general trend in the convergence of the different OH vibrational levels upon going from 93 to 63 K. The bimolecular plots for the OH(v=1,2,3) + methanol reaction at 65 K are shown in Figure 7.12 and the rate coefficients obtained from these are shown in Table 7.2 along with all the other rate coefficients measured in the current work.

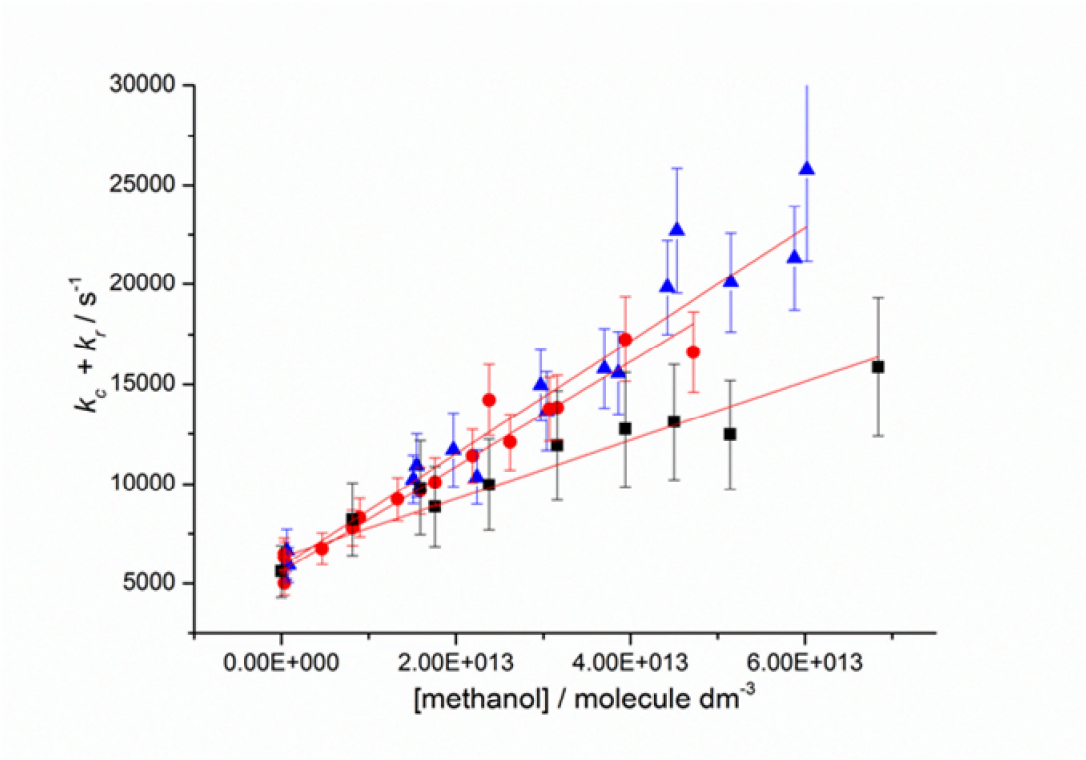

Figure 7.12: Bimolecular plots for the OH(v=3) (blue) OH(v=2) (red) and OH(v=1) (black) reactions with methanol at 63±2 K. The pseudo first order rate coefficients were obtained from fitting the experimental data with Eq 12 and they incorporate 2σ errors both from the fitting process and from [methanol]. Bimolecular rate coefficients were obtained from a weighted linear fit to each data set and these results are given in Table 7.2. The errors were obtained from the 95% confidence limits of the linear fits.

From these rate coefficient it can be seen that $k_{(OH(v=3))}$ increases to 2.8×10^{-10} molecule^{-1} cm^3 s^{-1} at 63±2 K. Assuming that the association rate to form the energised OH-methanol complex displays little dependence upon temperature, this value can be used to refine the lower limit of $k^{\infty}_{(OH+methanol)}$ obtained from $k_{(OH(v=3)+methanol)}$ at 93 K. From this data it is also seen that $k_{(OH(v=1))}$ /$k_{(OH(v=3))}$ increases between 93 K and 63 K showing that lowering the temperature appears to promote the proxy limit for the OH + methanol reaction.

Although proxy method measurements have not currently been performed for the OH + acetylene reaction at 63 , the convergence of the vibrational levels as the temperatures is decreased, can be explored by considering the higher temperature data of Mckee *et al.* (6) The bimolecular rate coefficients

for the v=1 and 2 vibrational levels are shown versus temperature in Figure 13. Here it can be seen that the value of $k_{bi\ OH(v=1)}$ shows no sign of approaching $k_{bi\ OH(v=2)}$ as the temperature is lowered and this suggests that $k_{bi\ OH(v=3)}$ measured here could be a significant underestimate of the true value of $k\infty$(OH + acetylene). Surprisingly the difference between $k_{bi\ OH(v=1)}$ and $k_{bi\ OH(v=2)}$, can be seen to increase as the temperature is lowered in the OH + acetylene although this could be due to a change in mechanism at low temperatures since as the thermal energy is reduced the system will increasingly sample IM1(OH+acetylene) rather than IM2(OH+acetylene).

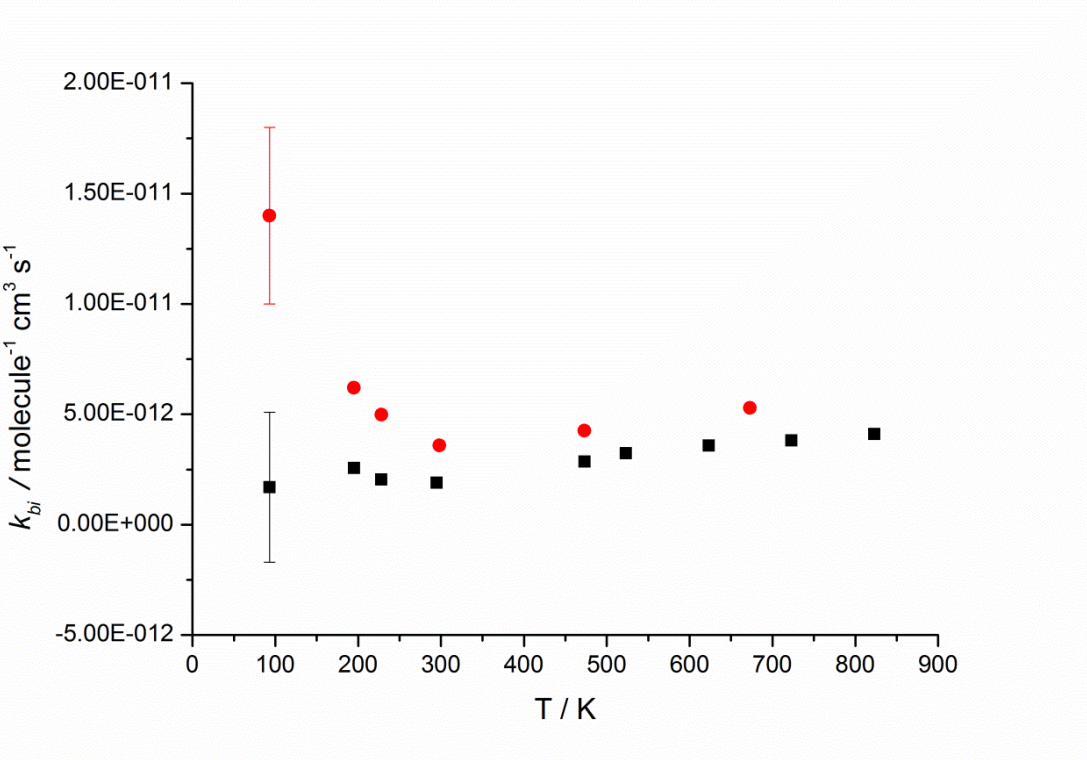

Figure 13: Bimolecular rate coefficients for the OH(v=2) + acetylene (red) and OH(v=1) + acetylene (black) reactions versus temperature. Data above 93K is taken from McKee et al. (6) and it can be seen that despite the large errors on the 93 K data, the V=1 and V=2 rate coefficients do not appear any more converged at 93 K

7.4. Conclusions

In this chapter, the first investigations of the proxy method to determine $k\infty$ at low temperatures have been performed, and it has been shown that by

going to lower temperatures, high pressure limiting rate coefficients for stabilisation into weak collision complexes can be explored.

In the introduction, two limits, the proxy limit and the SSH limit were defined and it was suggested that by going to lower temperatures the proxy limit could be promoted. At the proxy limit, the OH(v=1,2,3) rate coefficients would be expected to converge to a common value and in the current work, measurements of $k_{bi\,(OH(v=1))}/k_{bi\,(OH(v=3))}$ show that convergence increases with both the size of the co-reagent and with decreased temperature, as observed in the OH + methanol rate coefficients at 63 K. This shows that as the lifetime of the energised association complex increases the reaction's proximity to the proxy limit is also increased, as would be expected.

Interestingly, values of $k_{bi\,(OH(v=2))}/k_{bi\,(OH(v=3))}$ for the four reactions, show a less consistent trend and for all co-reagents, even acetylene, these two rate coefficients agree within error. In the introduction, it was stated that at the SSH limit $k_{bi\,(OH(v=3))} \approx 3\,k_{bi(OH(v=2))}/2$ and given the experimental errors, it is understandable that these two rate coefficients could appear converged in our experiments. Given this it is found here that $k_{bi\,(OH(v=1))}/k_{bi\,(OH(v=3))}$ is a better diagnostic for whether the proxy limit has been reached.

Although none of the systems studied, have reached the proxy limit, the results obtained here have given good lower estimates to the rate coefficients for the OH + methanol, OH+ DME and OH+ acetone reactions. For both acetone and methanol, $k_{(OH(v=3))}$ is approaching 3×10^{-10} molecule^{-1} cm^3 s^{-1} which is the estimate that we have used in the master equation calculations for the ILT A factor. For the OH + DME reaction $k_{(OH(v=3))}$ has reached 3.8×10^{-10} molecule^{-1} cm^3 s^{-1} suggesting that the collision rate for OH + DME is slightly larger than for OH + methanol and OH+ acetone. The lower limit obtained here for the OH + acetylene reaction, is considerably lower than for the other three systems. It is possible that this reaction is never 100% efficient (reaction occurs upon every collision), even at the high pressure limit and there are examples of systems where the capture rate is significantly lower than the gas kinetic limit. However it is more likely that this reaction is simply further from the proxy limit at 93 K than the other systems.

It is clear that rate coefficient measurements need to be extended to lower temperatures, particularly in the case of the OH + acetylene, and theoretical investigations are also desirable. However, in this preliminary study on the proxy method at low temperatures, it has been show that as predicted, the proxy limit is promoted as the temperature is reduced. The ratio of rate coefficients $k_{(OH(v=1))}$ /$k_{(OH(v=3))}$ has been shown to be a good diagnostic for this, and these results show that care needs to be taken in associating $k_{(OH(v=1))}$ with the high pressure limit for a reaction as was done in the case of the OH + acetone reaction at 298 K. This study has also obtained valuable lower limits to the the high pressure limiting rate coefficients for a number of reactions, showing as has been assumed throughout this thesis, that the high pressure limit for forming these weak pre-reaction complexes is determined by the rate at which the reaction partners collide.

7.5. References

1. ROBERTSON, S.H., M.J. PILLING, D.L. BAULCH and N.J.B. GREEN. Fitting of Pressure-Dependent Kinetic Rate Data by Master Equation Inverse Laplace Transform Analysis. *Journal of Physical Chemistry*, 1995, **99**(36), pp.13452-13460.
2. QUACK, M. and J. TROE. Complex-Formation in Reactive and Inelastic-Scattering - Statistical Adiabatic Channel Model of Unimolecular Processes Iii. *Berichte Der Bunsen-Gesellschaft-Physical Chemistry Chemical Physics*, 1975, **79**(2), pp.170-183.
3. SMITH, I.W.M., D.J. WRIGLEY and D.H. JAFFER. Kinetics of Molecules in High Vibrational-States Studied by Time-Resolved Vibrational Chemi-Luminescence. *Abstracts of Papers of the American Chemical Society*, 1980, **180**(Aug), pp.96-Phys.
4. JAFFER, D.H. and I.W.M. SMITH. Time-Resolved Measurements on the Relaxation of Oh(V = 1) by No, No2 and O-2. *Faraday Discussions*, 1979, **67**, pp.212-220.
5. SILVENTE, E., R.C. RICHTER and A.J. HYNES. Kinetics of the vibrational deactivation of OH X-2 Pi (upsilon=3, 2, 1) with hydrides and reduced sulfides. *Journal of the Chemical Society-Faraday Transactions*, 1997, **93**(16), pp.2821-2830.
6. MCKEE, K.W., M.A. BLITZ, P.A. CLEARY, D.R. GLOWACKI, M.J. PILLING, P.W. SEAKINS and L.M. WANG. Experimental and master equation study of the kinetics of OH+C2H2: Temperature dependence of the limiting high pressure and pressure dependent rate coefficients. *Journal of Physical Chemistry A*, 2007, **111**(19), pp.4043-4055.
7. TALUKDAR, R.K., T. GIERCZAK, D.C. MCCABE and A.R. RAVISHANKARA. Reaction of hydroxyl radical with acetone. 2.

Products and reaction mechanism. *Journal of Physical Chemistry A*, 2003, **107**(25), pp.5021-5032.

8. SMITH, I.W.M. The temperature-dependence of elementary reaction rates: beyond Arrhenius. *Chemical Society Reviews*, 2008, **37**(4), pp.812-826.
9. HERBST, E. Chemistry in the Interstellar-Medium. *Annual Review of Physical Chemistry*, 1995, **46**, pp.27-53.
10. SMITH, I.W.M. Reactions at very low temperatures: Gas kinetics at a new frontier. *Angewandte Chemie-International Edition*, 2006, **45**(18), pp.2842-2861.
11. Collisional energy transfer, intramolecular vibrational relaxation and unimolecular reactions. *Journal of the Chemical Society-Faraday Transactions*, 1997, **93**(21), pp.3741-3750.
12. EHRENFEST, P., H.B.G. CASIMIR and M.J. KLEIN. *Collected scientific papers.* Amsterdam: North-Holland Publishing Company, 1959.
13. LAMBERT, J.D. *Vibrational and rotational relaxation in gases.* The international series of monographs on chemistry. Oxford: Clarendon Press, 1977.
14. SCHWARTZ, R.N., Z.I. SLAWSKY and K.F. HERZFELD. Calculation of Vibrational Relaxation Times in Gases. *Journal of Chemical Physics*, 1952, **20**(10), pp.1591-1599.
15. TANCZOS, F.I. Calculation of Vibrational Relaxation Times of the Chloromethanes. *Journal of Chemical Physics*, 1956, **25**(3), pp.439-447.
16. AKER, P.M. and J.J. SLOAN. The Initial Product Vibrational-Energy Distribution in the Reaction between O(1D) and H2. *Journal of Chemical Physics*, 1986, **85**(3), pp.1412-1417.
17. G. DIXON-LEWIS, D.J.W. The oxidation of hydrogen and carbon monoxide C.H. Bamford,C.F.H. Tipper (Eds.)

    Comprehensive Chemical Kinetics, 1977, **17**, pp.1-248.
18. CALLEAR, A.B. and H.E. VAN DEN BERGH. An hydroxyl radical infrared laser. *Chemical Physics Letters*, 1971, **8**(1), pp.17-18.
19. ANDERSON, J.G. Free-Radicals in the Earths Atmosphere - Their Measurement and Interpretation. *Annual Review of Physical Chemistry*, 1987, **38**, pp.489-520.
20. WANG, W., R. GONZALEZ-JONTE and A.J.C. VARANDAS. Quasiclassical trajectory study of the environmental reaction O+HO(2)-> OH+O(2). *Journal of Physical Chemistry A*, 1998, **102**(35), pp.6935-6941.
21. DOBBYN, A.J. and P.J. KNOWLES. A comparative study of methods for describing non-adiabatic coupling: diabatic representation of the $\Sigma+ / \Pi$ HOH and HHO conical intersections. *Molecular Physics*, 1997, **91**(6), pp.1107-1123.
22. AHMED, M., D.S. PETERKA and A.G. SUITS. Crossed-beam reaction of O(1D)+D2 -> OD+D by velocity map imaging. *Chemical Physics Letters*, 1999, **301**(3-4), pp.372-378.
23. AOIZ, F.J., L. BANARES, J.F. CASTILLO, V.J. HERRERO, B. MARTINEZ-HAYA, P. HONVAULT, J.M. LAUNAY, X. LIU, J.J. LIN, S.A. HARICH, C.C. WANG and X. YANG. The O(1D)+H_2 reaction at 56 meV collision energy: A comparison between quantum

mechanical, quasiclassical trajectory, and crossed beam results. *Journal of Chemical Physics*, 2002, **116**(24), pp.10692-10703.

24. ALTHORPE, S.C. and D.C. CLARY. Quantum scattering calculations on chemical reactions. *Annual Review of Physical Chemistry*, 2003, **54**, pp.493-529.
25. AOIZ, F.J., L. BANARES and V.J. HERRERO. Dynamics of insertion reactions of H-2 molecules with excited atoms. *Journal of Physical Chemistry A*, 2006, **110**(46), pp.12546-12565.
26. DURAND, G. and X. CHAPUISAT. An Abinitio Description of the Excited-States of the Reaction O(3p, 1d) + H2-]Oh(2pi,2sigma+) + H - an Attempt to Describe Several Potential-Energy Surfaces with Constant Accuracy. *Chemical Physics*, 1985, **96**(3), pp.381-407.
27. TALUKDAR, R.K. and A.R. RAVISHANKARA. Rate coefficients for O(D-1)+H-2, D-2, HD reactions and H atom yield in O(D-1)+HD reaction. *Chemical Physics Letters*, 1996, **253**(1-2), pp.177-183.
28. *LIFBASE: Database and spectral simulation* [CD-ROM]. SRI International Report MP 99-009, 1999.
29. ROBERTSON, S.H., GLOWACKI, D. R., LIANG, C.-H.; MORLEY, C., PILLING, M. J.,. MESMER (Master Equation Solver for Multi-Energy Well Reactions), an object oriented C++ program for carrying out ME calculations and eigenvalue-eigenvector analysis on arbitrary multiple well systems. http://sourceforge.net/projects/mesmer. 2008.

Chapter 8: Conclusions and future work.

In this thesis, low temperature rate coefficients have been presented for a number of reactions with energy barriers upon their potential energy surfaces (PES) between reactants and products. All of these reactions exhibit rate coefficients of less than 5×10^{-12} molecule^{-1} cm^3 s^{-1} at room temperature and as such it would be expected that these reactions would be slow at very low temperatures (T < 100 K). However it is demonstrated in this thesis, that in each of these reactions a negative temperature dependence is observed to the rate coefficients below 200 K and in some cases (OH + acetone, OH + methanol), the rate coefficient is found to have increased by over an order of magnitude between 200 K and 80 K.

In the current work the lowest temperatures at which rate coefficients have been performed is 63 K but theoretical extrapolations of these rate coefficients down to interstellar medium (ISM) conditions (10 K, 1000 molecule^{-1} cm^3 s^{-1}) suggest that these reactions could be approaching the capture limit, (every collision between reactants results in a successful reaction). The reactions studied all involve the OH radical reacting with some oxygenated organic molecule and many of these molecules have been observed in the ISM. However the databases used to model chemical kinetics in the ISM contain none of the reactions studied here. Furthermore there are many reactions which occur over similar potential energy surfaces to the reactions studied here, and there could be many more neutral-neutral reactions which warrant inclusion in the astrochemical kinetic databases.

In the context of low temperature kinetics, the key feature of all the PES's considered in this thesis, is the presence of a pre-reaction complex between the associating reactants. In Chapters 4 and 5, the reactions between the OH radical and acetone, DME and methanol, all involve the formation of a hydrogen bonded complex (bound by ~ 20 kJ mol^{-1}). At low temperature such a complex can then facilitate an increase in the rate coefficient for OH loss in one of two ways, either through stabilisation of this complex via a barrierless reaction path, or through providing an increased, energised

adduct lifetime, which in conjunction with quantum mechanical tunnelling, increases the rate of OH loss due to hydrogen abstraction through a barrier.

In the OH + acetone and OH + DME reactions studied in Chapter 4, it was found that a stabilised hydrogen complex was the dominant product at 80 K and pressure dependence was observed to the rate coefficients for both of these reactions. Such a stabilisation mechanism is not relevant to the very low density conditions of the ISM, however theoretical calculations performed for these reactions, predict that at 10 K these reactions are approaching the capture limit due to quantum mechanical tunnelling to form abstraction products. In contrast to this the rate coefficients for OH + methanol, presented in Chapter 5 were found to be independent of pressure at 80 K suggesting that a tunnelling mechanism rather than a stabilisation mechanism was occurring. This was then confirmed by observation of the methoxy radical abstraction product on the experimental timescale and master equation modelling.

In Chapter 6 the reactions between OH and ammonia and acetylene were studied. In these reactions the association complexes are more weakly bound Van der Waals complexes (5 – 10 kJ mol^{-1}) however it was found that these weak complexes were sufficient to produce a negative temperature dependence in the rate coefficients for each reaction below 200 K due to both stabilisation (acetylene) and tunnelling (ammonia). Considering these results in conjunction with those from chapters 4 and 5 reactions, it is proposed here that any hydrogen transfer reaction with a weak association complex (>5 kJ mol^{-1}) on its PES, is likely to exhibit kinetic behaviour similar to the reactions studied here, and as such, is worth consideration in the context of low temperature environments.

A key step in all the reactions studied in chapters 4,5 and 6 is the barrierless association of the reagents to form the association complex. In Chapter 7 vibrationally excited OH radical are used to in order to probe the high pressure limiting capture rates for complex formation in the reactions between OH and acetone, DME, methanol and acetylene. These represent the first proxy method measurements below 200 K and it is proposed that as the temperature is reduced and the vibrational energy level in increased,

the rate coefficients for OH(v=i) + B approach the high pressure limit for the OH + B reaction. From this work it appears that the capture rate coefficients for OH + acetone, OH + DME and OH + methanol are greater 3×10^{-10} molcule^{-1} cm^{3} s^{-1} validating the choice of parameters used in the inverse Laplace transform calculations presented in this thesis.

The results in this thesis have highlighted an overlooked class of reaction in the context of low temperature environments but further studies are required to explore these reactions. In terms of experiments it would be desirable to study these reactions over a wider range of temperatures in particular in the 100 – 200 K regime to fill in the gap in rate coefficients between the high and low temperature regimes. Additionally future experiments could be performed in order to attempt to observe some more reaction products via laser induced fluorescence, as was done in the case of the methoxy radical in Chapter 5.

From a theoretical point of view, the reactions studied in this thesis have highlighted some of the uncertainties in the master equation analysis. For these reactions, accurate determinations of density of states and transmission coefficients are important and future work would ideally aim to couple some more sophisticated methods of determining these quantities with the MESMER code. Finally considering the proxy method work, trajectory calculations would be an interesting addition to these experiments in order to probe the way the assumptions of the proxy method as the temperature is reduced.

Appendix A.
The hindered rotation potentials used in the OH + acetone reaction.

In this appendix the hindered rotation potentials for the OH + acetone system are shown as described in Section 4.1.2.2

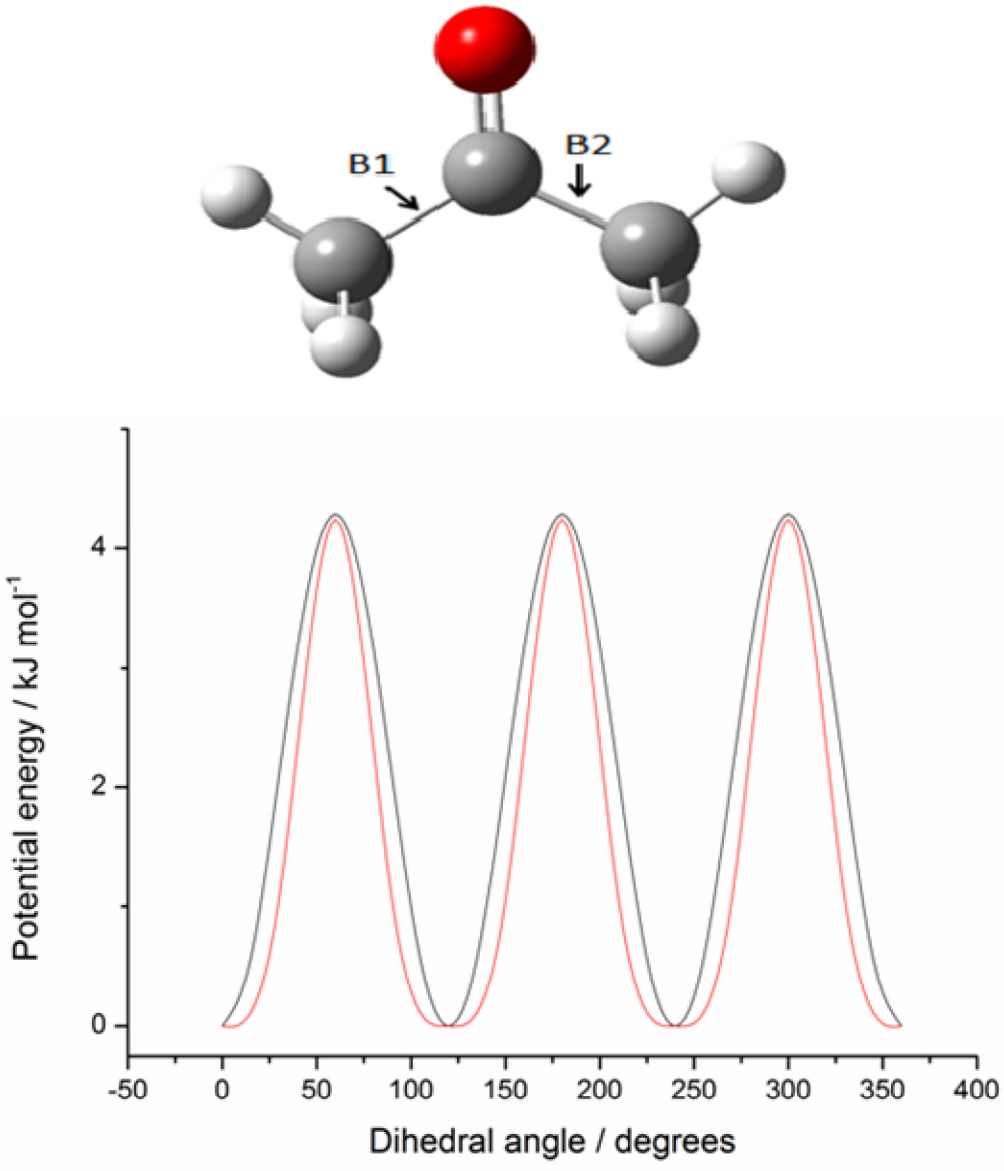

Figure A.1: The above diagram shown the structure of acetone optimised at the MPW1K/6-31+G(2d,2p) level of theory. The bonds about which the hindered rotation normal modes rotate are labelled B1(both CH_3 groups rotating in the same direction) and B2 (both CH_3 groups rotating in opposite directions). Below the total electronic energy calculated at the MPW1K/6-31+G(2d,2p) is plotted versus dihedral angle for both B1 (red) and B2(black).

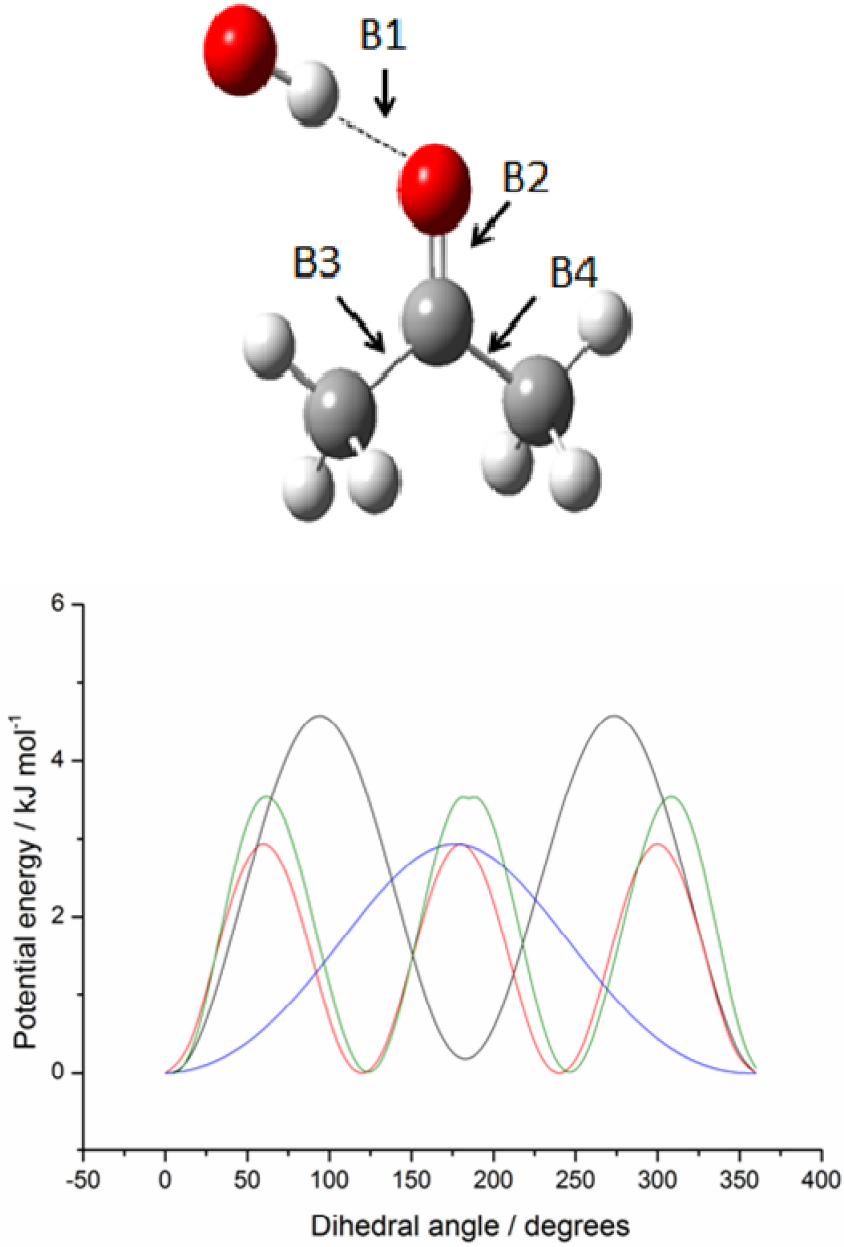

Figure A.2: The above diagram shown the structure for the acetone_OH complex IM1(OH+acetone), optimised at the MPW1K/6-31+G(2d,2p) level of theory. The bonds about which the hindered rotation normal modes rotate are labelled. Below the total electronic energy calculated at the MPW1K/6-31+G(2d,2p) is plotted versus dihedral angle for B1 (blue), B2(black), B3(green) and B4(red).

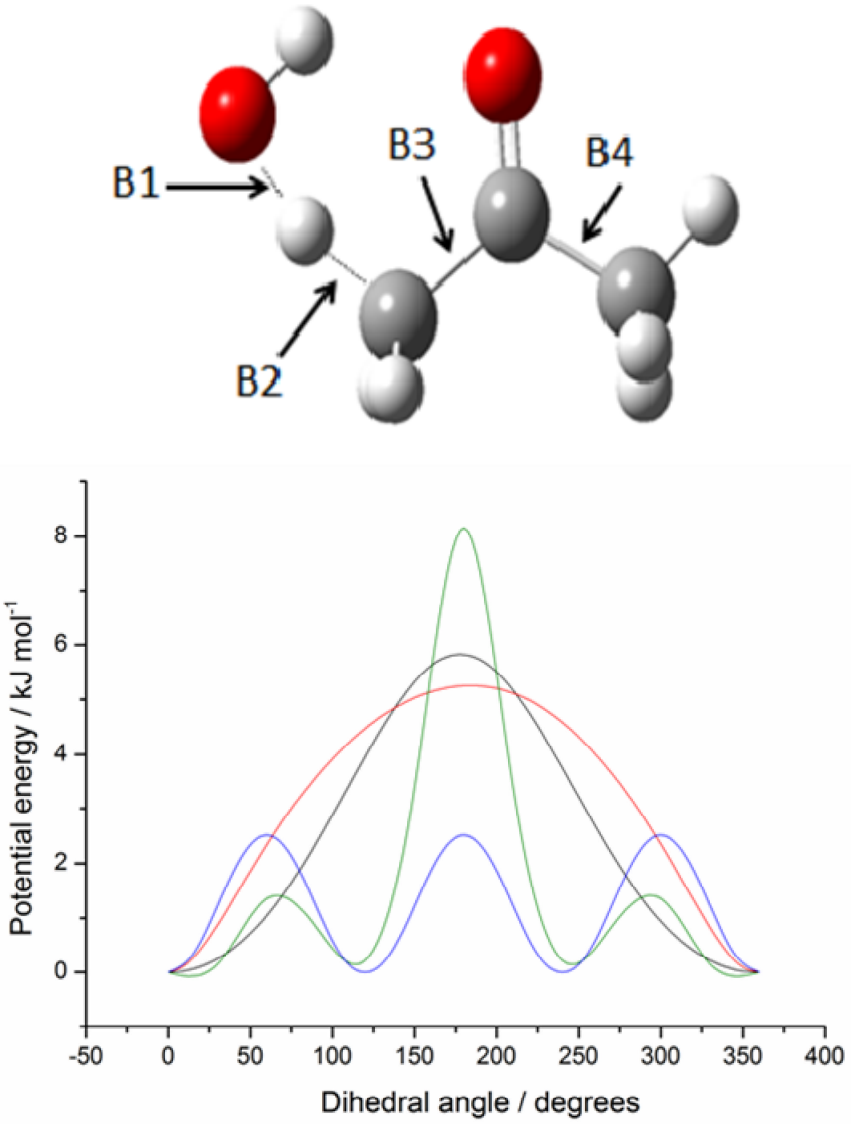

Figure A.3: The above diagram shown the structure for the acetone_OH transition state TS1(OH+acetone), optimised at the MPW1K/6-31+G(2d,2p) level of theory. The bonds about which the hindered rotation normal modes rotate are labelled. Below the total electronic energy calculated at the MPW1K/6-31+G(2d,2p) is plotted versus dihedral angle for B1 (red), B2(black), B3(green) and B4(blue).

Appendix B
The hindered rotation potentials used in the OH + DME reaction

In this appendix the hindered rotation potentials for the OH + DME system are shown as described in Section 4.2.2.2.

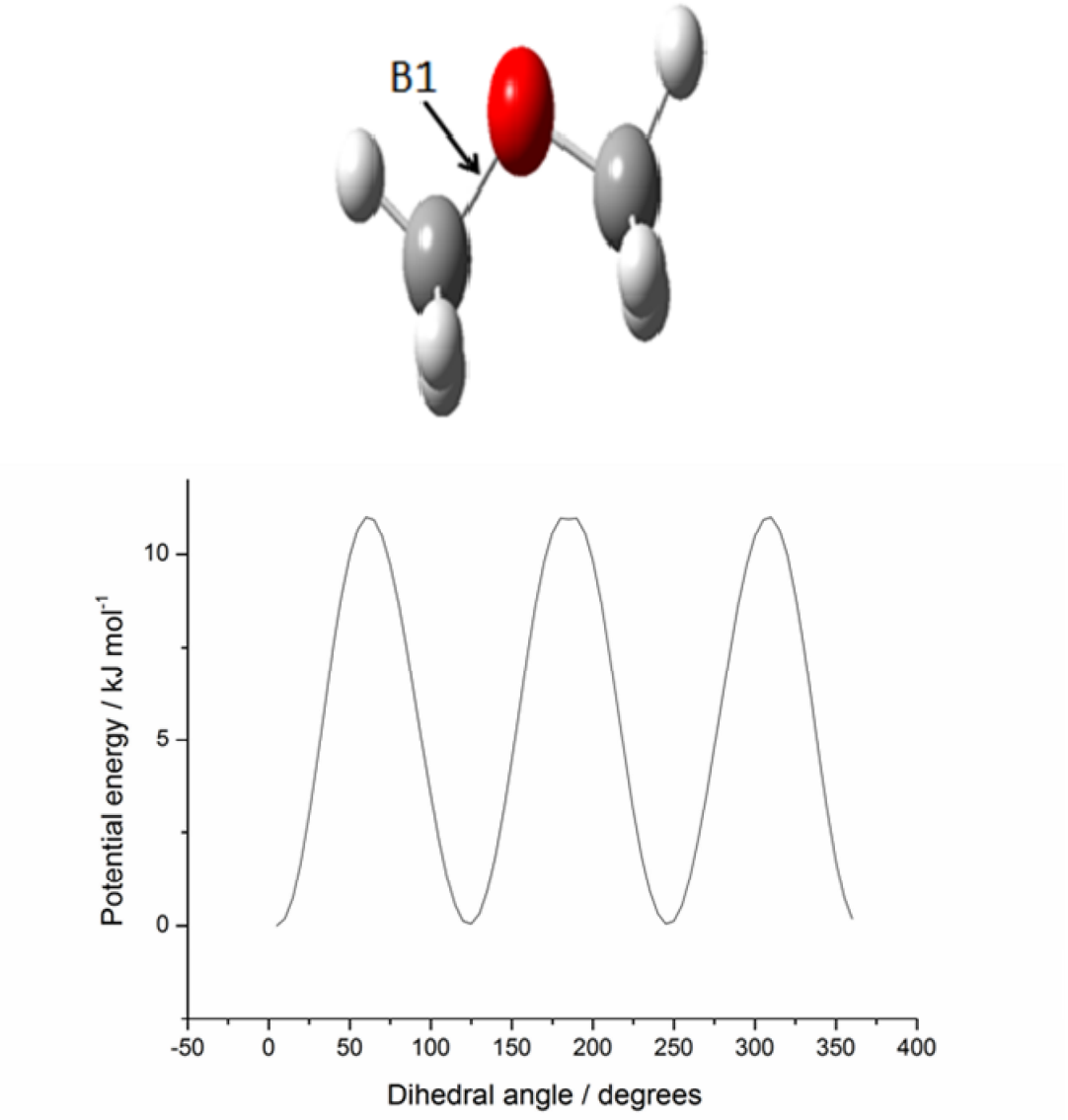

Figure B.1: The above diagram shown the structure of DME, optimised at the MPW1K/6-31+G(2d,2p) level of theory. The bond about which the hindered rotation normal modes rotate is labelled. Below the total electronic energy calculated at the MPW1K/6-31+G(2d,2p) is plotted versus dihedral angle for B1.

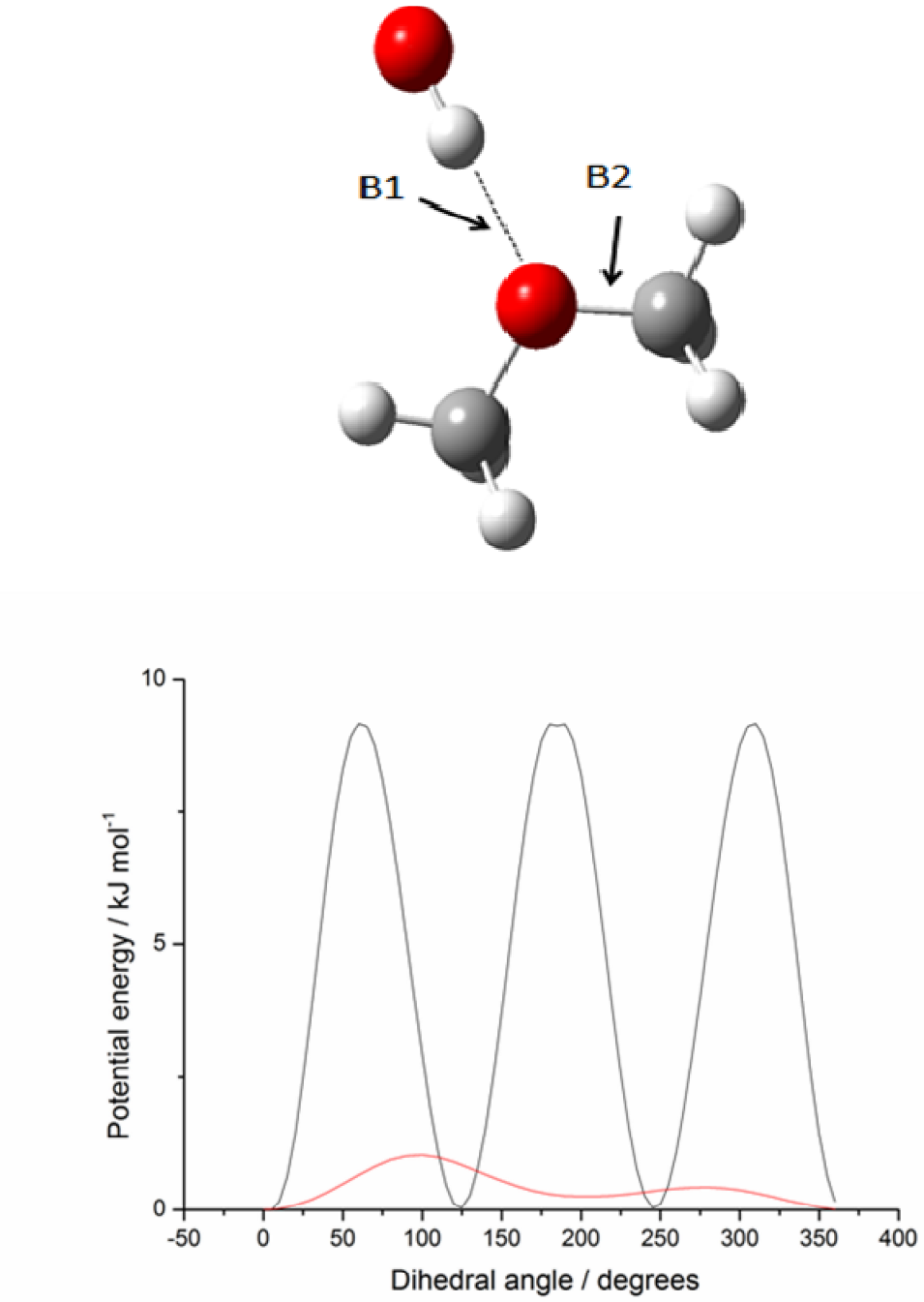

Figure B.2: The above diagram shown the structure of the OH_DME complex IM1(OH+DME), optimised at the MPW1K/6-31+G(2d,2p) level of theory. The bonds about which the hindered rotation normal modes rotate are labelled. Below the total electronic energy calculated at the MPW1K/6-31+G(2d,2p) is plotted versus dihedral angle for B1(red) and B2(black).

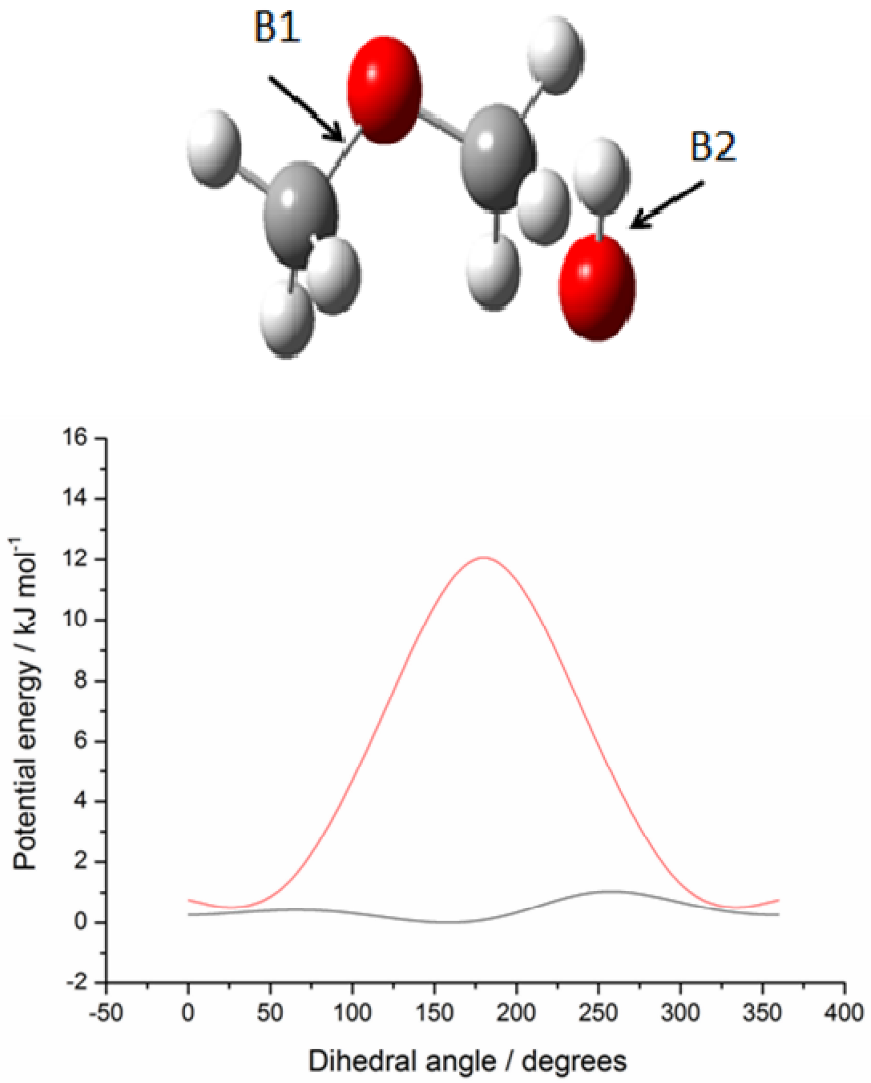

Figure B.3: The above diagram shown the structure of the OH_DME transition state TS1(OH+DME), optimised at the MPW1K/6-31+G(2d,2p) level of theory. The bonds about which the hindered rotation normal modes rotate are labelled. Below the total electronic energy calculated at the MPW1K/6-31+G(2d,2p) is plotted versus dihedral angle for B1(red) and B2(black).

Appendix C
The hindered rotation potentials used in the OH + DME reaction

In this appendix the hindered rotation potentials for the OH + methanol system are shown as described in Section 5.2.2. In this case the CH_3 rotations in methanol, IM1(OH+methanol), IM1b(OH+methanol) and TS1_H(OH+methanol) have almost identical potentials and only hindered rotations for TS1_H and TS1_M are shown.

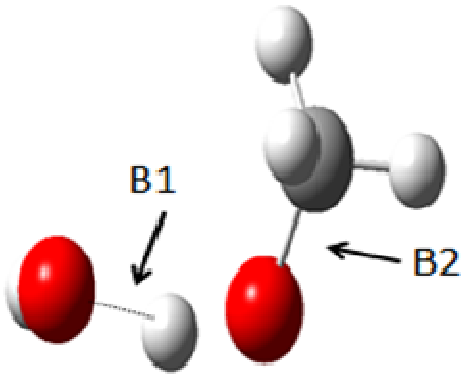

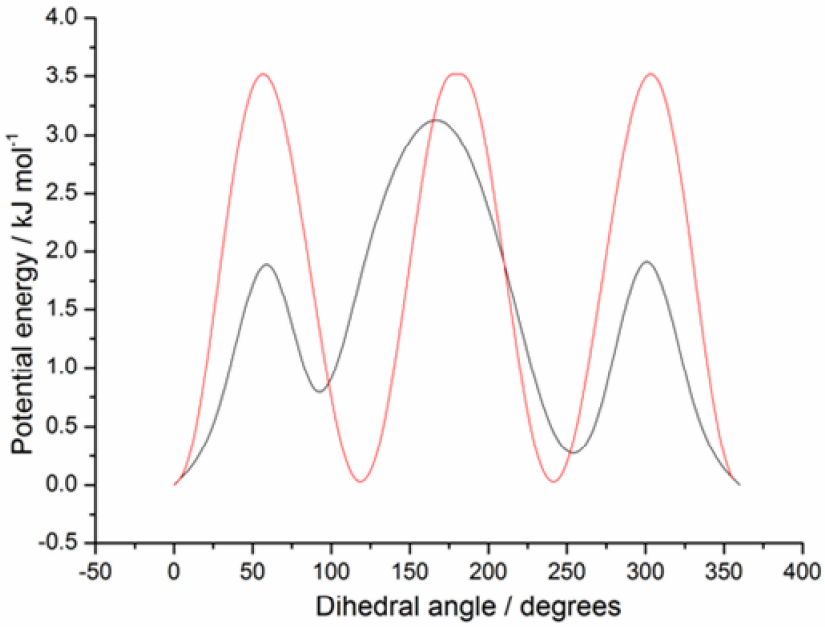

Figure C.1: The above diagram shown the structure of the OH_methanol transition state TS1_H(OH+methanol), optimised at the MPW1K/6-31+G(2d,2p) level of theory. The bonds about which the hindered rotation normal modes rotate are labelled. Below the total electronic energy calculated at the MPW1K/6-31+G(2d,2p) is plotted versus dihedral angle for B1(black) and B2(red).

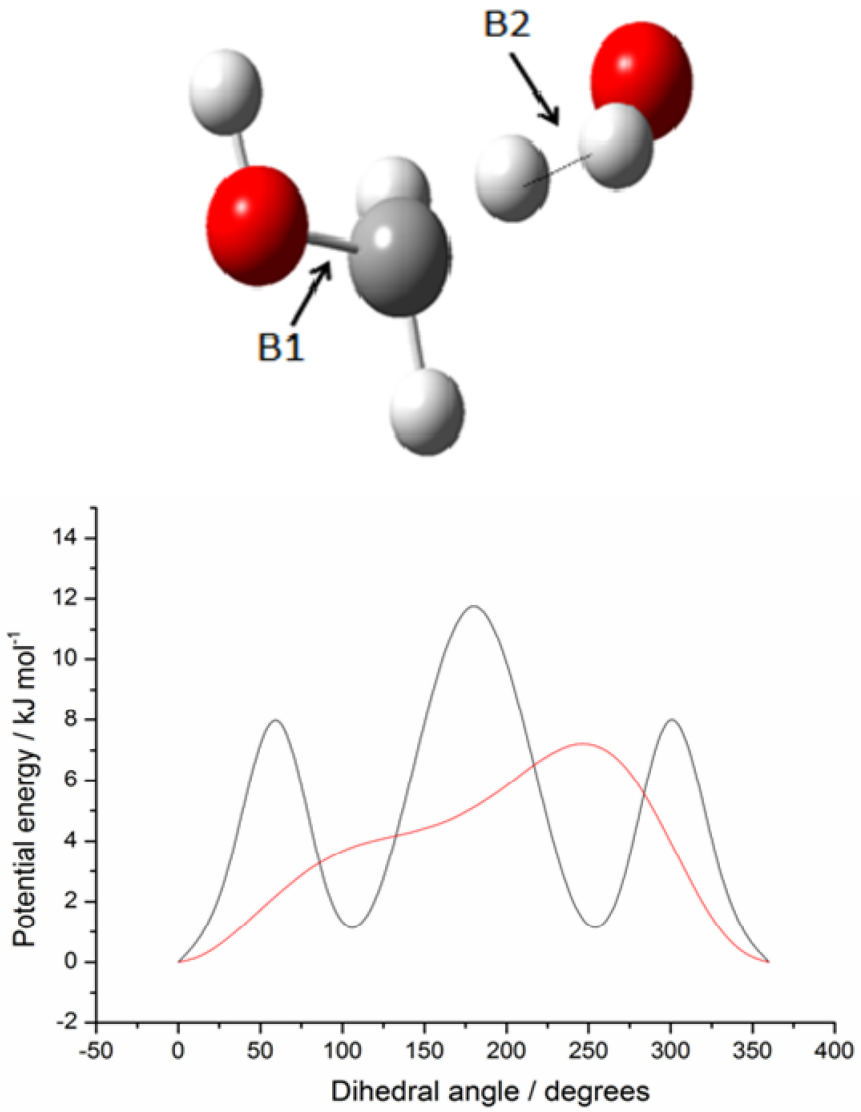

Figure C.2: The above diagram shown the structure of the OH_methanol transition state TS1_M(OH+methanol), optimised at the MPW1K/6-31+G(2d,2p) level of theory. The bonds about which the hindered rotation normal modes rotate are labelled. Below the total electronic energy calculated at the MPW1K/6-31+G(2d,2p) is plotted versus dihedral angle for B1(black) and B2(red).